

UNIVERSITÀ DEGLI STUDI DI NAPOLI “FEDERICO II”

FACOLTÀ DI INGEGNERIA

DIPARTIMENTO DI INGEGNERIA DEI MATERIALI E DELLA PRODUZIONE



PhD thesis in

Ingegneria dei Materiali e delle Strutture

XXIV Cycle

**MECHANICAL-BASED OPTIMIZATION PROCESSES
IN BIOLOGICAL STRUCTURES**

Coordinator

Ch.^{mo} Prof. G. Mensitieri

Tutor

Ch.^{mo} Prof. P.A. Netti

CoTutor

Ch.^{mo} Prof. M. Fraldi

PhD Student

Ing. Aurora Marzullo

INDEX

INTRODUCTION

I. REMARKS ON THE THEORY OF ELASTICITY

1. Deformation Theory	1
1.1. Deformation in \mathbb{R}^n	1
1.2. Volume element in deformation configuration	5
1.3. The Piola transform; area element in the deformed configuration	6
1.4. Length element in the deformed configuration; Strain Tensor	9
2. The Equation of Equilibrium	14
2.1. Applied Forces	15
2.2. The stress principle of Euler and Cauchy	17
2.3. Cauchy's theorem; The Cauchy stress tensor	19
3. Linear Anisotropic Elastic Media	21
3.1. Elastic Stiffnesses	21
3.2. Elastic Compliances	24
3.3. Contracted Notations	25
3.4. Material Symmetry	28
3.5. The Elasticity Tensor for Materials with Symmetry Planes	30
3.6. Restrictions on Elastic Constants	35

II. HETEROGENEOUS MATERIALS

1. Inhomogeneous solids: SAS/DAS theorems	37
1.1. Stress Associated Solution (SAS) Theorem for inhomogeneous elasticity	38
1.1.a. Zero- eigenvalue stress and zero-eigenvalue strain fields	39
1.1.b. Stress Associated Solutions (SAS) Theorem	39
2. Anisotropic media: volume fraction and Fabric Tensors	43
2.1. Mean Intercept Length (MIL) Tensor	44
2.2. Fabric Tensor and Damage Distribution	45
2.4. Relationship between Fabric Tensor and Elasticity Tensor	51

III. THEORY OF HOMOGENIZATION & MICROMECHANICS

1. Thermodynamic framework and mathematically well-posed homogenization approaches	56
1.1. Representative Volume Element (RVE)	56
1.2. Localization Problem	58
1.3. Example of pure elasticity	60
1.3.a. The localization problem	60
1.3.b. Case where \mathbf{E} is prescribed	61
1.3.c. Case where Σ is prescribed	62
1.3.d. Equivalence between 'prescribed stress' and 'prescribed strain'	64

2. Micro mechanics of porous materials: J-tensor and dilute distribution of voids cases	65
2.1. Average strain for prescribed macro-stress	68
2.2. Overall compliance tensor for porous elastic solids	70
2.3. Average stress for prescribed macro-strain	73
2.4. Overall elasticity tensor for porous elastic solids	75
3 Micromechanics	78
3.1 Unidirectional short fiber composite	78
3.2 Random short fiber composite	81
IV. OPTIMIZATION STRATEGIES BEHIND BIOLOGICAL FEATURES	
1. Introduction	83
2. Biological materials vs engineering materials	84
3. Simple geometry in complex organism	87
3.1. The Bee's cell	92
4. Mathematics in Nature: Fibonacci Numbers	94
5. Classification of biological structures	94
5.1. Experimental observation on time	95
5.2.1 Experimental observation on scale	97
5.2.2 Hierarchical structures	97
5.2.3 Mathematics and growth: fractal structures	99
5.2.4 To observe for imitation	100
5.2.5 To observe for applying functioning logic	102
5.2.6 Classical model	107
5.2.7 Non classical model	107
V. OPTIMIZATION STRATEGIES BEHIND BIOLOGICAL FEATURES	
1. Introduction	120
1.1. Topology Optimization: Etymology and History	123
1.2. Formulation Problem	125
1.3. Basic problem statement	127
1.4. Isotropic models for solid-void interpolation in elasticity	129
1.4.1 The SIMP model	129
1.4.2 Microstructures realizing the SIMP-model	130
1.4.3 Variable thickness sheets - the Voigt bound	136
1.4.4 The Hashin-Shtrikman bound	137
1.4.5 Other models	138
1.4.6 Example designs	139
1.5. Homogenization models with anisotropy	140
1.6. Multiple materials in elasticity	145
1.6.1 Two materials with non-vanishing stiffness	145
1.6.2 Three-materials design	147
1.7. Multiple physics, nonlinear problems and anisotropic phases	149

1.7.1 Multiple physics	149
1.7.2 Nonlinear problems	151
1.7.3 Anisotropic phases	152
1.8. Conclusions and perspectives	152
VI. OPTIMIZATION PROCESSES IN NATURE	
1. Mechanical-based motivation of evolutionary process in moles: “optimization over time”	154
1.1. Introduction	154
1.2. Failure Criteria	154
1.3. Classification of mole rats	157
1.4. Soil and Burrow characteristics	161
1.5. Conclusions	168
2. Mechanical-based design of “fiber-reinforced” cartilage structures: “optimization over space”	169
2.1. Cartilage	169
2.2. Mathematical model	173
2.3. Conclusions	182
3. Mechanical-based design of “Bi-layer poroelastic plates: “optimization over space”	183
3.1 Introduction	183
3.2 Formulation and solution	185
3.3 Values of the parameters	191
3.4 Result and qualitative remarks	191
3.5 Conclusions	200
VII. CONCLUSIONS	201
REFERENCES	204

INTRODUCTION

The process of the evolution on earth during the last approximately 3.4 billion years resulted in a vast variety of living structures. The organisms were able to dynamically adapt to various environmental conditions. It is therefore the principal goal of biomimetics to provide an in-depth understanding of the solutions and strategies, having evolved over time and their possible implementation into technological practice. (Bar-Cohen 2006)

Engineers, scientists, and business people are increasingly turning toward Nature for design inspiration.

Nature, through billions of years of trial and error, has produced effective solutions to innumerable complex real-world problems.

The rigorous competition of natural selection means that waste and efficiency are not tolerated in natural systems, unlike many of the technologies devised by humans.

Nature has developed materials, objects and processes that function from the macroscale to the nanoscale.

The understanding of the functions provided by objects and processes found in Nature can guide us to imitate and produce nanomaterials, nanodevices and processes. The inspiration from a natural system, also referred to as bio-inspiration, is now becoming a widespread practice in design: in spite of the limited number of patented products which can be considered fully inspired to Nature, the incorporation of biological concepts and functions in design objects is increasingly common (Vincent 2009). Bio-inspiration is not to be intended as a formal imitation of the natural geometry, aimed at mimicking functions and morphologies of natural structures. In contrast, bio-inspiration would rather imply transferring to the culture of design new qualities and strategies inspired by Nature, this process requires to establish a correlation between the design issues and the solutions offered by Nature. The analogy between the problem to be solved and the natural solution may be conceived at different levels, as suggested in the chapter IV of this thesis.

In this work we have classified the structures into two main areas: experimental observation on time and experimental observation on scale. As regard the classification on time, time rangings were considered from ere to seconds.

As regards, the experimental observations on scale, it has been referred to the hierarchical structures, whereas, therefore, a macro, micro and nano-scale.

Once the classification has been made, we divided them according to their ability to imitate Nature: they could be observed for simple imitation or for applying functioning logic. The last sub-division is related to the complexity of the problem and, therefore, the number of variables involved. The problems are divided, therefore, in the classical and non classical.

The evolution principle, provides an explanation for the differences in structures, functions, and behaviors among organisms and describes the adaptation process that ensures the survival of different species in their environment. As examples of this kind of optimization, we have studied the structures of mole-rat burrows and the objective of this study consists in exploring the possible mechanical-based relationship between the geometry of burrows and geo-mechanical characteristics of the soil that have evolved over time.

Biological materials, over millions of years of evolution, were developed into hierarchical structures with intricate architectures from nm to m that often extend into macro scale resulting in unique, species-specific overall morphology with characteristic functions that provide an advantage for the organism in its environment. As example of optimization over space, we have studied fiber-reinforced cartilage structures showing how the biological tissues are made to minimized the strain energy function.

As a final example, the poroelastic solution by Cowin (Cowin 1994) obtained for homogeneous plates was generalized to the case where the material is constituted by two components. The variation of the response function, in terms of stresses, pressure and fluid content and velocity, was analyzed by using several parametric values of permeabilities values, Young's moduli and Poisson's ratios. The results allow to better interpret the adaptive processes governing many biological tissue, in

which the hierarchical heterogeneous features result from optimization logics aimed to obtain best varying stiffness and permeability features.

Additionally, the analytical solution could be helpfully employed for designing controlled release systems of drugs, as those named “ *.mechanically activated drug delivery devices*”

The present dissertation, within a mechanical framework aims to highlight how Nature always finds the best way to join a goal by optimizing the use of resources and by changing accordingly to external stimuli.

It is felt that this contribution can be addressed to investigate and better understand the principles that Nature exploits for determining its functions and shapes, at the different scale levels, in this manner paving the way for overcoming imitation of Nature and designing new intelligent materials and structures.

CHAPTER I

REMARKS ON THE THEORY OF ELASTICITY

1. Deformation Theory

A central problem in nonlinear, three-dimensional elasticity consists in finding the equilibrium position of an elastic body that occupies a *reference configuration* $\bar{\Omega}$ in the absence of applied forces, where Ω is a bounded open connected subset of \mathbb{R}^3 with a Lipschitz-continuous boundary. When subjected to applied forces, the body occupies a *deformed configuration* $\varphi(\bar{\Omega})$, characterized by mapping $\varphi: \bar{\Omega} \rightarrow \mathbb{R}^3$ that must be in particular *orientation-preserving* in the set $\bar{\Omega}$ and *injective* on the set Ω , in order to be physically acceptable.

Such mapping φ are called *deformations*, and in the next sections their *geometrical properties* are studied. It is shown in particular that the changes in *volume*, *surfaces* and *lengths* associated with a deformation φ , are respectively governed by the scalar $\nabla \varphi$, the matrix $\text{Cof } \nabla \varphi$ and the *right Cauchy-Green strain tensor* $\mathbf{C} = \nabla \varphi^T \nabla \varphi$.

1.1 Deformation in \mathbb{R}^3

We assume once and for all that an origin \mathbf{o} and an orthonormal basis $\{\mathbf{e}_1, \mathbf{e}_2, \mathbf{e}_3\}$ have been chosen in three-dimensional Euclidean space, which will therefore be identified with the space \mathbb{R}^3 . From the notational viewpoint, we identify the point \mathbf{x} with the vector $\mathbf{o}\mathbf{x}$. Whenever we consider components of vectors in \mathbb{R}^3 , or elements of matrices in \mathbb{M}^3 , we make the convention that Latin indices (i, j, p, \dots) always take their values in the set $\{1, 2, 3\}$, and we combine this rule with the standard summation convention.

Let there be given a bounded, open, connected, subset Ω of \mathbb{R}^3 with a sufficiently smooth boundary (specific smoothness assumptions will be made subsequently). We shall think of the closure $\bar{\Omega}$ of the set Ω as representing the volume occupied by a body “before it is deformed”; for this reason, the set $\bar{\Omega}$ is called the *reference configuration*.

A deformation of the reference configuration $\bar{\Omega}$ is a vector field:

$$\boldsymbol{\varphi}: \bar{\Omega} \rightarrow \mathbb{R}^3 \quad (1.1)$$

that is smooth enough, injective possibly on the boundary of the set Ω , and orientation-preserving.

We denote by \mathbf{x} a generic point in the set $\bar{\Omega}$, by x_i its components with respect to the basis $\{\mathbf{e}_i\}$, and by $\partial_i = \partial/\partial x_i$ the partial derivative with respect to variable x_i .

Given a deformation $\boldsymbol{\varphi} = \varphi_i \mathbf{e}_i$, we define at each point of the set Ω the matrix

$$\nabla \boldsymbol{\varphi} := \begin{pmatrix} \partial_1 \varphi_1 & \partial_2 \varphi_1 & \partial_3 \varphi_1 \\ \partial_1 \varphi_2 & \partial_2 \varphi_2 & \partial_3 \varphi_2 \\ \partial_1 \varphi_3 & \partial_2 \varphi_3 & \partial_3 \varphi_3 \end{pmatrix}. \quad (1.2)$$

The matrix $\nabla \boldsymbol{\varphi}$ is called the deformation gradient. Since a deformation is orientation-preserving by definition, the determinant of the deformation gradient satisfies the orientation-preserving condition:

$$\det \nabla \boldsymbol{\varphi}(\mathbf{x}) > 0 \quad \text{for all } \mathbf{x} \in \bar{\Omega} \quad (1.3)$$

In particular, the matrix $\nabla \boldsymbol{\varphi}(\mathbf{x})$ is invertible at all points \mathbf{x} of the reference configuration $\bar{\Omega}$.

Together with a deformation $\boldsymbol{\varphi}$, it is often convenient to introduce the displacement \mathbf{u} , which is the vector field:

$$\mathbf{u} : \bar{\Omega} \rightarrow \mathbb{R}^3 \quad (1.4)$$

defined by the relation

$$\boldsymbol{\varphi} = \mathbf{id} + \mathbf{u}, \quad (1.5)$$

where \mathbf{id} denotes the (restriction to $\bar{\Omega}$ of the) identity map from \mathbb{R}^3 onto \mathbb{R}^3 . Notice that the displacement gradient

$$\nabla \mathbf{u} := \begin{pmatrix} \partial_1 u_1 & \partial_2 u_1 & \partial_3 u_1 \\ \partial_1 u_2 & \partial_2 u_2 & \partial_3 u_2 \\ \partial_1 u_3 & \partial_2 u_3 & \partial_3 u_3 \end{pmatrix} \quad (1.6)$$

and the deformation gradient are related by the equation

$$\nabla \boldsymbol{\varphi} = \mathbf{I} + \nabla \mathbf{u}. \quad (1.7)$$

Given a reference configuration $\bar{\Omega}$ and a deformation $\boldsymbol{\varphi} : \bar{\Omega} \rightarrow \mathbb{R}^3$, the set $\boldsymbol{\varphi}(\bar{\Omega})$ is called a deformed configuration. At each point

$$\mathbf{x}^\varphi := \boldsymbol{\varphi}(\mathbf{x}) \quad (1.8)$$

of a deformed configuration, we define the three vectors (Fig. 1.1)

$$\partial_j \boldsymbol{\varphi}(\mathbf{x}) = \partial_j \varphi_i(\mathbf{x}) \mathbf{e}_i. \quad (1.9)$$

Each vector $\partial_j \boldsymbol{\varphi}(\mathbf{x})$ measures the “local deformation in the direction of the vector \mathbf{e}_j ” in the sense that, to within the first order with respect to dt , the vector $\mathbf{e}_j dt$ is transformed into the vector $\partial_j \boldsymbol{\varphi}(\mathbf{x}) dt$. Equivalently, the vector $\partial_j \boldsymbol{\varphi}(\mathbf{x})$ is the tangent

vector to the j th coordinate line passing through the point \mathbf{x}^φ (i.e. the image by the deformation φ of a segment parallel to the vector \mathbf{e}_j containing the point \mathbf{x} in its interior, and parametrized by t). Since the vector $\partial_j \varphi(\mathbf{x})$ is precisely the j th column of the matrix $\nabla \varphi$, the knowledge of the deformation gradient completely define the local deformation to within the first order.

We next compute the volume, area, and length elements in the deformed configuration. In each case, the objective is, for a given deformation, to express quantities (volumes, surfaces, lengths) defined over the deformed configuration in terms of the same quantities, but defined over the reference configuration. To emphasize the crucial distinction between both types of quantities, we adopt the following notational device: the superscript “ φ ” is systematically attached to a quantity defined over the deformed configuration, while the related quantity over the reference configuration is designed by the same letter, but without the superscript “ φ ”; this rule has already been applied, for denoting a generic point $\mathbf{x} \in \bar{\Omega}$ and the corresponding point $\mathbf{x}^\varphi \in \varphi(\mathbf{x}) \in \varphi(\bar{\Omega})$.

This correspondence between a quantity defined as a function of the Lagrange variable \mathbf{x} , and a similar quantity defined as a function of the Euler variable $\mathbf{x}^\varphi \in \varphi(\mathbf{x})$, can be extended to other quantities than volume, surfaces, and lengths. As we shall see, it applies equally well to divergences of tensor fields and applied forces.

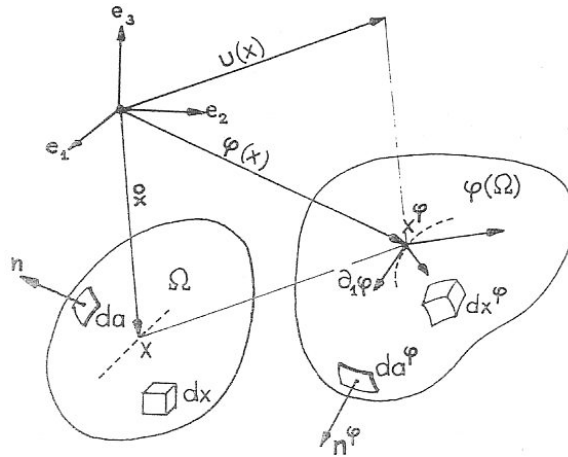


Figure 1.1.

Geometry of a deformation: the volume element, the area element, the unit outer normal, are denoted dx , da , \mathbf{n} in the reference configuration $\bar{\Omega}$, and dx^φ , da^φ , \mathbf{n}^φ in the deformed configuration $\varphi(\bar{\Omega})$. The vectors $\partial_j \varphi(\mathbf{x})$ define the deformation at a point $x \in \bar{\Omega}$ to within the first order.

1.2 Volume element in deformation configuration

Let φ be a deformation. If dx denotes the volume element at the point \mathbf{x} of the reference configuration, the volume element dx^φ at the point $\mathbf{x}^\varphi = \varphi(\mathbf{x})$ of the deformed configuration (Fig. 1.1) is given by

$$dx^\varphi = \det \nabla \varphi(x) dx, \quad (1.10)$$

since $|\det \nabla \varphi(x)| = \det \nabla \varphi(x) > 0$ by assumption.

The volume element dx^φ is used for computing volumes in the deformed configuration: If A denotes a measurable subset of the reference configuration $\bar{\Omega}$, the volume of the set A and the volume of the deformed set $A^\varphi := \varphi(A)$ are respectively given by:

$$\text{vol } A := \int_A dx, \quad \text{vol } A^\varphi := \int_{A^\varphi} dx^\varphi = \int_A \det \nabla \varphi(x) dx. \quad (1.11)$$

Notice that the last equality is nothing but a special case of the formula for changes of variables in multiple integrals: Let $\varphi: A \rightarrow \varphi(A) = A^\varphi$ be an injective, continuously differentiable mapping with a continuous inverse $\varphi^{-1}: A^\varphi \rightarrow A$. Then a function $u: x^\varphi \in A^\varphi \rightarrow \mathbf{R}$ is dx^φ -integrable over the set A^φ if and only if the function

$$x \in A \rightarrow (u \circ \varphi)(x) |\det \nabla \varphi(x)| \quad (1.12)$$

is dx -integrable over the set A and if this is the case,

$$\int_{A^\varphi = \varphi(A)} u(x^\varphi) dx^\varphi = \int_A (u \circ \varphi)(x) |\det \nabla \varphi(x)| dx. \quad (1.13)$$

It should be remembered that the validity of this formula hinges critically on the assumption that the mapping φ is injective. Otherwise, it must be replaced by the more general relation:

$$\int_{\varphi(A)} u(x') \text{card} \varphi^{-1}(x') dx' = \int_A (u \circ \varphi)(x) |\det \nabla \varphi(x)| dx \quad (1.14)$$

where $\text{card } B$ denote in general the number of elements in a set B . For details, see Schwartz (1967), Rado & Reichelderfer (1955), Federer (1969), Smith (1983), Bojarski & Iwaniec (1983), Marcus & Mizel (1973), Vodopyanov, Goldshtein & Reshetnyak (1979) for its extension to Sobolev space-valued mappings.

These properties hold in \mathbb{R}^n , for arbitrary n . The volume $\int_A dx$ of a dx -measurable subset of \mathbb{R}^n is denoted dx -means A .

1.3 The Piola transform; area element in the deformed configuration

As a preparation for computing the area element in the deformed configuration in terms of the area element in the reference configuration, it is convenient to introduce

a particular transformation between tensors defined over the reference configuration $\bar{\Omega}$ and tensors defined over the deformed configuration $\bar{\Omega}^\varphi$. Besides, this transform plays a crucial role in the definition of the first Piola-Kirchhoff tensor, following introduced.

Let us first review some definitions and results pertaining to tensor fields defined over either sets $\bar{\Omega}$ or $\bar{\Omega}^\varphi$. By a tensor, we mean here a second-order tensor

$$\mathbf{T} = (T_{ij}), \quad i: \text{row index}, j: \text{column index}.$$

Since we ignore the distinction between covariant and contravariant components, the set of all such tensors will be identified with the set \mathbb{M}^3 of all square matrices of order three.

Given a smooth enough tensor field $\mathbf{T}: \bar{\Omega} \rightarrow \mathbb{M}^3$ defined over the reference configuration $\bar{\Omega}$, we define at each point of $\bar{\Omega}$ its divergence $\mathbf{div} \mathbf{T}$ as the vector whose components are the divergences of the transposes of the row vectors of the matrix \mathbf{T} . More explicitly,

$$\mathbf{T} = T_{ij} = \begin{pmatrix} T_{11} & T_{12} & T_{13} \\ T_{21} & T_{22} & T_{23} \\ T_{31} & T_{32} & T_{33} \end{pmatrix} \Rightarrow \mathbf{div} \mathbf{T} := \begin{pmatrix} \partial_1 T_{11} + \partial_2 T_{12} + \partial_3 T_{13} \\ \partial_1 T_{21} + \partial_2 T_{22} + \partial_3 T_{23} \\ \partial_1 T_{31} + \partial_2 T_{32} + \partial_3 T_{33} \end{pmatrix} = \partial_j T_{ij} \mathbf{e}_i. \quad (1.15)$$

Of course, a similar definition holds for the divergence $\mathbf{div}^\varphi \mathbf{T}^\varphi$ of tensor fields $\mathbf{T}^\varphi: \mathbf{B}^\varphi \rightarrow \mathbb{M}^3$ defined over the deformed configuration:

$$\mathbf{T}^\varphi = (T_{ij}^\varphi) \Rightarrow \mathbf{div}^\varphi \mathbf{T}^\varphi := \partial_j^\varphi T_{ij}^\varphi \mathbf{e}_i \quad (1.16)$$

where $\partial_j^\varphi := \partial / \partial x_j^\varphi$ denote the partial derivatives with respect to the variables x_j^φ .

A Simple application of the fundamental Green's formula over the set $\bar{\Omega}$ shows that the divergence of a tensor field satisfies:

$$\int_{\bar{\Omega}} \mathbf{div} \mathbf{T} dX = \left(\int_{\bar{\Omega}} \partial_j T_{ij} dx \right) \mathbf{e}_i = \left(\int_{\partial \bar{\Omega}} T_{ij} n_j da \right) \mathbf{e}_i \quad (1.17)$$

or equivalently in matrix form:

$$\int_{\Omega} \mathbf{div} \mathbf{T} dx = \int_{\partial\Omega} \mathbf{T} \mathbf{n} da \quad (1.18)$$

Recall that a vector is always understood as a column vector when viewed as a matrix; thus the notation $\mathbf{T} \mathbf{n}$ in the previous formula represents the column vector obtained by applying the matrix \mathbf{T} to the column vector \mathbf{n} . This Green formula is called the divergence theorem for tensor fields. A tensor field $\mathbf{T}^\varphi = \bar{\Omega}^\varphi \rightarrow \mathbb{M}^3$ likewise satisfies:

$$\int_{\Omega^\varphi} \mathbf{div}^\varphi \mathbf{T}^\varphi dx^\varphi = \int_{\partial\Omega^\varphi} \mathbf{T}^\varphi \mathbf{n}^\varphi da^\varphi, \quad (1.19)$$

where \mathbf{n}^φ denotes the unit outer normal vector along the boundary of the deformed configuration.

We now come to an important definition. Let φ be a deformation that is injective on $\bar{\Omega}$, so that the matrix $\nabla \varphi$ is invertible at all points of the reference configuration. Then if $\mathbf{T}^\varphi(\mathbf{x}^\varphi)$ is a tensor defined at the point $\mathbf{x}^\varphi = \varphi(\mathbf{x})$ of the deformed configuration, we associate with $\mathbf{T}^\varphi(\mathbf{x}^\varphi)$ a tensor $\mathbf{T}(\mathbf{x})$ defined at the point \mathbf{x} of the reference configuration by:

$$\begin{aligned} \mathbf{T}(\mathbf{x}) &:= (\det \nabla \varphi(x)) \mathbf{T}^\varphi(\mathbf{x}^\varphi) \nabla \varphi(x)^{-T} = \mathbf{T}^\varphi(\mathbf{x}^\varphi) \mathbf{Cof}(\nabla \varphi(x)), \\ \mathbf{x}^\varphi &= \varphi(\mathbf{x}). \end{aligned} \quad (1.20)$$

In this fashion, a correspondence, called the Piola transform, is established between tensor fields defined over the deformed and reference configurations, respectively. The reason we proceed the other way is that the starting point in elasticity is a tensor field defined over the deformed configuration (the Cauchy stress tensor field), and it

is its Piola transform over three reference configuration (the first Piola –Kirchhoff stress tensor field) that subsequently plays a key role.

As shown in the next theorem, the main interest of the Piola transform is that it yields a simple relation between the divergences of the tensors \mathbf{T}^φ and \mathbf{T} and (as a corollary) the desired relation between corresponding area elements da^φ and da .

1.4 Length element in the deformed configuration; Strain Tensor

If a deformation φ is differentiable at a point $x \in \bar{\Omega}$, then (by definition of differentiability) we can write, for all points $x + \delta\mathbf{x} \in \bar{\Omega}$:

$$\varphi(x + \delta\mathbf{x}) - \varphi(x) = \nabla\varphi(x)\delta\mathbf{x} + o(|\delta\mathbf{x}|) \quad (1.21)$$

and whence

$$|\varphi(x + \delta\mathbf{x}) - \varphi(x)|^2 = \delta\mathbf{x}^T \nabla\varphi^T(x) \nabla\varphi(x) \delta\mathbf{x} + o(|\delta\mathbf{x}|^2) \quad (1.22)$$

The symmetric tensor

$$\mathbf{C} := \nabla\varphi^T \nabla\varphi \quad (1.23)$$

found in the above expression is called in elasticity the **right Cauchy-Green strain tensor**. Notice that the associated quadratic form:

$$(\xi, \xi) \in \mathbf{R}^3 \times \mathbf{R}^3 \rightarrow \xi^T \mathbf{C}(x) \xi = |\nabla\varphi(x)\xi|^2 \quad (1.24)$$

is positive definite at all points $x \in \bar{\Omega}$, since the deformation gradient $\nabla \boldsymbol{\varphi}$ is everywhere invertible by assumption. As expected, this quadratic form is used for computing lengths: Let

$$\gamma = f(I), \quad f: I \rightarrow \bar{\Omega}, \quad I: \text{compact interval of } \mathbb{R} \quad (1.25)$$

be a curve in the reference configuration (Fig. 1.2). Denoting by f_i the components of the mapping \mathbf{f} , the length of the curve γ is given by ($f' = df/dt$):

$$\text{length } \gamma := \int_L |f'(t)| dt = \int_L \{f'(t) f'(t)\}^{1/2} dt, \quad (1.26)$$

while the length of the deformed curve $\gamma^\varphi : \boldsymbol{\varphi}(\gamma)$ is given by

$$\text{length } \gamma^\varphi := \int_L |\boldsymbol{\varphi}' \circ f'(t)| dt = \int_L \{C_{ij}(f(t)) f'(t) f'(t)\}^{1/2} dt \quad (1.27)$$

Consequently, the length elements dl and dl^φ in the reference and deformed configurations may be symbolically written as:

$$dl = \{\mathbf{dx}^T \mathbf{dx}\}^{1/2}, \quad dl^\varphi = \{\mathbf{dx}^T \mathbf{C} \mathbf{dx}\}^{1/2}. \quad (1.28)$$

If in particular $\mathbf{dx} = dt \mathbf{e}_j$, the corresponding length element in the deformed configuration is $\{C_{jj}\}^{1/2} dt = |\partial_j \boldsymbol{\varphi}| dt$.

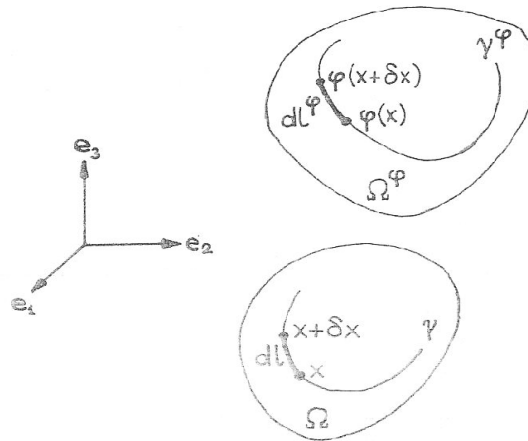


Figure. 1.2.

The length elements $dl = \{\mathbf{dx}^T \mathbf{dx}\}^{1/2}$ and $dl^\varphi = \{\mathbf{dx}^T \mathbf{C} \mathbf{dx}\}^{1/2}$ in the reference and deformed configurations. The tensor $\mathbf{C} = \nabla \boldsymbol{\varphi}^T \nabla \boldsymbol{\varphi}$ is the right Cauchy-Green tensor.

Although it has no immediate geometric interpretation, the left Cauchy-Green strain tensor

$$\mathbf{B} = \nabla \boldsymbol{\varphi} \nabla \boldsymbol{\varphi}^T \quad (1.29)$$

which is also symmetric, is equally important; in particular, it plays an essential role in the representation theorem for the response function of the Cauchy stress tensor. For the time being, we simply notice that the two matrices $\mathbf{C} = \mathbf{F}^T \mathbf{F}$ and $\mathbf{B} = \mathbf{F} \mathbf{F}^T$ have the same characteristic polynomial, since this is true in general of the products $\mathbf{F} \mathbf{G}$ and $\mathbf{G} \mathbf{F}$ of two arbitrary matrices \mathbf{F} and \mathbf{G} of the same order. When $\mathbf{G} = \mathbf{F}^T$, this result is a direct consequence of the polar factorization theorem.

In view of showing that the tensor \mathbf{C} is indeed a good measure of “strain”, understood here in its intuitive sense of “change in form or size”, let us first consider a class of deformations that induce no “strain”: A deformation is called a rigid deformation if it is of the form

$$\boldsymbol{\varphi}(x) = \mathbf{a} + \mathbf{Q} \circ x, \quad \mathbf{a} \in \mathbf{R}, \quad \mathbf{Q} \in \mathbf{O}_+^3, \quad \text{for all } x \in \bar{\Omega}, \quad (1.30)$$

where \mathbf{O}_+^3 denotes the set of rotations in \mathbb{R}^3 , i.e., the set of orthogonal matrices of order 3 whose determinant is +1. In other words, the corresponding deformed configuration is obtained by rotating the reference configuration around the origin by the rotation \mathbf{Q} and by translating it by the vector \mathbf{a} : this indeed corresponds to the idea of a “rigid” deformation, where the reference configuration is “moved”, but without any “strain” (Fig. 1.3). Observe that the rotation \mathbf{Q} may be performed around any point $\tilde{x} \in \mathbb{R}^3$ (Fig. 1.3), since we can also write

$$\boldsymbol{\varphi}(x) = \boldsymbol{\varphi}(\tilde{x}) + \mathbf{Q} \tilde{x} \quad (1.31)$$

If $\boldsymbol{\varphi}$ is a rigid deformation, then $\nabla \boldsymbol{\varphi}(x) = \mathbf{Q} \in \mathbf{O}_+^3$ at all points $x \in \bar{\Omega}$, and therefore

$$\mathbf{C} = \mathbf{I} \text{ in } \bar{\Omega}, \text{ i.e., } \nabla \boldsymbol{\varphi}(x)^T \nabla \boldsymbol{\varphi}(x) = \mathbf{I} \text{ for all } x \in \bar{\Omega}. \quad (1.32)$$

It is remarkable that conversely, if $\mathbf{C} = \mathbf{I}$ in $\bar{\Omega}$ and $\det \nabla \boldsymbol{\varphi} > 0$, the corresponding deformation is necessarily rigid.

Theorem 1.2. (characterization of rigid deformations). Let Ω be an open connected subset of \mathbb{R}^n , and let there be given a mapping

$$\boldsymbol{\varphi} \in C^1(\Omega, \mathbb{R}^n) \quad (1.33)$$

that satisfies

$$\nabla \boldsymbol{\varphi}(x)^T \nabla \boldsymbol{\varphi}(x) = \mathbf{I} \text{ for all } x \in \Omega \quad (1.34)$$

then there exists a vector $\mathbf{a} \in \mathbb{R}^n$ and an orthogonal matrix $\mathbf{Q} \in \mathbf{O}^n$ such that

$$\boldsymbol{\varphi}(x) = \mathbf{a} + \mathbf{Q} \circ x \text{ for all } x \in \Omega. \quad (1.35)$$

The result of theorem 1.2 can be viewed as a special case (let $\boldsymbol{\psi}$ be any rigid deformation in the theorem 1.3) of the following result, which shows that two deformations corresponding to the same tensor \mathbf{C} can be obtained from one another by composition with a rigid deformation.

Theorem 1.3. Let Ω be an open connected subset of \mathbb{R}^n , and let here be given two mappings

$$\boldsymbol{\varphi}, \boldsymbol{\psi} \in C^1(\Omega, \mathbb{R}^n) \quad (1.36)$$

such that

$$\nabla \boldsymbol{\varphi}(x)^T \cdot \nabla \boldsymbol{\varphi}(x) = \nabla \boldsymbol{\psi}(x)^T \cdot \nabla \boldsymbol{\psi}(x) \text{ for all } x \in \Omega \quad (1.37)$$

$\psi : \Omega \rightarrow \mathbb{R}^n$ is injective, and let $\nabla \psi(\mathbf{x}) \neq 0$ for all $\mathbf{x} \in \Omega$.

Then there exist a vector $\mathbf{a} \in \mathbb{R}^n$ and an orthogonal matrix $\mathbf{Q} \in O^n$ such that :

$$\boldsymbol{\varphi}(\mathbf{x}) = \mathbf{a} + \mathbf{Q}\boldsymbol{\psi}(\mathbf{x}) \text{ for all } \mathbf{x} \in \Omega. \quad (1.38)$$

The previous two theorems are useful for understanding the role played by the tensor \mathbf{C} . First, theorem 1.2. shows that the difference

$$2\mathbf{E} := \mathbf{C} - \mathbf{I} \quad (1.39)$$

is a measure of the “deviation” between a given deformation and a rigid deformation, since $\mathbf{C} = \mathbf{I}$ if and only if the deformation is rigid. Secondly, theorem 1.3. shows that the knowledge of the tensor field $\mathbf{C} : \Omega \rightarrow \mathbb{S}_>^3$ completely determines the deformation, up to composition with rigid deformations (the question of proving the existence of deformations for which the associated tensor field $\mathbf{C} : \Omega \rightarrow \mathbb{S}_>^3$ is equal to a given tensor field is quite another matter). These considerations are illustrated in figure 1.3.

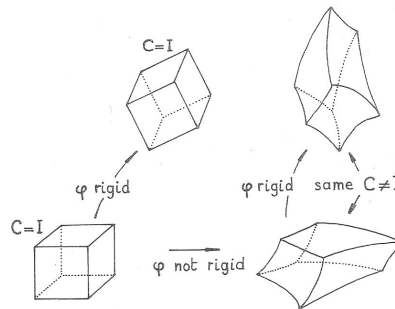


Figure. 1.3.

The right Cauchy-Green tensor \mathbf{C} is equal to \mathbf{I} if and only if the deformation is rigid. Two deformations corresponding to the same tensor \mathbf{C} differ by a rigid deformation.

The tensor \mathbf{E} is called the Green-St Venant strain tensor. Expressed in terms of the displacement gradient $\nabla \mathbf{u}$, in lieu of the deformation gradient $\nabla \boldsymbol{\varphi} = \mathbf{I} + \nabla \mathbf{u}$ (recall that $\boldsymbol{\varphi} = \mathbf{id} + \mathbf{u}$), the strain tensor \mathbf{C} becomes

$$\mathbf{C} = \nabla \boldsymbol{\varphi}^T \nabla \boldsymbol{\varphi} = \mathbf{I} + \nabla \mathbf{u}^T + \nabla \mathbf{u} + \nabla \mathbf{u}^T \nabla \mathbf{u} = \mathbf{I} + 2\mathbf{E} \quad (1.40)$$

with

$$\mathbf{E}(\mathbf{u}) := \mathbf{E} = \frac{1}{2}(\nabla \mathbf{u}^T + \nabla \mathbf{u}) \quad (1.41)$$

whose “first order” part $\frac{1}{2}(\nabla \mathbf{u}^T + \nabla \mathbf{u})$ coincide with the *linearized strain tensor*, which played a key role in the earlier linearized theories that prevailed in elasticity.

2. The Equation of Equilibrium

A body occupying a deformed configuration $\bar{\Omega}^\varphi$, and subjected to applied body forces in its interior Ω^φ and to applied surfaces forces on a portion $\Gamma_1^\varphi = \varphi(\Gamma_1)$ of its boundary, is in static equilibrium if the fundamental stress principle of Euler and Cauchy is satisfied. This axiom, which is the basis of continuum mechanics, implies the celebrated Cauchy theorem, according to which there exists a symmetric tensor field $\mathbf{T}^\varphi : \bar{\Omega}^\varphi \rightarrow \mathbb{S}^3$ such that

$$\begin{cases} -\text{div}^\varphi \mathbf{T}^\varphi = \mathbf{f}^\varphi & \text{in } \Omega^\varphi \\ \mathbf{T}^\varphi \mathbf{n}^\varphi = \mathbf{g}^\varphi & \text{on } \Gamma_1^\varphi \end{cases} \quad (2.1)$$

where \mathbf{f}^φ and \mathbf{g}^φ denote the densities of the applied body and surface forces respectively, and \mathbf{n}^φ is the unit outer normal vector along Γ_1^φ . These equation are called the equilibrium over the deformed configuration, and the tensor \mathbf{T}^φ is called the Cauchy stress tensor.

A remarkable feature of these equations is their “divergence structure”, which makes them amenable to a variational formulation; a disadvantage is that they are expressed in terms of the unknown $\mathbf{x}^\varphi = \varphi(\mathbf{x})$. In order to obviate this difficulty while retaining

the divergence structure of the equations, we use the Piola transform $\mathbf{T}:\bar{\Omega} \rightarrow \mathbb{M}^3$ of the Cauchy stress tensor field, which is defined by $\mathbf{T}(\mathbf{x}) = \mathbf{T}^\varphi(\mathbf{x}^\varphi) \text{Cof} \nabla \boldsymbol{\varphi}(\mathbf{x})$. In this fashion, it is found that the equilibrium equations over $\bar{\Omega}^\varphi$ are equivalent to the equilibrium equations over the reference configuration $\bar{\Omega}$,

$$\begin{cases} -\text{div} \mathbf{T} = \mathbf{f} & \text{in } \Omega \\ \mathbf{T} \mathbf{n} = \mathbf{g} & \text{on } \Gamma_1 \end{cases} \quad (2.2)$$

where \mathbf{n} denotes the unit outer normal vector along Γ_1 , and the fields $\mathbf{f}:\Omega \rightarrow \mathbb{R}^3$ and $\mathbf{g}:\Gamma_1 \rightarrow \mathbb{R}^3$ are related to the fields $\mathbf{f}^\varphi:\Omega^\varphi \rightarrow \mathbb{R}^3$ and $\mathbf{g}^\varphi:\Gamma_1^\varphi \rightarrow \mathbb{R}^3$ by the simple formulas $\mathbf{f} dx = \mathbf{f}^\varphi dx^\varphi$ and $\mathbf{g} dx = \mathbf{g}^\varphi dx^\varphi$. Because they are still in divergence form, these equations can be given a variational formulation, known as the principle of virtual work. This principle plays a key role as the starting point of the theory of hyperelastic materials, as well in the asymptotic theory of two-dimensional plate models.

The tensor \mathbf{T} is called the first Piola-Kirchhoff stress tensor. We also introduce the symmetric second Piola-Kirchhoff stress tensor $\boldsymbol{\Sigma} = \nabla \boldsymbol{\varphi}^{-1} \mathbf{T}$, which naturally arises in the expression of the constitutive equations of elastic materials.

2.1 Applied Forces

We assume that in the deformed configuration $\bar{\Omega}^\varphi$ associated with an arbitrary deformation $\boldsymbol{\varphi}$, the body is subjected to applied forces of two types:

- (i) applied **body forces**, defined by a vector field

$$\mathbf{f}^\varphi:\Omega^\varphi \rightarrow \mathbb{R}^3, \quad (2.3)$$

called the density of the applied body forces per unit volume in the deformed configuration;

(ii) applied **surface forces**, defined by a vector field

$$\mathbf{g}^\varphi : \Gamma_1^\varphi \rightarrow \mathbb{R}^3 \quad (2.4)$$

on a da^φ -measurable subset Γ_1^φ of the boundary

$$\Gamma^\varphi := \partial\Omega^\varphi \quad (2.5)$$

called the density of the applied surface force per unit area in the deformed configuration.

Let $\rho^\varphi : \Omega^\varphi \rightarrow \mathbb{R}$ denote the mass density in the deformed configuration, so that the mass of every dx^φ -measurable subset A^φ of $\bar{\Omega}^\varphi$ is given by the integral $\int_{A^\varphi} \rho^\varphi(x^\varphi) dx^\varphi$. We assume that

$$\rho^\varphi(x^\varphi) > 0 \quad \text{for all } x^\varphi \in \Omega \quad (2.6)$$

The applied body forces can be equivalently defined by their density $\mathbf{b}^\varphi : \Omega^\varphi \rightarrow \mathbb{R}^3$ per unit mass in the deformed configuration, which is related to the density \mathbf{f}^φ by the equation

$$\mathbf{f}^\varphi = \rho^\varphi \mathbf{b}^\varphi \quad (2.7)$$

The applied forces describe the action of the outside world on the body: An elementary force $\mathbf{f}^\varphi(x^\varphi) dx^\varphi$ is exerted on the elementary volume dx^φ at each point x^φ of the deformed configuration. For example, this is the case of the gravity field, for which $\mathbf{f}(x^\varphi) = -g\rho^\varphi(x^\varphi)\mathbf{e}_3$ for all $x^\varphi \in \Omega^\varphi$ (assuming that the vector \mathbf{e}_3 is vertical and oriented “upward”), where g is the gravitational constant. Another example is given by the action of electrostatic forces.

Likewise, an elementary force $\mathbf{g}^\varphi(x^\varphi)dx^\varphi$ is exerted on the elementary area da^φ at each point x^φ of the subset Γ_1^φ of the boundary of the deformed configuration (Fig. 1.3). Such forces generally represent the action of another body (whatever its nature its may be) along the portion Γ_1^φ of the boundary.

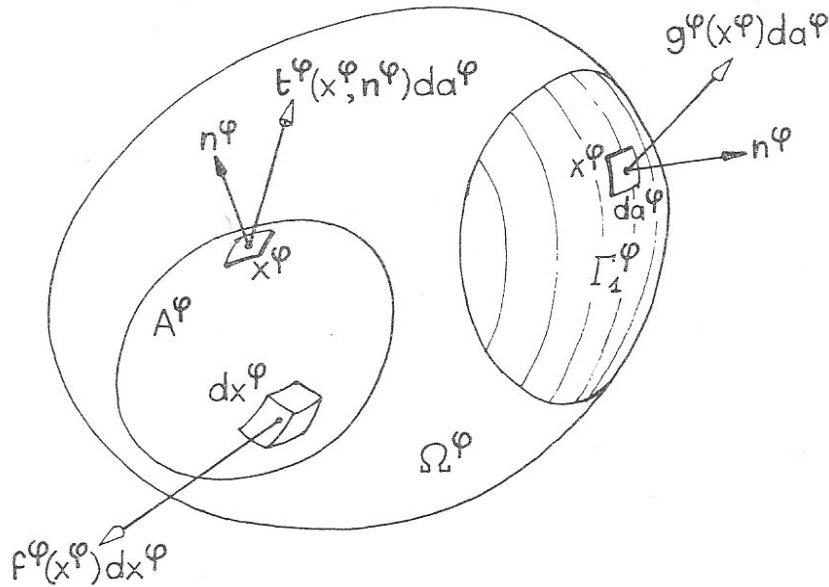


Figure 1.3.

Applied forces comprise applied body forces $\mathbf{f}^\varphi(x)dx^\varphi$, $x^\varphi \in \Omega^\varphi$ and applied surface forces $\mathbf{g}^\varphi(x)dx^\varphi$, $x^\varphi \in \Gamma_1^\varphi$. The stress principle of Euler and Cauchy asserts in addition the existence of elementary surface forces $\mathbf{t}^\varphi(\mathbf{x}^\varphi, \mathbf{n}^\varphi)da^\varphi$, $x^\varphi \in \partial A^\varphi$, along the boundary ∂A^φ , with unit outer normal vector \mathbf{n}^φ , of any sub-domain A^φ of the deformed configuration $\bar{\Omega}^\varphi$.

2.2 The stress principle of Euler and Cauchy

Continuum mechanics for static problems is founded on the following axiom, named after the fundamental contributions of Euler (1757,1771) and Cauchy (1823,1827a).

Note that the exterior product in \mathbb{R}^3 is denoted \wedge .

Axiom 1. (stress principle of Euler and Cauchy). Consider a body occupying a deformed configuration $\bar{\Omega}^\varphi$, and subjected to applied forces represented by densities $\mathbf{f}^\varphi := \Omega^\varphi \rightarrow \mathbb{R}^3$ and $\mathbf{g}^\varphi := \Omega^\varphi \rightarrow \mathbb{R}^3$. Then there exists a vector field

$$\mathbf{t}^\varphi : \Omega^\varphi \times S_1 \rightarrow \mathbb{R}^3, \quad \text{where } S_1 = \{v \in \mathbb{R}^3; |v| = 1\}, \quad (2.8)$$

such that:

(a) For any sub-domain A^φ of $\bar{\Omega}^\varphi$, and at any point $\mathbf{x}^\varphi \in \Gamma_1^\varphi \cap \partial A^\varphi$ where the unit outer normal vector \mathbf{n}^φ to $\Gamma_1^\varphi \cap \partial A^\varphi$ exists: $\mathbf{t}^\varphi(\mathbf{x}^\varphi, \mathbf{n}^\varphi) = \mathbf{g}^\varphi(\mathbf{x}^\varphi)$.

(b) Axiom of **force balance**: For any sub-domain A^φ of $\bar{\Omega}^\varphi$,

$$\int_{A^\varphi} \mathbf{f}^\varphi(\mathbf{x}^\varphi) dx^\varphi + \int_{\partial A^\varphi} \mathbf{t}^\varphi(\mathbf{x}^\varphi, \mathbf{n}^\varphi) dx^\varphi = \mathbf{0} \quad (2.9)$$

where \mathbf{n}^φ denotes the unit outer normal vector along ∂A^φ .

(c) Axiom of **moment balance**: For any sub-domain A^φ of $\bar{\Omega}^\varphi$,

$$\int_{A^\varphi} \mathbf{ox}^\varphi \wedge \mathbf{f}^\varphi(\mathbf{x}^\varphi) dx^\varphi + \int_{\partial A^\varphi} \mathbf{ox}^\varphi \wedge \mathbf{t}^\varphi(\mathbf{x}^\varphi, \mathbf{n}^\varphi) dx^\varphi = \mathbf{0}. \quad (2.10)$$

The stress principle thus first asserts the existence of elementary **surface forces** $\mathbf{t}^\varphi(\mathbf{x}^\varphi, \mathbf{n}^\varphi) da^\varphi$ along the boundaries of all domains of the reference configuration (Fig. 1.3.).

Secondly, the stress principle asserts that at a point \mathbf{x}^φ of the boundary ∂A^φ of a sub-domain A^φ , the elementary surface force depends on the sub-domain A^φ , only via the normal vector \mathbf{n}^φ to ∂A^φ at \mathbf{x}^φ . While it would be equally conceivable a priori that the elementary surface force at \mathbf{x}^φ be also dependent on other geometrical properties of the sub-domain A^φ , for instance the curvature of ∂A^φ at \mathbf{x}^φ , etc., it is possible to rigorously rule out such further geometrical dependences by constructing a general theory of surfaces forces, as shown by Noll (1959).

Thirdly, the stress principle asserts that any sub-domain A^φ of the deformed configuration $\bar{\Omega}^\varphi$, including $\bar{\Omega}^\varphi$ itself, is in static equilibrium, in the sense that the torsor formed by the elementary forces $\mathbf{t}^\varphi(\mathbf{x}^\varphi, \mathbf{n}^\varphi) da^\varphi$, $x^\varphi \in \partial A^\varphi$, \mathbf{n}^φ normal to ∂A^φ at

\mathbf{x}^φ , and the body forces $\mathbf{f}^\varphi(\mathbf{x}^\varphi)d\mathbf{x}^\varphi$, $\mathbf{x}^\varphi \in A^\varphi$, is equivalent to zero. This means that its resultant vector vanishes (axiom of force balance) and that its resulting moment with respect to the origin (and thus with respect to any other point, by a classical property of torsos) vanishes (axiom of moment balance).

Hence the stress principle mathematically express, in the form of an axiom, the intuitive idea that the static equilibrium of any sub-domain A^φ of $\bar{\Omega}^\varphi$, already subjected to given applied body forces $\mathbf{f}^\varphi(\mathbf{x}^\varphi)d\mathbf{x}^\varphi$, $\mathbf{x}^\varphi \in A^\varphi$, and (possibly) to given applied surface forces $\mathbf{g}^\varphi(\mathbf{x}^\varphi)da^\varphi$ at those points $\mathbf{x}^\varphi \in \Gamma_1^\varphi \cap \partial A^\varphi$ where the outer normal vector to $\Gamma_1^\varphi \cap \partial A^\varphi$ exists, is made possible by the added effect of elementary surfaces forces of the specific form indicated, acting on the remaining part of the boundary ∂A^φ .

2.3 Cauchy's theorem; The Cauchy stress tensor

We now derive consequences of paramount importance from the stress principle. The first one, due to Cauchy (1823,1827a), is one of the most important results in continuum mechanics. It asserts that the dependence of the Cauchy stress vector $\mathbf{t}^\varphi(\mathbf{x}^\varphi, \mathbf{n}^\varphi)$ with respect to its second argument $\mathbf{n} \in S_1$ is linear, i.e., at each point $\mathbf{x}^\varphi \in \Omega^\varphi$, there exists a tensor $\mathbf{T}^\varphi(\mathbf{x}^\varphi) \in \mathbb{M}^3$ such that $\mathbf{t}^\varphi(\mathbf{x}^\varphi, \mathbf{n}^\varphi) = \mathbf{T}^\varphi(\mathbf{x}^\varphi)\mathbf{n}$ for all $\mathbf{n} \in S_1$; the second one asserts that at each point $\mathbf{x}^\varphi \in \Omega^\varphi$, the tensor $\mathbf{T}^\varphi(\mathbf{x}^\varphi)$ is symmetric; the third one, again due to Cauchy (1827b, 1828), is that the tensor field $\mathbf{T}^\varphi : \Omega^\varphi \rightarrow \mathbb{M}^3$ and the vector fields $\mathbf{f}^\varphi : \Omega^\varphi \rightarrow \mathbb{R}^3$ and $\mathbf{g}^\varphi := \Gamma_1^\varphi \rightarrow \mathbb{R}^3$ are related by a partial differential equation in Ω^φ , and by a boundary condition on Γ_1^φ , respectively.

Theorem 1.2. (Cauchy's theorem). Assume that the applied body force density $\mathbf{f}^\varphi : \Omega^\varphi \rightarrow \mathbb{R}^3$ is continuous, and that the Cauchy stress vector field

$$\mathbf{t}^\varphi : (\mathbf{x}^\varphi, \mathbf{n}^\varphi) \in \bar{\Omega}^\varphi \times S_1 \rightarrow \mathbf{t}^\varphi(\mathbf{x}^\varphi, \mathbf{n}) \in \mathbb{R}^3 \quad (2.11)$$

is continuously differentiable with respect to the variable $\mathbf{x}^\varphi \in \bar{\Omega}^\varphi$ for each $\mathbf{n} \in S_1$ and continuous with respect to the variable $\mathbf{n} \in S_1$ for each $\mathbf{x}^\varphi \in \bar{\Omega}^\varphi$. Then the axioms of force and moment balance imply that there exists a continuously differentiable tensor field

$$\mathbf{T}^\varphi : \mathbf{x}^\varphi \in \bar{\Omega}^\varphi \rightarrow \mathbf{T}^\varphi(\mathbf{x}^\varphi) \in \mathbb{M}^3, \quad (2.12)$$

such that the Cauchy stress vector satisfies

$$\mathbf{t}^\varphi(\mathbf{x}^\varphi, \mathbf{n}) = \mathbf{T}^\varphi(\mathbf{x}^\varphi) \mathbf{n} \quad \text{for all } \mathbf{x}^\varphi \in \bar{\Omega}^\varphi \quad \text{and all } \mathbf{n} \in S_1, \quad (2.13)$$

and such that

$$-div^\varphi \mathbf{T}^\varphi(\mathbf{x}^\varphi) = \mathbf{f}^\varphi(\mathbf{x}^\varphi) \quad \text{for all } \mathbf{x}^\varphi \in \Omega^\varphi, \quad (2.14)$$

$$\mathbf{T}^\varphi(\mathbf{x}^\varphi) = \mathbf{T}^\varphi(\mathbf{x}^\varphi)^T \quad \text{for all } \mathbf{x}^\varphi \in \bar{\Omega}^\varphi, \quad (2.15)$$

$$\mathbf{T}^\varphi(\mathbf{x}^\varphi) \mathbf{n}^\varphi = \mathbf{g}^\varphi(\mathbf{x}^\varphi) \quad \text{for all } \mathbf{x}^\varphi \in \Gamma_1^\varphi \quad (2.16)$$

where \mathbf{n}^φ is the unit outer normal vector along Γ_1^φ .

The symmetry tensor \mathbf{T}^φ is called the Cauchy stress tensor at the point $\mathbf{x}^\varphi \in \bar{\Omega}^\varphi$. It is helpful to keep in mind the interpretation of its elements $\mathbf{T}_{ij}^\varphi(\mathbf{x}^\varphi)$: Since $\mathbf{t}^\varphi(\mathbf{x}^\varphi, \mathbf{e}_j) = \mathbf{T}_{ij}^\varphi(\mathbf{x}^\varphi) \cdot \mathbf{e}_i$, the elements of the j -th row of the tensor $\mathbf{T}^\varphi(\mathbf{x}^\varphi)$ represent the components of the Cauchy stress vector $\mathbf{t}^\varphi(\mathbf{x}^\varphi, \mathbf{n})$ at the point \mathbf{x}^φ corresponding to the particular choice $\mathbf{n} = \mathbf{e}_j$ (Fig. 1.4. where the case $j=1$ is considered). The knowledge of the three vectors $\mathbf{t}^\varphi(\mathbf{x}^\varphi, \mathbf{e}_j)$ in turn completely determines the Cauchy stress vector $\mathbf{t}^\varphi(\mathbf{x}^\varphi, \mathbf{n})$ for an arbitrary vector $\mathbf{n} = n_i \mathbf{e}_i \in S_1$, since

$$\mathbf{t}^\varphi(x^\varphi, \mathbf{n}) = n_j \mathbf{t}^\varphi(x^\varphi, \mathbf{e}_j) \quad (2.17)$$

This observation is used in the drawing of figures, where the Cauchy stress vector is often represented on three mutually perpendicular faces of a rectangular parallelepiped.

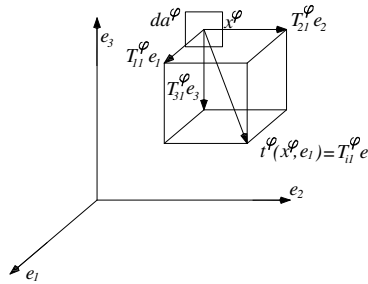


Fig. 1.4.

Interpretation of the elements \mathbf{T}_{ii}^φ of the Cauchy stress tensor $\mathbf{T}^\varphi = (T_{ij}^\varphi)$.

3. Linear Anisotropic Elastic Media

The relation between stress and strain in an anisotropic elastic material are presented in this section. A linear anisotropic elastic material can have as many as 21 elastic constants. This number is reduced when the material possesses a certain material symmetry. The number of elastic constants is also reduced, in most cases, when a two-dimensional deformation is considered. An important condition on elastic constants is that the strain energy must be positive. This condition implies that the 6x6 matrices of elastic constants presented herein must be positive definite.

3.1 Elastic Stiffnesses

Referring to a fixed rectangular coordinate system x_1, x_2, x_3 , let σ_{ij} and ε_{ij} be the stress and strain, respectively, in an anisotropic elastic material. The stress-strain law can be written as

$$\sigma_{ij} = C_{ijkl} \varepsilon_{kl} \quad (3.1)$$

in which C_{ijkl} , are the *elastic stiffnesses* which are components of a fourth rank tensor. They satisfy the full symmetry conditions

$$C_{ijkl} = C_{jikl}, \quad C_{ijkl} = C_{ijlk}, \quad C_{ijkl} = C_{klij}. \quad (3.2)$$

Before we present justifications for the three conditions in (3.2), we show that (3.2)₁ and (3.2)₃ imply (3.2)₂. Using (3.2)₃, (3.2)₁ and (3.2)₃ in that order we have

$$C_{ijkl} = C_{klij} = C_{lkij} = C_{ijlk}$$

which proves (3.2)₂. Therefore the three conditions in (3.2) are written as

$$C_{ijkl} = C_{jikl} = C_{klij}. \quad (3.3)$$

One can also show that (3.2)₂ and (3.2)₃ imply (3.2)₁.

The first equation of (3.2) follows directly from the symmetry of the stress tensor $\sigma_{ij} = \sigma_{ji}$. The second equation of (3.2) does *not* follow directly from the symmetry of the strain tensor $\varepsilon_{ij} = \varepsilon_{ji}$. However, if the C_{ijkl} in (3.2) do not satisfy (3.2)₂, we rewrite (3.2) as

$$\sigma_{ij} = \frac{1}{2} C_{ijkl} \varepsilon_{kl} + \frac{1}{2} C_{ijlk} \varepsilon_{kl} = \frac{1}{2} C_{ijkl} \varepsilon_{kl} + \frac{1}{2} C_{ijlk} \varepsilon_{lk}$$

or since $\varepsilon_{lk} = \varepsilon_{kl}$,

$$\sigma_{ij} = \frac{1}{2} (C_{ijkl} + C_{ijlk}) \varepsilon_{kl}. \quad (3.4)$$

The coefficients of ε_{kl} are symmetric with the subscripts kl . We can therefore redefine the coefficients of ε_{kl} in (3.4) as the new C_{ijkl} which satisfy (3.2)₂.

The third equation follows from the consideration of strain energy. The strain energy W per unit volume of the material is

$$W = \int_0^{\varepsilon_{pq}} \sigma_{ij} d\varepsilon_{ij} = \int_0^{\varepsilon_{pq}} C_{ijkl} \varepsilon_{kl} d\varepsilon_{ij}. \quad (3.5)$$

We demand that the integral be independent of the path ε_{ij} takes from 0 to ε_{pq} .

If not, say path 1 yields a larger integral than path 2, one can consider loading the material from 0 to ε_{pq} through path 1, and unloading from ε_{pq} to 0 through the reverse of path 2. The energy gained is the difference between the W 's for path 1 and path 2. If we repeat the process we can extract unlimited amount of energy from the material, which is physically impossible for a real material. Therefore the integral in (3.5) must be independent of the path taken by ε_{ij} , and W depends on the final strain ε_{pq} only. This implies that the integrand must be the total differential dW , i.e.,

$$C_{ijkl} \varepsilon_{kl} d\varepsilon_{ij} = dW = \frac{\partial W}{\partial \varepsilon_{ij}} d\varepsilon_{ij}. \quad (3.6)$$

Since $d\varepsilon_{ij}$ is arbitrary we must have

$$\sigma_{ij} = C_{ijkl} \varepsilon_{kl} = \frac{\partial W}{\partial \varepsilon_{ij}} \quad (3.7)$$

in which the first equality follows from (3.1). Differentiation of (3.7) with ε_{kl} leads to

$$C_{ijkl} = \frac{\partial^2 W}{\partial \varepsilon_{kl} \partial \varepsilon_{ij}}$$

The double differentiations on the right are interchangeable. Therefore

$$C_{ijkl} = C_{klij}$$

is the condition for the integral in (3.5) to be Independent of the loading path.

This proves (3.2)₃. With (3.2), (3.6) is written as

$$dW = C_{ijkl} \epsilon_{kl} d\epsilon_{ij} = \frac{1}{2} d(C_{ijkl} \epsilon_{ij} \epsilon_{kl}).$$

Hence

$$W = \frac{1}{2} C_{ijkl} \epsilon_{ij} \epsilon_{kl} = \frac{1}{2} \sigma_{ij} \epsilon_{ij}. \quad (3.8)$$

and since the strain energy must be positive, it results

$$C_{ijkl} \epsilon_{ij} \epsilon_{kl} > 0 \quad (3.9)$$

for any real, nonzero, symmetric tensor ϵ_{kl} .

3.2 Elastic Compliances

The inverse of (3.1) is written as

$$\epsilon_{ij} = S_{ijkl} \sigma_{kl} \quad (3.10)$$

where S_{ijkl} are the elastic compliance which are components of a four rank tensor.

They also possess the full symmetry

$$S_{ijkl} = S_{jikl}, \quad S_{ijkl} = S_{ijlk}, \quad S_{ijkl} = S_{klij} \quad (3.11)$$

or, as in (3.3)

$$S_{ijkl} = S_{jikl} = S_{klij}. \quad (3.12)$$

The justifications of the first and second equations in (3.11) are similar to their counterparts in (3.3). The justification of (3.11)₃ also follows from the energy consideration. Integration by parts of (3.12)₁ leads to

$$W = \sigma_{pq} \varepsilon_{pq} - \int_0^{\sigma_{pq}} \varepsilon_{ij} d\sigma_{ij} = \sigma_{pq} \varepsilon_{pq} - \int_0^{\sigma_{pq}} S_{ijkl} \sigma_{kl} d\sigma_{ij} .$$

If W depends on the final strain ε_{pq} it depends on the final stress σ_{pq} . The last integral which represents the *complementary energy* must be independent of the path σ_{ij} takes from 0 to the final stress σ_{pq} . Following a similar argument for C_{ijkl} , we deduce that (3.12)₃ must hold for the integral to be path independent. Since the strain energy must be positive, the substitution of the (3.10) into the (3.8) yields

$$S_{ijkl} \sigma_{ij} \sigma_{kl} > 0 \quad (3.13)$$

3.3 Contracted Notations

Introducing the contracted notation (Voigt, 1928; Lekhnitskii, 1963; Christensen, 1979)

$$\begin{aligned} \sigma_{11} = \sigma_1, \quad \sigma_{22} = \sigma_2, \quad \sigma_{33} = \sigma_3, \\ \sigma_{32} = \sigma_4, \quad \sigma_{31} = \sigma_5, \quad \sigma_{12} = \sigma_6, \end{aligned} \quad (3.14)$$

$$\begin{aligned} \varepsilon_{11} = \varepsilon_1, \quad \varepsilon_{22} = \varepsilon_2, \quad \varepsilon_{33} = \varepsilon_3, \\ 2\varepsilon_{32} = \varepsilon_4, \quad 2\varepsilon_{31} = \varepsilon_5, \quad 2\varepsilon_{12} = \varepsilon_6, \end{aligned} \quad (3.15)$$

the stress-strain law (3.1) and (3.2) can be written as

$$\sigma_\alpha = C_{\alpha\beta} \varepsilon_\beta, \quad C_{\alpha\beta} = C_{\beta\alpha}, \quad (3.16)$$

or, in matrix notation,

$$\mathbf{T} = \mathbf{C}\mathbf{E}, \quad \mathbf{C} = \mathbf{C}^T. \quad (3.17)$$

In the above \mathbf{T} and \mathbf{E} are 6×1 column matrices and \mathbf{C} is the 6×6 symmetric matrix given by

$$\mathbf{C} = \begin{bmatrix} C_{11} & C_{12} & C_{13} & C_{14} & C_{15} & C_{16} \\ C_{12} & C_{22} & C_{23} & C_{24} & C_{25} & C_{26} \\ C_{13} & C_{23} & C_{33} & C_{34} & C_{35} & C_{36} \\ C_{14} & C_{24} & C_{34} & C_{44} & C_{45} & C_{46} \\ C_{15} & C_{25} & C_{35} & C_{45} & C_{55} & C_{56} \\ C_{16} & C_{26} & C_{36} & C_{46} & C_{56} & C_{66} \end{bmatrix} \quad (3.18)$$

The transformation between C_{ijkl} and $C_{\alpha\beta}$ is accomplished by replacing the subscripts ij (or kl) by α (or β) using the following rules:

$$\begin{aligned} ij(\text{or } kl) &\leftrightarrow \alpha(\text{or } \beta) \\ 11 &\leftrightarrow 1 \\ 22 &\leftrightarrow 2 \\ 33 &\leftrightarrow 3 \\ 32 \text{ or } 23 &\leftrightarrow 4 \\ 31 \text{ or } 13 &\leftrightarrow 5 \\ 12 \text{ or } 21 &\leftrightarrow 6 \end{aligned} \quad (3.19)$$

The presence of the factor 2 in (3.15)₄₋₅₋₆ but not in (3.14)₄₋₅₋₆ is necessary for the symmetry of \mathbf{C} .

Analogously, with reference to the equation (3.14) and (3.15), the stress-strain law in the form (3.10) may be expressed in a matrix form, as it follows:

$$\mathbf{E} = \mathbf{S}\mathbf{T}, \quad \mathbf{S} = \mathbf{S}^T \quad (3.20)$$

where the compliance tensor \mathcal{S} is expressed in form of the 6×6 symmetric matrix, given by:

$$\mathcal{S} = \begin{bmatrix} S_{11} & S_{12} & S_{13} & S_{14} & S_{15} & S_{16} \\ S_{12} & S_{22} & S_{23} & S_{24} & S_{25} & S_{26} \\ S_{13} & S_{23} & S_{33} & S_{34} & S_{35} & S_{36} \\ S_{14} & S_{24} & S_{34} & S_{44} & S_{45} & S_{46} \\ S_{15} & S_{25} & S_{35} & S_{45} & S_{55} & S_{56} \\ S_{16} & S_{26} & S_{36} & S_{46} & S_{56} & S_{66} \end{bmatrix} \quad (3.21)$$

Note that the transformation between S_{ijkl} and $S_{\alpha\beta}$ is similar to that one between C_{ijkl} and $C_{\alpha\beta}$ except the following:

$$\begin{aligned} S_{ijhk} &= S_{\alpha\beta} && \text{if both } \alpha, \beta \leq 3 \\ 2S_{ijhk} &= S_{\alpha\beta} && \text{if either } \alpha \text{ or } \beta \leq 3 \\ 4S_{ijhk} &= S_{\alpha\beta} && \text{if both } \alpha, \beta > 3. \end{aligned} \quad (3.22)$$

From (3.17)₁ and (3.20)₁, it is obtained the expression of the strain energy, the strain energy W becomes:

$$W = \frac{1}{2} \mathbf{T}^T \mathbf{E} = \frac{1}{2} \mathbf{E}^T \mathcal{C} \mathbf{E} = \mathbf{T}^T \mathcal{S} \mathbf{T} \quad (3.23)$$

and, for the positiveness of W , it must be:

$$\begin{aligned} \mathbf{E}^T \mathcal{C} \mathbf{E} &> 0 \\ \mathbf{T}^T \mathcal{S} \mathbf{T} &> 0 \end{aligned} \quad (3.24)$$

This implies that the matrices \mathcal{C} and \mathcal{S} are both positive definite. Moreover, the substitution of the (3.20)₁ into the (3.17)₁ yields:

$$\mathcal{C} \mathcal{S} = \mathbf{I} = \mathcal{S} \mathcal{C} \quad (3.25)$$

where the second equality follows from the first one which says that \mathcal{C} and \mathcal{S} are the inverses of each other and, hence their product commute.

3.4 Material Symmetry

The 6×6 matrices \mathcal{C} and \mathcal{S} contain 21 independent elastic constants. The number of independent constants is reduced when the material possesses a certain material symmetry.

Under an orthogonal transformation

$$x_i^* = Q_{ij} x_j \quad \text{or} \quad \mathbf{x}^* = \mathbf{Q} \mathbf{x} \quad (3.26)$$

in which \mathbf{Q} is an orthogonal matrix that satisfies the relations:

$$\mathbf{Q} \cdot \mathbf{Q}^T = \mathbf{I} = \mathbf{Q}^T \mathbf{Q}, \quad (3.27)$$

the four rank elasticity tensor C_{ijkl}^* , referred to the x_i^* coordinate system becomes

$$C_{ijkl}^* = Q_{ip} Q_{jq} Q_{kr} Q_{ls} C_{pqrs} \quad (3.28)$$

If it results $C_{ijkl}^* = C_{ijkl}$, i.e.,

$$C_{ijkl} = Q_{ip} Q_{jq} Q_{kr} Q_{ls} C_{pqrs} \quad (3.29)$$

material is said to possess a *symmetry* with respect to \mathbf{Q} .

An anisotropic material possesses the symmetry of *central inversion* if (3.29) is satisfied for

$$\mathbf{Q} = \begin{bmatrix} -1 & 0 & 0 \\ 0 & -1 & 0 \\ 0 & 0 & -1 \end{bmatrix} = -\mathbf{I}. \quad (3.30)$$

It is obvious that the (3.29) is satisfied by the \mathbf{Q} given in the (3.30) for any C_{ijkl} .

Therefore, all the anisotropic materials have the symmetry of central inversion.

If \mathbf{Q} is a proper orthogonal matrix, the transformation (3.26) represents a rigid body rotation about an axis. So, an anisotropic material is said to possess a *rotational symmetry* if the (3.29) is satisfied for:

$$\mathbf{Q}^r(\theta) = \begin{bmatrix} \cos\theta & \sin\theta & 0 \\ -\sin\theta & \cos\theta & 0 \\ 0 & 0 & 1 \end{bmatrix} \quad (3.31)$$

which represents, for example, a rotation about the x_3 -axis an angle θ .

An orthogonal transformation \mathbf{Q} is a *reflection* if

$$\mathbf{Q} = \mathbf{I} - 2\mathbf{n} \otimes \mathbf{n}^T \quad (3.32)$$

where \mathbf{n} is a unit vector normal to the reflection plane. If \mathbf{m} is any vector on the plane,

$$\mathbf{Q}\mathbf{n} = -\mathbf{n}, \quad \mathbf{Q}\mathbf{m} = \mathbf{m}. \quad (3.33)$$

Thus a vector normal to the reflection plane reverses its direction after the transformation while a vector on the reflection plane remains unchanged. When (3.29) is satisfied by the \mathbf{Q} of (3.32), the material is said to possess a *symmetry plane*. For example, let

$$\mathbf{n}^T = [\cos \theta, \sin \theta, 0] \quad (3.34)$$

the symmetry plane. In this case, the orthogonal matrix \mathbf{Q} of the (3.32) has the following expression

$$\mathbf{Q}(\theta) = \begin{bmatrix} 2 + \cos 2\theta & \sin 2\theta & 0 \\ \sin 2\theta & 2 - \cos 2\theta & 0 \\ 0 & 0 & 1 \end{bmatrix}, \quad -\frac{\pi}{2} < \theta \leq \frac{\pi}{2}, \quad (3.35)$$

which is an improper orthogonal matrix. Since θ and $\theta + \pi$ represent the same plane, θ is limited to the range shown in (3.35)₂.

When $\theta = 0$, \mathbf{Q} becomes:

$$\mathbf{Q}(0) = \begin{bmatrix} -1 & 0 & 0 \\ 0 & 1 & 0 \\ 0 & 0 & 1 \end{bmatrix} \quad (3.36)$$

which represents a reflection about the plane $x_1 = 0$. When (3.29) is satisfied by (3.36), the material has a symmetry plane at $x_1 = 0$. If (3.29) is satisfied by (3.35) for any θ , the material is *transversely isotropic*. The x_3 -axis is the *axis of symmetry*. Two extreme cases of anisotropic elastic materials are *triclinic materials* and *isotropic materials*. A triclinic material possesses no rotational symmetry or a plane of reflection symmetry. An isotropic material possesses infinitely many rotational symmetries and planes of reflection symmetry.

3.5 The Elasticity Tensor for Materials with Symmetry Planes

Depending on the number of rotations and/or reflection symmetry a crystal possesses, Voigt (1928) has classified crystals into 32 classes. (See also Gurtin,

1972; Cowin and Mehrabadi, 1987; and Mehrabadi and Cowin. 1990). In terms of the 6×6 matrix \mathcal{C} however there are only 8 basic groups. For a non-crystalline material the structure of \mathcal{C} can also be represented by one of the 8 basic groups. We list below the 8 basic groups for \mathcal{C} according to the number of symmetry planes that each group has. Consideration of rotational symmetry does not change the structure of \mathcal{C} in each group. Without loss in generality we choose the symmetry plane (or planes) to coincide with the coordinate planes whenever possible. We will therefore employ the orthogonal matrix \mathbf{Q} (3.35) which represents a reflection with respect to a plane whose normal is on the (x_1, x_2) plane making an angle θ with the x_1 -axis. We will also employ the orthogonal matrix

$$\hat{\mathbf{Q}}(\psi) = \begin{bmatrix} 1 & 0 & 0 \\ 0 & -\cos 2\psi & -\sin 2\psi \\ 0 & -\sin 2\psi & \cos 2\psi \end{bmatrix}, \quad -\frac{\pi}{2} < \psi \leq \frac{\pi}{2} \quad (3.37)$$

which represents a reflection with respect to a plane whose normal is on the (x_2, x_3) plane making an angle ψ with the x_2 -axis, (Fig. 1.6.). The plane $x_2 = 0$ can be represented by either $\theta = \pi/2$ or $\psi = 0$.

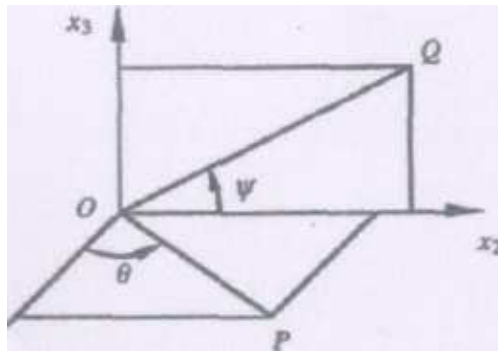


Figure. 1.6.

- I. *Triclinic Materials*. No symmetry planes exist.

$$\mathcal{C} = \begin{bmatrix} C_{11} & C_{12} & C_{13} & C_{14} & C_{15} & C_{16} \\ C_{12} & C_{22} & C_{23} & C_{24} & C_{25} & C_{26} \\ C_{13} & C_{23} & C_{33} & C_{34} & C_{35} & C_{36} \\ C_{14} & C_{24} & C_{34} & C_{44} & C_{45} & C_{46} \\ C_{15} & C_{25} & C_{35} & C_{45} & C_{55} & C_{56} \\ C_{16} & C_{26} & C_{36} & C_{46} & C_{56} & C_{66} \end{bmatrix} \quad n = 21 \quad (3.38)$$

II. *Monoclinic Materials.* One symmetry plane.

(a) Symmetry plane at $x_1 = 0$, i.e., $\theta = 0$.

$$\mathcal{C} = \begin{bmatrix} C_{11} & C_{12} & C_{13} & C_{14} & 0 & 0 \\ C_{12} & C_{22} & C_{23} & C_{24} & 0 & 0 \\ C_{13} & C_{23} & C_{33} & C_{34} & 0 & 0 \\ C_{14} & C_{24} & C_{34} & C_{44} & 0 & 0 \\ 0 & 0 & 0 & 0 & C_{55} & C_{56} \\ 0 & 0 & 0 & 0 & C_{56} & C_{66} \end{bmatrix} \quad n = 13 \quad (3.39)$$

(b) Symmetry plane at $x_2 = 0$, i.e., $\theta = \pi/2$ or $\psi = 0$.

$$\mathcal{C} = \begin{bmatrix} C_{11} & C_{12} & C_{13} & 0 & C_{15} & 0 \\ C_{12} & C_{22} & C_{23} & 0 & C_{25} & 0 \\ C_{13} & C_{23} & C_{33} & 0 & C_{35} & 0 \\ 0 & 0 & 0 & C_{44} & 0 & C_{46} \\ C_{15} & C_{25} & C_{35} & 0 & C_{55} & 0 \\ 0 & 0 & 0 & C_{46} & 0 & C_{66} \end{bmatrix} \quad n = 13 \quad (3.40)$$

(c) Symmetry plane at $x_3 = 0$, i.e., $\psi = \pi/2$.

$$\mathcal{C} = \begin{bmatrix} C_{11} & C_{12} & C_{13} & 0 & 0 & C_{16} \\ C_{12} & C_{22} & C_{23} & 0 & 0 & C_{26} \\ C_{13} & C_{23} & C_{33} & 0 & 0 & C_{36} \\ 0 & 0 & 0 & C_{44} & C_{45} & 0 \\ 0 & 0 & 0 & C_{45} & C_{55} & 0 \\ C_{16} & C_{26} & C_{36} & 0 & 0 & C_{66} \end{bmatrix} \quad n=13 \quad (3.41)$$

- II. *Orthotropic (or Rhombic) Materials.* The three coordinate planes $\theta=0$, $\pi/2$, and $\psi = \pi/2$ are the symmetry planes.

$$\mathcal{C} = \begin{bmatrix} C_{11} & C_{12} & C_{13} & 0 & 0 & 0 \\ C_{12} & C_{22} & C_{23} & 0 & 0 & 0 \\ C_{13} & C_{23} & C_{33} & 0 & 0 & 0 \\ 0 & 0 & 0 & C_{44} & 0 & 0 \\ 0 & 0 & 0 & 0 & C_{55} & 0 \\ 0 & 0 & 0 & 0 & 0 & C_{66} \end{bmatrix} \quad n=9 \quad (3.42)$$

- III. *Trigonal Materials.* Three symmetry planes at $\theta=0$ and $\pm\pi/3$.

$$\mathcal{C} = \begin{bmatrix} C_{11} & C_{12} & C_{13} & C_{14} & 0 & 0 \\ C_{12} & C_{11} & C_{13} & -C_{14} & 0 & 0 \\ C_{13} & C_{13} & C_{33} & 0 & 0 & 0 \\ C_{14} & -C_{14} & 0 & C_{44} & 0 & 0 \\ 0 & 0 & 0 & 0 & C_{44} & C_{14} \\ 0 & 0 & 0 & 0 & C_{14} & \frac{C_{11}-C_{12}}{2} \end{bmatrix} \quad n=6 \quad (3.43)$$

- IV. *Tetragonal Materials.* Five symmetry planes at $\theta=0$, $\pm\pi/4$, $\pi/2$ and $\psi = \pi/2$.

$$\mathcal{C} = \begin{bmatrix} C_{11} & C_{12} & C_{13} & 0 & 0 & 0 \\ C_{12} & C_{11} & C_{13} & 0 & 0 & 0 \\ C_{13} & C_{13} & C_{33} & 0 & 0 & 0 \\ 0 & 0 & 0 & C_{44} & 0 & 0 \\ 0 & 0 & 0 & 0 & C_{44} & 0 \\ 0 & 0 & 0 & 0 & 0 & C_{66} \end{bmatrix} \quad n=6 \quad (3.44)$$

- V. *Transversely Isotropic (or Hexagonal) Materials.* The symmetry planes are the $x_3 = 0$ plane and any plane that contains the x_3 -axis. The x_3 -axis is the axis of symmetry.

$$\mathcal{C} = \begin{bmatrix} C_{11} & C_{12} & C_{13} & 0 & 0 & 0 \\ C_{12} & C_{11} & C_{13} & 0 & 0 & 0 \\ C_{13} & C_{13} & C_{33} & 0 & 0 & 0 \\ 0 & 0 & 0 & C_{44} & 0 & 0 \\ 0 & 0 & 0 & 0 & C_{44} & 0 \\ 0 & 0 & 0 & 0 & 0 & \frac{C_{11}-C_{12}}{2} \end{bmatrix} \quad n=5 \quad (3.45)$$

- VI. *Cubic Materials.* Nine planes of symmetry whose normals are on the three coordinate axes and on the coordinate planes making an angle $\pi/4$ with the coordinate axes.

$$\mathcal{C} = \begin{bmatrix} C_{11} & C_{12} & C_{12} & 0 & 0 & 0 \\ C_{12} & C_{11} & C_{12} & 0 & 0 & 0 \\ C_{12} & C_{12} & C_{11} & 0 & 0 & 0 \\ 0 & 0 & 0 & C_{44} & 0 & 0 \\ 0 & 0 & 0 & 0 & C_{44} & 0 \\ 0 & 0 & 0 & 0 & 0 & C_{44} \end{bmatrix} \quad n=3 \quad (3.46)$$

VII. *Isotropic Materials.* Any plane is a symmetry plane.

$$\mathcal{C} = \begin{bmatrix} C_{11} & C_{12} & C_{12} & 0 & 0 & 0 \\ C_{12} & C_{11} & C_{12} & 0 & 0 & 0 \\ C_{12} & C_{12} & C_{11} & 0 & 0 & 0 \\ 0 & 0 & 0 & \frac{C_{11}-C_{12}}{2} & 0 & 0 \\ 0 & 0 & 0 & 0 & \frac{C_{11}-C_{12}}{2} & 0 \\ 0 & 0 & 0 & 0 & 0 & \frac{C_{11}-C_{12}}{2} \end{bmatrix} \quad n = 2 \quad (3.47)$$

Note that while the number of nonzero elements in \mathcal{C} may increase when different coordinate system are employed, the number of independent elastic constants n does not depend on the choice of the coordinate systems.

3.6 Restrictions on Elastic Constants

As shown above, the positiveness of the strain energy, yields that the stiffness tensor \mathcal{C} is positive defined, as well as, the positive definiteness of the stress energy, yields that the compliance tensor \mathcal{S} is defined positive. In particular, in the contracted notation, the (3.9) is equivalent to the (3.24)₁ which implies that the 6×6 matrix \mathcal{C} is also positive definite and, therefore, all its principal minors are positive, i.e.:

$$\begin{aligned} C_{ii} &> 0 \quad (i \text{ not summed}), \\ \begin{vmatrix} C_{ii} & C_{ij} \\ C_{ij} & C_{jj} \end{vmatrix} &> 0 \quad (i, j \text{ not summed}), \\ \begin{vmatrix} C_{ii} & C_{ij} & C_{ih} \\ C_{ij} & C_{jj} & C_{jh} \\ C_{ih} & C_{jh} & C_{hh} \end{vmatrix} &> 0 \quad (i, j, k \text{ not summed}), \\ &\vdots \end{aligned}$$

where i, j, h are distinct integers which can have any value from 1 to 6.

In particular, according to the theorem which states that a real symmetric matrix is positive definite if and only if its *leading* principal minors are positive, the *necessary* and *sufficient conditions* for the 6×6 matrix \mathcal{C} to be positive definite are the positivity of its 6 *leading* principal minors. Same considerations may be applied to the compliance tensor \mathcal{S} . By imposing these conditions of positivity on the minors of the matrices, some restrictions on the elastic coefficients can be found.

CHAPTER II

HETEROGENEOUS MATERIALS

1. Inhomogeneous solids: SAS/DAS Theorems

It is well known the difficulty to find solutions to anisotropic inhomogeneous material problems. A very few restricted classes of these problems are solved in a general way.

One example of these solutions is for cylinders subjected to pure torsion and possessing cylindrical orthotropy, with a variation of the shear moduli with the local normal direction to the family of curves of which the lateral boundary is a member (Cowin, 1987). This solution is a generalization, to a set of arbitrary cross-sectional shapes, of a problem solved by Voigt (Voigt, 1928) for a circular cross-section with radial variation of its cylindrical anisotropy. These cylinders are said to possess *shape intrinsic orthotropy* since it is the boundary of the cylinder that establishes the possible directional variation of the elastic moduli. A second example was given by Chung & Ting (Chung & Ting, 1995) who presented an exact solution for the case of an anisotropic half-space with elastic moduli dependent upon one coordinate, the angle θ , when the loads on the half-space are represented by a straight line of force. These kinds of problems were called *angularly inhomogeneous problems* by the authors. Closely related to these solutions is a third example called *radially inhomogeneous problems* (Alshits and Kirchner, 2001). As the name suggests, the variation of the elastic constants is in the radial direction in this case.

In spite of this difficulty, in the last years, it has been a growing interest about the mechanical behaviour of anisotropic and inhomogeneous solids, above all in biomechanics. Moreover, the necessity to build thermodynamically consistent

theories for this kind of materials, by means the employment of the mathematical theory of the *homogenization*, has determined the necessity to find exact analytical solutions in the ambit of this more complex section of the theory of elasticity, (Lions, 1985), (Maugin, 1993).

In the next sections, it is presented a useful method enables one to find solutions for inhomogeneous, anisotropic elastostatic problems under particular conditions by means of the use of two theorems, *S.A.S. theorem* and *D.A.S. theorem* (Fraldi and Cowin, 2004).

1.1 Stress Associated Solutions (SAS) Theorem for inhomogeneous elasticity

The Stress Associated Solution Theorem lets to find solutions for inhomogeneous, anisotropic elastostatic problems if two conditions are satisfied: (1) a knowledge of the solution for a homogeneous elastic *reference* problem (the *associated problem*) whose solution has a stress state with a zero eigenvalue everywhere in the domain of the problem, and (2) an inhomogeneous anisotropic elastic tensor related to the homogeneous anisotropic elastic tensor of (1) by

$$\mathcal{C}^I = \varphi(\mathbf{x})\mathcal{C}^H, \quad \varphi(\mathbf{x})|_{\forall \mathbf{x} \in B}, \varphi(\mathbf{x}) > \alpha > 0, \quad \alpha \in \mathbb{R}^+ \quad (2.1)$$

where $\mathcal{C}^H = \mathcal{C}^{H^T}$ is the elasticity tensor of a generic anisotropic homogeneous elastic material of the *reference problem*, \mathcal{C}^I is the elasticity tensor of the corresponding anisotropic inhomogeneous elastic problem, B is the domain occupied by both the homogeneous object B^H and the inhomogeneous one B^I , $\alpha \in \mathbb{R}^+$ is an arbitrary positive real number, while $\varphi(\mathbf{x})$ is a $C^2(B)$ scalar function. The assumption (2.1) means that the inhomogeneous character of the material is due to the presence of a scalar parameter producing the inhomogeneity in the elastic coefficients.

This method makes it possible to find analytical solutions for an *inhomogeneous* anisotropic elastic problem if the elastic solution of the corresponding *homogeneous*

anisotropic *reference* problem is known and characterized everywhere by a stress state with a zero eigenvalue. The solutions to the *inhomogeneous* anisotropic elastic problem are called the *associated solutions* of the *homogeneous problem*.

1.1.a Zero-eigenvalue stress and zero-eigenvalue strain fields

A zero-eigenvalue stress state (zero-eigenvalue strain state) is characterized by the condition that the determinant of the stress (strain) is zero

$$\det \mathbf{T} = 0, \quad (\det \mathbf{E} = 0). \quad (2.2)$$

It is easy to show that a zero-eigenvalue stress (strain) state is a necessary condition for a plane stress (strain) state. The components of the stress tensor \mathbf{T} (strain tensor \mathbf{E}) are denoted by σ_{ij} (ε_{ij}). The strain tensor \mathbf{E} is related to the displacement field \mathbf{u} by

$$\mathbf{E} = \frac{1}{2}[(\nabla \otimes \mathbf{u}) + (\nabla \otimes \mathbf{u})^T] = \text{sym} \nabla \otimes \mathbf{u} \quad \forall \mathbf{x} \in B \quad (2.3)$$

in which $\text{grad } \mathbf{u} = (\nabla \otimes \mathbf{u})$ and the symbol \otimes represents the *tensor product*. In components we have

$$\varepsilon_{ij} = \frac{1}{2}(u_{i,j} + u_{j,i}), \quad (2.4)$$

where the comma denotes differentiation and \mathbf{u} is the displacement field.

1.1.b Stress Associated Solutions (SAS) Theorem

Consider the following mixed boundary-value elastostatic homogeneous and anisotropic problem P^H in the absence of action-at-a-distance forces

$$\nabla \cdot \mathbf{T}(\mathbf{u}) = \mathbf{0} \quad \text{in } B^H, \quad \mathbf{T}(\mathbf{u}) \cdot \mathbf{n} = \mathbf{t} \quad \text{on } \partial B_t^H, \quad \mathbf{u} = \mathbf{u}_0 \quad \text{on } \partial B_u^H \quad (2.5)$$

where B^H is the domain occupied by the homogeneous elastic object, $\partial B^H = \{\partial B_t^H \cup \partial B_u^H\}$ is its boundary and \mathbf{t} and \mathbf{u}_0 are the traction field and the displacements assigned on the corresponding partition of the boundary, respectively (Barber, 1992; Gurtin, 1972). The notation for the divergence of the stress tensor is $\nabla \cdot \mathbf{T}(\mathbf{u}) = \text{div} \mathbf{T}(\mathbf{u})$, where the *del operator* is a vectorial differential operator defined by $\nabla \equiv \partial_i \mathbf{e}_i$, $\partial_i \equiv \partial / \partial x_i = (*),_i$ is the partial differential operator and \mathbf{e}_i is the base unit vector of the i -axis.

The anisotropic Hooke's law is written

$$\mathbf{T}(\mathbf{u}) = \mathbb{C}^H : \mathbf{E}(\mathbf{u}) = \mathbb{C}^H : \text{sym}(\nabla \otimes \mathbf{u}) = \mathbb{C}^H : (\nabla \otimes \mathbf{u}) \quad (2.6)$$

or, in components

$$\sigma_{ij} = C_{ijhk}^H \varepsilon_{hk} = C_{ijhk}^H u_{h,k}. \quad (2.7)$$

Let $\mathfrak{S}^H = \{\mathbf{u}^H, \mathbf{E}^H, \mathbf{T}^H\}$ be the solution of the homogeneous problem (2.5).

Consider now an associated anisotropic elastic inhomogeneous problem P^I , described by modifying the system (2.5), with $\mathbf{t}^I = \boldsymbol{\varphi} \mathbf{t}$ representing the traction field applied on ∂B_t^I and the inhomogeneous anisotropic elasticity tensor given by (2.1), thus

$$\nabla \cdot \mathbf{T}(\mathbf{u}) = \mathbf{0} \quad \text{in } B^I, \quad \mathbf{T}(\mathbf{u}) \cdot \mathbf{n} = \mathbf{t}^I \quad \text{on } \partial B_t^I, \quad \mathbf{u} = \mathbf{u}_0 \quad \text{on } \partial B_u^I \quad (2.8)$$

The solid domains B^H and B^I , as well as their corresponding boundary partitions made on ∂B^H and ∂B^I , are geometrically the same in the homogeneous and inhomogeneous problems. Then, if we expand the equation (2.8)₁ it is possible to write

$$\begin{aligned}\nabla \cdot \mathbf{T}(\mathbf{u}) &= \nabla \cdot [\varphi(\mathbf{x}) \mathbf{C}^H : \mathbf{E}(\mathbf{u})] = \\ &= \varphi(\mathbf{x}) \nabla \cdot [\mathbf{C}^H : \mathbf{E}(\mathbf{u})] + [\mathbf{C}^H : \mathbf{E}(\mathbf{u})] \cdot \nabla \varphi(\mathbf{x}) = \mathbf{0}\end{aligned}\quad (2.9)$$

where $\nabla(*) = \text{grad}(*)$ is the gradient operator applied on a generic scalar-valued function $(*)$. Consider now the situation in which the displacements are equal for the homogeneous and inhomogeneous problems. Then, by substituting the displacement solution \mathbf{u}^H obtained for the homogeneous problem P^H in (2.9) in place of the displacement vector \mathbf{u} , we have that

$$\nabla \cdot \mathbf{T}(\mathbf{u}^H) = \varphi(\mathbf{x}) [\nabla \cdot \mathbf{T}^H(\mathbf{u}^H)] + [\mathbf{T}^H(\mathbf{u}^H)] \cdot \nabla \varphi(\mathbf{x}) = \mathbf{0}\quad (2.10)$$

But, since $\nabla \cdot [\mathbf{T}^H(\mathbf{u}^H)] = \nabla \cdot [\mathbf{C}^H : \mathbf{E}(\mathbf{u}^H)] = \mathbf{0}$, it follows that

$$[\mathbf{T}^H(\mathbf{u}^H)] \cdot \nabla \varphi(\mathbf{x}) = \mathbf{0} \quad \forall \mathbf{x} \in B^I\quad (2.11)$$

By excluding the trivial case in which $\varphi(\mathbf{x}) = \text{constant}$, it follows that

$$\det \mathbf{T}^H = 0, \quad \forall \mathbf{x} \in B^H\quad (2.12)$$

This means that the stress state at \mathbf{x} of the *reference* homogeneous problem is required to be a zero eigenvalue stress state everywhere in the domain. To investigate the geometrical meaning of the equation (2.11), since (2.11) must be true everywhere in B^I , we consider, without loss of generality, the *local principal stress reference system* $\{\xi_1, \xi_2, \xi_3\}$, in which the stress tensor \mathbf{T}^H takes the component form

$$\mathbf{T}^H = \begin{bmatrix} \sigma_{\xi_1}^H & 0 & 0 \\ 0 & \sigma_{\xi_2}^H & 0 \\ 0 & 0 & \sigma_{\xi_3}^H \end{bmatrix}.\quad (2.13)$$

Representing the gradient of the scalar function φ as

$$\nabla\varphi(\xi)^T = [\varphi_{,\xi_1} \quad \varphi_{,\xi_2} \quad \varphi_{,\xi_3}], \quad (2.14)$$

the three scalar equations implied by (2.11) are written as

$$\sigma_{\xi_1}^H \varphi_{,\xi_1} = 0, \quad \sigma_{\xi_2}^H \varphi_{,\xi_2} = 0, \quad \sigma_{\xi_3}^H \varphi_{,\xi_3} = 0 \quad (2.15)$$

The system (2.15) is satisfied if the stress tensor T^H for the reference homogeneous problem P^H is, at each internal point $x \in B^H$, a locally variable *zero eigenvalue stress* state. If there is only one zero eigenvalue, say in the ξ_3 -direction, the only non-zero component of the vector $\nabla\varphi$, is $\varphi_{,\xi_3}$ at the corresponding points $x \in B^I$. If there are two zero eigenvalues there can be two non-zero components of $\nabla\varphi$. The case of three zero eigenvalues of the stress tensor T^H is trivial and will not be mentioned further. It follows that, at each internal point, the equipotential surfaces of φ admit as a tangent plane the plane whose normal is coaxial with the eigenvector associated with the zero stress eigenvalue (or a direction, in the case of two zero stress eigenvalues). This is illustrated in Figure 2.1. for the case of one zero eigenvalue of stress.

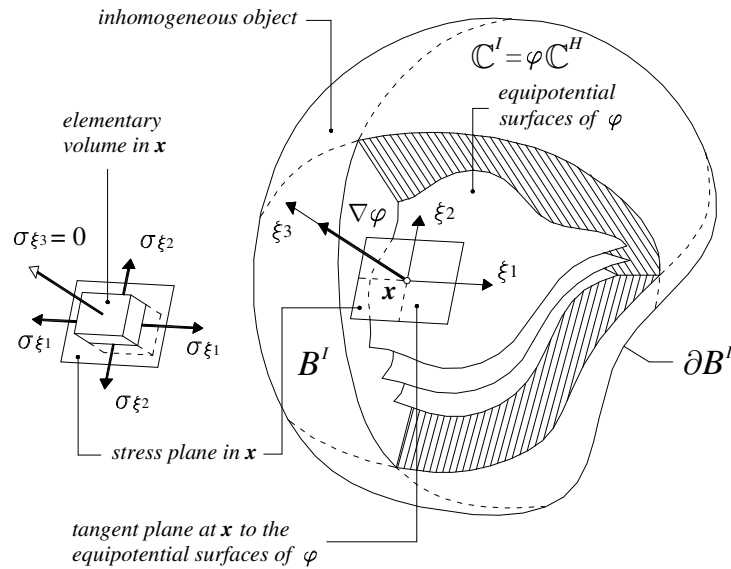


Fig. 2.1.

Geometrical interpretation of the relationship between the equipotential surfaces of φ and the distribution of the planes of stresses in the associated anisotropic problem

The geometrical relationship (2.11) between the stress tensor T^H and the vector $\nabla\varphi$ may be rewritten in the form

$$\{T^H \cdot \nabla\varphi = \mathbf{0}\} \Leftrightarrow \{\forall \mathbf{v} \in V, T^H : (\nabla\varphi \otimes \mathbf{v}) = 0\} \quad (2.16)$$

where \mathbf{v} is any unit vector defined in the three-dimensional Euclidean space \mathbb{E}^3 and V represents the corresponding vector space. It follows that the stress vector on the plane whose normal is \mathbf{v} is always orthogonal to the vector $\nabla\varphi$.

2 Anisotropic media: volume fraction and Fabric Tensors

In multiphase or damage materials, mechanical properties are closely related to the underlying microstructure or crack distribution. Although the volume fraction is the primary parameter in the geometric characterization of the microstructure of such materials, it does not provide information about the arrangement and the orientation of the microstructure. It is therefore necessary to introduce further parameters able to describe such orientations. The approach commonly used to modelling the material microstructure consists on introducing tensors of higher rank which characterize the microstructural architecture. In particular, in many applications, microstructural anisotropy seems to be sufficiently well described by a scalar and a symmetric second rank fabric tensor, which restricts the material symmetry to orthotropy.

Fabric tensors may be defined in a wide number of ways but it is required to be a positive definite tensor that is a quantitative stereological measure of the microstructural architecture, a measure whose principal axes are coincident with the principal microstructural direction and whose eigenvalues are proportional to the distribution of the microstructure in the associated principal direction. The fabric tensor may be measured on a finite test volume and it is considered a continuous function of the position in the material. It should be highlighted that since the fabric tensor is a continuum point property, its applicability to solve real problems is really difficult because it would require a wide number of measures. In other words it would be necessary to evaluate the fabric tensor in each point of the material.

In the next sections, some way to construct fabric tensors proposed in scientific literature are illustrate.

2.1 Mean Intercept Length (MIL) Tensor

In order to characterize the microstructural anisotropy in orthotropic materials, Harrigan and Mann (1984) proposed a particular second order tensor – the so-called mean intercept length (MIL) tensor – related to the stereological measurement of the microstructural arrangement. In particular, the MIL in a material is define as the average distance, measured along a particular straight line, between two interfaces of the two different constituents. The value of the MIL is a function of the slope θ of the line along which the measurement is made in a specific plane. If, by plotting in a polar diagram the MIL – measured in the selected plane passing through a particular point in the specimen – as function of θ , the polar diagram produced ellipses (see Figure 2.4), than the values of all MILs in the plane may be represented by a second-order tensor in two dimension. By extending these consideration to a three-dimensional case, the MILs in all direction would be represented by an ellipsoid that is by a positive define second rank tensor \mathbf{M} which is commonly related to the mean intercept length $L(\mathbf{n})$ by the relationship $1/L^2(\mathbf{n}) = \mathbf{n} \cdot \mathbf{M} \mathbf{n}$, where \mathbf{n} is the unit vector in the direction of the mean intercept length measurement.

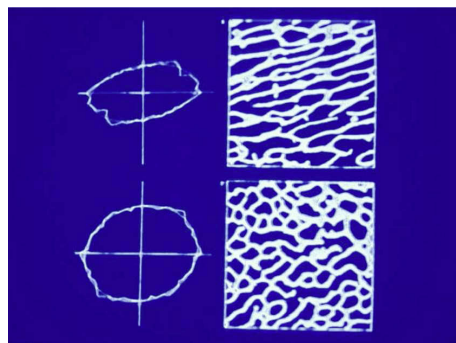


Fig. 2.4.

Polar diagram of the Mean Intercept Length function of a cancellous bone

The MIL approach as well as other stereological methods – e.g. the volume orientation method, the star volume distribution method – were proposed to construct the fabric tensor for biphasic materials, with particular reference to a specific porous material, the cancellous bone (Odgaard *et al.*, 1997). However, it is worth to highlight that for particular microstructure – e.g. planar fibre networks or materials made of a set of plates – the MIL distribution is not in general elliptic and so it may not be analytically expressed in terms of a second-order tensor (Tözeren and Skalak, 1989).

Cowin (Cowin, 1986) defined a fabric tensor \mathbf{H} related to the MIL tensor \mathbf{M} by $\mathbf{H} = \mathbf{M}^{-1/2}$. Such tensor is well defined being the positive square root of the inverse of the positive definite symmetric tensor \mathbf{M} . The difference between \mathbf{H} and \mathbf{M} is in the shape of ellipsoid while the principal axes coincide.

2.2 Fabric Tensor and Microcrack Distribution

In the characterization of mechanical response of damaged materials, a central problem is represented by the development of the formalism which enables a traditional continuum representation of the statistical distribution of microcracks compiled from the stereological data measured on a statistically homogeneous volume of damaged microstructure. The selection of the damage parameter approximating the measured data is not unique due to the contradictory requirements of accuracy and simplicity.

In the framework of damage mechanics, the effective continuum theories (Krajcinovic, 1996) are based on the assumption that the exact location of a microcrack within a representative volume element is not very important for the determination of the effective properties. This statement is, rigorously speaking, valid only in the dilute concentration limit. In other case, it is necessary to determine the distribution of crack surface densities as a function, for example, of the orientation of their bedding planes. For this purpose, the damage at a material point x is defined by a finite set of doublets $[\rho_i, n_i]$ ($i=1,2,\dots,m$) where ρ_i is the

microcrack density in a plane with normal n_i . Geometrically this set of doublets represents a binned histogram. Each bin defines the microcrack density in planes with orientations belonging to a particular range of angles. To determine the density of microcracks sharing a particular orientation (defined by a normal \mathbf{n} to their bedding plane) it is necessary to make a large number of parallel cuts through a representative volume element of the actual material which maps on the observed material point in the effective continuum. In the limit of a very large number of orientations the density function $\rho(\mathbf{n})$ tends to a continuous distribution of the densities of microcracks in planes with normals \mathbf{n} passing through the material point \mathbf{x}_0 (Iankamban and Krajcinovic 1987, Curran, *et al.* 1987).

The principal problem in the formulation of an analytical representation of the experimental data is related to the representation of the raw statistical data in a frame indifferent (objective) manner. This question was explored and answered by Kanatani (1984) and later elaborated upon in connection to the damage distribution by Budiansky and O'Connell (1976), Onat and Leckie (1984), Wong (1985) and Lubarda and Krajcinovic (1993). The central task is to establish a procedure relating a measured distribution of microcrack densities as a function of their orientation $\rho(\mathbf{n})$ to an appropriate damage measure in form of a tensor invariant to coordinate transformations. This procedure must provide a criterion needed to measure the fit between the experimental data and various analytical descriptions of the microcrack distributions. The empirical function $\rho(\mathbf{n})$, typically determined for a limited number of bedding planes and samples, is seldom smooth. Depending on the heterogeneity of the material, size of the representative volume element, experimental technique, available equipment and finally the chance itself the function $\rho(\mathbf{n})$ may substantially change from one sample to the other. A large number of samples and sections may be needed for a statistically valid characterization of the function $\rho(\mathbf{n})$. In most cases a task like this is not cheap enough to be feasible. It is possible to utilize the measured or conjectured directional dependence of the crack surface area density $\rho(\mathbf{n})$ directly into an appropriately

formulated computational model (Ilankamban and Krajcinovic 1987, Curran, *et al.* 1987). For the present purposes it is obviously advantageous to use a tensor function which approximates the distribution $\rho(\mathbf{n})$ with sufficient accuracy. The procedure, shown in the previous section, is developed in order to derive a tensor approximation of the raw data arranged into the histogram, expanding the function $\rho(\mathbf{n})$ into a Fourier-type series of certain families of Laplace spherical harmonics (Kanatani 1984, Onat and Leckie 1988) which represent the dyadic products of the unit vector \mathbf{n} and the Kronecker delta tensor δ . Since a surface is defined by an axial vector the analytical expression for the distribution $\rho(\mathbf{n})$ can involve only even order tensors. A rigorous approximation of an empirical or actually measured function $\rho(\mathbf{n})$ involves an infinite series of tensors of even order. In many cases the details of this distribution may not have a discernible effect on the macro properties and may not be reproducible when testing "identical" specimens under "identical" circumstances. For purely practical purposes this series must be truncated to a rather moderate number of terms limited to the lowest order tensors. The truncation introduces inevitable errors into the selected representation and some non-physical effects which were not noticed until recently.

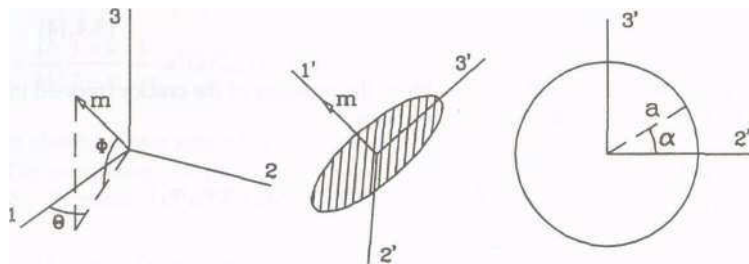


Fig. 2.5.

Geometry of a penny-shaped crack

With reference to penny-shaped cracks defined by their radii a and two Euler angles (θ, ϕ) , shown in Figure 2.5., it is possible to write (Krajcinovic, 1996) the average crack density within a selected unit sphere centered at a material point as

$$\begin{aligned}\bar{w} &= \frac{1}{4\pi} \int_{a^-}^{a^+} a^3 \vartheta(a) da \int_0^{2\pi} \int_{-\pi/2}^{\pi/2} \rho(\phi, \theta) \cos \phi d\theta d\phi = \\ &= \frac{1}{4\pi} N \langle a^3 \rangle \int_0^{2\pi} \int_{-\pi/2}^{\pi/2} \rho(\phi, \theta) \cos \phi d\theta d\phi = N \langle a^3 \rangle \bar{\rho}(\mathbf{n})\end{aligned}\quad (2.1)$$

where $N \langle a^3 \rangle = \int_{a^-}^{a^+} a^3 \vartheta(a) da$ is the non-dimensional microcracks density. To be able to compare different microcrack distributions with respect to the orientations $w(\mathbf{n}) = N \langle a^3 \rangle \rho(\mathbf{n}) = N \langle a^3 \rangle \rho(\phi, \theta)$ the product $N \langle a^3 \rangle = 1$ will be fixed in the sequel.

Scalar Representation of the Damage Variable. The microcrack distribution can be assumed to be approximately isotropic when the microcrack density is a weak function of the plane orientation (defined by the normal \mathbf{n} to the bedding plane through the material point). In this special case (which is preferred primarily by analysts if not by the geometry, nature and the physics of defect nucleation and growth) the microcrack distribution is fully defined by a single scalar ρ_0 which represents the total microcrack density or by the density $\bar{\rho}$ averaged over the solid angle. These two scalar measures of the crack distribution are related by the well known formula

$$\rho^0 \equiv D^0 = \int_{\Omega} \rho(n) d\Omega = 4\pi \bar{\rho}. \quad (2.2)$$

The integration in (2.2) is extended over all orientations within the solid angle $\Omega = 4\pi$. In this, simplest of all cases, the damage is defined by a single parameter ρ^0 (microcrack density). All symmetries of the original solid are preserved. The scalar damage variable (2.2) is introduced for the sake of consistency and uniformity. Due to its simplicity the scalar damage variable representation has been extensively utilized in the past (see, for example, Lemaitre and Chaboche 1978, Lemaitre 1986, 1992).

Second Order Tensor Representation of the Damage Variable. The isotropic distribution of microcracks is a relatively rare phenomenon which may occur in rocks in crustal conditions (i.e. well confined in all directions) which are exposed to large temperatures and internal pressures and/or expansive exothermic reactions. In a general case the microcracks distribution is characterized by a varying degree of anisotropy. In a frequently encountered class of problems and tests the microcrack distribution may render the specimen statistically (macro) orthotropic. The orthotropy may also be a function of the variations of strength and stiffness with direction. This may happen in sedimentary rocks characterized by a strong dependence of the cohesive strength on the primary depositional petrofabric and also in laminate composites made of fiber reinforced laminae. The microcrack induced orthotropy can also be stress induced. The damage density in an initially isotropic solid subjected to proportional loading will reach maximum densities in the planes perpendicular to the largest principal stress. Similarly, the microcrack densities will be minimal in planes which are orthogonal to the minimum principal stress. The principal planes of the damage density will often be perpendicular assuming that the state of stress is simple and the loads proportional. This class of microcrack distributions may be adequately represented by a second order tensor. The microcrack density in planes with a normal \mathbf{n} can be in this case defined by the expression

$$\rho(\mathbf{n}) = \rho_{ij} n_i n_j \quad (2.3)$$

(Lubarda, Krajcinovic 1993) where ρ_{ij} is a symmetric second order tensor. Integrating (2.3) over the entire solid angle, and using the identity

$$\int_{\Omega} n_i n_j d\Omega = \frac{4\pi}{3} \delta_{ij} \quad (2.4)$$

where δ_{ij} is the Kronecker (identity) delta tensor, it follows that the first invariant (trace) of the second order tensor ρ_{ij} is

$$\rho_{kk} = \frac{3}{4\pi} \rho^0 \quad (2.5)$$

The scalar damage variable ρ^0 in (2.5) is defined by (2.2). Multiplying both sides of (2.3) by $n_m n_n$ and integrating the product over the solid angle while making use of the identity

$$\int_{\Omega} n_i n_j n_m n_n d\Omega = \frac{4\pi}{5} I_{ijmn} \quad (2.6)$$

leads to the following expression

$$\frac{8\pi}{15} \left(\rho_{ij} + \frac{1}{2} \rho_{kk} \delta_{ij} \right) = \int_{\Omega} \rho(n) n_i n_j d\Omega. \quad (2.7)$$

The fourth order tensor I in (2.6) is defined by the tensor products of two delta second order tensors as

$$I_{ijmn} = \frac{1}{3} (\delta_{ij} \delta_{mn} + \delta_{im} \delta_{jn} + \delta_{in} \delta_{jm}) \quad (2.8)$$

The microcrack density tensor can now be derived by substituting (2.5) into (2.7)

$$\rho_{ij} = \frac{15}{8\pi} \left(D_{ij} - \frac{\rho^0}{5} \delta_{ij} \right) \quad (2.9)$$

where

$$D_{ij} = \int_{\Omega} \rho(n) n_i n_j d\Omega \quad (2.10)$$

is referred to as the second order damage tensor. The microcrack density distribution (2.3) is, in view of (2.9), a function of the scalar and second order tensor damage parameters

$$\rho(n) = \frac{15}{8\pi} n_i n_j D_{ij} - \frac{3}{8\pi} D^0. \quad (2.11)$$

2.3 Relationship between Fabric Tensor and Elasticity Tensor

From a mathematical point of view, identifying the dependence of the elastic behaviour of the material on its microstructure consists in analyzing the formal relationship between the fabric tensor and the elasticity tensor.

The main attempt to relate a fabric tensor describing microstructure to a fourth rank elasticity tensor – with specific reference to porous materials – is due to Cowin (Cowin, 1985). He proposed a model based on a normalized second rank fabric tensor and developed a general representation of $\bar{\mathbf{C}}$ as a function of the solid volume fraction γ and of the invariants of the fabric tensor \mathbf{H} based on the notion that the matrix material of the porous elastic solid is isotropic and that the anisotropy of the porous elastic solid itself is due only to the geometry of microstructure represented by the fabric tensor. The mathematical statement of this notion is that the stress tensor \mathbf{T} is an isotropic function of the strain tensor \mathbf{E} and the fabric tensor \mathbf{H} as well as the solid volume fraction γ . Thus, the tensor valued function

$$\mathbf{T} = \mathbf{T}(\gamma, \mathbf{E}, \mathbf{H}) \quad (2.12)$$

has the property that

$$\mathbf{Q}\mathbf{T}\mathbf{Q}^T = \mathbf{T}(\gamma, \mathbf{Q}\mathbf{E}\mathbf{Q}^T, \mathbf{Q}\mathbf{H}\mathbf{Q}^T) \quad (2.13)$$

for all orthogonal tensors \mathbf{Q} . This definition of an isotropic tensor valued function is given, for example, by Truesdell and Noll (1965). In accord with the isotropy assumption, the stress tensor \mathbf{T} has the representation

$$\begin{aligned} \mathbf{T} = & f_1 \mathbf{I} + f_2 \mathbf{H} + f_3 \mathbf{H}^2 + f_4 \mathbf{E} + f_5 \mathbf{E}^2 + f_6 (\mathbf{HE} + \mathbf{EH}) \\ & + f_7 (\mathbf{H}^2 \mathbf{E} + \mathbf{EH}^2) + f_8 (\mathbf{HE}^2 + \mathbf{E}^2 \mathbf{H}) + f_9 (\mathbf{H}^2 \mathbf{E}^2 + \mathbf{E}^2 \mathbf{H}^2) \end{aligned} \quad (2.14)$$

where f_i through f_9 are function of the ten invariants $Tr\mathbf{H}$, $Tr\mathbf{H}^2$, $Tr\mathbf{H}^3$, $Tr\mathbf{E}$, $Tr\mathbf{E}^2$, $Tr\mathbf{E}^3$, $Tr\mathbf{HE}$, $Tr\mathbf{H}^2\mathbf{E}$, $Tr\mathbf{HE}^2$, $Tr\mathbf{E}^2\mathbf{H}^2$. This representation is reduced by the requirement that \mathbf{T} be linear in \mathbf{E} and that \mathbf{T} vanish when \mathbf{E} vanishes, thus

$$\mathbf{T} = f_1 \mathbf{I} + f_2 \mathbf{H} + f_3 \mathbf{H}^2 + f_4 \mathbf{E} + f_6 (\mathbf{HE} + \mathbf{EH}) + f_7 (\mathbf{H}^2 \mathbf{E} + \mathbf{EH}^2) \quad (2.15)$$

where f_1 , f_2 , f_3 must be of the form

$$\begin{aligned} f_1 &= a_1 Tr\mathbf{E} + a_2 Tr\mathbf{HE} + a_3 Tr\mathbf{H}^2\mathbf{E}, \\ f_2 &= d_1 Tr\mathbf{E} + b_1 Tr\mathbf{HE} + b_2 Tr\mathbf{H}^2\mathbf{E}, \\ f_3 &= d_2 Tr\mathbf{E} + d_3 Tr\mathbf{HE} + b_3 Tr\mathbf{H}^2\mathbf{E}, \end{aligned} \quad (2.16)$$

and where a_1 , a_2 , a_3 , b_1 , b_2 , b_3 , d_1 , d_2 and d_3 , are function of $Tr\mathbf{H}$, $Tr\mathbf{H}^2$ and $Tr\mathbf{H}^3$. It follows then that

$$\begin{aligned} \mathbf{T} = & \mathbf{I} (a_1 Tr\mathbf{E} + a_2 Tr\mathbf{HE} + a_3 Tr\mathbf{H}^2\mathbf{E}) + \mathbf{H} (d_1 Tr\mathbf{E} + b_1 Tr\mathbf{HE} + b_2 Tr\mathbf{H}^2\mathbf{E}) \\ & + \mathbf{H}^2 (d_2 Tr\mathbf{E} + d_3 Tr\mathbf{HE} + b_3 Tr\mathbf{H}^2\mathbf{E}) + 2c_1 \mathbf{E} + 2c_2 (\mathbf{HE} + \mathbf{EH}) \\ & + 2c_3 (\mathbf{H}^2 \mathbf{E} + \mathbf{EH}^2) \end{aligned} \quad (2.17)$$

where we have set $f_4 = 2c_1$, $f_6 = 2c_2$ and $f_7 = 2c_3$. This result may be expressed in indicial notation as

$$\begin{aligned}
 T_{ij} = & \delta_{ij} (a_1 E_{kk} + a_2 H_{rp} E_{pr} + a_3 H_{rq} H_{qp} E_{pr}) + H_{ij} (d_1 E_{kk} + b_1 H_{rp} E_{pr} + b_2 H_{rq} H_{qp} E_{pr}) \\
 & + H_{is} H_{sj} (d_2 E_{kk} + d_3 H_{rp} E_{pr} + b_3 H_{rq} H_{qp} E_{pr}) + 2c_1 E_{ij} + 2c_2 (H_{ir} E_{rj} + E_{ir} H_{rj}) \\
 & + 2c_3 (H_{ip} H_{pr} E_{rj} + E_{ir} H_{rp} H_{pj})
 \end{aligned} \tag{2.18}$$

Comparison of this result with the constitutive equation $T_{ij} = C_{ijhk} E_{hk}$ suggests that C_{ijhk} should be of the form

$$\begin{aligned}
 C_{ijhk} = & (a_1 \delta_{ij} + d_1 H_{ij} + d_2 H_{is} H_{sj}) \delta_{hk} + (a_2 \delta_{ij} + b_1 H_{ij} + d_3 H_{is} H_{sj}) H_{hk} \\
 & + (a_3 \delta_{ij} + b_2 H_{ij} + b_3 H_{is} H_{sj}) H_{hq} H_{qk} + 2c_1 \delta_{hi} \delta_{kj} \\
 & + 2c_2 (H_{ih} \delta_{kj} + \delta_{ih} H_{kj}) + 2c_3 (H_{ip} H_{pk} \delta_{kj} + \delta_{ih} H_{kp} H_{ps}).
 \end{aligned} \tag{2.19}$$

In order to satisfy the symmetry conditions (1.90) we must set $d_1 = a_2$, $d_2 = a_3$, and $d_3 = b_2$ and take the symmetric parts of the terms multiplied by $2c_1$, $2c_2$, and $2c_3$ with respect to hk and ij . The final results may be express as follow

$$\begin{aligned}
 C_{ijhk} = & a_1 \delta_{ij} \delta_{hk} + a_2 (H_{ij} \delta_{ij} + H_{hk} \delta_{hk}) + a_3 (\delta_{ij} H_{hq} H_{qk} + \delta_{hk} H_{iq} H_{qj}) + \\
 & + b_1 H_{ij} H_{hk} + b_2 (H_{ij} H_{hq} H_{qk} + H_{is} H_{sj} H_{hk}) + b_3 H_{is} H_{sj} H_{hq} H_{qk} + \\
 & + c_1 (\delta_{hi} \delta_{kj} + \delta_{ki} \delta_{hj}) + c_2 (H_{ih} \delta_{kj} + H_{hj} \delta_{ki} + H_{ik} \delta_{hj} + H_{kj} \delta_{hi}) + \\
 & + c_3 (H_{ir} H_{rh} \delta_{kj} + H_{rj} H_{hr} \delta_{ki} + H_{ir} H_{rk} \delta_{hj} + H_{kr} H_{rj} \delta_{ih})
 \end{aligned} \tag{2.20}$$

where a_1 , a_2 , a_3 , b_1 , b_2 , b_3 , c_1 , c_2 and c_3 are functions of γ and $Tr\mathbf{H}$, $Tr\mathbf{H}^2$ and $Tr\mathbf{H}^3$.

It is possible to show that the representation (2.20) for the fourth rank elasticity tensor is not capable of representing all possible elastic material symmetry. The last material symmetry that may be represented by is orthotropy. In fact, expanding in

indicial notation in the coordinate system that diagonalized the fabric tensor ($H_{12} = H_{13} = H_{23} = 0$), only the following nine components of the elastic tensor are non-zero and are function of the nine coefficient $a_1, a_2, a_3, b_1, b_2, b_3, c_1, c_2, c_3$ and of the three eigenvalues of \mathbf{H} , H_{11}, H_{22} and H_{33}

$$\begin{aligned}
 C_{1111} &= a_1 + 2c_1 + 2(a_2 + 2c_2)H_{11} + (2a_3 + b_1 + 4c_3)H_{11}^2 + 2b_2H_{11}^3 + b_3H_{11}^4 \\
 C_{2222} &= a_1 + 2c_1 + 2(a_2 + 2c_2)H_{22} + (2a_3 + b_1 + 4c_3)H_{22}^2 + 2b_2H_{22}^3 + b_3H_{22}^4 \\
 C_{3333} &= a_1 + 2c_1 + 2(a_2 + 2c_2)H_{33} + (2a_3 + b_1 + 4c_3)H_{33}^2 + 2b_2H_{33}^3 + b_3H_{33}^4 \\
 C_{1122} &= a_1 + a_2(H_{11} + H_{22}) + a_3(H_{11}^2 + H_{22}^2) + b_1H_{11}H_{22} + b_2(H_{11}H_{22}^2 + H_{22}H_{11}^2) \\
 &\quad + b_3H_{11}^2H_{22}^2 \\
 C_{1133} &= a_1 + a_2(H_{11} + H_{33}) + a_3(H_{11}^2 + H_{33}^2) + b_1H_{11}H_{33} + b_2(H_{11}H_{33}^2 + H_{33}H_{11}^2) \\
 &\quad + b_3H_{11}^2H_{33}^2 \\
 C_{3322} &= a_1 + a_2(H_{33} + H_{22}) + a_3(H_{33}^2 + H_{22}^2) + b_1H_{33}H_{22} + b_2(H_{33}H_{22}^2 + H_{22}H_{33}^2) \\
 &\quad + b_3H_{33}^2H_{22}^2 \\
 C_{1212} &= c_1 + c_2(H_{11} + H_{22}) + c_3(H_{11}^2 + H_{22}^2) \\
 C_{1313} &= c_1 + c_2(H_{11} + H_{33}) + c_3(H_{11}^2 + H_{33}^2) \\
 C_{3232} &= c_1 + c_2(H_{33} + H_{22}) + c_3(H_{33}^2 + H_{22}^2)
 \end{aligned} \tag{2.21}$$

Note that these nine components of the elasticity tensor are distinct if and only if the eigenvalues of \mathbf{H} are distinct. In fact, it is easy to see that by setting $H_{22} = H_{33}$ in the (2.21), only the following six constants are different

$$\begin{aligned}
 C_{1111} &= a_1 + 2c_1 + 2(a_2 + 2c_2)H_{11} + (2a_3 + b_1 + 4c_3)H_{11}^2 + 2b_2H_{11}^3 + b_3H_{11}^4 \\
 C_{2222} &= C_{3333} = a_1 + 2c_1 + 2(a_2 + 2c_2)H_{22} + (2a_3 + b_1 + 4c_3)H_{22}^2 + 2b_2H_{22}^3 + b_3H_{22}^4 \\
 C_{1122} &= C_{1133} = a_1 + a_2(H_{11} + H_{22}) + a_3(H_{11}^2 + H_{22}^2) + b_1H_{11}H_{22} + b_2(H_{11}H_{22}^2 + H_{22}H_{11}^2) \\
 &\quad + b_3H_{11}^2H_{22}^2 \\
 C_{3322} &= a_1 + a_2(H_{33} + H_{22}) + a_3(H_{33}^2 + H_{22}^2) + b_1H_{33}H_{22} + b_2(H_{33}H_{22}^2 + H_{22}H_{33}^2) \\
 &\quad + b_3H_{33}^2H_{22}^2 \\
 C_{1212} &= C_{1313} = c_1 + c_2(H_{11} + H_{22}) + c_3(H_{11}^2 + H_{22}^2) \\
 C_{3232} &= c_1 + c_2(H_{33} + H_{22}) + c_3(H_{33}^2 + H_{22}^2)
 \end{aligned} \tag{2.22}$$

and only five of which are independent being $C_{2222} = C_{2233} + 2C_{2323}$. Thus, the represented material symmetry is the transversely isotropy. In the same way, if the eigenvalues of \mathbf{H} are all equal the represented material symmetry is the isotropy, being only the following three constant different

$$\begin{aligned}
 C_{1111} = C_{2222} = C_{3333} &= a_1 + 2c_1 + 2(a_2 + 2c_2)H_{11} + (2a_3 + b_1 + 4c_3)H_{11}^2 \\
 &\quad + 2b_2H_{11}^3 + b_3H_{11}^4 \\
 C_{1122} = C_{1133} = C_{2233} &= a_1 + a_2(H_{11} + H_{22}) + a_3(H_{11}^2 + H_{22}^2) + b_1H_{11}H_{22} \\
 &\quad + b_2(H_{11}H_{22}^2 + H_{22}H_{11}^2) + b_3H_{11}^2H_{22}^2 \\
 C_{1212} = C_{1313} = C_{3232} &= c_1 + c_2(H_{11} + H_{22}) + c_3(H_{11}^2 + H_{22}^2)
 \end{aligned} \tag{2.23}$$

and only two of which are independent, being $C_{1111} = C_{1122} + 2C_{1212}$.

The nine functions $a_1, a_2, a_3, b_1, b_2, b_3, c_1, c_2$ and c_3 depending upon $\gamma, Tr\mathbf{H}, Tr\mathbf{H}^2$ and $Tr\mathbf{H}^3$, can be determine by means of experimental tests.

CHAPTER III

THEORY OF HOMOGENIZATION & MICROMECHANICS

1. Thermodynamic framework and mathematically well-posed homogenization approaches

Homogenization is the modelling of a heterogeneous medium by means of a *unique* continuous medium. A heterogeneous medium is a medium of which material properties (e. g., elasticity coefficients) vary pointwise in a continuous or discontinuous manner, in a periodic or nonperiodic way, deterministically or randomly. While, obviously, homogenization is a modelling technique that applies to all fields of macroscopic physics governed by nice partial differential equations, we focus more particularly on the mechanics of deformable bodies.

1.1 Representative Volume Element (RVE)

Two different scales are used in the description of heterogeneous media. One of these is a **macroscopic** (x) scale at which homogeneities are weak. The other one is the scale of inhomogeneities and is referred to as the **microscopic** (y) scale. The latter defines the size of the representative volume element (Fig. 3.1). The basic cell of a periodic composite is an example of RVE.

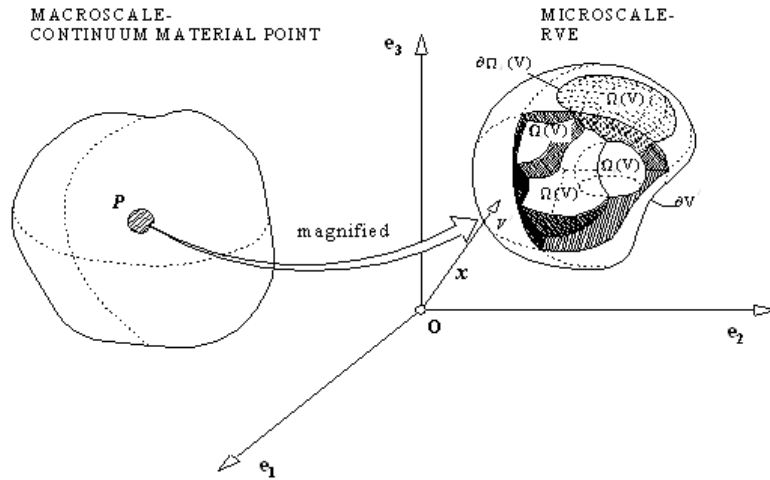


Fig. 3.1.

Representative Volume Element

From the experimental point of view, we can say that there exists a kind of statistical homogeneity in the sense that any RVE at a specific point looks very much like any other RVE taken at random at another point.

The mathematical problem presents itself in the following manner. Let $\boldsymbol{\sigma}(y)$ and $\boldsymbol{\varepsilon}(y)$ be the stress and strain at the micro scale in the framework of small-perturbation hypothesis. We denote by $\boldsymbol{\Sigma}$ and \mathbf{E} the same notion at the macro scale. Let $\langle \dots \rangle$ indicate the *averaging operator*. For a volume averaging we have

$$\begin{aligned}\boldsymbol{\Sigma}(\mathbf{x}) &= \langle \boldsymbol{\sigma} \rangle = \frac{1}{|V|} \int_V \boldsymbol{\sigma}(\mathbf{x}, y) dy \\ \mathbf{E}(\mathbf{x}) &= \langle \boldsymbol{\varepsilon} \rangle = \frac{1}{|V|} \int_V \boldsymbol{\varepsilon}(\mathbf{x}, y) dy\end{aligned}\tag{3.1}$$

where V is the volume of the RVE.

It is important to notice that any quantity that is an additive function is averaged in the micro-macro transition. Thus, if $\bar{\rho} = \langle \rho \rangle$ denotes the averaged density, then we have

$$\begin{aligned}\bar{\rho}E &= \langle \rho e \rangle, & \text{internal energy,} \\ \bar{\rho}S &= \langle \rho \eta \rangle, & \text{entropy,} \\ \Phi &= \langle \phi \rangle, & \text{dissipation.}\end{aligned}\tag{3.2}$$

1.2 Localization Problem

We can state the following

- the process that relates (Σ, \mathbf{E}) by means of equations (3.1) and (3.2) and the microscopic constitutive equations is called **homogenization**;
- the inverse process that consists in determining $\boldsymbol{\sigma}(y)$ and $\boldsymbol{\varepsilon}(y)$ from Σ and \mathbf{E} is called **localization**.

Therefore, the data are Σ and \mathbf{E} in the localization process which corresponds to the following problem:

$$(P \ L) \begin{cases} \langle \boldsymbol{\sigma} \rangle = \Sigma \\ \langle \boldsymbol{\varepsilon} \rangle = \mathbf{E} \\ \text{div } \boldsymbol{\sigma} = \mathbf{0} \end{cases}\tag{3.3}$$

This problem is original, because of the following two reasons:

- the load is the averaged value of a field and not a prescription at points in the bulk or at a limiting surface;
- there are *no* boundary conditions.

It follows from (ii) that the problem (3.3) is *ill-posed*. The missing boundary condition must, in some way, reproduce the internal state of the RVE in the most satisfactory manner. They therefore depend on the choice of RVE, more specifically on its size. As a rule, different choices of RVE will provide different macroscopic laws.

The following give some examples of boundary conditions:

$$\boldsymbol{\sigma} \cdot \mathbf{n} = \Sigma \cdot \mathbf{n} \quad \text{on } \partial V \quad - \quad \text{uniform traction on } \partial V ;\tag{3.4}$$

$$\mathbf{u} = \mathbf{E} \cdot \mathbf{y} \quad \text{on } \partial V \quad - \quad \text{uniform traction on } \partial V .\tag{3.5}$$

With this and $\text{div } \boldsymbol{\sigma} = \mathbf{0}$, in V , it is verified that (3.1) holds good. Indeed, for (3.5) we have

$$\frac{1}{2} \int_V \left(\frac{\partial u_i}{\partial y_j} + \frac{\partial u_j}{\partial y_i} \right) dv = \frac{1}{2} \int_{\partial V} (u_i n_j + u_j n_i) ds = \frac{1}{2} \int_{\partial V} (\mathbf{E}_{ik} y_k n_j + \mathbf{E}_{jk} y_k n_i) ds \quad (3.6)$$

or

$$\langle \boldsymbol{\varepsilon}(\mathbf{u}) \rangle = \mathbf{E} \quad (3.7)$$

The proof for (3.4) is self-evident.

The above reasoning does not apply to the case of a periodic structure. In that case, $\boldsymbol{\sigma}$ and $\boldsymbol{\varepsilon}$ are locally periodic (they are only quasi-periodic for a large sample) and the periodicity condition read as follows:

- the traction $\boldsymbol{\sigma} \cdot \mathbf{n}$ are opposite on opposite faces of ∂V (where \mathbf{n} corresponds to $-\mathbf{n}$);
- the local strain $\boldsymbol{\varepsilon}(\mathbf{u})$ is made of two part, the mean \mathbf{E} and the fluctucation part $\boldsymbol{\varepsilon}(\mathbf{u}^*)$ such that

$$\boldsymbol{\varepsilon}(\mathbf{u}) = \mathbf{E} + \boldsymbol{\varepsilon}(\mathbf{u}^*), \quad \langle \boldsymbol{\varepsilon}(\mathbf{u}^*) \rangle = 0, \quad (3.8)$$

where \mathbf{u}^* can be shown to be periodic. Therefore, the condition are

$$\begin{cases} \boldsymbol{\sigma} \cdot \mathbf{n} & \text{is antiperiodic,} \\ \mathbf{u} = \mathbf{E} \cdot \mathbf{y} + \mathbf{u}^*, \mathbf{u}^* & \text{periodic.} \end{cases} \quad (3.9)$$

On account of (3.4), (3.5) and (3.9), the problem (3.3) now is theoretically well-posed, but this must be verified for each constitutive behaviour.

1.3 The example of pure elasticity

In this section the localization problem in the case of *anisotropic linear elastic* components are examined.

1.3.a *The localization problem*

This problem is written in the following form (here $\mathcal{C}(y)$ is the tensor of elasticity coefficient at the micro scale):

$$\begin{cases} \boldsymbol{\sigma}(y) = \mathcal{C}(y) : \boldsymbol{\varepsilon}(y) = \mathcal{C}(y) : [\mathbf{E} + \boldsymbol{\varepsilon}(\mathbf{u}^*(y))] \\ \operatorname{div} \boldsymbol{\sigma} = \mathbf{0} \\ \text{boundary conditions} \end{cases} \quad (3.10)$$

where \mathbf{E} or $\boldsymbol{\Sigma}$ is prescribed. Accordingly, the fluctuation displacement \mathbf{u}^* is the solution of the following problem:

$$\begin{cases} \operatorname{div}(\mathcal{C} : \boldsymbol{\varepsilon}(\mathbf{u}^*)) = -\operatorname{div}(\mathcal{C} : \mathbf{E}) \\ \text{boundary conditions} \end{cases} \quad (3.11)$$

Whenever \mathbf{E} is constant for each constituent component, it can be shown that

$$\operatorname{div}(\mathcal{C} : \mathbf{E}) = ([[\mathcal{C}]] : \mathbf{E}) \mathbf{n} \delta(S), \quad (3.12)$$

where $[[\mathcal{C}]] = \mathcal{C}^+ - \mathcal{C}^-$, $\delta(S)$ is Dirac's distribution, and \mathbf{n} is the unit normal oriented from the '-' to the '+' side of the surface S separating components. Then we can state the following:

Proposition. Under classical working hypotheses applying to \mathcal{C} (symmetry and positivity), the problem (3.11) admits a unique solution for all three types of boundary condition.

To prove this we must distinguish whether it is \mathbf{E} or $\boldsymbol{\Sigma}$ which is prescribed.

1.3.b Case where \mathbf{E} is prescribed

For the existence and uniqueness proofs one can see Suquet (1981b). We shall only give the representation of the solution. As the problem is linear, the solution $\boldsymbol{\varepsilon}(\mathbf{u}^*)$ depends linearly on the prescribed field \mathbf{E} . The latter can be decomposed into six elementary states of macroscopic strains (stretch in three directions and three shears). Let $\boldsymbol{\varepsilon}(\chi_{kl})$ be the fluctuation strain field induced by these six elementary states at the microscopic level. The solution $\boldsymbol{\varepsilon}(\mathbf{u}^*)$ for a general macrostrain \mathbf{E} is the superposition of the six elementary solutions, so that we can write (summation over k and l)

$$\boldsymbol{\varepsilon}(\mathbf{u}^*) = E_{kl} \boldsymbol{\varepsilon}(\chi_{kl}). \quad (3.13)$$

In all we have

$$\boldsymbol{\varepsilon}(\mathbf{u}) = \mathbf{E} + \boldsymbol{\varepsilon}(\mathbf{u}^*) = \mathbf{E}(\mathbf{I} + \boldsymbol{\varepsilon}(\boldsymbol{\chi})) \quad (3.14)$$

or, in components,

$$\varepsilon_{ij}(\mathbf{u}) = D_{ijkl} E_{kl} = (\mathbf{D} : \mathbf{E})_{ij} \quad (3.15)$$

where

$$D_{ijkl} = I_{ijkl} + \varepsilon_{ij}(\chi_{kl}) \quad (3.16)$$

Here $I_{kl ij} = \frac{1}{2}(\delta_{ik} \delta_{jl} + \delta_{il} \delta_{jk})$ is the tensorial representation in \mathbb{R}^3 of the unity of \mathbb{R}^6 and D_{ijkl} is called, depending on the author, the **tensor of strain localization**, or **tensor of concentrations** (Mandel, 1971) or the **tensor of influence** (Hill, 1967).

Homogenization

We can write in an obvious manner

$$\boldsymbol{\Sigma} = \langle \boldsymbol{\sigma} \rangle = \langle \mathbf{C} : \boldsymbol{\varepsilon}(\mathbf{u}) \rangle = \langle \mathbf{C} : \mathbf{D} : \mathbf{E} \rangle = \langle \mathbf{C} : \mathbf{D} \rangle : \mathbf{E} \quad (3.17)$$

so that

$$\boldsymbol{\Sigma} = \mathbf{C}^{\text{hom}} : \mathbf{E}, \quad \mathbf{C}^{\text{hom}} = \langle \mathbf{C} : \mathbf{D} \rangle. \quad (3.18)$$

We note that

$$\langle \mathbf{D} \rangle = \mathbf{I}, \quad \langle \mathbf{D}^T \rangle = \mathbf{I}.$$

Equation (3.18)₂ shows that the tensor of ‘macro’ elasticity coefficients is obtained by taking the average of ‘micro’ elasticity coefficients, the latter being *weighted* by the tensor of strain localization. It is possible to prove that the tensor \mathbf{C}^{hom} is symmetric. For a direct proof we compute $\langle \mathbf{D}^T : \bar{\boldsymbol{\sigma}} \rangle$ for an admissible field $\bar{\boldsymbol{\sigma}}$, obtaining thus

$$\langle \mathbf{D}^T : \bar{\boldsymbol{\sigma}} \rangle_{ij} = \langle D_{ijkl}^T : \bar{\sigma}_{kl} \rangle = \langle [I_{ijkl} + \varepsilon_{kl}(\chi_{ij})] \bar{\sigma}_{kl} \rangle = \bar{\Sigma}_{ij}$$

i.e.,

$$\boldsymbol{\Sigma} = \langle \mathbf{D}^T : \boldsymbol{\sigma} \rangle = \langle \mathbf{D}^T : \mathbf{C} : \boldsymbol{\varepsilon}(\mathbf{u}) \rangle = \langle \mathbf{D}^T : \mathbf{C} : \mathbf{D} \rangle : \mathbf{E},$$

so that

$$\mathbf{C}^{\text{hom}} = \langle \mathbf{D}^T : \mathbf{C} : \mathbf{D} \rangle, \quad (3.19)$$

which is symmetric.

1.3.c Case where Σ is prescribed

The localization problem than reads

$$\begin{cases} \boldsymbol{\varepsilon}(\mathbf{u}) = \boldsymbol{\varepsilon}(\mathbf{u}^*) + \mathbf{E} = \mathcal{S} : \boldsymbol{\sigma} \\ \operatorname{div} \boldsymbol{\sigma} = \mathbf{0} \\ \langle \boldsymbol{\sigma} \rangle = \boldsymbol{\Sigma} \\ \text{boundary conditions} \end{cases} \quad (3.20)$$

where \mathcal{S} is the tensor of the ‘micro’ elastic compliance and \mathbf{E} is an unknown. The existence and uniqueness of the solution may be proved (Suquet, 1981b). Thus, here, we assume that a unique solution $\boldsymbol{\sigma}$ exists. This solution depends linearly on data by virtue of the linearity of the problem. Let us call S_{kl} the solution of the problem (3.20) for the datum $\boldsymbol{\Sigma} = \mathbf{I}_{kl}$ - note that $I_{ijkl} = (\mathbf{I}_{kl})_{ij}$.

Then the general solution, obtained by superposition, is written

$$\begin{aligned} \boldsymbol{\sigma} &= \mathbf{A} : \boldsymbol{\Sigma}, \quad \text{i.e.,} \quad \boldsymbol{\sigma}(y) = \Sigma_{kl} A_{kl}(y), \\ \text{or} \quad \sigma_{ij} &= A_{ijkl} \Sigma_{kl}, \quad A_{ijkl} = (\mathbf{A}_{kl})_{ij}, \end{aligned} \quad (3.21)$$

where \mathbf{A} is the tensor of stress localization.

The homogenized compliance tensor \mathcal{S}^{hom} is evaluated thus. We have directly

$$\mathbf{E} = \langle \boldsymbol{\varepsilon}(\mathbf{u}) \rangle = \langle \mathcal{S} : \boldsymbol{\sigma} \rangle = \langle \mathcal{S} : \mathbf{A} \rangle : \boldsymbol{\Sigma} = \mathcal{S}^{\text{hom}} : \boldsymbol{\Sigma}, \quad (3.22)$$

whence

$$\mathcal{S}^{\text{hom}} = \langle \mathcal{S} : \mathbf{A} \rangle. \quad (3.23)$$

We note that

$$\langle \mathbf{A}^T \rangle = \mathbf{I}, \quad (3.24)$$

and for any admissible field $\langle \boldsymbol{\varepsilon}(\bar{\mathbf{u}}) \rangle$ we can write

$$\langle \mathbf{A}^T : \boldsymbol{\varepsilon}(\bar{\mathbf{u}}) \rangle_{ij} = \langle A_{ijkl}^T \varepsilon_{kl}(\bar{\mathbf{u}}) \rangle = \langle (A_{ij})_{kl} \varepsilon_{kl}(\bar{\mathbf{u}}) \rangle = \langle (A_{ij})_{kl} \rangle \langle \varepsilon_{kl}(\bar{\mathbf{u}}) \rangle = \bar{\mathbf{E}}_{ij}$$

so that

$$\mathbf{E} = \langle \mathbf{A}^T : \boldsymbol{\varepsilon}(\mathbf{u}) \rangle = \langle \mathbf{A}^T : \mathcal{S} : \boldsymbol{\sigma} \rangle = \langle \mathbf{A}^T : \mathcal{S} : \mathbf{A} \rangle : \boldsymbol{\Sigma},$$

whence

$$\mathcal{S}^{\text{hom}} = \langle \mathbf{A}^T : \mathcal{S} : \mathbf{A} \rangle \quad (3.25)$$

and thus \mathcal{S}^{hom} is symmetric.

1.3.d Equivalence between ‘prescribed stress’ and ‘prescribed strain’

First we note that \mathcal{C}^{hom} and \mathcal{S}^{hom} are *inverse* tensors (in \mathbb{R}^6) of one another if they correspond to the *same* choice of boundary conditions in the localization problem. Indeed, using the symmetry of \mathcal{C}^{hom} we can write

$$\mathcal{C}^{\text{hom}} : \mathcal{S}^{\text{hom}} = (\mathcal{C}^{\text{hom}})^T : \mathcal{S}^{\text{hom}} = \langle \mathbf{D}^T : \mathcal{C} \rangle : \langle \mathcal{S} : \mathbf{A} \rangle \quad (3.26)$$

in which the first factor is an admissible stress field (from the definition of \mathbf{D} and \mathbf{A}) and the second factor is an admissible strain field.

Applying the *principle of macrohomogeneity of Hill and Mandel* (Hill, 1965a, Mandel 1971) about which, let $\bar{\boldsymbol{\sigma}}$ and $\bar{\mathbf{u}}$ be, respectively, a statistically admissible (SA) stress field and a kinematically admissible (KA) displacement field, it is possible to prove that

$$\langle \bar{\boldsymbol{\sigma}} : \boldsymbol{\varepsilon}(\bar{\mathbf{u}}) \rangle = \bar{\boldsymbol{\Sigma}} : \bar{\mathbf{E}}. \quad (3.27)$$

therefore applies we can write ($\mathcal{C} : \mathcal{S} = \mathbf{I}$)

$$\mathcal{C}^{\text{hom}} : \mathcal{S}^{\text{hom}} = \langle \mathbf{D}^T : \mathcal{C} : \mathcal{S} : \mathbf{A} \rangle = \langle \mathbf{D}^T : \mathbf{A} \rangle = \langle \mathbf{D}^T \rangle : \langle \mathbf{A} \rangle = \mathbf{I} \quad (3.28)$$

However, if *different* boundary conditions are used, one then has the estimate of Hill (1967) and Mandel (1971),

$$\mathcal{C}^{\text{hom}} : \mathcal{S}^{\text{hom}} = \mathbb{I} + O\left(\left(\frac{d}{l}\right)^3\right), \quad (3.29)$$

where \mathcal{C}^{hom} is evaluated by using the condition (3.5), while \mathcal{S}^{hom} is computed through use of the condition (3.4), d is a characteristic size of an inhomogeneity and l is the typical size of the RVE. If $l \gg d$, then the choice of boundary condition is hardly important. For *periodic* media where $d/l = O(1)$, this choice is most important.

2. Micromechanics of porous materials: j-tensor and dilute distribution of voids cases

In this section, the overall stress-strain/strain stress relations are developed with reference to an RVE consisting of a linearly elastic material which contains stress-free cavities.

Consider an RVE with total volume V , bounded *externally* by surface ∂V . On this surface, either uniform tractions,

$$\boldsymbol{t}^0 = \boldsymbol{n} \cdot \boldsymbol{\sigma}^0 \quad \text{on } \partial V, \quad (3.30)$$

or linear displacements,

$$\boldsymbol{u}^0 = \boldsymbol{x} \cdot \boldsymbol{\varepsilon}^0 \quad \text{on } \partial V, \quad (3.31)$$

are assumed to be prescribed, where $\boldsymbol{\sigma}^0$ and $\boldsymbol{\varepsilon}^0$ are second-order symmetric *constant* stress and strain tensors for the macro-element. It is emphasized that either (3.30) or

(3.31) (4.1.1 a), but not both, can be prescribed. In other words, if the traction boundary data (3.30) corresponding to the constant macrostress $\Sigma = \sigma^0$, are prescribed, then the surface displacements on ∂V , corresponding to these tractions, in general, are *not* spatially linear, being affected by the microstructure of the RVE. Similarly, if the linear displacement boundary data (3.31) corresponding to the constant macrostrain $E = \epsilon^0$, are prescribed, then the surface tractions on ∂V , produced by these displacements, are *not*, in general, spatially uniform. In the sequel, therefore, the two cases are treated separately and independently, and then the relation between the results is discussed.

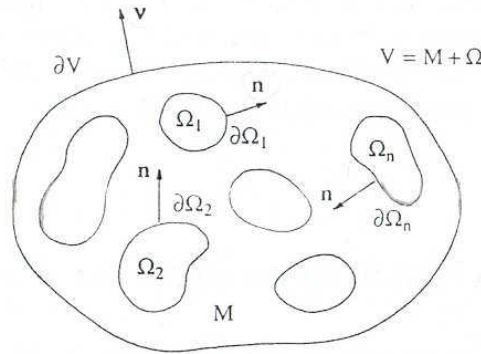


Fig. 3.2.

Matrix M and microcavities Ω_α

Assume that the material of the RVE is linearly elastic and *homogeneous* (but not necessarily isotropic). The inhomogeneity, therefore, stems solely from the presence of cavities. Denote a typical cavity by Ω_α , with the boundary $\partial\Omega_\alpha$ ($\alpha=1,2,\dots,n$), so that there are a total of n individual cavities in V . The union of these cavities is denoted by Ω , having the boundary $\partial\Omega$ which is the union of all $\partial\Omega_\alpha$, i.e.,

$$\Omega \equiv \bigcup_{\alpha=1}^n \Omega_\alpha \quad \partial\Omega \equiv \bigcup_{\alpha=1}^n \partial\Omega_\alpha \quad (3.32)$$

The remainder of the RVE (i.e, when Ω is excluded) is called the *matrix*. The matrix is denoted by M . The boundary of M is the sum of ∂V and $\partial\Omega$, Figure 3.2.,

$$M \equiv V - \Omega \quad \partial M \equiv \partial V - \partial \Omega. \quad (3.33)$$

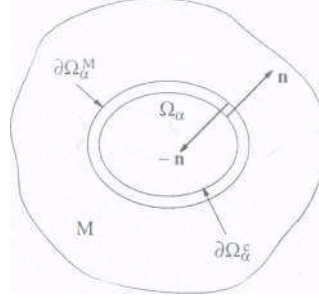


Fig. 3.3.

$\partial \Omega_\alpha^M$ and $\partial \Omega_\alpha^c$

The total boundary surface of the RVE can include some portion of $\partial \Omega$. For simplicity, however, exclude this possibility. Thus, all cavities are within the RVE, each being fully surrounded by the matrix material. For a typical cavity, Ω_α , two faces of its surface boundary, $\partial \Omega_\alpha$, may be distinguished, as follows:

- the *exterior* face of the cavity, denoted by $\partial \Omega_\alpha^c$ which is the face toward the matrix material, denoted by the direction of the exterior unit normal \mathbf{n} of the cavity;
- the *exterior* face of the *surrounding matrix*, denoted by $\partial \Omega_\alpha^M$, which is the face toward the interior of the cavity, denoted by the direction of the exterior unit normal $(-\mathbf{n})$ of the matrix (i.e., the interior unit normal of the cavity). $\partial \Omega_\alpha$ coincides with $\partial \Omega_\alpha^c$, for the cavity Ω_α , while ∂M at the cavity Ω_α coincides with $\partial \Omega_\alpha^M$ (Fig. 3.3). In view of this convention, the integral of a surface quantity taken over ∂M can always be decomposed as

•

$$\begin{aligned} \int_{\partial M} (\cdot) dS &= \int_{\partial V} (\cdot) dS + \sum_{\alpha=1}^n \int_{\partial \Omega_\alpha^M} (\cdot) dS = \\ &= \int_{\partial V} (\cdot) dS - \sum_{\alpha=1}^n \int_{\partial \Omega_\alpha^c} (\cdot) dS = \int_{\partial V} (\cdot) dS - \int_{\partial \Omega} (\cdot) dS. \end{aligned} \quad (3.34)$$

Thus $\partial\Omega$ always stands for the union of $\partial\Omega_\alpha^c$ ($\alpha=1,2,\dots,n$).

To distinguish the boundary of M at the cavities from that at the exterior of the RVE, which is ∂V , the exterior unit normal on ∂V is systematically denoted by \mathbf{n} (as before), and the *exterior* unit normal on the surface $\partial\Omega_\alpha$ for a typical cavity Ω_α , by \mathbf{n} , *pointing from the inside of the cavity toward the matrix* M .

The matrix material is linearly elastic and homogeneous. Denote the corresponding constant elasticity tensor by \mathcal{C} and the compliance tensor by \mathcal{S} .

2.1 Average strain for prescribed macro-stress

Suppose that uniform tractions $\mathbf{t}^0 = \mathbf{n} \cdot \boldsymbol{\sigma}^0$ are prescribed on ∂V , associated with the constant symmetric macrostress $\boldsymbol{\Sigma} = \boldsymbol{\sigma}^0$. If the RVE is homogeneous, having *no* cavities, then the corresponding average strain associated with the average stress $\boldsymbol{\sigma}^0$ would be

$$\boldsymbol{\varepsilon}^0 = \mathcal{S} : \boldsymbol{\sigma}^0, \quad (3.35)$$

and hence, in conjunction with $\bar{\boldsymbol{\sigma}} = \boldsymbol{\sigma}^0$, the average strain would be $\boldsymbol{\varepsilon}^0$. The presence of cavities disturbs the uniform stress and strain fields, producing the variable stress field $\boldsymbol{\sigma} = \boldsymbol{\sigma}(\mathbf{x})$ and strain field $\boldsymbol{\varepsilon} = \boldsymbol{\varepsilon}(\mathbf{x})$, in M , with $\boldsymbol{\sigma} = \mathbf{0}$ in Ω . Nevertheless, from the (3.1)

$$\bar{\boldsymbol{\sigma}} = \langle \boldsymbol{\sigma} \rangle = \frac{1}{V} \int_V \boldsymbol{\sigma} \, dv = \frac{1}{V} \int_M \boldsymbol{\sigma} \, dv = \boldsymbol{\sigma}^0. \quad (3.36)$$

On the other hand, the average strain is *not*, in general, equal to $\boldsymbol{\varepsilon}^0$. Instead,

$$\bar{\boldsymbol{\varepsilon}} = \langle \boldsymbol{\varepsilon} \rangle = \boldsymbol{\varepsilon}^0 + \bar{\boldsymbol{\varepsilon}}^c, \quad (3.37)$$

where $\boldsymbol{\varepsilon}^0$ is *defined* by (3.35), and $\bar{\boldsymbol{\varepsilon}}^c$ is the additional strain due to the presence of cavities.

To calculate the additional strain $\bar{\boldsymbol{\varepsilon}}^c$ due to cavities, one may apply the reciprocal theorem, as follows. Consider two sets of loads, one defined by

$$\boldsymbol{t}^{(1)} = \begin{cases} \boldsymbol{n} \cdot \delta \boldsymbol{\sigma}^0 & \text{on } \partial V \\ -\boldsymbol{n} \cdot \delta \boldsymbol{\sigma}^0 & \text{on } \partial \Omega \end{cases} \quad (3.38)$$

which corresponds to uniform *virtual* stress $\delta \boldsymbol{\sigma}^0$ and strain $\delta \boldsymbol{\varepsilon}^0 = \mathcal{S} : \delta \boldsymbol{\sigma}^0$ within the entire RVE (as illustrated in Figure 3.3, $-\boldsymbol{n}$ is the *interior* unit normal on the *cavity* surface $\partial \Omega$, or the *exterior* unit normal to the boundary of the *matrix*), and the other defined by

$$\boldsymbol{t}^{(2)} = \begin{cases} \boldsymbol{n} \cdot \boldsymbol{\sigma}^0 & \text{on } \partial V \\ \mathbf{0} & \text{on } \partial \Omega \end{cases} \quad (3.39)$$

which is the actual loading considered for the RVE.

Denote the displacement, strain, and stress fields associated with the first loading (3.38) by

$$\{\boldsymbol{u}^{(1)}, \boldsymbol{\varepsilon}^{(1)}, \boldsymbol{\sigma}^{(1)}\} = \{(\boldsymbol{x} \cdot \delta \boldsymbol{\varepsilon}^0), \delta \boldsymbol{\varepsilon}^0, \delta \boldsymbol{\sigma}^0\} \quad (3.40)$$

which follows from the fact that, for loading (3.38), the strain and stress fields are both uniform throughout the matrix M. And denote the fields associated with the second (i.e., the actual) loading (3.39) by

$$\{\boldsymbol{u}^{(2)}, \boldsymbol{\varepsilon}^{(2)}, \boldsymbol{\sigma}^{(2)}\} = \{\boldsymbol{u}, \boldsymbol{\varepsilon}, \boldsymbol{\sigma}\}. \quad (3.41)$$

From the reciprocal theorem, it follows that

$$\int_{\partial V} (\boldsymbol{n} \cdot \boldsymbol{\sigma}^0) \cdot (\boldsymbol{x} \cdot \delta \boldsymbol{\varepsilon}^0) ds = \int_{\partial V} (\boldsymbol{n} \cdot \delta \boldsymbol{\sigma}^0) \cdot \boldsymbol{u} ds - \int_{\partial \Omega} (\boldsymbol{n} \cdot \delta \boldsymbol{\sigma}^0) \cdot \boldsymbol{u} ds \quad (3.42)$$

which can be written as

$$\delta\boldsymbol{\sigma}^0 : \left\{ \int_{\partial V} \mathcal{S} : \{(\mathbf{x} \otimes \mathbf{n}) \cdot \boldsymbol{\sigma}^0\} ds - \int_{\partial V} \mathbf{n} \otimes \mathbf{u} ds + \int_{\partial\Omega} \mathbf{n} \otimes \mathbf{u} ds \right\} = 0. \quad (3.43)$$

Since $\delta\boldsymbol{\sigma}^0$ is an arbitrary symmetric tensor, the symmetric part of the quantity within the braces must vanish identically. Noting that the first integral within the braces yields

$$\frac{1}{V} \int_{\partial V} \mathcal{S} : \{(\mathbf{x} \otimes \mathbf{n}) \cdot \boldsymbol{\sigma}^0\} ds = \mathcal{S} : \{\mathbf{I} \cdot \boldsymbol{\sigma}^0\} = \boldsymbol{\epsilon}^0, \quad (3.44)$$

and using the averaging scheme, it follows that

$$\bar{\boldsymbol{\epsilon}} = \frac{1}{V} \int_V \frac{1}{2} \{ \nabla \otimes \mathbf{u} + (\nabla \otimes \mathbf{u})^T \} dv = \boldsymbol{\epsilon}^0 + \frac{1}{V} \int_{\partial\Omega} \frac{1}{2} (\mathbf{n} \otimes \mathbf{u} + \mathbf{u} \otimes \mathbf{n}) ds. \quad (3.45)$$

Comparison with (3.37) shows that the additional strain $\bar{\boldsymbol{\epsilon}}^c$ due to cavities, is given by

$$\bar{\boldsymbol{\epsilon}}^c = \frac{1}{V} \int_{\partial\Omega} \frac{1}{2} (\mathbf{n} \otimes \mathbf{u} + \mathbf{u} \otimes \mathbf{n}) ds. \quad (3.46)$$

2.2 Overall compliance tensor for porous elastic solids

Define *the overall compliance* $\bar{\mathcal{S}}$ of the porous RVE with a linearly elastic homogeneous matrix, through

$$\bar{\boldsymbol{\epsilon}} = \bar{\mathcal{S}} : \bar{\boldsymbol{\sigma}} = \bar{\mathcal{S}} : \boldsymbol{\sigma}^0, \quad (3.47)$$

where the macrostress, $\boldsymbol{\Sigma} = \boldsymbol{\sigma}^0$, is regarded prescribed, and the average strain is given by (3.37). To obtain the overall compliance in an explicit form, the strain $\bar{\boldsymbol{\epsilon}}^c$ due to

cavities will now be expressed in terms of the applied stress $\boldsymbol{\sigma}^0$. Since the matrix of the RVE is linearly elastic, for a given microstructure the displacement $\mathbf{u}(\mathbf{x})$ at a point \mathbf{x} on $\partial\Omega$ is linearly dependent on the uniform overall stress $\boldsymbol{\sigma}^0$, as show following. By remembering that the displacement field may be expressed in terms of Green function as

$$\mathbf{u}(\mathbf{x}) = \int_{\partial V} \mathbf{G}(\mathbf{x}, \mathbf{y}) \cdot \mathbf{t}(\mathbf{y}) ds \quad (3.48)$$

where $\mathbf{t}(\mathbf{y})$ are the self-equilibrating surface traction prescribed on the boundary ∂V of the RVE, if the applied tractions (3.30) are substituting into (3.48), to arrive at

$$\mathbf{u}(\mathbf{x}) = \int_{\partial V} \mathbf{G}(\mathbf{x}, \mathbf{y}) \cdot \{\mathbf{n}(\mathbf{y}) \cdot \boldsymbol{\sigma}^0\} ds, \quad (3.49)$$

where the integration is taken with respect to \mathbf{y} over the boundary ∂V of the RVE. Since $\boldsymbol{\sigma}^0$ is a symmetric constant tensor, (3.49) can be expressed as

$$u_i(\mathbf{x}) = K_{ijk}(\mathbf{x}) \sigma_{jk}^0 \quad (3.50)$$

where the third-order tensor,

$$K_{ijk}(\mathbf{x}) = K_{jik}(\mathbf{x}) = \int_{\partial V} \frac{1}{2} \{G_{ij}(\mathbf{x}, \mathbf{y}) n_k(\mathbf{y}) + G_{ik}(\mathbf{x}, \mathbf{y}) n_j(\mathbf{y})\} dS, \quad (3.51)$$

depends on the geometry and the elastic properties of the matrix of the RVE.

To obtain the additional overall strain, $\bar{\boldsymbol{\epsilon}}^c$, due to the presence of cavities in terms of the prescribed overall stress, $\boldsymbol{\sigma}^0$, substitute from (3.51) into (3.46), to arrive at

$$\bar{\boldsymbol{\epsilon}}_{ij}^c = H_{ijkl} \sigma_{kl}^0, \quad (3.52)$$

where the *constant* fourth-order tensor, \mathbb{H} , is given by

$$H_{ijkl} \equiv H_{jikl} \equiv H_{ijlk} \equiv \frac{1}{V} \int_{\partial\Omega} \frac{1}{2} \{n_i(\mathbf{x})K_{jkl}(\mathbf{x}) + n_j(\mathbf{x})K_{ikl}(\mathbf{x})\} dS. \quad (3.53)$$

Hence, for an RVE with a linearly elastic matrix containing cavities *of arbitrary shapes and sizes*, the following general result is obtained, when the overall macrostress is regarded prescribed (Horii and Nemat-Nasser, 1983):

$$\bar{\boldsymbol{\epsilon}}^c = \mathbb{H} : \boldsymbol{\sigma}^0. \quad (3.54)$$

It should be noted that this exact result is valid whether or not the linearly elastic constituent of the RVE is homogeneous. The requirements are:

- the matrix of the RVE is linearly elastic;
- the microstructure of the RVE remains unchanged under the applied macrostress $\boldsymbol{\Sigma} = \boldsymbol{\sigma}^0$.

To obtain the overall elastic compliance tensor $\bar{\mathcal{S}}$, in terms of the constant compliance of the matrix, \mathcal{S} , and the *constant* tensor \mathbb{H} , substitute (3.35), (3.47) and (3.54) into (3.37), and noting that the resulting equation must hold for any macrostress $\boldsymbol{\sigma}^0$, arrive at

$$\bar{\mathcal{S}} = \mathcal{S} + \mathbb{H}, \quad (3.55)$$

Note that in many situation, the tensor \mathbb{H} can be computer directly, using the (3.46).

2.3 Average stress for prescribed macro-strain

Suppose that the linear displacements $\mathbf{u}^0 = \mathbf{x} \cdot \boldsymbol{\epsilon}^0$ (associated with the constant symmetric macrostrain $\mathbf{E} = \boldsymbol{\epsilon}^0$) are prescribed on ∂V . The matrix of the RVE is assumed to be homogeneous, as marked before. *In the absence of cavities*, the

corresponding average stress associated with the prescribed macrostrain, $\boldsymbol{\varepsilon}^0$, would be

$$\boldsymbol{\sigma}^0 = \mathbb{C} : \boldsymbol{\varepsilon}^0 . \quad (3.56)$$

Due to the presence of cavities, the actual field quantities are nonuniform. From the (3.6),

$$\boldsymbol{\varepsilon} = \langle \boldsymbol{\varepsilon} \rangle = \frac{1}{V} \int_V \boldsymbol{\varepsilon} dv = \frac{1}{V} \int_{\partial V} \frac{1}{2} (\mathbf{n} \otimes \mathbf{u} + \mathbf{u} \otimes \mathbf{n}) ds = \boldsymbol{\varepsilon}^0 \quad (3.57)$$

which is valid for any RVE of any material and microstructure. Note that the surface integral in (3.57) extends over the exterior boundary, ∂V , of the RVE only. It does *not* include the cavity boundaries $\partial\Omega$. Equation (3.57) is the direct consequence of the fact that the average strain for an RVE is given in terms of its boundary displacements which are prescribed here to be $\mathbf{u}^0 = \mathbf{x} \cdot \boldsymbol{\varepsilon}^0$.

In general, for a prescribed macrostrain, the average stress is not equal to $\boldsymbol{\sigma}^0$ but

$$\bar{\boldsymbol{\sigma}} = \langle \boldsymbol{\sigma} \rangle = \boldsymbol{\sigma}^0 + \bar{\boldsymbol{\sigma}}^c , \quad (3.58)$$

where $\boldsymbol{\sigma}^0$ is *defined* by (3.56), and $\bar{\boldsymbol{\sigma}}^c$ is the decrement in the overall stress due to the presence of cavities.

As in Subsection 3.1., the reciprocal theorem will be applied to calculate the average stress $\bar{\boldsymbol{\sigma}}$ in (3.58). To this end, a third set of boundary data defined by

$$\begin{aligned} \mathbf{u}^{(3)} &= \mathbf{n} \cdot \boldsymbol{\sigma}^0 && \text{on } \partial V \\ \mathbf{t}^{(3)} &= \mathbf{0} && \text{on } \partial\Omega. \end{aligned} \quad (3.59)$$

The displacement, strain, and stress fields associated with these boundary conditions are denoted by

$$\{\mathbf{u}^{(3)}, \boldsymbol{\varepsilon}^{(3)}, \boldsymbol{\sigma}^{(3)}\} = \{\mathbf{u}, \boldsymbol{\varepsilon}, \boldsymbol{\sigma}\} \quad (3.60)$$

which are actual fields, in general, different from those given by (3.41) for the boundary conditions (3.39). The actual tractions on the boundary of the RVE now are

$$\mathbf{t}(\mathbf{x}) = \mathbf{n}(\mathbf{x}) \cdot \boldsymbol{\sigma}(\mathbf{x}), \quad (3.61)$$

where \mathbf{x} is on ∂V . These tractions are required in order to impose the boundary displacements prescribed by (3.59).

Applying the reciprocal theorem to the two sets of loads, (3.38) and (3.59), it follows that

$$\int_{\partial V} \mathbf{t} \cdot (\mathbf{x} \cdot \delta \boldsymbol{\varepsilon}^0) ds = \int_{\partial V} (\mathbf{n} \cdot \delta \boldsymbol{\sigma}^0) \cdot (\mathbf{x} \cdot \delta \boldsymbol{\varepsilon}^0) ds - \int_{\partial \Omega} (\mathbf{n} \cdot \delta \boldsymbol{\sigma}^0) \cdot \mathbf{u} ds \quad (3.62)$$

which can be written as

$$\delta \boldsymbol{\varepsilon}^0 : \left\{ \int_{\partial V} \mathbf{t} \otimes \mathbf{x} ds - \int_{\partial V} \mathbb{C} : \{(\mathbf{x} \otimes \mathbf{n}) \cdot \boldsymbol{\varepsilon}^0\} ds + \int_{\partial \Omega} \mathbb{C} : (\mathbf{n} \otimes \mathbf{u}) ds \right\} = 0 \quad (3.63)$$

where, in using loading (3.40), the quantity $\delta \boldsymbol{\varepsilon}^0$ is regarded as a virtual spatially constant strain field with the corresponding stress field, $\delta \boldsymbol{\sigma}^0 = \mathbb{C} : \delta \boldsymbol{\varepsilon}^0$. Since $\delta \boldsymbol{\varepsilon}^0$ is an arbitrary symmetric tensor, the symmetric part of the quantity within the braces in (3.63) must vanish identically. Noting that the second integral within the parentheses can be expressed as

$$\frac{1}{V} \int_{\partial V} \mathbb{C} : \{(\mathbf{x} \otimes \mathbf{n}) \cdot \boldsymbol{\varepsilon}^0\} ds = \mathbb{C} : \{\mathbf{I} \cdot \boldsymbol{\varepsilon}^0\} = \boldsymbol{\sigma}^0, \quad (3.64)$$

and using the averaging procedure, it now follows that

$$\bar{\boldsymbol{\sigma}} = \frac{1}{V} \int_{\partial v} \mathbf{t} \otimes \mathbf{x} \, ds = \boldsymbol{\sigma}^0 - \mathcal{C} : \left\{ \frac{1}{V} \int_{\partial \Omega} \frac{1}{2} (\mathbf{n} \otimes \mathbf{u} + \mathbf{u} \otimes \mathbf{n}) \, ds \right\} \quad (3.65)$$

Comparison with (3.58) shows that the decremental stress $\bar{\boldsymbol{\sigma}}^c$ due to the presence of cavities, is given by

$$\bar{\boldsymbol{\sigma}}^c = -\mathcal{C} : \bar{\boldsymbol{\varepsilon}}^c \quad (3.66)$$

where $\bar{\boldsymbol{\varepsilon}}^c$ is the strain due to the presence of cavities given by (3.46), which now must be computed for the prescribed boundary displacements $\mathbf{u}^0 = \mathbf{x} \cdot \boldsymbol{\varepsilon}^0$.

2.4 Overall elasticity tensor for porous elastic solids

When the overall macrostrain is regarded prescribed, $\mathbf{E} = \boldsymbol{\varepsilon}^0$, designate the overall elasticity tensor of the porous RVE with a linearly elastic and homogeneous matrix, by $\bar{\mathcal{C}}$, and define it through

$$\bar{\boldsymbol{\sigma}} = \bar{\mathcal{C}} : \boldsymbol{\varepsilon}^0. \quad (3.67)$$

Substitution of (3.56), (3.66), and (3.67) into (3.58) then yields

$$(\bar{\mathcal{C}} - \mathcal{C}) : \boldsymbol{\varepsilon}^0 + \mathcal{C} : \bar{\boldsymbol{\varepsilon}}^c = \mathbf{0}. \quad (3.68)$$

For a given microstructure (i.e., for existing cavities with fixed shapes, sizes, and distribution), the response of the RVE is linear. Hence, the displacement field anywhere within the linearly elastic matrix of the RVE is a linear and homogeneous function of the prescribed overall constant strain $\boldsymbol{\varepsilon}^0$. Therefore, in line with results (3.50) and (3.51) for the case when the macrostresses were considered to be prescribed, at a typical point \mathbf{x} on the boundary of the cavities, $\partial \Omega$,

$$u_i(\mathbf{x}) = L_{ijk}(\mathbf{x}) \varepsilon_{jk}^0 \quad (3.69)$$

where $L(\mathbf{x})$ is a third-order tensor-valued function with the symmetry property, $L_{ijk} = L_{ikj}$. Now, from the definition of $\bar{\boldsymbol{\epsilon}}^c$, given by the (3.46),

$$\bar{\boldsymbol{\epsilon}}_{ij}^c = J_{ijkl} \boldsymbol{\epsilon}_{kl}^0, \quad (3.70)$$

where the *constant* fourth-order tensor, \mathcal{J} , is given by

$$J_{ijkl} \equiv J_{jikl} \equiv J_{ijlk} \equiv \frac{1}{V} \int_{\partial\Omega} \frac{1}{2} \{n_i(\mathbf{x}) J_{jkl}(\mathbf{x}) + n_j(\mathbf{x}) J_{ikl}(\mathbf{x})\} dS. \quad (3.71)$$

Hence, for an RVE with a linearly elastic matrix (whether homogeneous or not) containing cavities of arbitrary shapes and sizes, the following general result is obtained, when the overall macrostrains are regarded prescribed:

$$\bar{\boldsymbol{\epsilon}}^c = \mathcal{J} : \boldsymbol{\epsilon}^0. \quad (3.72)$$

To obtain an expression for the overall elastic moduli of the porous RVE, substitute (3.72) into (3.68) and, noting that the resulting expression must be valid for any constant symmetric macrostrain $\boldsymbol{\epsilon}^0$, arrive at

$$\bar{\mathbf{C}} = \mathbf{C} - \mathbf{C} : \mathcal{J}. \quad (3.73)$$

It should be noted that in many practical problems the tensor \mathcal{J} , similarly to the tensor \mathcal{H} , can be calculated *directly* from (3.46), and therefore, the overall elastic moduli can be estimated from (3.73).

It may, however, be instructive to seek to construct the tensor \mathcal{J} in terms of the Green functions $\mathbf{G}(\mathbf{x}, \mathbf{y})$ and $\mathbf{G}^{-1}(\mathbf{x}, \mathbf{y})$.

To this end, for the linear displacements, $\mathbf{u}^0 = \mathbf{z} \cdot \boldsymbol{\epsilon}^0$, *prescribed* on the outer boundary ∂V of the RVE, by remembering that the *resulting* tractions, $\mathbf{t}(\mathbf{y})$, may be written as

$$\mathbf{t}(\mathbf{y}) = \int_{\partial V} \mathbf{G}^{-1}(\mathbf{y}, \mathbf{z}) \cdot (\mathbf{z} \cdot \boldsymbol{\varepsilon}^0) ds, \quad (3.74)$$

where the integration is taken with respect to \mathbf{z} over the outer boundary ∂V (excluding the traction-free cavity boundaries) of the RVE. Substituting (3.74) into (3.48), the displacement field for points on $\partial\Omega$ is obtained in terms of the prescribed macrostrain $\boldsymbol{\varepsilon}^0$, as

$$\mathbf{u}(\mathbf{x}) = \int_{\partial V} \mathbf{G}(\mathbf{x}, \mathbf{y}) \cdot \left\{ \int_{\partial V} \mathbf{G}^{-1}(\mathbf{y}, \mathbf{z}) \cdot (\mathbf{z} \cdot \boldsymbol{\varepsilon}^0) ds \right\} ds \quad (3.75)$$

where both the \mathbf{y} - and \mathbf{z} -integral are taken over ∂V . Noting that $\boldsymbol{\varepsilon}^0$ is a symmetric tensor, tensor \mathbf{L} in (3.69) may now be written in terms of \mathbf{G} and \mathbf{G}^{-1} , as

$$L_{ijk}(\mathbf{x}) = \int_{\partial V} G_{im}(\mathbf{x}, \mathbf{y}) \left\{ \int_{\partial V} \frac{1}{2} \left\{ G_{mj}^{-1}(\mathbf{y}, \mathbf{z}) z_k + G_{mk}^{-1}(\mathbf{y}, \mathbf{z}) z_j \right\} ds \right\} ds. \quad (3.76)$$

Therefore, from comparison of (3.72) with (3.76), a fourth-order tensor, $\mathcal{J}(\mathbf{x}, \mathbf{y})$, can be introduced as

$$j_{ijkl} = \int_{\partial V} \frac{1}{4} \left\{ n_i(\mathbf{x}) G_{jm}(\mathbf{x}, \mathbf{y}) G_{mk}^{-1}(\mathbf{y}, \mathbf{z}) z_l + n_i(\mathbf{x}) G_{jm}(\mathbf{x}, \mathbf{y}) G_{ml}^{-1}(\mathbf{y}, \mathbf{z}) z_k + \right. \\ \left. n_j(\mathbf{x}) G_{im}(\mathbf{x}, \mathbf{y}) G_{mk}^{-1}(\mathbf{y}, \mathbf{z}) z_l + n_j(\mathbf{x}) G_{im}(\mathbf{x}, \mathbf{y}) G_{ml}^{-1}(\mathbf{y}, \mathbf{z}) z_k + \right\} dS, \quad (3.77)$$

where the integral is taken with respect to \mathbf{z} over ∂V . The constant tensor \mathcal{J} in (3.72) now becomes

$$\mathcal{J} = \frac{1}{V} \int_{\partial\Omega} \int_{\partial V} \mathcal{J}(\mathbf{x}, \mathbf{y}) ds ds, \quad (3.78)$$

where the \mathbf{y} -integration is over ∂V , and the \mathbf{x} -integration is over $\partial\Omega$.

3 Micromechanics

Composite materials are one of the strongest candidates as a structural material for many automobile, aerospace and other applications (D. Agarwal 1974). Recently, short fiber-reinforced composite materials have been extensively investigated because they are more economical and impact resistant (M. Taya 1989). One of the earliest attempts to explain the reinforcing effect of fibers was described by [3], and is now referred to as the shear lag theory, which considers long straight discontinuous fibers completely embedded in a continuous matrix (Cox 1952).

Fiber-reinforced composites are often characterized by their high specific strength and specific modulus parameters (i.e., strength to weight ratios), and are widely used for applications in low-weight components. The high strength and damage resistance of the composites are very important for a number of practical applications. In order to predict the strength and other properties of composites, a number of mathematical models of deformation, damage and failure of fiber reinforced composites have been developed.

Short fiber reinforced composites have several attractive characteristics that make them worthy of consideration for other applications. Therefore, short fiber reinforced composite materials have been extensively investigated because they are more economical and impact resistant.

3.1 Unidirectional short fiber composite

A unidirectional fibre composite is highly anisotropic. Stiffness and strength in the fibre direction are of the order of the fibre value, and thus very large, while normal to the fibre direction they are of the order of the matrix value and are thus much lower. In an injection-moulded discontinuous-fibre composite, stiffness and strength are much more complex owing to the multitude of fibre orientations. The resultant properties are largely controlled by material parameters e.g. E_f (fibre elastic

modulus), E_m (matrix elastic modulus), v_f (fibre volume fraction), FLD (fibre length distribution) and FOD (fibre orientation distribution) and test conditions. The prediction of the elastic properties of discontinuous fibre reinforced materials has received much attention in the past. Three of the most commonly used methods are: (i) aggregate model, (ii) Cox shear-lag theory, and (iii) the rule of mixtures.

The aggregate model uses the concept of subunits, each of which possess the elastic properties of a reinforced composite in which the fibres are continuous and fully aligned. In this way, elastic moduli have been estimated for various composite systems (Halpin JC, Pagano NJ 1969). Brody and Ward (Brody H, Ward, IM 1971) have compared measured moduli for compression moulded 30% w/w short glass and carbon fibre polyethylene and polypropylene composites with those determined by using the aggregate model. Reasonable correlation was found although it should be remembered that the FOD was fairly isotropic compared with that produced during the injection moulding process.

More recently (Toll S. 1992) a modified aggregate model was applied to plaque mouldings, identifying limitations of the previous aggregate models as: (1) the unit-cell stiffnesses require estimation by micromechanical approximations, since the unidirectional composite is normally unavailable; (2) it is reasonably accurate only at nearly unidirectional orientations. To overcome these short-comings a two-parameter model was developed which describes the unit-cell stiffnesses, which are easily determined from elastic constants measured for a material in a known but arbitrary orientation state. When measured moduli were compared with predicted values, excellent agreement was found.

Other methods have been based on various forms of the rule of mixtures (RoM):

$$E_{//} = v_f E_f + v_m E_m \quad \text{and} \quad E_{\perp} = \frac{E_f E_m}{E_m v_f + E_f v_m} \quad (3.79)$$

where $E_{//}$ and E_{\perp} are moduli determined parallel and normal to the principle fibre orientation direction in a continuous unidirectional fibre system.

These equations were modified by Halpin and Tsai (Halpin JC, Tsai SW 1967) for discontinuous-fibre materials to yield longitudinal and transverse moduli,

$$E_{\parallel} = E_m \left[\frac{1 + 2 \frac{l}{d} \eta_{\parallel} \nu_f}{1 - \eta_{\parallel} \nu_f} \right], \quad \text{where } \eta_{\parallel} = \left[\frac{\left(\frac{E_f}{E_m} \right) - 1}{\left(\frac{E_f}{E_m} \right) + 2 \left(\frac{l}{d} \right)} \right], \quad (3.80)$$

$$E_{\perp} = E_m \left[\frac{1 + \alpha \eta_{\perp} \nu_f}{1 - \eta_{\perp} \nu_f} \right], \quad \text{where } \eta_{\perp} = \left[\frac{\left(\frac{E_f}{E_m} \right) - 1}{\left(\frac{E_f}{E_m} \right) + \alpha} \right]; \quad (3.81)$$

η_{\parallel} and η_{\perp} describe longitudinal and transverse efficiency factors, $\left(\frac{l}{d} \right)$ the fibre aspect ratio and α a geometric factor.

Further modifications were made to the rule of mixtures by Cox (H. L. Cox 1952) to derive the shear lag analysis,

$$E_c = E_m (1 - \nu_f) + E_f \nu_f \left(1 - \frac{\tanh\left(\frac{\beta l}{2}\right)}{\left(\frac{\beta l}{2}\right)} \right) \quad (3.82)$$

where the last term in brackets is described as a fibre-length correction factor, l is the fibre length and β , which governs the rate of stress build up at the fibre ends, is given by

$$\beta = \frac{1}{r} \left[\frac{E_m}{E_f (1 + \nu) \ln\left(\frac{R}{r}\right)} \right]^{\frac{1}{2}} \quad (3.83)$$

where E_m is the matrix modulus, ν is Poisson's ratio, r is the fibre radius and $2R$ the mean inter-fibre spacing. For a square fibre packing system, the inter-fibre spacing is related to the volume fraction by

$$R = r \sqrt{\frac{\pi}{4\nu_f}} \quad (3.84)$$

so that β may be written as

$$\beta = \frac{1}{r} \sqrt{\frac{E_m}{E_f (1+\nu) \ln \sqrt{\frac{\pi}{4\nu_f}}}} \quad (3.85)$$

Several assumptions were made: (1) the fibre and the matrix remain elastic in their mechanical response; (2) the interface between the fibre and the matrix is perfect; and (3) no axial force is transmitted through the fibre ends.

3.2 Random Short Fiber Composite

To account for fibre orientation effects in short fibre materials, the RoM is adapted as

$$E_c = E_m (1 - \nu_f) + E_f \nu_f \eta_L \eta_0 \quad (3.86)$$

η_L is a fibre-length correction factor, and η_0 often described as the Krenchel orientation efficiency factor (Krenchel 1964), is given by the general form,

$$\eta_0 = \frac{\sum_n a_{fn} \cos^4 \alpha_n}{\sum_n a_{fn}}, \quad \text{where} \quad \sum_n a_{fn} = 1 \quad (3.87)$$

and where a_{fn} is the ratio between the cross-sectional area presented by a group of fibres orientated at an angle α_n to the applied load direction and the total area of all the fibres at a given cross-section of the composite. The number of groups are designated by $n = 1, 2, \dots, n$. Eq. (9) was further modified (O'Donnell B. 1990) to yield the through-thickness fibre orientation efficiency,

$$\eta_0 = \frac{N_{f1} \cos^3 \alpha_1 + N_{f2} \cos^3 \alpha_2 + \dots + N_{fn} \cos^3 \alpha_n}{N_{f1} \sec \alpha_1 + N_{f2} \sec \alpha_2 + \dots + N_{fn} \sec \alpha_n} \quad (3.88)$$

where the notations given above apply, and N_{f_1} is the fraction of the total number of fibres orientated at angle α_1 in any field of view. Thus measuring the through-thickness fibre orientation angles, using a series of layers of fields-of-view and determining corresponding efficiency factors will allow the composite stiffness to be determined through the moulding thickness.

CHAPTER IV

CLASSIFICATION OF BIOLOGICAL STRUCTURES: DESIGN OPTIMIZATION STRATEGIES

1. INTRODUCTION

Nature has gone through evolution over the 3.8 Gyr since life is estimated to have appeared on the Earth (Gordon 1976). Nature has evolved objects with high performance using commonly found materials. The understanding of the functions provided by objects and processes found in Nature can guide us to imitate and produce nanomaterials, nanodevices and processes. Biologically inspired design or adaptation or derivation from Nature is referred to as ‘biomimetics’. It means mimicking biology or Nature. Biomimetics is derived from the Greek word biomimesis. The word was coined by polymath Otto Schmitt in 1957, who, in his doctoral research, developed a physical device that mimicked the electrical action of a nerve. Other words used include bionics (coined in 1960 by Jack Steele of Wright-Patterson Air Force Base in Dayton, OH), biomimicry and biognosis.

Nature has always been an invaluable source of inspiration for technological progress. Great scientific revolutions were started by the work of men such as Leonardo da Vinci and Galileo Galilei, who were able to learn from Nature and apply their knowledge most effectively

The field of biomimetics is highly interdisciplinary. It involves the understanding of biological functions, structures and principles of various objects found in Nature by biologists, physicists, chemists and material scientists, and the design and fabrication of various materials and devices of commercial interest by engineers, material scientists, chemists and others. The word biomimetics first appeared in Webster’s dictionary in 1974 and is defined as ‘the study of the formation, structure or function

of biologically produced substances and materials (as enzymes or silk) and biological mechanisms and processes (as protein synthesis or photosynthesis) especially for the purpose of synthesizing similar products by artificial mechanisms which mimic natural ones'. Biological materials are highly organized from the molecular to the nanoscale, microscale and macroscale, often in a hierarchical manner with intricate nanoarchitecture that ultimately makes up a myriad of different functional elements (Alberts et al. 2008). Nature uses commonly found materials. Properties of the materials and surfaces result from a complex interplay between the surface structure and the morphology and physical and chemical properties. Many materials, surfaces and devices provide multifunctionality. Molecular-scale devices, superhydrophobicity, self-cleaning, drag reduction in fluid flow, energy conversion and conservation, high adhesion, reversible adhesion, aerodynamic lift, materials and fibres with high mechanical strength, biological self-assembly, antireflection, structural coloration, thermal insulation, self-healing and sensoryaid mechanisms are some of the examples found in Nature that are of commercial interest. (B. Bhunshan 2010)

1.1 Biological materials vs engineering materials

Biological materials are omnipresent in the world around us. They are the main constituents

in plant and animal bodies and have a diversity of functions. A fundamental function is obviously mechanical providing protection and support for the body. But biological materials may also serve as ion reservoirs (bone is a typical example), as chemical barriers (like cell membranes), have catalytic function (such as enzymes), transfer chemical into kinetic energy (such as the muscle), etc.

Nature has developed a large number of ingenious solutions which still wait to be discovered

and serve as a source of inspiration (Aksay 1998). This subject was pioneered by Schwendener (Schwendener S 1874) and D'Arcy Wentworth Thomson in the classical book from 1917 (revised and reprinted in 1942) "On Growth and Form",

which has been republished almost a century later (Thomson 1992). This early text mostly relates the “form” (or shape) of biological objects to their function. A similar approach specifically focusing on trees has been pursued in the book by Mattheck and Kubler (Mattheck C 1995) with the specific aim to extract useful engineering principles from their observations. Adapting the form (of a whole part or organ, such as a branch or a vertebra) is one aspect of functional adaptation. A second, which relates more directly to Materials Science, is the functional adaptation of the microstructure of the material itself (such as the wood in the branch or the bone in the vertebra). This dual optimization of the part’s form and of the material’s microstructure is well known for any engineering problem. However, in natural materials shape and microstructure are intimately related due to their common origin, which is the growth of the organ. Growth implies that “form” and “microstructure” are created in the same process. The shape of a branch is created by the assembly of molecules to cells, and of cells to wood with a specific shape. Hence, at every size level, the branch is both form and material – the structure becomes hierarchical.

It is not evident at all that the lessons learned from hierarchical biological materials will be applicable immediately to the design of new engineering materials. The reason arises from striking differences between the design strategies common in Engineering and those used by Nature (see Fig. 4.1). These differences are contributed by the different sets of elements used by Nature and the Engineer – with the Engineer having a greater choice of elements to choose from in the “toolbox”. Elements such as iron, chromium, nickel, etc. are very rare in biological tissues and are certainly not used in metallic form as, for example, in steels. Iron is found in red blood cells as an individual ion bound to the protein hemoglobin: its function is certainly not mechanical but rather chemical, to bind oxygen. Most of the structural materials used by Nature are polymers or composites of polymers and ceramic particles. Such materials would not be the first choice of an engineer who intends to build very stiff and long-lived mechanical structures. Nevertheless, Nature makes the best out of the limitations in the chemical environment, adverse temperatures and uses polymers and composites to build trees and skeletons (Gibson LJ 1995). Another major difference between materials from Nature and the Engineer is in the

way they are made. While the Engineer selects a material to fabricate a part according to an exact design, Nature goes the opposite direction and grows both the material and the whole organism (a plant or an animal) using the principles of (biologically controlled) self-assembly. Moreover, biological structures are even able to remodel and adapt to changing environmental conditions during their whole lifetime. This control over the structure at all levels of hierarchy is certainly the key to the successful use of polymers and composites as structural materials.


Biological Material	Engineering Material
Light Elements dominate: C, N, O, H, Ca, P, S, Si,	Large Variety of Elements: Fe, Cr, Ni, Al, Si, C, N, O, ...
Growth by biologically controlled self-assembly (approximate design)	Fabrication from melts, powders, solutions, etc. (exact design)
	
Hierarchical Structuring at all size levels	Forming (of the part) and Micro-structuring (of the material)
Adaptation of form and structure to the function	Selection of material according to function
Modeling and Remodeling: Capability of adaptation to changing environmental conditions.	Secure Design (considering possible maximum loads as well as fatigue)
Healing: Capability of self-repair	

Fig. 4.1

Biological and engineering materials are governed by a very different choice of base elements and by a different mode of fabrication. From this are resulting different strategies for materials choice and development (under the arrow).

Different strategies in designing a material result from the two paradigms of “growth” and “fabrication” are shown in Fig. 4.1. In the case of engineering materials, a machine part is designed and the material is selected according to the functional prerequisites taking into account possible changes in those requirements

during service (e.g. typical or maximum loads, etc.) and considering fatigue and other lifetime issues of the material. Here the strategy is a static one, where a design is made in the beginning and must satisfy all needs during the lifetime of the part. The fact that natural materials are growing rather than being fabricated leads to the possibility of a dynamic strategy. Taking a leaf as an example, it is not the exact design that is stored in the genes, but rather a recipe to build it. This means that the final result is obtained by an algorithm instead of copying an exact design. This approach allows for flexibility at all levels. Firstly, it permits adaptation to changing function during growth. A branch growing into the wind may grow differently than against the wind without requiring any change in the genetic code. Secondly, it allows the growth of hierarchical materials, where the microstructure at each position of the part is adapted to the local needs (Jeronimidis G 2000). Functionally graded materials are examples of materials with hierarchical structure. Biological materials use this principle and the functional grading found in Nature may be extremely complex. Thirdly, the processes of growth and “remodeling” (this is a combination of growth and removal of old material) allow a constant renewal of the material, thus reducing problems of material fatigue. A change in environmental conditions can be (partially) compensated for by adapting the form and microstructure to new conditions. One may think about what happens to the growth direction of a tree after a small land-slide occurs. In addition to adaptation, growth and remodeling, processes occur which enable healing allowing for self-repair in biological materials.

1.2 Simple geometry in complex organism

Many cultures throughout history have used the regularities of numbers and patterns as a means of describing their environment. The ancient Greeks believed that just five archetypal forms – the ‘platonic solids’ – were part of natural law and could describe everything in the universe because they were pure and perfect (Fuller, 1975). This platonic conception of Nature persisted up until the mid nineteenth century when Charles Darwin published his revolutionary ‘Origin of Species’, “After Darwin the whole lawful scheme was overthrown and organic forms came to

be seen as contingent mutable assemblages of matter e ‘clever artefact like contrivances’ e put together gradually during the course of evolution primarily by natural selection for biological function’’ (Denton et al., 2003). A recognition of natural patterns and shapes derived from physical laws seemed to reassert itself in 1917 when d’Arcy Thompson published his classic ‘On Growth and Form’(Thompson, 1961), but in the scientific mainstream this remained little more than interesting. Using simple geometry to describe a complex organism is likely to generate a certain amount of skepticism, as esoteric and occult descriptions seem rather simplistic compared to modernscientific thinking. However, in 1928 Frank Ramsey proved that every complex or random structure necessarily contains an orderly substructure. His proof established the fundamentals of a branch of mathematics known as Ramsey theory, which is used to study the conditions under which order must appear, such as in large communication networks and the recognition of patterns in physical systems. The theory suggests that much of the essential structure of mathematics consists of extremely large numbers (with very complicated calculations) derived from problems which are deceptively simple (Graham and Spencer, 1990; Fuller, 1975, sec.227.00). From the perspective of the human body, Ramsey theory implies that simple shapes might form part of that underlying substructure, and an examination of how these could arise through the interactions of physical forces is presented. This supports recent research which reinstates physical law, and not natural selection, as the major determinant of biological complexity in the subcellular realm (Denton et al., 2003). The development of these shapes into more complex structures, and how they model biology, with implications for manual therapy then follows.

One of the problems that Nature seems to solve repeatedly is that of the most efficient ways of packing objects close together. A circle drawn on a piece of paper, i.e. in two dimensions (2D), demonstrates this. The circle encloses the largest area within the minimum boundary, which makes it a ‘minimal-energy’ shape (requiring the least amount of energy to maintain). Circles enclose space, as well as radiate out into it, as can be seen in a drop of oil floating on water, the growth of fruit mould, and the ripples in a pond.

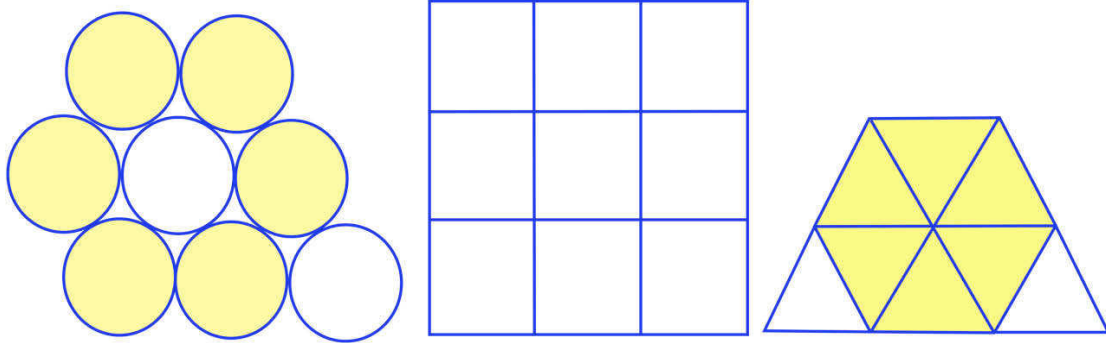


Figure 4.2

The tessellation of different shapes on a flat plane showing the appearance of the hexagon (shaded).

However, this efficiency is severely compromised when several circles are put next to each other as gaps are left in between (Figure 4.2). Other shapes, such as squares and triangles will both fill the space completely, but the proportion of area to boundary is not as good as with the circle. A square is inherently unstable; while triangles are very stable, even with flexible joints (Figure 4.2). Structures that are not triangulated can generate torque and bending moments at their joints, and must be rigidly fixed to prevent them from collapsing. The best compromise between efficient space filling of the circle and stability of the triangle is the hexagon (Figure 4.2).

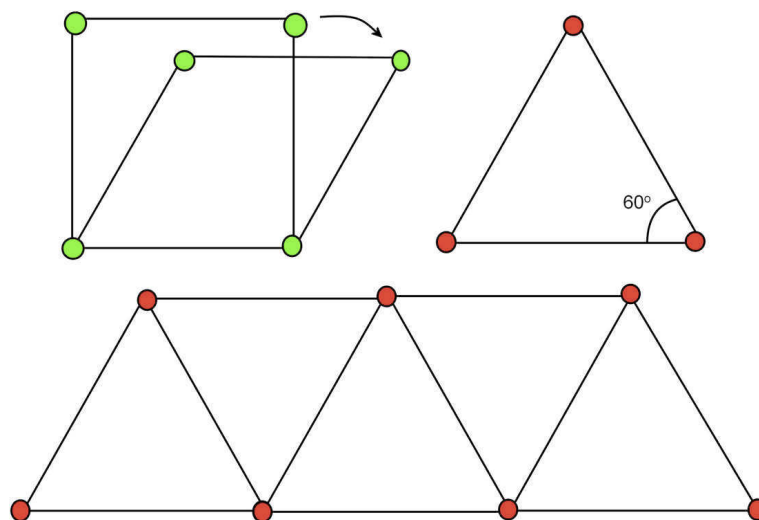


Figure 4.3

show that square trusses are inherently unstable at their joints, whereas triangular trusses are rigid.

Isolated hexagons are also liable to collapsing, but when several hexagons are packed together, they support each other as stresses balance at their 3-way junctions (Figure 4.3).

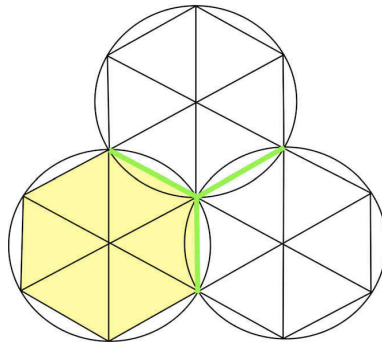


Figure 4.4
The relationship between hexagons, circles and triangles.

Soap bubbles spontaneously join together with outside surfaces that always meet at 120°, just like hexagons, whether the bubbles are equal in size or not (Figure 5.4). This is because soap molecules hold together through their surface tension, which tries to minimize itself and reduce the surface area (Fuller, 1975, sec.825.20; Stewart, 1998.). Some examples of naturally occurring hexagons are shown in Figure 7 (Bassnett et al., 1999; Weinbaum et al., 2003; Sanner et al., 2005). All this would seem to make the hexagon the obvious choice for close-packing in two dimensions. In 3D, however, a structure which fulfills the same purpose may not be so readily apparent. The ancient Greeks recognized the importance of the five regular polyhedra because of their intriguing properties (Fuller, 1975).

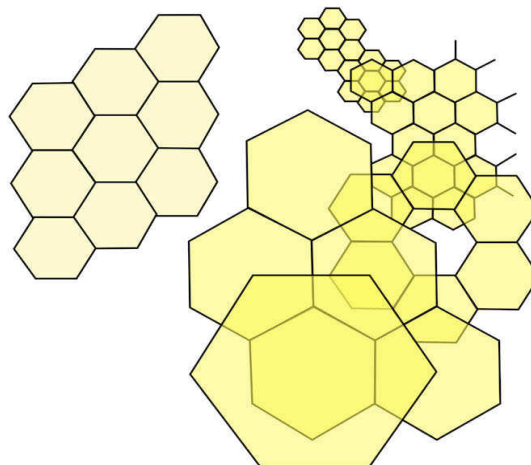


Figure 4.5
Hexagonal close-packing and a hierarchy of hexagons.

Their outer faces are made from shapes which are all the same; a sphere circumscribed around each one will touch all the corners, while one inscribed within will touch the centre of all the faces; and they all have 3, 4 or 5 sides. Joining up the face centres creates the ‘dual’ of that shape, i.e. the octahedron and cube are duals of each other; and the dodecahedron and icosahedron similarly; the tetrahedron is unique in that it is a dual of itself. Not a hexagon in sight. yet! Just as the circle is the most efficient shape for enclosing space in 2D, so its equivalent in 3D is the sphere. Atoms, bubbles, oranges, and planets all approximate to spheres. Putting lots of spheres next to each other still leaves all those wasteful spaces in between, just like the circles did; but there is a more efficient solution. In order to tease out some of the consequences of packing spheres closely together, plastic balls have been glued together (Figure 8). The same arrangements are also shown as lattices of steel balls, with coloured magnetic sticks representing the inherent ‘minimal-energy’ characteristic of close-packing (i.e. their centres of mass are at the minimum possible distance apart) (Connelly and Back, 1998). Adding more spheres to a particular shape creates higher-order structures of the same shape, numbered according to the [magnetic] connections on their outer edge (Fuller, 1975).

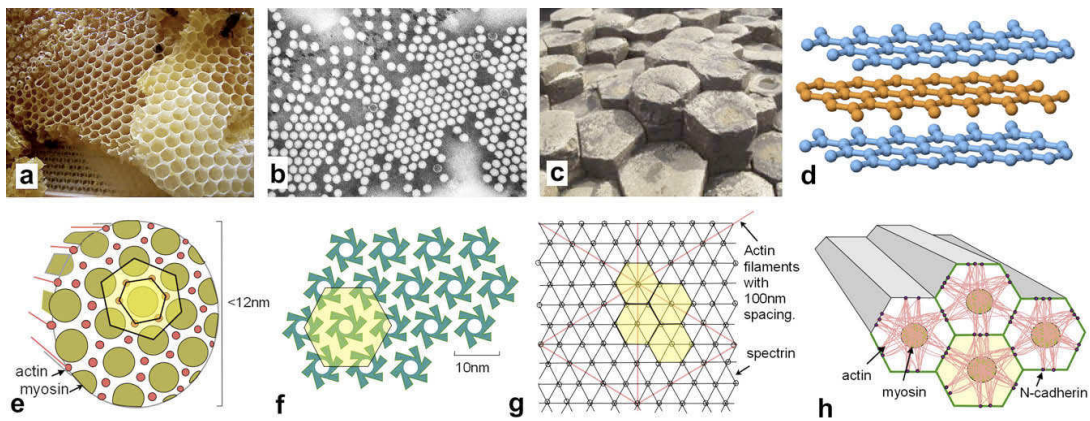


Figure 4.6

Some examples of hexagons in natural structures: (a) honeycomb (Wikipedia); (b) close-packing of Polio virus (Fred Murphy & Sylvia Whitfield, Wikipedia); (c) Basalt blocks on the Giants Causeway in Ireland, formed from cooling lava (Matthew Mayer, Wikipedia); (d) stacked layers of carbon atoms in graphite (Benjah-bmm27, Wikipedia); (e) hexagonal close-packing of actin and myosin in a muscle fibril; (f) hexameric complexes of uroplakin covering the epithelial lining of the urinary bladder (redrawn after Sanner *et al.*, 2005); (g) idealized diagram of the sub-cortical cytoskeleton (redrawn after Weinbaum *et al.*, 2003); and (h) cells in the optic lens arranged as hexagons (redrawn after Bassnett *et al.*, 1999).

1.3 The Bee's Cell

The most famous of all hexagonal conformations, and one of the most beautiful, is the bee's cell. As in the basalt or the coral, we have to deal with an assemblage of co-equal cylinders, of circular section, compressed into regular hexagonal prisms.

The axes of honeycomb cells are always quasi-horizontal, and the non-angled rows of honeycomb cells are always horizontally (not vertically) aligned. Thus, each cell has two vertical walls, with "floors" and "ceilings" composed of two angled walls. The cells slope slightly upwards, between 9 and 14 degrees, towards the open ends.

There are two possible explanations for the reason that honeycomb is composed of hexagons, rather than any other shape. One, given by Jan Brožek, is that the hexagon tiles the plane with minimal surface area. Thus a hexagonal structure uses the least material to create a lattice of cells within a given volume. Another, given by D'Arcy Wentworth Thompson, is that the shape simply results from the process of individual bees putting cells together: somewhat analogous to the boundary shapes created in a field of soap bubbles. In support of this he notes that queen cells, which are constructed singly, are irregular and lumpy with no apparent attempt at efficiency. (Wikipedia). If a single cell be isolated, it will be seen that the sides rise from the outer edges of the three lozenges, so that there are, of course, six sides, the transverse section of which gives a perfect hexagon. Many years ago, Maraldi, being struck with the fact that the lozenge-shaped plates always had the same angles, took the trouble to measure them, and found that in each lozenge the large angles measured 109 degrees 28', and the smaller 70 degrees 32', the two together making 180 degrees, the equivalent of two right angles. He also noted the fact that the apex of the three-sided cup was formed by the union of three of the greater angles. The three united lozenges are seen in the figure below.

Some time afterward, Reaumur, thinking that this remarkable uniformity of angle might have some connection with the wonderful economy of space which is observed in the bee-comb, hit upon a very ingenious plan. Without mentioning his reasons for the question, he asked Koenig, the mathematician, to make the following

calculation: Given a hexagonal vessel terminated by three lozenge-shaped plates, what are the angles which would give the greatest amount of space with the amount of material?

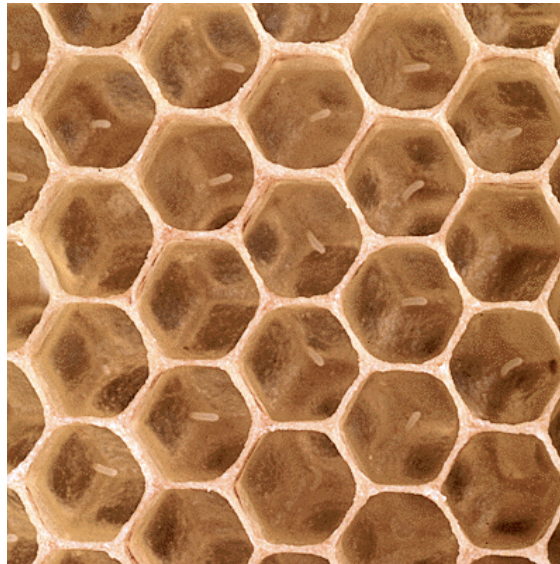


Figure 4.7

Honeycomb

Koenig made his calculations, and found that the angles were 109 degrees 26' and 70 degrees 34', almost precisely agreeing with the measurements of Maraldi. Reaumur, on receiving the answer, concluded that the bee had very nearly solved the difficult mathematical problem, the difference between the measurement and the calculation being so small as to be practically negative in the actual construction of so small an object as the bee-cell.

Mathematicians were naturally delighted with the results of the investigation, for it showed how beautifully practical science could be aided by theoretical knowledge; and the construction of the bee-cell became a famous problem in the economy of Nature. In comparison with the honey which the cell is intended to contain, the wax is a rare and costly substance, secreted in very small quantities, and requiring much time and a large expenditure of honey for its production. It is, therefore, essential that

the quantity of wax employed in making the comb should be as little, and that of the honey which could be stored in it as great, as possible.

1.4 Mathematics in Nature: Fibonacci Numbers

The Fibonacci numbers are Nature's numbering system. They appear everywhere in Nature, from the leaf arrangement in plants, to the pattern of the florets of a flower, the bracts of a pinecone, or the scales of a pineapple. The Fibonacci numbers are therefore applicable to the growth of every living thing, including a single cell, a grain of wheat, a hive of bees, and even all of mankind

2 Classification of biological structures

Nature has an enormous pool of inventions that passed the harsh test of practicality and durability in changing environment. In order to harness the most from Nature's capabilities, it is critical to bridge between the fields of biology and engineering and to see cooperation of experts from both fields. This bridging effort can help in turning Nature's capabilities into engineering capabilities, tools and mechanisms.

It was necessary a first step in which we are interested in a classification of biological structures, providing for a code assignment for an immediate discrimination. This classification provides a first upstream division into two main areas: experimental observation on time (T) and experimental observation on scale (S) and in sub-sequent division as shown in fig.4.8.

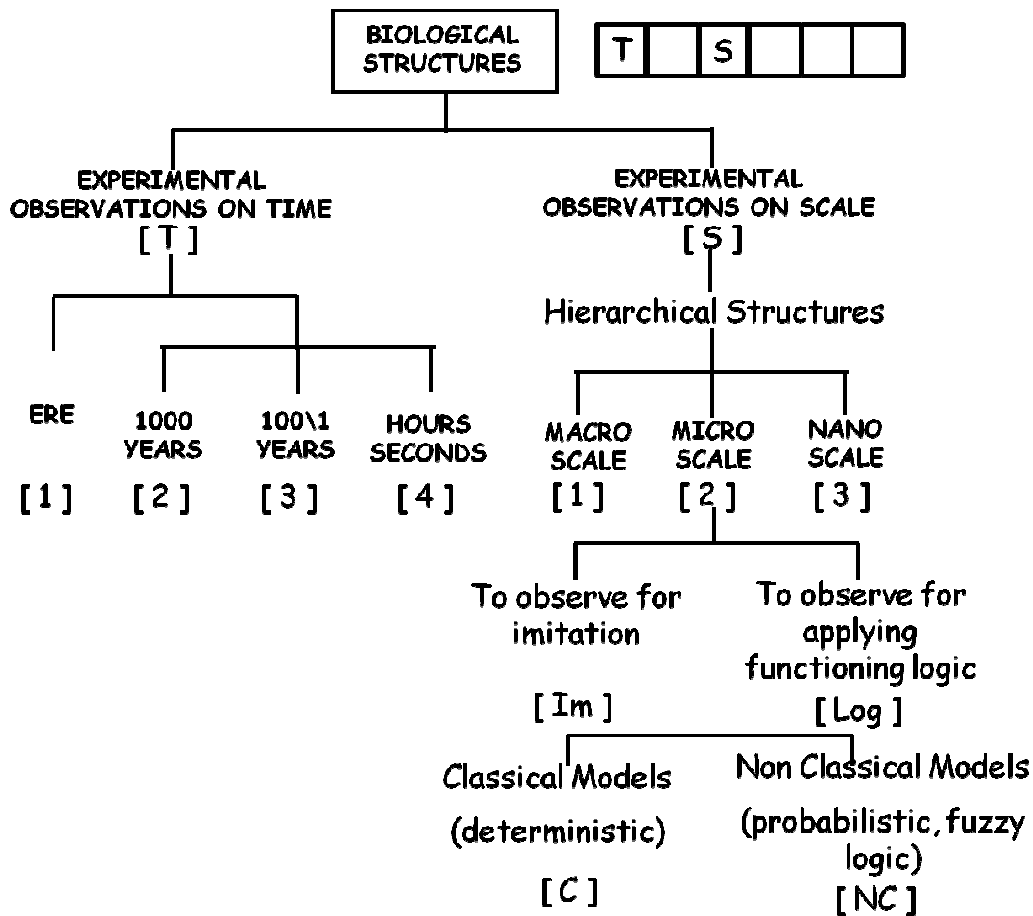


Figure 4. 8

Classification of biological structures

2.1 Classification of biological structures: experimental observation on time

As regard the classification on time, were considered time ranging from ere(1), for example, human evolution, pangea or evolution of solar system to 1000 yeas (2). More specifically, Nature, through billions of years of trial and error, has produced effective solutions to innumerable complex real-world problems. The rigorous competition of natural selection means waste and efficiency are not tolerated in natural systems, unlike many of the technologies devised by humans. Every living form emerges from 2 strongly coupled processes, operating over maximally differentiated time spans: the rapid process of embryological development from a single cell to adult form, and the long slow process of evolution of diverse

species of forms over multiple generations. (Hensel M., Menges A. and Weinstock M. 2010)

The perfection and variety of natural forms is the result of relentless experimentation of evolution. By means of profligate prototyping and ruthless rejection of flawed experiments, Nature has evolved a rich biodiversity of interdependent species of plants and animals that are in metabolic balance with their environment. Analogy of evolutionary architecture should not be taken just to imply a form of development through natural selection. Other aspects of evolution such as the tendency to self organization are equally or even more significant. (Frazer J. 1995)

Ecosystems optimise the system rather than its components” the relationship between form and function is emphasized, and as a result, form and behaviour are equally important.

Biological forms and their behaviour emerge from process. It is process that produces, elaborates and maintains the form and structure of biological organisms (and non-biological things), and that process consists of a complex series of exchanges between the organism and its environment. Furthermore, the organism has a capacity for maintaining its continuity and integrity by changing aspects of its behaviour. Form and behaviour are intricately linked. (Hensel M., Menges A. and Weinstock M. 2010)

The form of an organism affects its behaviour in the environment, and a particular behaviour will produce different result in different environments. Behaviour is non linear and context specific. (Hensel M., Menges A. and Weinstock M. 2010)

For times comparable to 1000 years an example is helical tree. Helices, in-fact, appear at every anatomical level across the nine orders of magnitude that span the range of size between molecules and the biggest organisms. They provide solutions to any number of the challenges of growth and form, structure and function including significantly movement, that evolution has thrown up, in particular, in this case, the tree trunk wheel to have the same amount of light at every point.

Also, were considered time ranging from 100 to 10 yeas (3) as growth and muscle development and times ranging from 1 hour to second (4) as meiosis and mitosis.

2.2 Classification of biological structures: experimental observation on scale

As regards, however, the experimental observations on scale, has been referred to the hierarchical structures, whereas, therefore, a macro (1), micro (2) and nano-scale (3). The classification made, then a subsequent division related to their ability to discriminate the structures on the way in which they are inspired by Nature: to observe for simple imitation (Im) or to observe for applying functioning logic (log). The last sub-division is related to the complexity of the problem and, therefore, the number of variables involved. The problems are divided, therefore, in the classical (C) and non classical (NC).

2.3 Classification of biological structures: experimental observation on scale- hierarchical structures

Many biological tissues are fiber composites with a hierarchical structure. The following are three examples of hierarchically structured biogenic tissues with entirely different chemical compositions: the wood cell wall, an almost pure polymeric composite, the skeleton of a glass sponge, which is composed of almost pure silica mineral, and bone, an organic–inorganic composite consisting of roughly half polymer and half mineral.

2.3.a Wood

At the macroscopic level, spruce wood can be considered as a cellular solid, mainly composed of parallel hollow tubes, the wood cells. The cell wall is a fiber composite made of cellulose microfibrils embedded into a matrix of hemicelluloses and lignin.

Wood can be regarded as a cellular material at the scale of hundred micrometers to centimetres . Parameters which can be varied at this hierarchical level (and, therefore, used for adaptation to biological and mechanical needs) are the diameter and shape of the cell cross-section, as well as the thickness of the cell wall. In

particular, the ratio of cell-wall thickness to cell diameter is directly related to the apparent density of wood which, in turn is an important determinant of the performance of light weight structures. The distribution of microfibril angles is used by the plant to introduce property gradients into the material and to tune the mechanical properties according to needs.

2.3.b Bone

The hierarchical structure of bone has been described in a number of reviews Starting from the macroscopic structural level, bones can have quite diverse shapes depending on their respective function. Long bones, such as the femur or the tibia, are found in our extremities and provide stability against bending and buckling. In other cases, for instance for the vertebra or the head of the femur, the applied load is mainly compressive. In such cases, the bone shell can be filled with a “spongy” material called trabecular or cancellous bone The walls of tube-like long bones and the walls surrounding trabecular bone regions are called cortical bone.

At the lower levels of hierarchy, bone is a composite of collagen and mineral nanoparticles made of carbonated hydroxyapatite.

Mineralized fibrils in cortical bone self-assemble into fibril arrays (sometimes called fibers) on the scale of 1–10 μm . While a diversity of structural motifs exist between bone tissues, the most common in bone is the lamellar unit. While the existence of the lamellar unit in bone has been known for over a century, the internal structure of this basic building block and its correlation to mechanical function have remained unclear for a long time. . The fiber axis orientation varies periodically with a period of 5 μm corresponding approximately to the width of a single lamella. This implies that each lamella consists of a series of fibril layers oriented at different angles to the osteon axis. What is more surprising is that the angles are always positive, implying that on average each lamellae has a non-zero spiral fibril angle with respect to the long axis of the osteon, with a right-handed helicity. These results thus show that osteonal lamellae are built as three-dimensional helicoids around the central blood vessel. Such helicoidal structures have been found in other connective tissues, for example in the secondary wood cell wall and in insect cuticle.

2.3.c Glass sponge skeletons

Glass is widely used as a building material in the biological world despite its fragility. Organisms have evolved means to effectively reinforce this inherently brittle material. It has been shown that spicules in siliceous sponges exhibit exceptional flexibility and toughness compared with brittle synthetic glass rods of similar length scales. The mechanical protection of diatom cells is suggested to arise from the increased strength of their silica frustules. Structural and optical properties of individual spicules of the glass sponge *Euplectella*, a deep-sea, sediment-dwelling sponge from the Western Pacific are recently described. Not only do these spicules have optical properties comparable to man-made optical fibers, but they are also structurally resistant. The individual spicules are, however, just one structural level in a highly sophisticated, nearly purely mineral skeleton of this siliceous sponge.

2.4 Mathematics and growth: fractal structures

Fractals have wide applications in biology, computer graphics, quantum physics and several other areas of applied sciences. Fractal sets are mathematical models of non-integer dimensional sets satisfying certain scaling properties. These may be thought of as objects that are obtained by an infinite recursive or inductive process of successive microscopic refinements.

A mathematical fractal looks the same at all scales of magnification. This is an approximation to physical fractals which appear similar to the original object only for a certain range of scales. Self-similar sets are special class of fractals and there are no objects in Nature which have exact structures of self similar sets. These sets are perhaps the simplest and the most basic structures in the theory of fractals which should give us much information on what would happen in the general case of fractals

A fractal often has a fine structure at arbitrarily small scales, it has a Hausdorff dimension which is greater than its topological dimension (although this requirement is not met by space-filling curves such as the Hilbert curve).

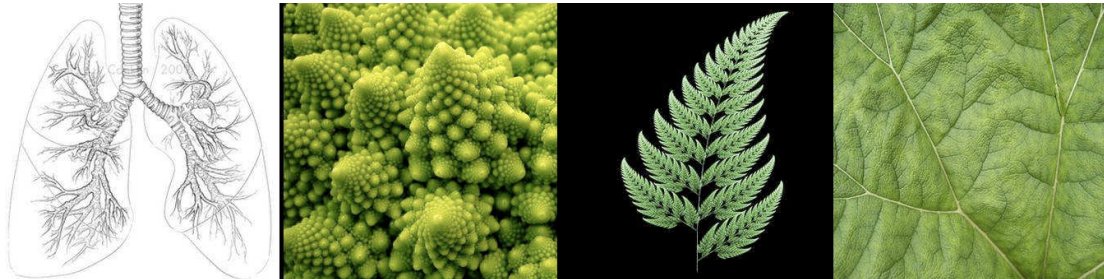


Figure 4.9

Fractal structure of respiratory system, fractal geometry of roman broccoli, fractal fern and fractal growth pattern of a leaf

Examples in Nature include clouds, river networks, fault lines, mountain ranges, craters, snow flakes, crystals, lightning, cauliflower or broccoli, and ocean waves. DNA and heartbeat can be analyzed as fractals. Even coastlines may be loosely considered fractal in Nature. But in particular, the respiratory, circulatory, and nervous systems are remarkable instances of fractal architecture

Careful analysis of the lungs reveal fractal scaling, and it has been noted that this fractal structure makes the lungs more fault-tolerant during growth.

In addition to fault-tolerance during growth, fractal branching makes available much more surface area for absorption and transfer in bronchial tubes, capillaries, intestinal lining, and bile ducts.

2.5 To observe for imitation

Skin is the largest organ in the body, a highly dynamic network of cells, nerves and blood vessels.

Thirty years ago, National Institutes of Health-funded burn surgeons determined that badly burned skin should be removed as quickly as possible, followed by immediate and permanent replacement of the lost skin. This seemingly simple idea ultimately

became standard practice for treating major burn injuries and led to the development of an artificial skin system called Integra® Dermal Regeneration Template.

When skin is damaged or lost due to severe injury or burns, bacteria and other microorganisms have easy access to warm, nutrient-rich body fluids. Loss of these vital fluids can lead to shock. Also known as “circulatory collapse,” shock can occur when the blood pressure in a person’s arteries is too low to maintain an adequate supply of blood to organs and tissues. To treat a severe burn, surgeons first remove the burned skin and then quickly cover the underlying tissue, usually with a combination of laboratory-grown skin cells and artificial skin.

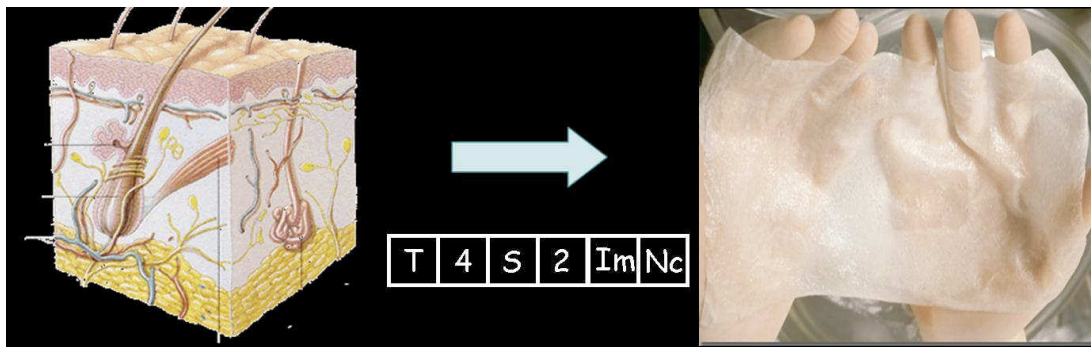


Figure 4.10
3D schema of the skin and artificial skin

After removing burn-damaged skin, surgeons blanket a wound with a covering like Integra®, then apply a skin graft on top of this biomaterial to encourage the growth of new skin to close the wound. Ideally, surgeons obtain skin grafts from an unburned area of skin elsewhere on the body. But when the burn is severe and covers 80 to 90 percent of a person’s body surface, there is not enough skin to use for this purpose. There are two types of skin grafts. An autologous skin graft transfers skin from one part of the body to another. In contrast, an allograft transfers skin from another person, sometimes even a cadaver. Allografts offer only temporary cover, as they are quickly rejected by a person’s immune system.

New epidermal skin can be produced by taking cells from a non-burned epidermal layer of skin, growing them into large sheets of cells in a laboratory, then placing the

cell sheets on top of Integra®. Scientists do not yet know how to grow the lower, dermal layer of skin in the lab. Integra® is an artificial substance that contains no living components. It is not designed to be a replacement skin. Rather, Integra® supplies a protective covering and a pliable scaffold onto which a person's own skin cells can regenerate the lower, dermal layer of skin destroyed by burn.

2.6 To observe for applying functioning logic

Sharks may conjure up notions of great and fear some predators, but one day, people may think of sharks equally as great teachers. Medical technologists to swimsuit designers today are scrutinizing sharks for design ideas. Pre-dating the dinosaurs, the design solutions generated over their 400-million-year evolutionary odyssey and embodied in their contemporary form give us plenty of reason to think sharks may hold design lessons for us. Over this enormous time period, shark evolution has successfully addressed a number of design challenges that turn out to relate directly to technological challenges currently facing humanity in our own quest to become a sustainable species.

Shark skin is a multifunctional marvel. Seawater and the countless potential ecto-parasites within it (barnacle larvae, algae, bacteria, etc.) are a constant flow hazard for sharks, for whom moving efficiently through water is an imperative. Most shark species move through water with high-efficiency in order to catch fast-moving prey, obtain sufficient oxygen through largely passive gills, and maintain buoyancy. Through its ingenious design, their skin turns out to be an essential aid in this behavior by reducing friction drag and auto-cleaning ecto-parasites from their surface. Boat manufacturers have recently taken an interest in how sharks achieve their unimpeded movement through water both because friction drag and the attachment of organisms on a ship's hull are major sources of energy inefficiency.

For decades, modern designers and engineers concerned with movement efficiency focused on the coarse shape and smoothness of an object. Howard Hughes' H-1 Racer, for example, an aircraft which broke numerous speed records in the 1930s,

sported revolutionary design features such as retractable landing gear and flush rivets. More recently, armed with greater tools for observation (such as scanning electron microscopes) and manufacturing, designers and engineers are developing an appreciation for the impact of finer-scale surface interaction dynamics. For example, while a shark's coarse shape is famously hydrodynamic, shark skin is anything but smooth. The very small individual scales of shark skin, called dermal denticles ("little skin teeth"), are ribbed with longitudinal grooves which result in water moving more efficiently over their surface than it would were shark scales completely featureless. Over smooth surfaces, fast-moving water begins to break up into turbulent vortices, or eddies, in part because the water flowing at the surface of an object moves slower than water flowing further away from the object. This difference in water speed causes the faster water to get "tripped up" by the adjacent layer of slower water flowing around an object, just as upstream swirls form along riverbanks. The grooves in a shark's scales simultaneously reduce eddy formation in a surprising number of ways: (1) the grooves reinforce the direction of flow by channeling it, (2) they speed up the slower water at the shark's surface (as the same volume of water going through a narrower channel increases in speed), reducing the difference in speed of this surface flow and the water just beyond the shark's surface, (3) conversely, they pull faster water towards the shark's surface so that it mixes with the slower water, reducing this speed differential, and finally, (4) they divide up the sheet of water flowing over the shark's surface so that any turbulence created results in smaller, rather than larger, vortices.

At the same time, three factors appear to help prevent marine organisms from being able to adhere to ("foul") shark skin: (1) the accelerated water flow at a shark's surface reduces the contact time of fouling organisms, (2) the roughened nano-texture of shark skin both reduces the available surface area for adhering organisms and creates an unstable surface repellant to microbes, and (3) the dermal scales themselves perpetually realign or flex in response to changes in internal and external pressure as the shark moves through water, creating a "moving target" for fouling organisms

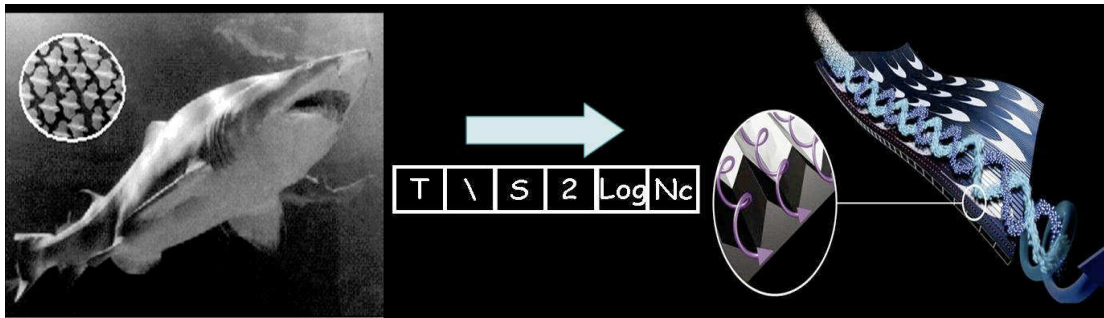


Figure 4.11
Silky shark skin photograph and Speedo's swimsuit

In late 1996, Speedo set out to develop the best and fastest swimsuits possible by improving upon the award winning Speedo Aquablade swim suit. They created the Fastskin. In 2004, they did it one better with the introduction of the Fastskin FSII. By reducing the total amount of drag over the surface of the swimsuit, and moving away from the traditional style of swimwear, SPEEDO looked to designs from Nature to produce suits that allow swimmers to move through water faster than ever before to achieve their personal best. Speedo focused upon managing existing forces to make better use of talents an athlete already has.

The shark, a creature that is fast in water but not naturally hydrodynamic, was used as a model for the Fastskin and Fastskin FSII swimsuits. The shark's quickness is attributed to V-shaped ridges on its skin called dermal denticles. Denticles decrease drag and turbulence around the shark's body allowing the surrounding water to pass over the shark more effectively. Due to the drag effect that occurs when an object travels through water, Fastskin fabric was constructed with built in ridges emulating sharkskin. Fastskin is composed of super stretch fabric made to improve the suit's fit and compress muscles. The result is a reduction of drag and muscle vibration, which increases productivity

Speedo used a revolutionary body scanning process to define and understand each swimmers' body shape. By scanning digital images of swimmers in eight different positions, Speedo engineers were able to identify exactly how the body moves and stretches. Using this information, Speedo created a suit with a much closer fit.

Using this technology, Speedo has created the only three dimensional swim suit pattern in existence. It emphasizes good position in the water and reduces drag. With no excess fabric and a maximum stretch, Speedo has produced a swimsuit that allows a full range of motion for a swimmer.

Since muscles work in groups, the Fastskin suits aid in connecting muscles through a combination of panels and unique seaming. Speedo created an anatomic/dynamic pattern where seams act like tendons and provide tension in the suit while the fabric panels act like muscles, stretching and returning to their original shape. Seams are an instrumental element in minimizing drag and optimizing performance.

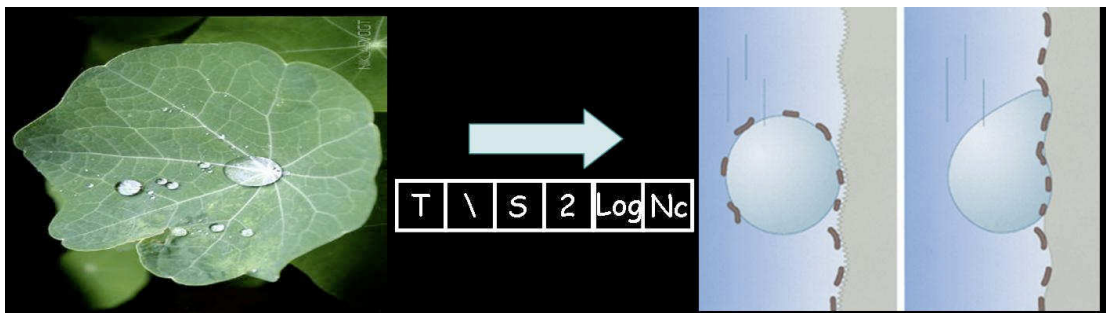


Figure 4.12
Lotus leaves and an example of self cleaning surface or usual surface

In the past few decades, the *Nelumbo nucifera*, better known as the lotus, has been intensively investigated for its self-cleaning properties. Known as the “Lotus effect”, the cuticle of this flower exhibits extreme water repellency known as superhydrophobicity which allows the plant to remove dirt passively (Solga, Cerman, Striffler, Spaeth & Barthlott, 2007). The cuticle is a waxy layer that surrounds a plant and prevents uncontrolled water loss. It is mainly made up of the biopolymer cutin among other lipids. Unlike other plants, the cuticle of superhydrophobic plants usually possesses an additional dense layer of epicuticular waxes which is composed of mainly hydrocarbons, alcohols, and ketones, thus making the surface hydrophobic (Solga et al, 2007). As hydrophobicity increases with an increased contact angle, superhydrophobic surfaces generally have static contact angles greater than 140° . In order to achieve this phenomenon, the lotus has many micro and nano surface structures and it is these papillae that enhance the self-cleaning ability of the lotus. Solga et al (2007) indicated that if the

plant cuticle is “structured in the micro or nanometre range, the water-air interface of a droplet lying on it is enlarged and the capillary forces between droplet and surface are significantly reduced. Thus, the droplet takes a spherical shape and rolls off easily.

Superhydrophobicity is an advantage to plants as it enables plants to get rid of dust as well as pathogenic spores thus enhancing the plant’s photosynthetic rate and prevents pathogenic fungi from penetrating the leaf’s surface (Solga et al, 2007). The self-cleaning property of the lotus leaf has been successfully applied to several industrial products, such as the façade paint *Lotusan*. A study was carried out on the effect of *Lotusan* and the results demonstrated that after 6 years of exposure under deciduous trees, tiles painted with *Lotusan* were significantly covered with less green algae than tiles covered with conventional paints (Spaeth, Solga, Barthlott & Cerman, 2006, cited in Solga et al, 2007). Other possible applications that are currently being investigated include self-cleaning glasses and various textiles, as well as employing superhydrophobicity to medical technology and laboratories as this will help to maintain sterility in a healthcare setting (Bhushan, Yong & Koch, 2009).

Despite the fact that superhydrophobicity has been heavily investigated in the lotus, there are still many answers that remain to be answered regarding the cuticle of a plant. In fact, the 3-D structure of the cuticle is still a puzzle as little is known regarding the molecular biology of this structure. Model species such as *Arabidopsis thaliana* have shed new light on the molecular biology and biosynthesis of the plant cuticle but since the chemical composition and structure of the cuticle and its waxes vary amongst different plant species, one cannot generalize the molecular mechanisms of the cuticle of model species to non-model species. Furthermore, the current model of wax tubule formation is “assumed to be based on a rolling-in process of plate-like wax structures. Tubules might rise from spontaneous folding of wax platelets but this proposed folding has never been observed experimentally” (Barge, Koch, Cerman & Neinhuis, 2006). Thus, more research needs to be done on the structure of the cuticle and this is important as filling these gaps of knowledge can revolutionize self-cleaning technology as demonstrated by the lotus.

2.7 Classical model

The last subdivision is related to the problem's complexity and, therefore, the number of variables involved. The problems are divided, therefore, in the classical (C), statistical problems, and non-classical (NC), characterized by a large number of variables, for which it is necessary to use probabilistic algorithms

The classical model are mathematical model characterized by few parameters in which ones understand the principles these are simply applied.

2.8 Non classical model

In the field of computer science, the study of bionics has produced artificial neural networks and swarm intelligence. Evolutionary computation was also motivated by bionics ideas but it took the idea further by simulating evolution in silico and producing well-optimized solutions that had never appeared in Nature Evolutionary Computing is the collective name for a range of problem-solving techniques based on principles of biological evolution, such as natural selection and genetic inheritance. These techniques are being increasingly widely applied to a variety of problems, ranging from practical applications in industry and commerce to leading-edge scientific research.

2.8.a Artificial neural networks

An artificial neural network ,is a mathematical model or computational model that is inspired by the structure and/or functional aspects of biological neural networks. A neural network consists of an interconnected group of artificial neurons, and it processes information using a connectionist approach to computation. Modern neural networks are non-linear statistical data modeling tools. They are usually used to model complex relationships between inputs and outputs or to find patterns in data.

The original inspiration for the term Artificial Neural Network came from examination of central nervous systems and their neurons, axons, dendrites, and synapses, which constitute the processing elements of biological neural networks

investigated by neuroscience. In an artificial neural network, simple artificial nodes, variously called "neurons", are connected together to form a network of nodes mimicking the biological neural networks, hence the term "artificial neural network".

Artificial Neural Networks (ANN) are currently a 'hot' research area in medicine at the moment, the research is mostly on modelling parts of the human body and recognising diseases from various scans (e.g. cardiograms, CAT scans, ultrasonic scans, etc.). Neural networks are ideal in recognising diseases using scans since there is no need to provide a specific algorithm on how to identify the disease. Neural networks learn by example so the details of how to recognise the disease are not needed.

They are used experimentally to model the human cardiovascular system. Diagnosis can be achieved by building a model of the cardiovascular system of an individual and comparing it with the real time physiological measurements taken from the patient. If this routine is carried out regularly, potential harmful medical conditions can be detected at an early stage and thus make the process of combating the disease much easier.

A model of an individual's cardiovascular system must mimic the relationship among physiological variables (i.e., heart rate, systolic and diastolic blood pressures, and breathing rate) at different physical activity levels. The reason that justifies the use of ANN technology, is the ability of ANNs to provide sensor fusion which is the combining of values from several different sensors. Sensor fusion enables the ANNs to learn complex relationships among the individual sensor values, which would otherwise be lost if the values were individually analysed. In medical modelling and diagnosis, this implies that even though each sensor in a set may be sensitive only to a specific physiological variable, ANNs are capable of detecting complex medical conditions by fusing the data from the individual biomedical sensors.

ANNs are used experimentally to implement electronic noses. Electronic noses have several potential applications in telemedicine. The electronic nose would identify odours in the remote surgical environment. These identified odours would then be electronically transmitted to another site where an odor generation system would recreate them. Because the sense of smell can be an important sense to the surgeon, tele-smell would enhance telepresent surgery.

An application developed in the mid-1980s called the "instant physician" trained an autoassociative memory neural network to store a large number of medical records, each of which includes information on symptoms, diagnosis, and treatment for a particular case. After training, the net can be presented with input consisting of a set of symptoms; it will then find the full stored pattern that represents the "best" diagnosis and treatment. Business is a diverted field with several general areas of specialisation such as accounting or financial analysis. Almost any neural network application would fit into one business area or financial analysis. There is some potential for using neural networks for business purposes, including resource allocation and scheduling. There is also a strong potential for using neural networks for database mining, that is, searching for patterns implicit within the explicitly stored information in databases. Most of the funded work in this area is classified as proprietary. Thus, it is not possible to report on the full extent of the work going on. Most work is applying neural networks, such as the Hopfield-Tank network for optimization and scheduling

2.8.b Swarm Intelligence

Swarm Intelligence (SI) is the emerging branch of Artificial Intelligence. It is normally used to refer to techniques that are inspired by social insects' behaviour. The swarm intelligence system usually comprises numerous agents interacting with one another and with their environment. These interactions often lead to emergent behaviour without any centralised control, that is, no one directs how the individuals should behave. We can easily find examples of such systems in Nature, for example

bird flocks, termite mounds, wolf packs, fish schools, bee hives and ant colonies, to name a few.

Ant colony behavior has been one of the most popular models of swarm behavior. Ants by themselves may seem to act randomly and without any discernible purpose, but when the collective interactions among ants are taken together, there will emerge a collective intelligence and behavior that has the capacity of solving a lot of problems. Through swarm intelligence, ants can determine the shortest path to a food source, feed the whole colony, build large structures, and adapt to situations.

Particle swarm optimization, on the other hand, is a type of swarm intelligence inspired by bird flocks and fish schools. This type of swarm optimization gives individual agents within the swarm the ability to change its position depending on its own limited intelligence and in comparison to other agents in the population. This enables individual agents to modify their paths depending on the success of the other agents in the population in finding the correct solution.

Swarm intelligence has applications in decentralized controls of unmanned vehicles for the military so single operators can control more unmanned vehicles. The use of swarm intelligence in medical nanobots may also help combat cancer. Using a swarm paradigm to model for traffic patterns, making the road longer and manipulating the speed limits has been shown to reduce gridlock and actually decrease travel time in certain cases.

Optimizing scheduling or distribution tasks can be very time consuming, or even virtually impossible in some instances. Southwest Airlines has used swarm to develop a more efficient model of cargo handling, saving the company \$2 million per year in labor costs. General Motors Corp. implemented software using adaptive technology to schedule car paint jobs and to avoid the scheduling conflicts from which the manual system suffered. The new system resulted in a 30% productivity improvement and 35% fewer business-process changes.

2.9 Bio-mimesis: Systematic technology transfer from biology to engineering

Biological hard tissues (bone, teeth, spicules, shells, spines, particles) have intricate hierarchical structures and unique combination of physical properties with engineering characteristics (Lowenstam, 1981). These biological materials are composites of minerals and

organic macromolecules, a combination of proteins, polysaccharides, and lipids. Normally, hard tissues are mechanical devices (skeletal units, protective armor, and anchoring devices), but they also have other physical functions, such as magnetic, optical, and piezoelectric (Simkiss & Wilbur, 1989). Mechanical properties of biocomposites are often superior to human-made materials with similar phase compositions (Wainwright et al., 1976). They are often made of simple and common materials, e.g., carbonates, oxides, sulfides). Regardless of their simple material components, biological composites have multifunctional properties. For example for a given material, both strength and toughness could be better than a synthetic material with the same phase composition (e.g., calcium carbonate). Furthermore, biomaterials may not only be superior to man-made materials in terms of mechanical properties, but also in other physical aspects.

The superiority of biological materials as engineering systems over the synthetic ones has a basis in their structural design and control of its formation by the organism. Furthermore, over the lifetime of organisms, these materials are also monitored and self-repaired leading to durability that is much longer than that is possible in synthetic systems.

Nature has an enormous pool of inventions that passed the harsh test of practicality and durability in changing environment. In order to harness the most from Nature's capabilities, it is critical to bridge between the fields of biology and engineering and to see cooperation of experts from both fields. This bridging effort can help in turning Nature's capabilities into engineering capabilities, tools and mechanisms. In order to approach Nature in engineering terms, it is necessary to sort biological capabilities along technological categories. Namely, one can take

biologically identified characteristics and seek an analogy in terms of engineering as shown in table 5. 1.

Biology	Engineering	Bioengineering, biomimetics, bionics and biomechanics
Body	System	System with multifunctional materials and structures are developed emulating the capability of biological systems
Skeleton and bones	Structure and support struts	Support structures are part of even man-made system
Brain	Computer	Advances in computers are being made emulating the operation of the human brain
Intelligence	Artificial intelligence	There are numerous aspects of artificial intelligence that have been inspired by biology including augmented reality, autonomous systems, computational intelligence, expert systems, fuzzy logic, etc.
Senses	Sensors	Computer vision, artificial vision, radar, and other proximity detectors all have direct biological analogies. However, at their best, the capability of the man-made sensors is nowhere near as good as biosensors
Muscle	Actuators	Electroactive polymers are actuators with functional similarity to natural muscles
Electrochemical power generation	Rechargeable batteries	The use of biological materials to produce power will offer mechanical systems enormous advantages

Tab 4.1:
Characteristic similarities of biology and engineering systems.

Biomimetic process can be classified in four level:

- first step, mere mimesis;
- second step, Why does Nature act in this way?
- third step How does Nature reach the goal ?
- Fourth step Apply Nature’s logic to other fields.

Some of Nature’s capabilities can inspire new mechanisms, devices and robots. Examples may include the woodpecker’s ability to impact wood while suppressing the effect from damaging its brain. Another inspiring capability is the ability of numerous creatures to operate with multiple mobility options including flying, digging, swimming, walking, hopping, running, climbing, crawling. Increasingly,

biologically inspired capabilities are becoming practical including collision avoidance using whiskers or sonar, controlled camouflage, and materials with self-healing

2.9.a The Bionic Car

An example of technology transfer from biology to engineering is DaimlerChrysler's prototype *Bionic Car*. In order to create a large volume, small wheel base car, the design for the car was based on the boxfish (*Ostracion meleagris*), a surprisingly aerodynamic fish given its box like shape. The chassis and structure of the car are also biomimetic, having been designed using a computer modelling method based upon how trees are able to grow in a way that minimises stress concentrations. The resulting structure looks almost skeletal, as material is allocated only to the places where it is most needed. (Vincent et al., 2006).



Figure 4.13

DaimlerChrysler bionic car inspired by the box fish and tree growth patterns.

(Pedersen Zari, M. 2007).

The possible implications of architectural design where biological analogues are matched with human identified design problems are that the fundamental approach to solving a given problem and the issue of how buildings relate to each other and the ecosystems they are part of is not examined. The underlying causes of a non-sustainable or even degenerative built environment are not therefore necessarily addressed with such an approach.

The *Bionic Car* is more efficient in terms of fuel use because the body is more aerodynamic due to the mimicking of the box fish. It is also more materials efficient due to the mimicking of tree growth patterns to identify the minimum amount of material need in the structure of the car. The car itself is however not a new approach to transport. Instead, small improvements have been made to existing technology

without a re-examination of the idea of the car itself as an answer to personal transport. (Pedersen Zari, M. 2007)

Designers are able to research potential biomimetic solutions without an in depth scientific understanding or even collaboration with a biologist or ecologist if they are able to observe organisms or ecosystems or are able to access available biological research. With a limited scientific understanding however, translation of such biological knowledge to a human design setting has the potential to remain at a shallow level. It is for example easy to mimic forms and certain mechanical aspects of organisms but difficult to mimic other aspects such as chemical processes without scientific collaboration. (Pedersen Zari, M. 2007)

Despite these disadvantages, such an approach might be a way to begin transitioning the built environment from an unsustainable to efficient to effective paradigm (McDonough, 2002).

2.9.b Thermoregulation process in penguins

Penguins are a specialized group of non-flying, aquatic birds that live in the southern hemisphere, most famously in the Antarctic. The ability of some species to withstand extreme cold whilst fasting for up to 120 days (during egg incubation) has excited much attention. Several studies have investigated the thermal resistance of penguin "coats" (feather and skin assembly).

For insulation the penguin requires a thick, air-filled, windproof coat (similar to an open-cell foam covered with a windproof layer) that eliminates convection and reduces radiative and convective heat losses to a minimum.

Mimicking this logic has been made winter sportswear

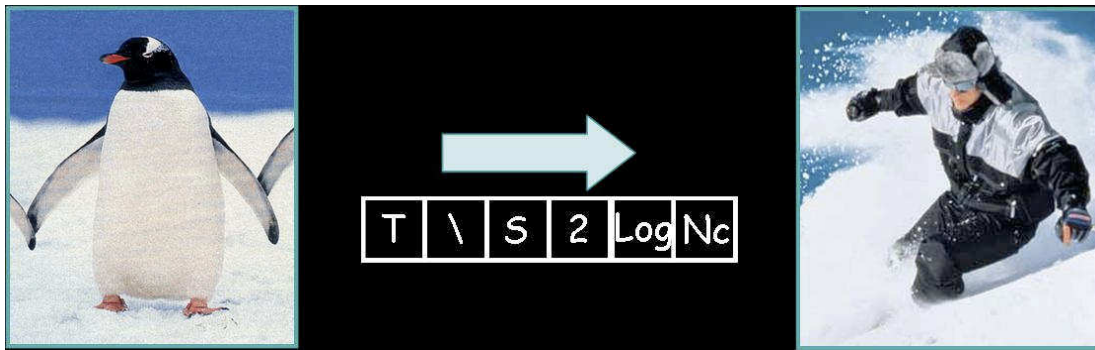


Figure 4.14

Penguins as example of the thermal resistance for realizing winter sportwear

2.9.c Namibian beetle

Species of living organisms have typically been evolving for millions of years. Those organisms that remain on Earth now have the survival mechanisms that have withstood and adapted to constant changes over time. Humans therefore have an extensive pool of examples to draw on to solve problems experienced by society that organisms may have already addressed, usually in energy and materials effective ways. This is helpful for humans, particularly as access to resources changes, the climate changes and more is understood about the consequences of the negative environmental impact that current human activities have on many of the world's ecosystems. (Alberti et al., 2003)

An example is the mimicking of the Namibian desert beetle, *stenocara* (Garrod et al., 2007). The beetle lives in a desert with negligible rainfall. It is able to capture moisture however from the swift moving fog that moves over the desert by tilting its body into the wind. Droplets form on the alternating hydrophilic – hydrophobic rough surface of the beetle's back and wings and roll down into its mouth (Parker and Lawrence, 2001). Matthew Parkes of KSS Architects demonstrates process biomimicry at the organism level inspired by the beetle, with his proposed fog-catcher design for the Hydrological Center for the University of Namibia (Killeen, 2002). Ravilious (2007) and Knight (2001) discuss a more specific material biomimicry at the organism level, where the surface of the beetle has been studied and mimicked to be used for other potential applications such as to clear fog from airport runways and improve dehumidification equipment for example.

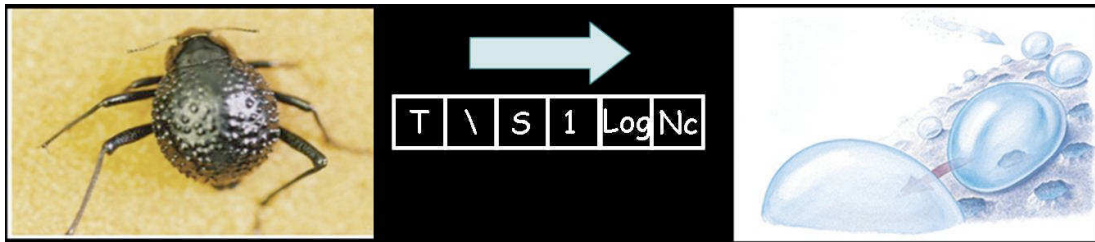


Figure 4.14

the beetle has been mimicked to be used for other potential applications such as clear fog.

Nicholas Grimshaw & Partners' design for the Waterloo International Terminal demonstrates an example of form and process biomimicry at the organism level. The terminal needed to be able to respond to changes in air pressure as trains enter and depart the terminal. The glass panel fixings that make up the structure mimic the flexible scale arrangement of the Pangolin so they are able to move in response to the imposed air pressure forces. (Aldersey-Williams, 2003)

Mimicking an organism alone however without also mimicking how it is able to participate in and contribute to the larger context of the ecosystem it is in, has the potential to produce designs that remain conventional or even below average in terms of environmental impact (Reap et al., 2005). Because mimicking of organisms tends to be of a specific feature, rather than a whole system, the potential also remains that biomimicry becomes technology that is added onto buildings rather than being integral to them, particularly if designers have little biological knowledge and do not collaborate with biologists or ecologists during the early design stages. While this method may result in new and innovative building technologies or materials, methods to increase sustainability are not necessarily explored. (Pedersen Zari, M. 2007).

2.9.d Micro-air vehicles

The wing motion in free flight has been described for insects ranging from 1 to 100 mm in wingspan. To support the body weight, the wings typically produce 2–3 times more lift than can be accounted for by conventional aerodynamics. Some insects use the fling mechanism: the wings are clapped together and then flung open before the

start of the downstroke, creating a lift-enhancing vortex around each wing. Most insects, however, rely on a leading-edge vortex (LEV) created by dynamic stall during flapping; a strong spanwise flow is also generated by the pressure gradients on the flapping wing, causing the LEV to spiral out to the wingtip. Technical applications of the fling are limited by the mechanical damage that accompanies repeated clapping of the wings, but the spiral LEV can be used to augment the lift production of propellers, rotors and micro-air vehicles (MAVs). Design characteristics of insect-based flying machines are presented, along with estimates of the mass supported, the mechanical power requirement and maximum flight speeds over a wide range of sizes and frequencies. To support a given mass, larger machines need less power, but smaller ones operating at higher frequencies will reach faster speeds.

The first appearance of winged insects is shrouded in the past, but they probably took to the air almost 350 million years ago (Wootton, 1981; Ellington, 1991a). Wingspans of the early fossils ranged from 10 to 710 mm, and the form of the wings suggests a variety of adaptations in flight style. The Protodonata, which were the ancestors of dragonflies, were among the early fliers; their wings were similar enough to modern forms to suggest comparable flight capabilities, although perhaps with less refinement. Through natural selection, the insects have been experimenting successfully with wings, kinematics, aerodynamics, control and sensory systems for hundreds of millions of years.

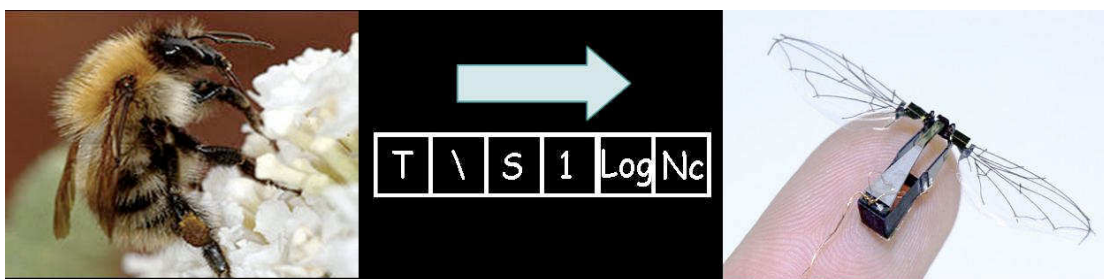


Figure 4.16

MAVs take inspiration from flying insects or birds to achieve unprecedented flight capabilities

Much more recently, interest has developed in small autonomous flying vehicles, largely motivated by the need for aerial reconnaissance robots inside buildings and confined spaces. Industry, commerce and the military have all identified potential

roles for such micro-air vehicles (MAVs). Research on MAVs is primarily conducted by aerodynamic and robotic engineers who are attempting to improve the performance at small sizes of conventional fixed wings and rotary wings. However, there already exists a very successful design for intelligent MAVs with much better aerodynamic performance than conventional wings and rotors: the insects. (Ellington 1999).

2.9.e Spiderman gloves

The gecko's ability to "run up and down a tree in any way", was firstly observed by Aristotle in his *Historia Animalium*, almost 25 centuries ago. A comparable adhesive system is found in spiders and in several insects. In general, when two solid (rough) surfaces are brought into contact with each other, physical/chemical/mechanical attraction occurs. Suction cups operate under the principle of air evacuation, i.e., when they come into contact with a surface, air is forced out of the contact area, creating a pressure difference. The adhesive force generated is simply the pressure difference multiplied by the cup area. Thus, in our (sea level) atmosphere the achievable suction strength is coincident with the atmospheric pressure, i.e. about 0.1MPa. Such an adhesive strength is of the same order of magnitude of those observed in geckos and spiders, even if their adhesive mechanisms are different, mainly due to van der Waals attraction and also capillarity. Thus, although several insects and frogs rely on sticky fluids to adhere to surfaces, gecko and spider adhesion is fully dry.

Hierarchical miniaturized hairs (without adhesive secretions) are characteristic features of both spiders and geckos.

A replication of the characteristics of gecko (Geim et al 2003) or spider feet would enable the development of a self-cleaning, like the lotus leaves, superadhesive and releasable hierarchical material and, with the conjunction of large invisible cables (Pugno 2006b), of a preliminary Spiderman suit

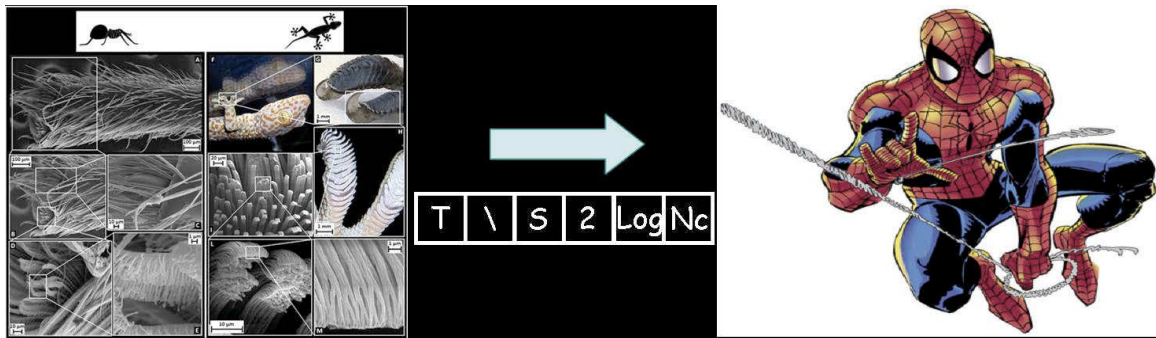


Figure 4.17

A replication of gecko or spider feet characteristics would enable the development of a preliminary Spiderman suit

Theoretical van der Waals gloves could generate an adhesion force comparable to the body weight of ~500 men. Even if such a strength remains practically unrealistic (and undesired, in order to achieve an easy detachment), due to the presence of contact defects, e.g. roughness and dust particles, its huge value suggests the feasibility of Spiderman gloves. The scaling-up procedure, from a spider to a man, is expected to decrease the safety factor (body weight over adhesion force) and adhesion strength, that however could remain sufficient for supporting a man. Scientists are developing new biomimetic materials, e.g. gecko-inspired, capable of supporting ~10 kilograms each on vertical walls. New Adhesive Optimization Laws are derived and applied for increasing the capability of the scaling-up.

CHAPTER V

TOPOLOGICAL OPTIMIZATION IN STRUCTURAL MECHANICS

1. INTRODUCTION

The design process of an object is a coherent set of operations that starts from the structure's conception and ends with its realization. One of the most important steps in designing a structure or a element is the definition of its form. Usually, the traditional approach to this problem is to use geometries that have already been tried or solutions already adopted before; this approach is insufficient in many engineering areas, where, on the contrary, the development of new products or new solutions in researching the best structural morphology in relation to design requirements, are very important. A rational approach to this type of problem is known as "*optimization*".

In a simple way, the word "*optimization*" can be defined as the rational procedure that allows reaching the best solution among all admissible ones, according with the required targets and with the physical and geometric constraints and limitations. It is easy to imagine that this concept is not just about the structural field, but it concerns a multitude of fields including bioengineering, fluid mechanics, electromagnetism, optics, natural sciences, economics and many others. The optimization provides engineers a means to determine optimal designs in terms of admissible structural responses (deformation, stress, etc.), through mathematical algorithms. Due to this multidisciplinary approach, most of the results today are obtained by experts from different fields working together. The preliminary operation is to define the geometry of the object, element or structure to be built and it is the most important moment as it can influence all following design choices.

Since the ‘50s, the evolution of the optimization has produced four main classes of distinct problems: sizing optimization, shape optimization, material optimization and topology optimization; the last one is the subject of this thesis work.

Actually, these four classes of problems have developed at different times. At the beginning, the optimization was the search for the “best” sectional properties, after having fixed topology and structural configuration. Later on, in 1950-60, thanks to the development of the Finite Element Method (FEM), shape optimization was introduced; then, in 1980, the topology optimization was developed. Now, the four techniques above mentioned will be briefly described (Cinquini C., Rovati M., 1995).

In the sizing optimization, geometry, material properties and loads are assigned; the designer task is to select the size of the section of all the various parts of the structure. So, the goal is to determine the optimal distribution of the area and the thickness of the structure we want to study.

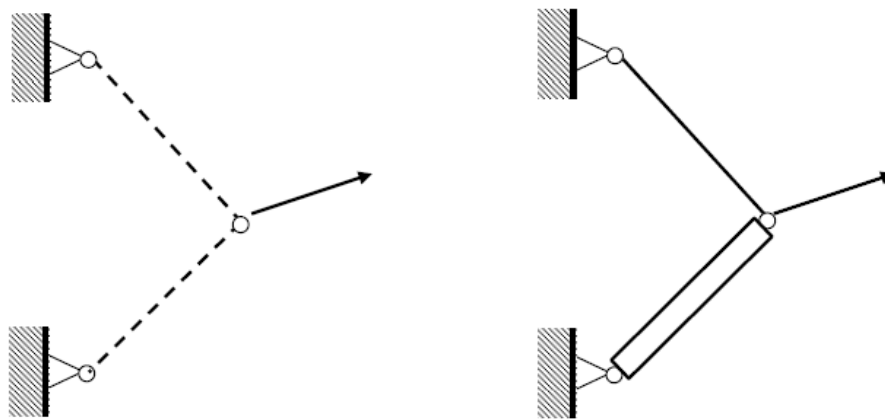


Figure 5.1 “sizing optimization”

In this case (Fig 5.1), the configuration and topology of the structure are defined beforehand and the optimization process is restricted to research the optimal size of the cross sections of the rods.

In the shape optimization the structural topology is established, i.e. the connection level of project domain; optimization becomes the search for “optimal” form, such as inner holes in general or the border of project domain.

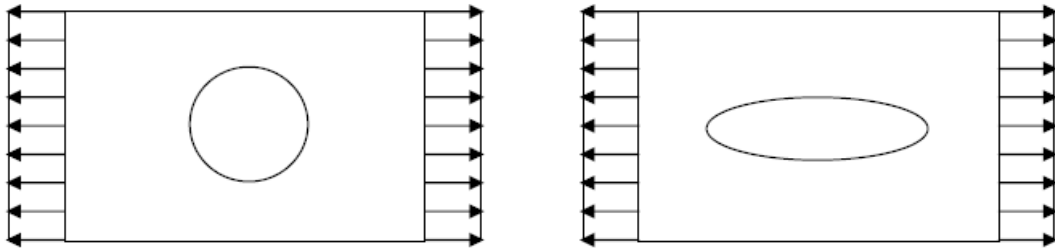


Figure 5.2
“shape optimization”

Material optimization can be considered as part of a class of problems, but it can be related to topology optimization.

In the case of topology optimization, the connection degree of domain is not fixed beforehand: we only know the form, the constraints and the loads. Therefore, the aim is to determine the distribution of material (or material properties), that minimizes or maximizes the objective function given for an assigned loads condition and observing appropriate constraints. The topology optimization is the latest in order of development, and compared to other optimization procedures, it offers several advantages; the most important one consists in the ability to design the domain’s level of connection without the need to determine a specific topology in advance, as it occurs in the case of shape optimization. Moreover, a great operational advantage lies in not modifying the discretization of the domain at every step of an iterative process; in this way we have the resolution of the problem (for example through the finite element method). Furthermore, topology optimization can act on several structural levels, allowing the definition of optimal shape at both microstructural (definition of material characteristics) and macrostructural (definition of the structural morphology) (Michell A. J., 1904) levels.

Now we have identified the contents of general references, and in the following chapters we will discuss the general aspects of topology optimization, and we will describe different techniques proposed in literature.

1.1 Topology Optimization: Etymology and History

Topology optimization is the search for optimal distribution in the project domain of one or more structural parameters such as density, mechanical properties such as rigidity, microstructural parameters, thickness, and other geometrical and mechanical parameters; for its versatility and potential, this design procedure represents the link between size and shape optimization (Eschenauer H.A. e Olhoff N., 2001)

The word “topology” comes from the Greek word “topos” and it means location, space or domain. In mathematical terms, the topology is linked to objects that are deformable in a manner called “rubber-like” (i.e. as a gum). “Topological transformations” and “topological mapping” indicate the topological transformations of a domain in another one that does not destroy or create close links. Two topological domains are called topologically equivalent if there is a topological mapping of one of the other two domains (*Fig5 .3*)

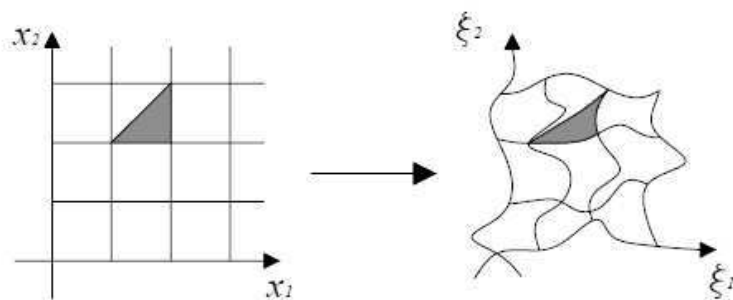


Figure 5.3

“topological transformations (or topological mapping)”

In addition, a topological property is the invariance of all topological mappings. In general, transformations can be formulated as a topological transformation of the

continuous, whose inverse transformations are still continuous. Finally, there is the homomorphism property, by which transformations are reversibly and continuous.

The word “optimization” comes from the Greek word “optimus” and it can be defined as the rational procedure that allows reaching the best solution among all admissible ones, according with the required objective and with the physical and geometric constraints and limitations.

Topology optimization is a relatively new and rapidly expanding field of structural mechanics that can result in much greater savings than mere cross-section or shape optimization. Owing to its complexity, it is an intellectually challenging field; its progress, however, has often been hampered by conceptual inconsistencies and terminological confusion. For this reason, a critical and systematic re-examination of the relevant issues seems needed. This section deals mainly with mechanical, structural and computational aspects, whilst investigations of purely mathematical interest are outside its scope.

For very low volume fractions, important principles of topology optimization were established already at the beginning of the century, in the context of trusses, by the versatile Australian inventor Michell (1904) (Rozvany, G.I.N. 2001) these were extended to grillages (beam systems) more or less seventy years later by Rozvany. Drawing on these applications, the basic principles of optimal layout theory were formulated by Prager and Rozvany (Prager, W.; Rozvany, G.I.N. 1977) and generalized considerably by the latter in the eighties and nineties.

Topology optimization for higher volume fractions is now called Generalized Shape Optimization (GSO) or Variable Topology Shape Optimization. It involves the simultaneous optimization of the topology and shape of internal boundaries in porous and composite continua.

In the context of discretized mechanics, this development was prompted by the observation of Cheng and Olhoff (Cheng, K.-T.; Olhoff, N. 1981) that optimized solid plates containing systems of ribs which are similar to optimized grillages. For compliance design of perforated plates (disks) in plane stress, optimal microstructures were studied by various mathematicians. The first exact analytical solutions for optimal perforated plates and the correct expressions for the rigidity

tensor of homogenized optimal microstructures were obtained by Rozvany, Olhoff, Bendsøe et al. (1985/87), and Ong, Rozvany and Szeto (1988).

The birth of practical, FE-based topology optimization for higher volume fractions was brought about by extensive pioneering research of Bendsøe (Bendsøe, M.P. 1989), and his “homogenization” school. This was followed by a parallel exploration of the SIMP approach, suggested originally by Bendsøe (1989) and used extensively by Zhou and the author Rozvany, who also suggested the term “SIMP”.

1.2 Formulation Problem

In the mathematical formulation of optimal design problems, we must consider four fundamental aspects (Cinquini C., Rovati M., 1995) :

I. Object function definition

The object function (or functional) is represented by a measure indicator (to maximize or minimize) of the structure quality, where quality is referred to the satisfaction of an assigned requirement. Among the structural properties most often used to define the objective of the optimization procedure, there are:

- the cost (the cost of materials, manufacturing cost, maintenance cost and usage);
- the mechanical properties (global or local);
- the aesthetic qualities.

If more objectives are considered, not in conflict among them, it generates a problem much more complex, precisely defined as a multi-objective optimization problem.

II. Choice of design variables

The design variables are related to the geometry of the structure. The geometry is usually defined by topological variables representing the numerical and spatial sequence of structural elements and nodes' position, or through mechanical variables

related to structural behavior. The shape of the structure can be considered as design variables.

III. The formulation of equations governing the problem

The equations controlling the problem, such as the equilibrium and consistency equations and the material's constitutive laws, depend on its characteristics.

IV. Definition of the constraints and limitations

From a mathematical point of view, constraints can be classified in equality or inequality and in global or local; from a structural point of view, we can have behavior or geometric constraints. Constraints limit the domain of admissible solutions.

In summary, in optimal problems all the constraints are written as mathematical expressions (equality or inequality) in order to define the set of possible projects, and then to look for the optimal solution through the minimization (or maximization) of the objective function.

In topology optimization of structure, material and mechanisms, parameterization of geometry is often performed by a grey-scale density-like interpolation function (Bendsøe M. P., Sigmund O., 1999). In the next section different approaches to this concept are analyzed and compared, in light of variational bounds on effective properties of materials are analyzed and compared. This allows to derive simple necessary conditions for the possible realization of grey-scale via composites, leading to a physical interpretation of all feasible designs as well as the optimal one. Thus it is shown that, in many circumstances, the so called artificial interpolation model actually falls within the framework of microstructurally based models. In many applications, the optimal topology of a structure should consist solely of a macroscopic variation of material and void, meaning that the density of the structure is given by a "0±1" integer parameterization (often called "black and white" design). Unfortunately, this class of optimal design problems is ill-posed in that, for example, non convergent, minimizing sequences of admissible design with finer and finer geometrical details can be found. Existence of "black and white" solutions can be achieved by confining the solution space to limit the

complexity of the admissible designs, making them dependent on the choice of parameters in the geometrical constraint. For reasonable raster representations of the “0±1” black and white design, the solution of the resulting large scale integer programming problem becomes a major challenge.

Recently, dual methods have been shown to be effective, in the absence of local constraints (Beckers M., 1999). However, the most commonly used approach is to replace the integer variables with continuous variables, and then introduce some form of penalty that steers the solution to discrete “0±1” values.

A key part of these methods is the introduction of an interpolation function that expresses various physical quantities, for example material stiffness, cost, etc., as a function of continuous variables. The continuous variables are often interpreted as material densities, as in the so-called penalized, proportional fictitious material model.

1.3 Basic problem statement

The continuum topology design problems considered are defined on a fixed reference domain Ω in \mathbb{R}^2 or \mathbb{R}^3 . In this domain, one tries the optimal distribution of material, with the term “optimal” being defined through choice of objective and constraint functions, and through choice of design parameterization. The objective and constraint functions involve some kind of physical modelling that provides a measure of efficiency within the framework of a given area of applications, for example structural mechanics.

The basis for our discussion is the minimum compliance problem for a linearly elastic structure in 2-D. Thus one consider a mechanical element as a body occupying a domain Ω^m which is part of a the reference domain Ω , on which applied loads and boundary conditions are defined *Fig 5.4*.

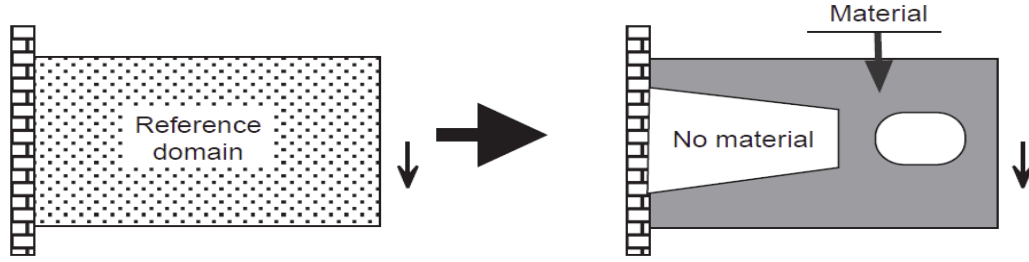


Figure 5.4

“The generalized shape design problem of finding the optimal material distribution”

This reference domain is often referred to as the ground-structure, in analogy with terminology in truss topology design (Bendsøe, M. P., 1995). Referring to the reference domain Ω it can define the optimal topology shape design problem as a minimization of force times displacement, over admissible designs and displacement fields satisfying equilibrium:

$$\min_{u \in U, \theta} \int_{\Omega} p u d\Omega + \int_{\Gamma_r} t u d s$$

Subject to:

$$\int_{\Omega} C_{ijkl}(x) \varepsilon_{ij}(u) \varepsilon_{kl}(v) d\Omega = \int_{\Omega} p v d\Omega + \int_{\Gamma_r} t v d s \quad \forall v \in U,$$

$$C_{ijkl}(x) = \theta(x) C_{ijkl}^0, \tag{5.1}$$

$$\theta(x) = \begin{cases} 1 & \text{if } x \in \Omega^m \\ 0 & \text{if } x \in \Omega/\Omega^m \end{cases}$$

$$Vol(\Omega^m) = \int_{\Omega} \theta(x) d\Omega \leq V$$

$$Geo(\Omega^m) \leq K$$

Here, the equilibrium equation is written in its weak, variational form, with U denoting the space of kinematically admissible displacement fields, u the equilibrium displacement, p the body forces, t boundary tractions and $\varepsilon(u)$ linearized strains.

Moreover, $Geo(\Omega^m)$ denotes a constraint function limiting the geometric complexity of the domain Ω^m , imposed here to obtain a well-posed problem.

In problem (1.1), C_{ijkl}^0 denotes the stiffness tensor of a given elastic material from which the structure is to be manufactured, with a total amount of material V ; $\theta(x)$ denotes the pointwise volume fraction of this material, and for a “black and white” design this can only attain the values 0 or 1.

Problem (6.1) is a discrete optimization problem, and for many applications it is useful to consider reformulations in terms of continuous variables, with the goal of using derivative based mathematical programming algorithms. This means that one changes the model for material properties, i.e., the relations defined in (5.1) as

$$C_{ijkl} = \theta C_{ijkl}^0 = \begin{cases} 0 & C_{ijkl}^0 \\ \text{oppure} & 0 \end{cases} \quad (5.2)$$

to a situation where the volume fraction is allowed any value between zero and one. It may also involve finding an appropriate method for limiting geometric complexity, for example, exchanging the total variation of a density for the perimeter of a domain.

1.4 Isotropic models for solid-void interpolation in elasticity

In the subsequent sections one we will concentrate solely on the interpolation models for the material properties, and will not address in further detail other aspects of the modelling and solution procedures connected with various choices of objective and constraint functions, physical modelling, discretization schemes, and optimization algorithms (Bendsøe M. P., Sigmund O., 1999)

1.4.1 The SIMP model

In order to set the scene for recent discussions of the various popular interpolation schemes, the first step is to start by studying the so-called penalized,

proportional “fictitious material” model, also names as the *solid isotropic material with penalization model* (SIMP). Here, a continuous variable ρ , $0 \leq \rho \leq 1$ is introduced, resembling a density of material by the fact that the volume of the structure is evaluated as

$$Vol = \int_{\Omega} \rho(x) d\Omega \quad (5.3)$$

In computations, a small lower bound, $0 < \rho_{min} \leq \rho$, is usually imposed, in order to avoid a singular FEM problem, when solving for equilibrium in the full domain Ω .

The relation between this density and the material tensor $C_{ijkl}(x)$ in the equilibrium analysis is written as

$$C_{ijkl}(\rho) = \rho^p C_{ijkl}^0 \quad (5.4)$$

where the given material is isotropic, so C_{ijkl}^0 is characterized by just two variables, here chosen as the Young's modulus E^0 and the Poisson ratio ν^0 . The interpolation (1.4) satisfies that

$$C_{ijkl}(0) = 0, \quad C_{ijkl}(1) = C_{ijkl}^0 \quad (5.5)$$

This means that if a final design has density 0 or 1 in all points, this design is a black and white design for which the performance has been evaluated with a correct physical model. For problems where the volume constraint is active, experience shows that optimization does actually result in such designs if one chooses p sufficiently big (in order to obtain true “0±1” designs, $p \geq 3$ is usually required). The reason is that, for such a choice, intermediate densities are penalized; volume is proportional to ρ , but stiffness is less than proportional.

1.4.2 Microstructures realizing the SIMP-model

For the SIMP interpolation (5.4) it is not immediately apparent that areas of grey can be interpreted in physical terms. However, it turns out that, under fairly simple conditions on p , any stiffness used in the SIMP model can be realized as the stiffness of a composite made of void and an amount of the base material

corresponding to the relevant density. Thus using the term density for the interpolation function ρ is quite natural.

The stiffness tensor $C_{ijkl}(\rho)$ of the SIMP model is isotropic, with a Young's modulus varying with ρ and a constant Poisson ratio, independent of ρ . If this tensor is to correspond to a composite material constructed from void and the given material at a real density ρ , the bulk modulus κ and the shear modulus μ of the tensor $C_{ijkl}(\rho)$ should satisfy the Hashin-Shtrikman bounds for two-phase materials (Torquato, S.; Gibiansky, L. V.; Silva, M. J.; Gibson, L. J., 1998), written here for plane elasticity and for the limit of one phase being void

$$0 \leq K \leq \frac{\rho K^0 \mu^0}{(1-\rho)K^0 + \mu^0}, \quad 0 \leq \mu \leq \frac{\rho K^0 \mu^0}{(1-\rho)(K^0 + 2\mu^0) + K^0} \quad (\text{in 2D}) \quad (5.6)$$

Here κ^0 and μ^0 are the bulk and shear moduli, respectively, of the base material. This implies that the Young modulus should satisfy

$$0 \leq E \leq E^* = \frac{\rho E^0}{3-2\rho} \quad (5.7)$$

From (5.7), the SIMP model should satisfy

$$\rho^p E^0 \leq \frac{\rho E^0}{3-2\rho} \quad \text{per } 0 \leq \rho \leq 1 \quad (5.8)$$

which is true if and only if $p \geq 3$. However, the SIMP model presumes that the Poisson's ratio is independent of the density, and this leads to a stronger condition. From the relationship

$$\kappa^0 = \frac{E^0}{2(1-\nu^0)}, \quad \mu = \frac{E^0}{2(1+\nu^0)} \quad (\text{in 2-D}) \quad (5.9)$$

the condition (1.6) for the SIMP model can be written for all $0 \leq \rho \leq 1$ as

$$\begin{aligned} 0 \leq \frac{\rho^0 E^0}{2(1-\nu^0)} &\leq \frac{\rho E^0}{4-2(1+\nu^0)\rho}, \\ 0 \leq \frac{\rho^0 E^0}{2(1+\nu^0)} &\leq \frac{\rho E^0}{2(1-\rho)(3-\nu^0) + 2(1+\nu^0)} \end{aligned} \quad (5.10)$$

After some algebra, this leads to a condition on the power p in the form

$$p \geq p^*(v^0) = \max \left\{ \frac{2}{1-v^0}, \frac{4}{1+v^0} \right\} \quad (\text{in 2-D}) \quad (5.11)$$

which in itself implies $p \geq 3$. The inequality $p \geq 2/(1-v^0)$ comes from the bulk modulus

bound, while the inequality $p \geq 4/(1+v^0)$ is due to the shear modulus bound.

Example values of p^* are

$$p^* \left(v^0 = \frac{1}{3} \right) = 3; \quad p^* \left(v^0 = \frac{1}{2} \right) = 4; \quad (5.12)$$

$$p^* \left(v^0 = -1 \right) = \infty \quad (\text{in 2-D})$$

and $p^* = 3$ holds only for $v^0 = 1/3$.

It is important to note that the condition (5.11) implies that the SIMP model can be made to satisfy the Hashin-Shtrikman bounds, so that it makes sense to look for composites which realize the stiffness tensor for the model. The form of this composite can be computed through a design process, where the desired material properties of a periodic medium are obtained by an inverse homogenization process (Sigmund O.,1994). The geometry of the composite may depend on the density, and one can normally not expect to obtain the wanted properties by analytical methods.

It is still an open problem if all material parameters satisfying the bounds also can be realized as composites of the given materials. For two materials, one infinitely stiff, one infinitely soft, it is shown in that composites can be build for any positive definite material tensor. However, in topology design the stiffness is restricted and the density specified.

In order to illustrate the realization of the SIMP model we use an example with a base material with $v^0 = 1/3$. For this case the requirement on the power p is $p \geq 3$, and the bulk and shear bounds as well as the Young's modulus bound (5.8) all give rise to this condition. As the Young's modulus bound (5.8) is achieved by a composite for which both the maximum bulk and shear modulus is attained, and as this material will also have Poisson ratio $\nu = 1/3$, independent of density, we can

compare the bounds and the SIMP model in one diagram which shows the values of Young's modulus as a function of density, Fig 6.5 and Fig 6.6.

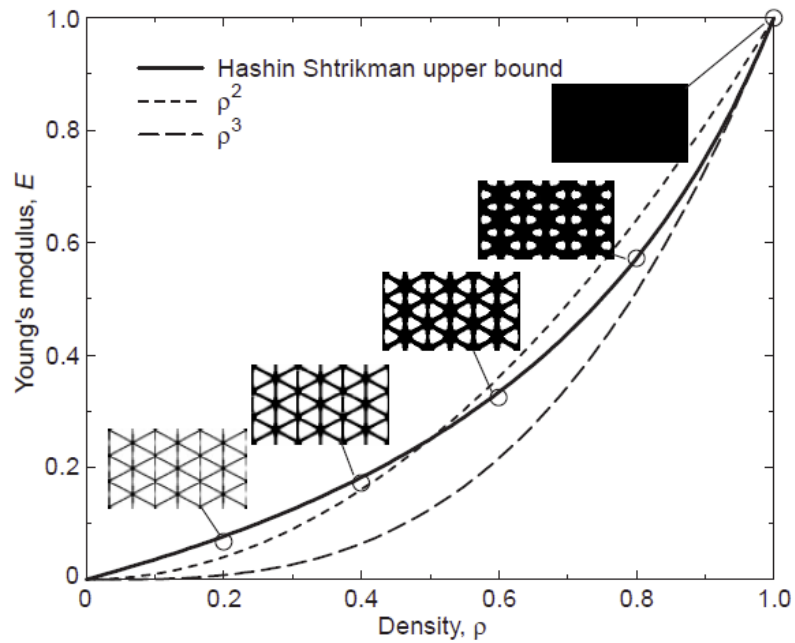


Figure 5.5

“A comparison of the SIMP model and the Hashin-Shtrikman upper bound for an isotropic material with Poisson ratio 1/3 mixed with void. For the H-S upper bound, microstructures with properties almost attaining the bounds are also shown”

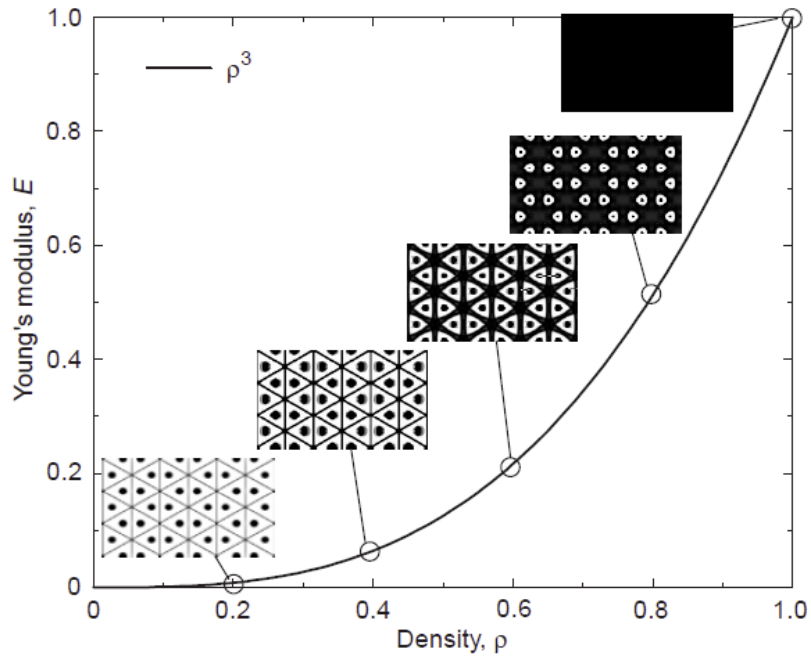


Figure 5.6

“Microstructures of material and void realizing the material properties of the SIMP model with $p = 3$ Eq. (1.11), for a base material with Poisson's ratio $\nu = 1/3$. As stiffer material microstructures can be constructed from the given densities, non-structural areas are seen at the cell centers”

In these figures we also show the geometry of the base cell of a periodic medium that realize the relevant corresponding Young's moduli and $\nu = 1/3$. These geometries are obtained through the methodology of inverse homogenization (material design) described in. An illustration of typical microstructures which realize the SIMP model with $p = 4$ and for Poisson's ratio $\nu = 0$ and $\nu = 1/2$ are shown in Fig 5.7.

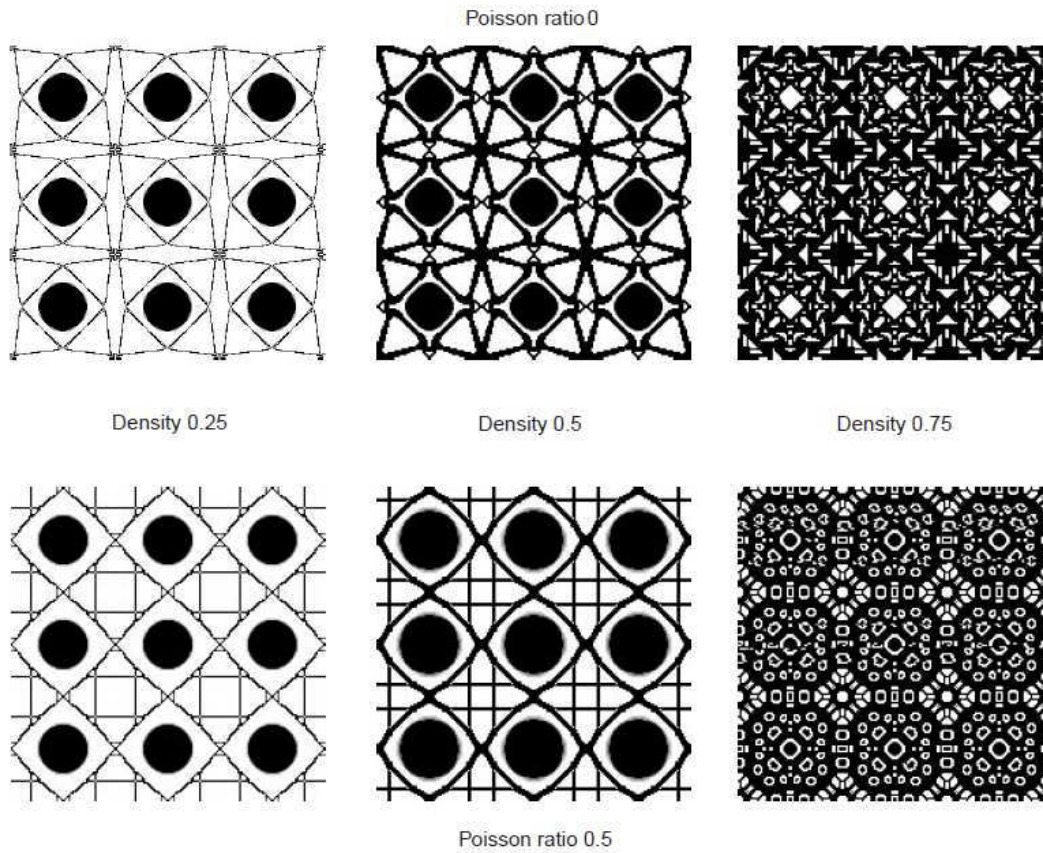


Figure 5.7

“Microstructures of material and void realizing the material properties of the SIMP model with $p = 4$, Eq. (1.11), for a base material with Poisson’s ratio $\nu = 0$ and $\nu = 0.5$, respectively. As in Fig 1.6, non structural areas are seen at the centers of the cells”

The discussion above holds for planar problems. In 3-D, there is, in a sense, more geometric freedom to construct microstructures, and here the Hashin-Shtrikman bounds lead to the condition

$$p \geq \max \left\{ 15 \frac{1-\nu^0}{7-5\nu^0}, \frac{3}{2} \frac{1-\nu^0}{1-2\nu^0} \right\} \quad (\text{in 3D}) \quad (5.13)$$

on the power p in the SIMP model. This condition can be derived as outlined above, but as the algebra is rather lengthy this is omitted here. Example bounds are here

$$\begin{aligned}
 p \geq 3 \quad \text{per } v^0 = \frac{1}{3}; \quad p \geq 2 \quad \text{per } v^0 = \frac{1}{5}; \quad p \geq \frac{15}{7} \quad \text{per } v^0 = 0; \\
 p \geq \frac{5}{2} \quad \text{per } v^0 \rightarrow -1; \quad p \rightarrow \infty \quad \text{per } v^0 \rightarrow \frac{1}{2} \quad (\text{in 3-D})
 \end{aligned} \tag{5.14}$$

so some lower values of p are possible in dimension three. Note, however, that for $v = 1/3$ we have the same bounds in 2-D and in 3-D.

1.4.3 Variable thickness sheets - the Voigt bound

Design of variable thickness sheets allows for a physical given linear interpolation of stiffness through the thickness variable of the sheet

$$C_{ijkl} = hC^0_{ijkl}, \quad 0 \leq h(x) \leq 1, \quad x \in \Omega \subset R^2, \quad Vol = \int_{\Omega} h(x) d\Omega \tag{5.15}$$

Here, the maximal thickness is set equal to 1, in order to maintain the setting of an interpolation scheme. This problem was first studied as a basis for computational topology design (Rossow M. P., Taylor J. E., 1973). Mathematically, the linear dependence of stiffness and volume on the thickness h leads to the existence of solutions for the compliance problem also in the case where geometric constraints are not imposed. Optimal designs within this framework of variable thickness sheets customarily possess large areas of intermediate thickness, but topology may also be identified from areas with $h = 0$. The discrete computational form of the variable thickness problem is analogous to what is seen in optimal truss topology design, and very efficient algorithms can be devised.

The variable thickness sheet problem is in essence a problem in “dimension $2^{1/2}$ ”. For purely planar and purely three dimensional problems, an interpolation of the form

$$C_{ijkl} = \rho C^0_{ijkl}, \quad 0 \leq \rho(x) \leq 1, \quad Vol = \int_{\Omega} \rho(x) d\Omega \tag{5.16}$$

where ρ is a density of material, corresponds to using the Voigt upper bound on stiffness, which cannot be realized by composites of material and void. The use of the Voigt upper-bound interpolation for general topology optimization is nevertheless fairly popular, especially in the so-called evolutionary design methods (Xie Y. M., Steven G. P., 1997) Also note that striving for “black and white” designs requires some form of penalization of “grey”, and such measures necessitates the reintroduction of geometric constraints in order to obtain a well-posed problem.

It is worth noting that the variable-thickness sheet problem plays an important role as an equivalent subproblem in the design labelled “free-material optimization”. Here, the design problem is defined over all possible material tensors, with a generalized, linear cost expressed in terms of tensor invariants.

1.4.4 The Hashin-Shtrikman bound

In light of the importance of the Hashin-Shtrikman bounds for the realization of intermediate densities and noting that the bounds have a similar penalization of intermediate density as does the SIMP model, it is rather surprising that these bounds have so far not been used as interpolation functions for topology design. Using these bounds one will have an interpolation of Young's modulus and of Poisson's ratio in the form

$$\begin{aligned} E(\rho) &= \frac{\rho E^0}{3-2\rho} \\ \nu(\rho) &= \frac{1-\rho(1-\nu^0)}{3-2\rho} \end{aligned} \tag{5.17}$$

where not only Young's modulus, but also Poisson's ratio, depends on density. Observe that independent of the Poisson ratio of the base material, the low volume fraction limit has a Poisson ratio equal to 1/3. The interpolation (5.17) corresponds to the material parameters of a composite that achieves simultaneously the Hashin-Shtrikman upper bounds on bulk and shear moduli, and such a material can be realized by, for example, an isotropic rank-3 lamination.

1.4.5 Other models

The Voigt upper-bound model (5.16) has been combined with the Reuss lower bound for mixtures of materials in order to obtain alternative schemes (Swan C. C., Kosaka I., 1997) For a mixture of void and material, the Reuss lower bound is zero, and in this case the interpolation (called the Reuss-Voigt interpolation in the sequel) reads

$$C_{ijkl}(\rho) = \begin{cases} \alpha \rho C_{ijkl}^0 & \text{se } \rho < 1 \\ C_{ijkl}^0 & \text{se } \rho = 1 \end{cases} \quad (5.18)$$

$$Vol = \int_{\Omega} \rho(x) d\Omega$$

Here, α is a parameter which weighs the contribution by the Voigt and Reuss bounds. The interpolation introduces a jump at $\rho = 1$ (a potential problem in computations), but this is not the case when void is exchanged with a material with higher stiffness.

Similarly to the analysis for the SIMP model above, one can check the range of the parameter α for which the Hashin-Shtrikman bounds are satisfied. For 2-D elasticity this leads to the condition

$$\alpha \leq \alpha^*(\nu^0) = \min \left\{ \frac{1-\nu^0}{2}, \frac{1+\nu^0}{4} \right\} \quad (5.19)$$

The largest value of α is thus $1/3$, and this is only possible if $\nu^0 = 1/3$. For comparison, the Young's modulus of the Hashin-Shtrikman bounds, the Reuss-Voigt interpolation and the Voigt bound, as a function of density, is illustrated in *Fig 6.8*; for consistence $\nu^0 = 1/3$ choose, as this results in a constant Poisson ratio of $\nu = 1/3$ for all three cases.

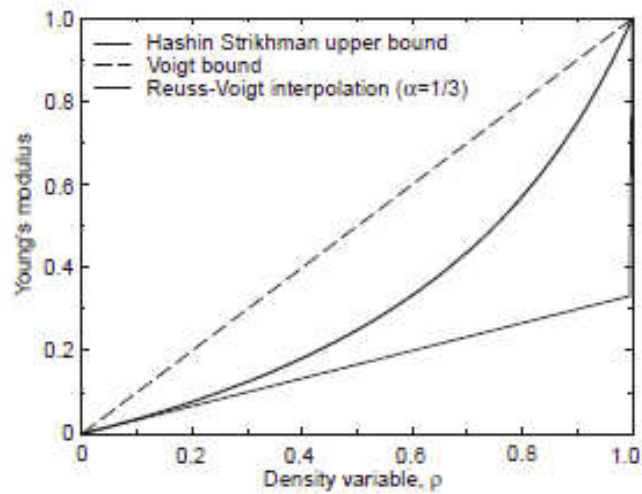


Figure 5.8

“A comparison of the Voigt upper bound, the Hashin-Strikhman upper bound and the Reuss-Voigt interpolation for a mixture of material and void (Poisson's ratio $\nu = 1/3$)”

1.4.6 Example designs

The interpolation schemes described above are, in essence, computational approximations to the “black and white” 0-1 problem. As the problems are different in form, the results obtained with the various methods are, as expected, not the same. Conceptually, there are strong similarities, but the differences in detail can be quite significant. This is not a major problem when employing the techniques in a design context, as long as these differences are understood and acknowledged.

In implementations of topology design schemes based on density interpolation it is often seen that a too severe penalization of intermediate density can lead to designs which are local minima, and which are very sensitive to the choice of the initial design for the iterative optimization procedure. Thus, a continuation method is often advisable, which, for example, for the SIMP method means that the power p is slowly raised through the computations, until the final design is arrived at for a power satisfying (5.11) or (5.13). This procedure is thus a compromise, since initial designs will be analyzed using an interpolation which is not realizable as a composite structure.

Fig 6.9 shows exemplary optimal designs for a simple, planar, minimum-compliance design problem using the Voigt upper-bound interpolation, the Hashin-Shtrikman upper-bound interpolation and SIMP for various powers of p . For the latter cases, the power is maintained fixed in the iterative optimization scheme, except in one situation. Note that the Voigt upper-bound interpolation does not satisfy our goal of finding a “black and white” design. The computations for all cases were here carried out with a filter technique for maintaining a limited geometric resolution, and in order to avoid checkerboard-like areas in the solution.

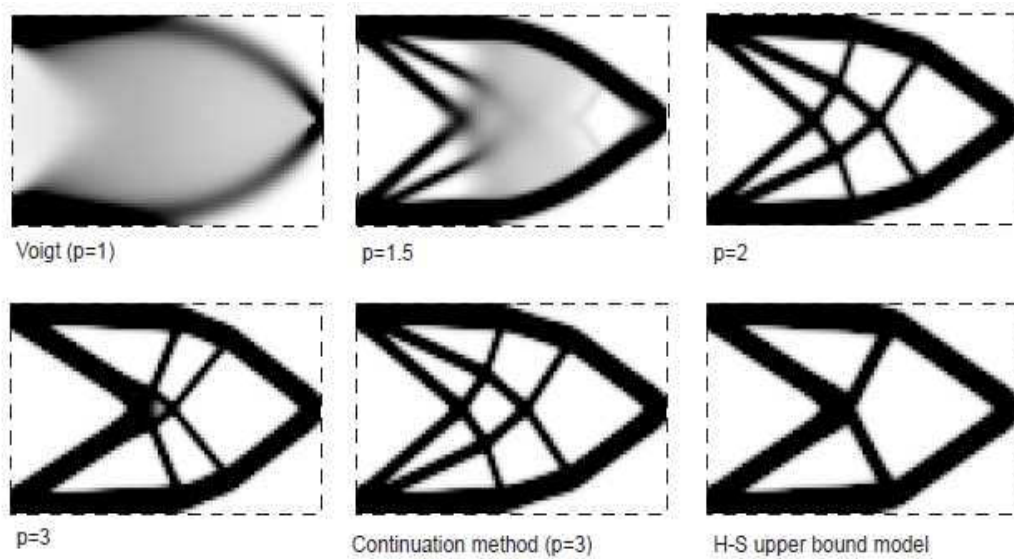


Figure 5.9

“Optimal design results for material and void, using various powers p in the SIMP interpolation scheme, and using the Hashin-Shtrikman upper bound. Problem definition as in Fig 5.4”

1.5 Homogenization models with anisotropy

The initial work on numerical methods for topology design of continuum structures used composite materials as the basis for describing varying material properties in space. This approach was strongly inspired by theoretical studies on generalized shape design in conduction and torsion problems, and by numerical and theoretical work related to plate design (Goodman J., Kohn R. V., Reyna L., 1986). Initially, composites consisting of square or rectangular holes in periodically

repeated square cells were used for planar problems. Later so-called ranked laminates (layers) have become popular, both because analytical expressions of their effective properties can be given and because investigations proved the optimality of such composites, in the sense of bounds on effective properties. Also, with layered materials existence of solutions to the minimum compliance problem for both single and multiple load cases is obtained, without any need for additional constraints on the design space e.g. without constraints on the geometric complexity. For all the models mentioned here, homogenization techniques for computing effective moduli of materials play a central role. Hence the use of the phrase “the homogenization method” for topology design for procedures involving this type of modelling.

The homogenization method for topology design involves working with orthotropic or anisotropic materials. This adds to the requirements of the finite element analysis code, but the main additional complication are the extra design variables required to describe the structure. Thus, a microstructure with rectangular holes in square cells requires three distributed variables, as the material properties at each point of the structure will depend on two size-variables characterizing the hole and one variable characterizing the angle of rotation of the material axes (the axes of the cell).

In topology design based on homogenization of periodic media, one always works with microstructures of a given type, so the realization of the interpolation is not an issue. However, a key question also in this case is a comparison of the stiffness parameters of the microstructure at hand with bounds on such parameters. For anisotropic materials, such bounds are expressed in terms of strain or complementary energies.

For planar problems, any composite, constructed from void and an isotropic, linearly elastic material with Young's modulus E^0 and Poisson ratio ν^0 , has an elasticity tensor C which satisfies the lower complementary energy bound

$$\frac{1}{2} [C^{-1}]_{ijkl} \sigma_{ij} \sigma_{kl} \geq \left\{ \begin{array}{ll} \frac{1}{2E^0 \rho} [\sigma^2_I + \sigma^2_{II} - 2(1 - \rho + \rho \nu^0) \sigma_I \sigma_{II}] & \text{se } \sigma_I \sigma_{II} \leq 0 \\ \frac{1}{2E^0 \rho} [\sigma^2_I + \sigma^2_{II} + 2(1 - \rho - \rho \nu^0) \sigma_I \sigma_{II}] & \text{se } \sigma_I \sigma_{II} \geq 0 \end{array} \right\} \quad (5.20)$$

for any stress tensor σ with principal stresses σ_I, σ_{II} . The inequalities (5.20) express an upper bound on the stiffness of the composite. This bound can also be expressed in terms of strain energy

$$\frac{1}{2} C_{ijkl} \varepsilon_{ij} \varepsilon_{kl} \leq \left\{ \begin{array}{l} \frac{E \left[\varepsilon^2_I + \varepsilon^2_{II} + 2(1-\rho + \rho\nu) \varepsilon_I \varepsilon_{II} \right]}{2(1-\nu)(2-\rho + \nu\rho)} \quad \text{se } \frac{\varepsilon_I + \varepsilon_{II}}{(1-\nu) \varepsilon_I} < \rho \\ \frac{E \left[\varepsilon^2_I + \varepsilon^2_{II} - 2(1-\rho - \rho\nu) \varepsilon_I \varepsilon_{II} \right]}{2(1+\nu)(2-\rho - \nu\rho)} \quad \text{se } \frac{\varepsilon_I - \varepsilon_{II}}{(1+\nu) \varepsilon_I} < \rho \\ \frac{\rho E \varepsilon^2_I}{2} \quad \text{altrimenti} \end{array} \right\} \quad (5.21)$$

This holds for any strain tensor e with principal strains $\varepsilon_I, \varepsilon_{II}$ ordered such that $|\varepsilon_I| \leq |\varepsilon_{II}|$. As void is allowed, the lower bound on stiffness is zero.

The bounds (5.20) and (5.21) can be attained by so-called rank-2 laminates, consisting of a layering at two length scales and with the layers (and axes of orthotropy) directed along the principal strain or principal stress axes (they coalesce). For stresses with $\sigma_I \sigma_{II} \geq 0$, single-scale, single inclusion microstructures (named after Vidgergauz) which attain the bounds. In a recent study it is shown that for $\sigma_I \sigma_{II} \leq 0$ no single-scale periodic composite obtain the bounds, and any composite obtaining the bound (in 2-D) must be degenerate (i.e. has a singular stiffness tensor). For illustration, Fig 6.10 shows a range of single inclusion Vigdergauz-like microstructures for a range of positive as well as negative values of σ_{II}/σ_I ; these structures have been computed by the inverse homogenization methodology.

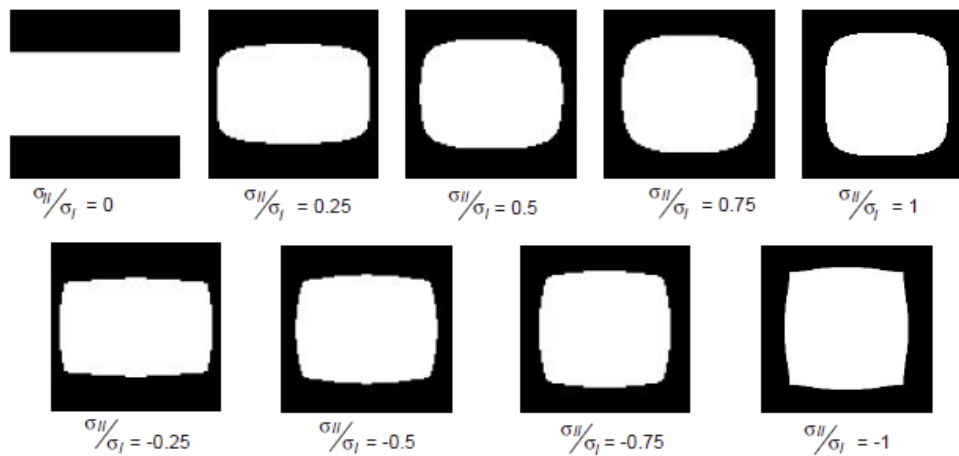


Figure 5.10

“The shape of single inclusions of void in a cell of a homogenized, periodic medium minimizing complementary energy (Vigdergauz-like structures for $\nu = 1/3$ and a density $\rho = 0.5$). Results for a range of principal stress ratios of a macroscopic stress field”

For their use in optimal topology design it is useful to compare energies attainable by other microstructures and interpolation schemes with the bound (5.20). Fig 6.11 thus shows a comparison of the optimal bound for $\rho = 0.5$, achievable by the ranked layered materials, with the range of minimal complementary energies which can be obtained by the SIMP interpolation, by microstructures with square holes, by microstructures with rectangular holes, and by the Vigdergauz microstructures. What is noticeable, is how close the various energies are for stress fields close to pure dilation, while shearing stress fields demonstrate a considerable difference. In the latter case, the microstructural based models are considerably stiffer than the SIMP model, an effect which can to a large extent be attributed to the possibility of rotation for the orthotropic microstructures. Moreover, the microstructure with square holes is notably less stiff for uniaxial stresses compared to the other microstructures, since the imposed symmetry of this microstructure here hinders an efficient use of material.

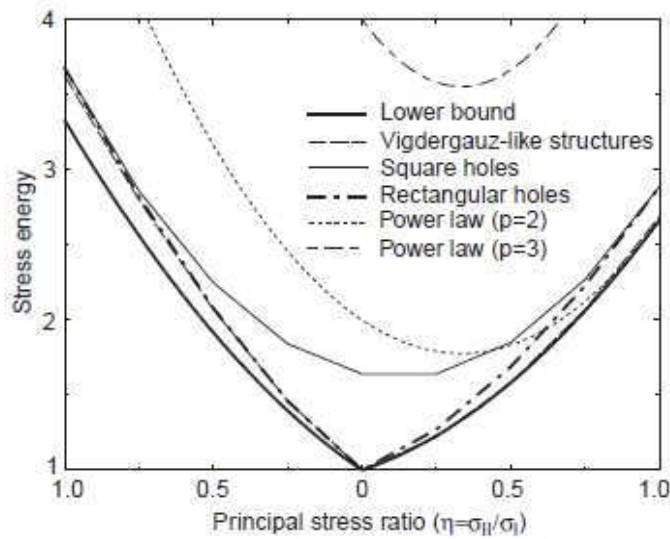


Figure 5.11

“Comparison of the optimal (minimal) complementary energy as a function of the ratio of the principal stresses, for a density $\rho = 0.5$, and for various types of microstructures and interpolation schemes (material and void mixtures). The Vidergauz-like structures are shown in Fig 5.10 “

The plots of the complementary energy explain many features of computational experience with various interpolation schemes. For compliance optimization, the complementary energy should be minimized. As ranked laminates are efficient also at intermediate densities, optimal design with this material model leads to designs with typically rather large areas of intermediate density. This is also the case when using the microstructures with rectangular holes and the Vigdergauz microstructures. Thus if such materials are used for obtaining “black and white” designs, some other form of penalization of intermediate density has to be introduced. One possibility is adding a term to the objective function (with K large).

$$K \int_{\Omega} \rho(x)(1-\rho(x)) d\Omega \quad (5.22)$$

On the other hand, the SIMP model and the microstructure with square holes usually lead to designs with very little “grey”, as intermediate values of density tend to give poor performance in comparison with cost.

1.6 Multiple materials in elasticity

1.6.1 Two materials with non-vanishing stiffness

For a topology design problem, where the aim is to seek the optimal distribution of two isotropic, linearly elastic materials with non-vanishing stiffness, the stiffness tensor of the problem (1.1) takes the form

$$C_{ijkl} = \theta C^1_{ijkl} + (1 - \theta) C^2_{ijkl} = \begin{cases} 0 & C^1_{ijkl} \\ \text{oppure} & C^2_{ijkl} \end{cases} \quad (5.23)$$

where the two materials are characterized by the stiffness tensors C^1_{ijkl} , C^2_{ijkl} . Here the material 1 is the stiffer, i.e., $C^1_{ijkl} \varepsilon_{ij} \varepsilon_{kl} \geq C^2_{ijkl} \varepsilon_{ij} \varepsilon_{kl}$ for any strain ε . Note that the volume constraint now signifies the amount of material 1 which can be used, as the total amount of material amounts to the total volume of the domain Ω .

The two-material problem has been the focal point of theoretical works on generalized shape design problems, as the possible singularity of stiffness is not an issue. Computational studies are scarcer, with early numerical work concentrating on conduction problems, but this variant of the topology design problem has gained recent interest, mainly as a method for generating microstructures with interesting (and extreme) behaviour.

An analysis of various interpolation schemes can follow exactly the same lines as above, as the bounds on effective properties used there are actually just special cases of the general results for mixtures of any two materials. The “special” case was here treated first, as the material-void problems is the most studied for topology design applications. Moreover, the algebra for this case is more transparent.

For the two-material problem, the SIMP model can be expressed

$$\begin{aligned} C_{ijkl}(\rho) &= \rho^p C^1_{ijkl} + (1 - \rho^p) C^2_{ijkl}, \\ Vol(\text{materiale 1}) &= \int_{\Omega} \rho(x) d\Omega \end{aligned} \quad (5.24)$$

while the Reuss-Voigt interpolation model takes the form

$$C_{ijkl}(\rho) = \alpha \left[\rho C_{ijkl}^1 + (1-\rho) C_{ijkl}^2 \right] + (1-\alpha) \left[\rho (C^1)^{-1} + (1-\rho) (C^2)^{-1} \right]^{-1}_{ijkl},$$

$$Vol(\text{materiale 1}) = \int_{\Omega} \rho(x) d\Omega \quad (5.25)$$

For the two-material problem, the lower Hashin-Shtrikman bound for isotropic composites is non-zero, so here a goal of realization with microstructures means that both lower and upper bounds will impose constraints on the interpolation models. In order to clarify the fundamental effects of these bounds, the discussion here will be limited to the 2-D case, where both base materials as well as the interpolations have Poisson's ratio equal to 1/3. In this case, the Hashin-Shtrikman bounds on the bulk and shear moduli for isotropic composites reduce to one and the same condition, which can be expressed as a condition on the Young's modulus

$$\frac{(2+\rho)E_1 + (1-\rho)E_2}{2(1-\rho)E_1 + (1+2\rho)E_2} E_2 \leq E(\rho) \leq \frac{\rho E_1 + (3-\rho)E_2}{(3-2\rho)E_1 + 2\rho E_2} E_1 \quad (\text{in 2-D}) \quad (5.26)$$

where E_1, E_2 denotes the Young's moduli of the two materials, for which $E_1 \geq E_2$.

The derivative at zero density of the lower bound in (5.25) is positive. Thus, condition (5.25) implies that a SIMP model in the form (5.23) will never satisfy the Hashin-Shtrikman bounds for all densities. However, it is possible to keep the SIMP model fairly close to the behaviour governed by these bounds, see Fig 6.12. Moreover, it can be shown that the Reuss-Voigt interpolation model (with $\nu=1/3$) satisfies the bounds if and only if $\alpha=1/3$. For comparison of the various models it is possible look Fig 5.13.

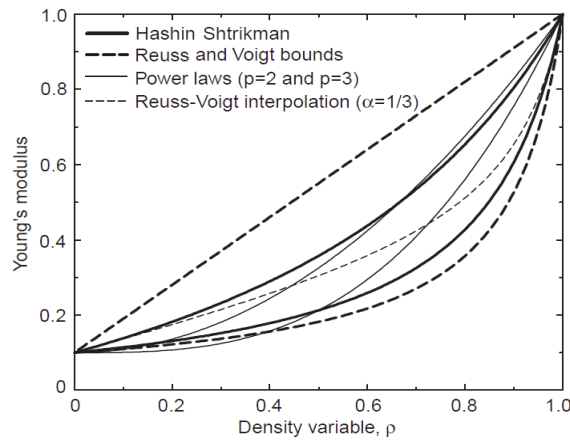


Figure 5.12

A comparison of the Voigt upper and the Reuss lower bound, the Hashin-Shtrikman upper and lower bound, SIMP models, and the Reuss-Voigt interpolation for mixtures of two material with equal Poisson's ratio $\nu=1/3$, and with Young's moduli $E_1=1$ and $E_2=0.1$

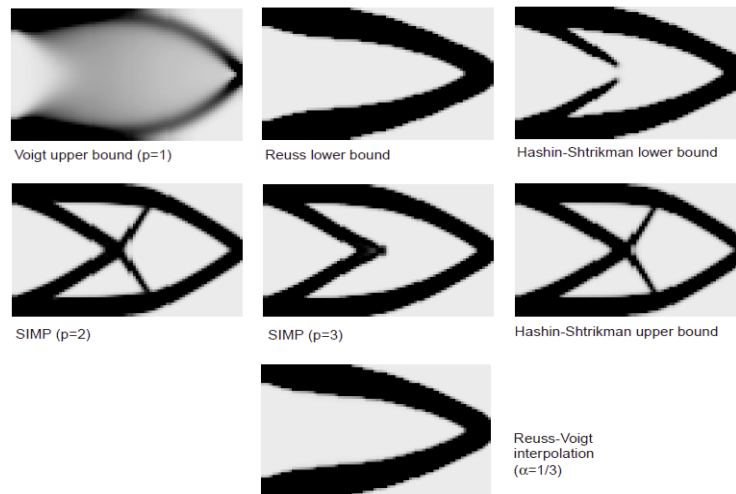


Figure 5.13

Optimal design results for two-materials design (for $E_1=1$, $E_2=0.1$, and $\nu_1=\nu_2=1/3$), using various interpolation schemes. The geometry and loading of the problem as in Fig 5.4, comp. Fig 5.9.

1.6.2 Three-materials design

Topology design involving void and two materials with non-vanishing stiffness has so far been used for design of sandwich-like structures and for design of multi-phase composites with extreme behaviour (Sigmund O., Torquato S., 1997).

In this case isotropic interpolation schemes can be compared to the multiphase Hashin-Shtrikman bounds for isotropic composites. As above, this is done here in the case of Poisson's ratio equal to 1/3 for all phases as well as the interpolation scheme. As one phase is 0, the bounds, expressed in terms of Young's modulus are (with $E_1 \geq E_2$)

$$0 \leq E(\rho_1, \rho_2) \leq \frac{\rho_1 E_1 (\rho_2 E_1 + (3 - \rho_2) E_2)}{(3 - 2\rho_1 \rho_2) E_1 + (6 - 6\rho_1 + 2\rho_1 \rho_2) E_2} \quad \text{if } \rho_1 < 1 \text{ (in 2D)} \quad (5.27)$$

Here ρ_1 , $0 \leq \rho_1 \leq 1$ is the density of the mixture of the two materials with stiffness, and

ρ_2 , $0 \leq \rho_2 \leq 1$ is the density of material 1 in this mixture, such that

$$\begin{aligned} Vol(material1) &= \int_{\Omega} \rho_1(x) \rho_2(x) d\Omega \\ Vol(material2) &= \int_{\Omega} \rho_1(x) (1 - \rho_2(x)) d\Omega \\ TotalVolumeOfMaterial &= \int_{\Omega} \rho_1(x) d\Omega \end{aligned} \quad (5.28)$$

For a SIMP-like interpolation model, it is most convenient to interpolate first between the two nonzero phases and then between this material and void. The resulting model is

$$E = \rho_1^{p_1} \left[\rho_2^{p_2} E_1 + (1 - \rho_2^{p_2}) E_2 \right] \quad (5.29)$$

which for example for $p_1 = p_2 = 3$ is compatible with(5.26) ,i.e., for $\nu_1 = \nu_2 = 1/3$.

Note,

however, that for $\rho_1=1$ the bounds (5.25) should be satisfied, and there is a natural singularity in the conditions when shifting from a solid mixture to a mixture involving void. Designs obtained using (5.28) are shown in Fig 5.14.

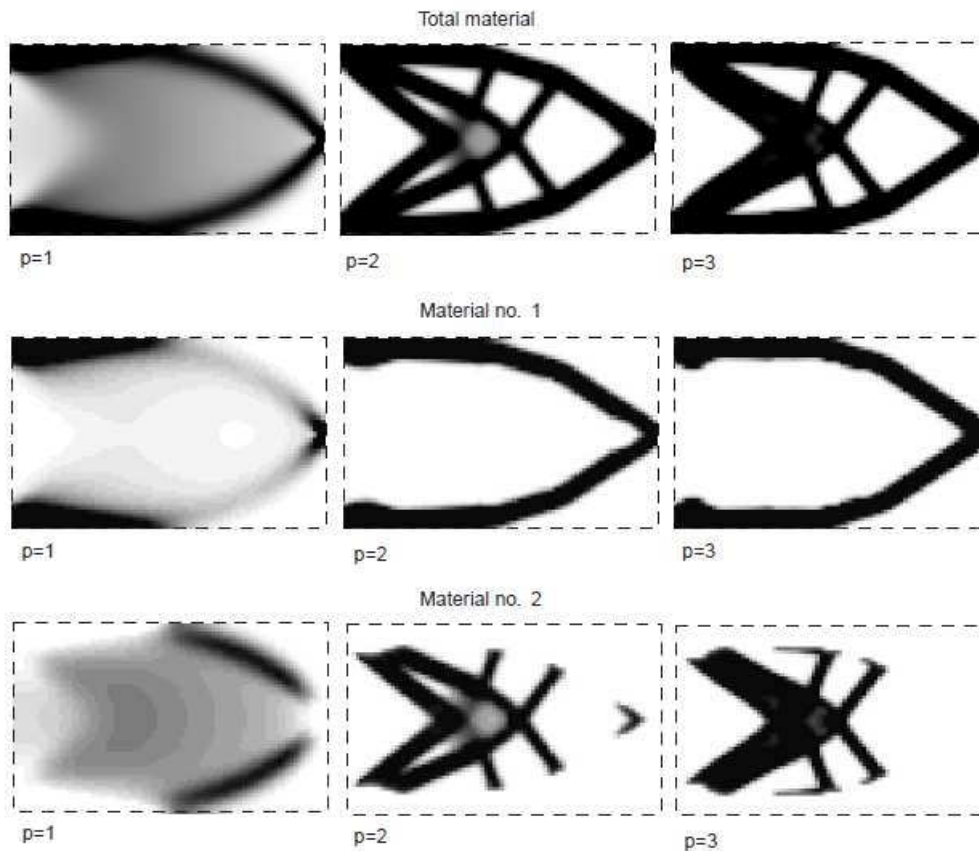


Figure 5.14

“Optimal design results for three-materials design (two materials with $\nu_1 = \nu_2 = 1/3$ and with stiffness $E_1 = 1, E_2 = 0.1$, and void), using various powers p in the interpolation scheme (5.28). The geometry and loading of the problem as in Fig 5.4

1.7 Multiple physics, nonlinear problems and anisotropic phases

1.7.1 Multiple physics

The phrase ‘multiple physics’ is used here to cover topology design where several physical phenomena are involved in the problem statement, thus covering situations where for example elastic, thermal and electromagnetic analyses are involved.

When modelling such situations, the basic concept of the homogenization method for topology design provides a general framework for computing interpolation schemes. As the theory and computational framework of homogenization of composite media is not limited to elasticity, choosing a specific class of composites and computing effective elastic, thermal and electromagnetic properties will lead to the required relationships between intermediate density and material properties. However, direct links between specific classes of composites and proofs of existence for such coupled problems have yet to be discovered.

The reduced complexity of the design description achieved by the SIMP approach has also led to the development of such interpolation schemes for multiple physics problems. Microstructures with extreme thermal expansion are designed by combining the three-materials interpolation of (5.28) for the elastic properties with an interpolation of the thermal expansion coefficients in the form

$$\alpha_{ij} = (1 - \rho_2^p) \alpha_{ij}^1 + \rho_2^p \alpha_{ij}^2 \quad (5.30)$$

Here α_{ij} is the thermal strain tensor which does not depend on the total density ρ_I of the mixture of the two materials 1 and 2. In recent work on topology design of thermo-electromechanical actuators, an interpolation of isotropic, thermal as well as electric conduction properties, with d^0 denoting the conductivity of the solid material

$$d(\rho) = \rho^p d^0 \quad (5.31)$$

has with success been combined with the basic SIMP interpolation (5.4). The condition (1.11) for the power p is sufficient for compatibility also with the Hashin-Shtrikman bounds for conduction

$$d(\rho) \leq \frac{\rho}{2 - \rho} d^0 \quad (5.32)$$

as well as the cross-property bounds

$$\frac{K^0}{K} - 1 \geq \frac{K^0 + \mu^0}{2\mu^0} \left[\frac{d^0}{d} - 1 \right]; \quad \frac{\mu^0}{\mu} - 1 \geq \frac{K^0 + \mu^0}{K^0} \left[\frac{d^0}{d} - 1 \right] \quad (5.33)$$

Topology design methods have also been implemented for the design of piezoelectric composites, which involves a coupled electrostatic and elastic analysis.

Here, material interpolation has been performed using a homogenized medium, as well as by a Voigt-type interpolation of the stiffness tensor, the piezoelectric tensor and the dielectric tensor, with a separate penalization of intermediate density.

1.7.2 Nonlinear problems

For nonlinear problems (elasto-plasticity etc.) both the “homogenization method” and the SIMP approach to topology design provide an even greater theoretical challenge, mainly due to the less developed and more involved theory of homogenization and to difficulties in deriving bounding theorems for such problems. It is here important to underline that micromechanical considerations should always play a role in the development of interpolation schemes, as experience shows that the computational feasibility of such schemes can be closely related to how faithfully the interpolations mimic physical reality.

For geometrically nonlinear problems, the constitutive laws remain linear so it is here natural to use the interpolation schemes developed for the linear problems. This has been done for large displacement problems, using the SIMP model to design structures and compliant mechanisms.

For materially nonlinear problems, a fundamental question is a reasonable description (interpolation) of the yield limit at intermediate densities, a problem that also is to be addressed for stress-constrained design problems. The stress-constrained problem is treated in the linear elastic domain. A micromechanical study of rank-2 laminates together with numerical experiments lead to a SIMP interpolation of the stiffness and stress limit in the form

$$E(\rho) = \rho^p E_0, \quad \sigma^Y(\rho) = \rho^p \sigma_0^Y \quad (5.34)$$

It is here convenient to interpret (5.34) as an interpolation between physical properties, which are relevant if material is present, and which should vanish when material is not present, and in order not to introduce bias, all properties are based on the same interpolation. For topology design involving damage models, a similar scheme is to express the linear and nonlinear strain energies in a form

$$\Psi(\rho) = \rho^p \Psi_0, \quad \Psi^D(\rho) = \rho^p \Psi_0^D \quad (5.35)$$

which is consistent for a “black and white” design (an index 0 indicates the energy expression valid at density 1).

1.7.3 Anisotropic phases

It is straight forward to extend the SIMP model to encompass also topology design with anisotropic materials, but for such cases the rotation of the base material should also be included as a design variable. The design of laminates (as stacks of plies of fiber-reinforced materials) can be seen as a topology design problem, where a combination of the Voigt bound (for the membrane stiffness), SIMP with $p = 2$ (coupling stiffness) and SIMP with $p = 3$ (bending stiffness) describes the design. This analogy allows for the application of a range of the theoretical tools developed for the homogenization method for topology design.

1.8 Conclusions and perspectives

The analyses presented here demonstrates that various approaches to “black and white” topology design can in many situations all be interpreted within the framework of micromechanically based models, thus clarifying a long ongoing discussion in the structural optimization community regarding the physical relevance of different interpolation schemes. However, it remains an important issue to examine models in relation to micromechanics, and to be fully aware of limitations or approximations used in the numerical schemes which are devised for solving topology design problems. Moreover, it is in this context crucial to recognize if a topology design study is supposed to lead to “black and white” designs or if composites can constitute part of the solution. It should again be emphasized that, if a numerical method leads to “black and white” designs, one can, in essence, choose to ignore the physical relevance of “grey”, and in many situations a better computational scheme can be obtained if one allows for a violation of the bounds on

properties of composites. This is especially the case where the bounds do not allow for a high enough penalization of intermediate density. The alternative is to introduce an explicit penalization of the density.

It is also evident from an overview of current methodologies that despite the abundance of results, there are still complicated theoretical and practical questions to overcome. Thus, the precise relationship between relaxation, microstructures, and existence of solutions is open for most classes of problems, and closely related to this are questions of bounds on properties for coupled and nonlinear problems. From a practical point of view, the most pressing question is no doubt the development of a general framework for devising interpolation schemes for coupled and nonlinear problems.

CHAPTER VI

OPTIMIZATION PROCESSES IN NATURE

1 Mechanical-based motivation of evolutionary process in moles: “optimization over time”

1.1 Introduction

Darwin's theory of natural selection has been able to explain optimization in biology: more efficient individuals leave more offspring.

The evolution principle, thus, provides an explanation for the differences in structure, functions, and behavior among organisms and describes the adaptation process that ensures the survival of different species in their environment.

The strategies adopted by Nature have attracted much attention in the study and design of the engineering systems and in the development of modern technology.

According to the literature mole rats assume a cylindrical shape to dig tunnels with diameters proportional to their size and this fact can be linked to the collapse mechanisms in tunnels, which has been recently treated in an analytical fashion in the case of Hoek-Brown soils.

As an example of optimization over time, we have studied burrow systems dug by mole-rats and the objective of this work consists in exploring the possible mechanical-based relationship between the geometry of burrows and geo-mechanical characteristics of the soil.

1.2 Failure Criteria

Traditionally, civil engineering has most relied on empirical methods to estimate the degree of safety of a dig. On the contrary, Failure Criteria are used at a theoretical

level to predict the conditions under which solid materials lose their resisting under the action of external loads.

Several criteria are available in literature, but the most widely employed in rock mechanics are the Mohr-Coulomb and the Hoek-Brown.

The first failure criterion was proposed by Coulomb in the late 1700's. The Coulomb failure criterion is given by the linear envelope obtained from a plot of the shear strength of a material versus the applied normal stress. This relation is expressed as

$$\tau = \sigma \tan \phi + c \quad (6.1)$$

where τ is the shear strength, σ is the normal stress, c is the cohesion and ϕ is the angle of internal friction .

The Mohr–Coulomb criterion is based on the observation that failure occurs when Mohr's Circle at a point in the body exceeds the envelope created by the two Mohr's circles for uniaxial tensile strength and uniaxial compression strength.

Another widely used criterion is the Hoek-Brown.

It was originally developed for the design of underground excavations and in contrast to Mohr–Coulomb criterion it is based on parameters that can be estimated by simple geological observations.

The Hoek–Brown generalized criterion can be written in the Mohr's plane σ_n, τ_n , see Fig. 1, with the unit vector n representing the normal to the failure plane,

$$\tau_n = \pm A \sigma_c [(\sigma_n + \sigma_t) \sigma_c^{-1}]^B \quad \{A, B \in (0,1) \subset \mathbb{R} \quad \gg \quad (6.2)$$

Where A and B are dimensionless parameters characterizing the rock mass and σ_c and σ_t are the compressive and tensile stresses at failure, respectively.

The Hoek-Brown criterion is made coincident with Mohr-Coulomb's (fig.6.1) τ_n^{M-C} if $B=1, A = \tan \phi$ and $\sigma_t = c(\tan \phi)^{-1}$:

$$\tau_n^{M-C} = \pm A (\sigma_n + \sigma_t) = \pm \sigma_n \tan \phi \pm c \quad (6.3)$$

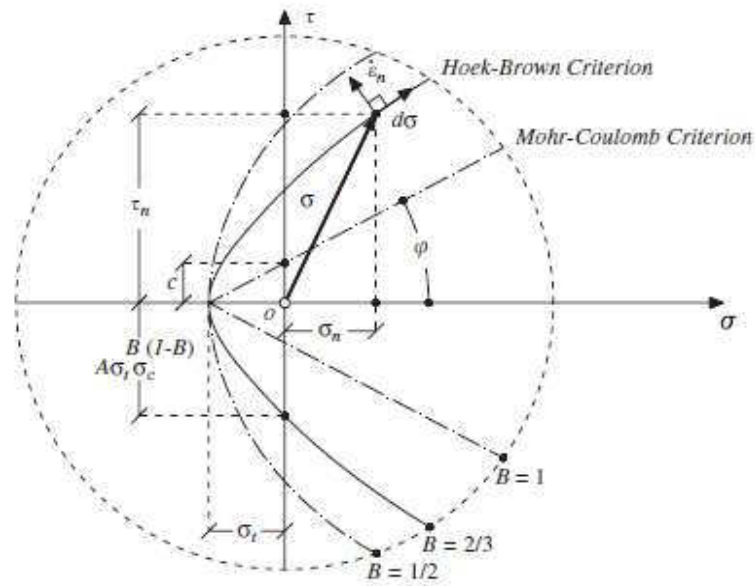


Figure 6.1:
Hoek-Brown generalized criterion in the Mohr's plane $\sigma_n - \tau_n$

On the basis of the Hoek–Brown failure criterion, Fraldi and Guarracino (Fraldi and Guarracino, 2009, 2010) have recently proposed an exact solution for the prediction of collapse in tunnels and natural cavities in the realm of the plasticity theory with the aid of classical tools of the calculus of variations.

The shape and dimensions of a rock bank which can actually collapse from the roof of the cavity for effect of the gravitational field (Fig. 7.2) is useful to estimate the stability of ceiling in tunnels and natural cavities in rock .

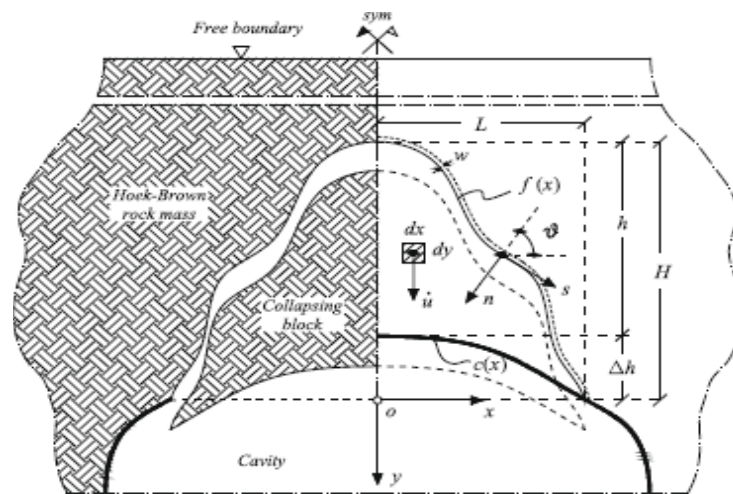


Figure 6.2
Generic Collapse mechanism

The formula which allows to evaluate the possible collapse of the tunnel roof provides the height and width of the collapsing block.

$$L = AB^{-B} (1+B)^B \rho^{-1} \bar{\sigma}_c^{-(1-B)} (\bar{\sigma}_t - \bar{p})^B \quad (6.4)$$

$$H = B^{-1} (1+B) (\bar{\sigma}_t - \bar{p}) \quad (6.5)$$

Where L and H are respectively the width and height of the collapsing block, ρ is the rock mass density and $\bar{\sigma}_t \equiv \rho^{-1} \sigma_t$, $\bar{\sigma}_c \equiv \rho^{-1} \sigma_c$, $\bar{p} \equiv \rho^{-1} p$, p is the generalized pressure.

Special attention is given to circular tunnels. In such a case the formula is :

$$L - AB^{-B} (1+B)^B \bar{\sigma}_c^{(1-B)} \left(\bar{\sigma}_t - \frac{1}{2L} R^2 \left[\arcsin \frac{L}{R} - \frac{L}{R} \sqrt{1 - \left(\frac{L}{R} \right)^2} \right] \right)^B = 0 \quad (6.6)$$

Where R is the radius of a circular tunnel.

In the present work special attention is paid to circular tunnels since subterranean rodents dig burrows with a circular shape. Indeed, a tunnel boring machine is called “Mole” because it imitates not only the cylindrical shape of the animals but also their technique of excavation.

6.3 Classification of mole rats

Digging animals belong to four classes of vertebrate: amphibians, reptiles, birds, mammalians.

The main advantages offered by digging consists in the microhabitat creation for hibernation, aestivation, reproduction or simply dugout, in the abundant underground presence of insects, roots of the plants and tubers that represent the main food resources, in the possibility to make food storage and places of retreat when the animals are alarmed or threatened.

Mole rats represent a special case among mammals. Over time, natural selection generated mole-rats showing convergent morphological features: compact bodies,

short necks and tails, large and powerful forefeet and microphthalmic eyes because vision had no survival advantage for them (Luna et al. 2009)

Following the natural evolution affected by the soil structure, the subterranean rodents have learnt to dig the compact soil with limbs and teeth and the unconsolidated one with limbs and head.

Subterranean rodents inhabit every continental land mass except Australia.

Mole rats can be split into two orders: Rodentia and Insectivora.

Because of the great number of mole rats belonging to the order Rodentia, they have been divided in 8 families (Table 6. 1), according to the geographical area they live in. Each family is characterized by different genera identified by the features of soil type and by their size.

Most of these mole rats live in open areas like steppes, grasslands, meadows or savannas even though few species occur in densely vegetated shrub (Wilson, Reeder 1993).

Also mole rats belonging to the same family can live in different kinds of soils. Luna et al.(2009) investigated the habitat characteristics of different species of *Ctenomys*, noting that they can live in very different soil types. *C. Australis*, for example, inhabits Coastal Grassland in Soft Soil, while *C. Talararum* in Medium Soil and *C Tuconax* lives in Highland Grassland in Hard Soil.

FAMILY	GENERA	NUMBER OF SPECIES	BODY SIZE	GENERAL HABITAT RANGE	GENERAL GEOGRAPHIC RANGE
Geomysidae	Geomys	5	Moderate (300-450 g)	Loose sandy soil in open or sparsely wooded area	Southeastern and central U.S. Northeastern Mexico
	Orthogeomys	11	Moderate to Large (500-800 g)	Arid tropical lowlands	Southern Mexico to Northwesten Colombia
	Pappogeomys	9	Small to Large (200-900 g)	Wide habitat range from desert to montane meadows	South-Central U.S. to central Mexico
	Thomomys	9	Very small (50 g) to moderate (550 g)	Wide range of soils and habitats from desert scrub to montane meadows	Southern Canada western U.S. to central Mexico
	Zygeogeomys	1	Moderate (300-550 g)	Montane meadows above 2.200 m	Michoacan, Mexico
Muridae Arvicolinae	Ellobius	5	Very small (75 g)	Steppe and semidesert	Ukraine and Crimea south to Turkey and east to Iran Afganistan, Pakistan
	Prometheomys	1	Very small (70 g)	Alpine and subalpine meadows	Caucasus, Georgia and northeastern Turkey
Muridae Myospalacine	Myospalax	7	Moderate (150-600 g)	Cultivated and wooded habitats in montane-valleys	Central Russia to northeastern China
Muridae Rhizomyinae	Cannomys	1	Large (500-800 g)	Meadows and bamboo forests in hilly	Eastern Nepal east to southern China, Thailand
	Rhizomys	3	Very Large (1-4 kg)	Bamboo thickets in uplood areas 1\4000 m	Nothern India to central China
	Tachyryctes	11	Small (150-300 g)	Moist open grasslands, moorlands up to 4100 m	Ethiopia, Tanzania, Uganda
Muridae Spalacine	Nanospalax	5	Small (100-250 g)	Sandy or loamy soils in a variety of habitats	Ukraine south through Balkan States, Egypt and Libia
	Spalax	5	Moderate (200-600 g)	Wide range of soils in plains below sea level, upland steppes and hilly region	Russia and Ukraine east to western shore of Caspian sea
Ctenomyidae	Ctenomys	56	Small (100 g) to large (> 750 g)	Extremely wide range of habitats and soils from sea level to above 4000 m	Southern Peru south to Tierra del Fuego and east to Southeastern Brazil
Octodontidae	Spalacopus	1	Small (110 g)	Moist to semiarid open shrublands from coastal areas to montane slopes above 3000 m	Central Chile
Bathyergidae	Bathergus	2	Large (850-1500 g)	Coastal sand dunes and sand flats from the coast to 1500 m	Namibia and South Africa
	Cryptomys	7	Small (200 g)	Compact or sandy soil in woodlands, savannas and secondary forests at elevation to 2200 m	Ghana east to Tanzania and South to South Africa
	Georchus	1	Small (180 g)	Wide range of soils	South Africa
	Heliophobius	1	Small (160 g)	Sandy soils in dry open plains or woodlands	Zaire and Kenya south through Tanzania Mozambique, Zambia and Zimbabwe
	Heterocephalus	1	Very small (30-80 g)	Arid open shrub or glassalands in a variety of soils from 400 to 1500 m	Somalia, Ethipia and Kenys

Table 6. 1

Classification of mole rats in family, genera, body weight, habitat and geographic range (Wilson, Reeder 1993)

Moreover, subterranean rodents have completely different size, small, medium or large, according to their weight.

Within the same family, such as Bathergydae, mole rats may have different weights. For example, *Bathergus* can reach 850-1500 g and live in wet soil while *Cryptomys* have a very low weight (200 g) and inhabit sandy and more compact soil.

FAMILY	GENERA	NUMER OF SPECIE	BOY SIZE	GENERAL HABITAT RANGE	GENERAL GEOGRAPHIC RANGE
Talpidae	Condylura	1	Very small (55 g)	Wetlands:swamps, wet meadows and woods	Eastern Canada and Northeastern United States
	Euroscaptor	6			Bangladesh, Brunei, Cambodia, Cina, Hong kong, India , Indonesia, Laos, Malaysia, Thailand and Vietnam
	Magera	5			Northwester,United States and British Columbia
	Parascalops	1	Very small (55 g)	Forested and open areas with dry loose soil	Eastern Canada and northeastern United States
	Parascaptor	1			China, India and Myanmar
	Scalopus	1	Very small (40-50 g)	Loamy soils found in thin woods, fields, pastures and meadows	Canada (Ontario).Mexico and eastern United States
	Scapanulus	1			China
	Scapanus	3	Very small (62-138 g)		North America and British Columbia
	Scaptochirus	1			China
	Scaptonyx	1			China and Myanmar
	Talpa	9	Very small (60-120 g)		Europe: Great Britain Sweden, Italy, Spain and Balkans. Asia: Caucasus ,Altaj and Mongolia

Table 6.2
Classification of Insectivora mole rats

Mole rats in the order Insectivora belong to the family Talpida and they share very similar physical characteristics (weight from 40 to 140 g).

According to the geographical area where they live in, mole rats show different digging techniques. For example, the Golden Mole, also known as sand swimmer, exhibit small dimensions, short limbs, shovel legs that allow them to swim in the soil. On the other hand, European moles, that have larger dimensions, long limbs and big claws through which they break up the soil are also called “scratch diggers”.

6.4 Soil and burrows characteristics

As anticipated, burrows play an important role for subterranean rodents, supplying them with shelter and access to food resources. The underground environment imposes constraints on physiology and morphology. (Luna and Antinuchi 2007)

Mole rats that spend most of their life in underground self-made burrows and forage (predominantly) above ground, are called fossorials. (Luna and Antinuchi 2007)

The construction of burrow systems, composed by a main tunnel connected to lateral branches that reach the soil surface (Antinuchi and Busch 1992; Busch et al. 2000), needs a very high energetic effort (Vleck 1979; Lovegrove 1989; Luna et al. 2002).

Mole rats inhabit in a structurally simple environment (Nevo 1999), characterized by several foraging tunnels connected to a single central deep tunnel (Busch et al. 2000). As mole rats belong to the fossorial specie, soil substrate properties influence their biological and ecological features.

Habitat type influences the burrow architecture. Soil type, in fact, may have an effect on the burrow architecture as a mechanism to compensate the differences in the cost of excavating and diffusion rate of gases (Jackson et al. 2008). Moreover, soil granulometry affects the diameter and depth of the tunnels, while soil humidity influences the main tunnel length of burrow (Antinuchi and Busch., 1992). There are also some further relations among the size of burrow occupants, hardness and food supply to burrow length, but the most important factor influencing the burrowing efficiency is represented by the relationship between soil hardness and the cost of tunneling. (Luna & Antinuchi, 2006).

Also extrinsic factors, such as porosity, water-holding capacity of the soil and humidity, as well as food availability, may determine burrow's location and design because, there is a connection between these factors and soil hardness and, hence, the digging cost (Busch et al. 2000; Luna and Antinuchi 2006).

Usually, a classic burrow system is composed of nest chambers, food stores, defecation sites and bolt holes, which serve as a place of retreat when the animal is alarmed or threatened. Males tend to realize linear-shaped burrow systems, whereas the burrows of females are more grid (Herbst and Bennett 2006).

Mole rats, generally, occur in dank and dark environments, with low primary productivity and low ventilation .

Mole rats exhibit morpho-physiological properties that allow them to sustain the high cost of expanding their tunnel systems.(Luna and Antinuchi 2007)

Besides, low primary productivity, or low porosity and soil transmittance, both related to soil hardness, might govern the absence of bigger subterranean rodents from arid deserts (Vleck, 1981). Thus, the bigger species inhabit soft soils with high primary productivity, as a strategy to lower the cost of digging in such soils (Vleck, 1979) or because the possibility to dig a deeper layer of the soil, and avoid overheating.

Sumbera et al. (2004) observed the changes in burrow architecture occurred in *Heliophobius argenteocinereus* due to density soil.

In particular, in a hard and compact soil like in Blantyre (bulk density valore) the foraging tunnels have a range between 7-20 cm while in a light and soft soil like in Mulanje the range is between 19-30 cm as shown in table 6.3

Heliophobius argenteocinereus	Blantyre	Mulanje
Foraging tunnels	11.9 ± 2.8 cm	24.8 ± 3.8 cm
Nest chambers	15.8 ± 5.0 cm	38.6 ± 13.5 cm
Food chambers	13.6 ± 3.3 cm	30.2 ± 15.6 cm

Table 6.3

Mean dimensions (cm) of Heliophobius argenteocinereus burrow system and differences of particular components between burrows system in Blantyre and Mulanje. (Sumbera et al. 2004)

Thomas H.G. et al. (2009) studied African mole rats, in particular, the Cape dune mole rats of the genus *Bathyergus*. Thomas H.G. et al have measured the burrow characteristics of *B. suillus* and they related them to sex of mole rats and their body properties. They have shown that males excavated significantly longer burrow systems with higher fractal dimensions, larger burrow areas and dig deeper burrows than females. In fact, males dug superficial and deep tunnels at a depth greater than females because sexual dimorphism in body size is shown in this specie (Table 6.4)

Cape dune mole rats	male	female
Superficial tunnels	17 ± 0,7 cm	16 ± 1 cm
Deep tunnels	32 ± 7,8 cm	29 ± 7,8 cm

Table 6.4
Burrow characteristics (cm) of male and female Bathyergus suillus.
 (Thomas et al. 2009)

The objective of the present work is to identify the allowable range of diameters to ensure the borrow stability. To that purpose, the Mohr-Coulomb and Hoek-Brown criteria have been plotted first to identify the necessary conditions for the structure stability. Then, the relationship existing between the tunnel width and radius have been represented to obtain the desired range.

First of all, the Mohr-Coulomb criterion has been applied in a $\tau - \sigma$ Mohr plane, as shown in the relationship (6.1), employing the characteristic values of the soils where mole rats usually dig, as reported in Table 7.5.

Moreover, since the presence of mole rats is influenced by the soil characteristics, in particular by the size distribution of sand particles, the values of the cohesion, c , and friction angle, ϕ have been chosen from the typical values of the environment. For example, the juliana's golden mole is confined to sandy soil characterized by a cohesion varying between 0 and 0.5 kg/cm² as reported in literature; the angle of internal friction, instead, for a sandy soil varying between 25° and 35°

Cape dune mole rats	Friction	Cohesion kg/cm²
Loose sand	20°	0
Cohesive Sand	27°	0,5

Table 6.5:
Soil characteristics

On the basis of these values, it is possible to identify an area constrained by two lines representing the limit cases of the Mohr-Coulomb criterion, as illustrated in Figure 7.3.

In the same graphics, the Hoek-Brown criterion has been also plotted with the parameter A kept constant, and B varying between 0.5 and 0.9, in order to keep the

Hoek-Brown curve within the area of interest of the plane σ - τ . The plots reported in the following have been obtained for $\sigma_t = 0,01 \text{ kg/cm}^2$.

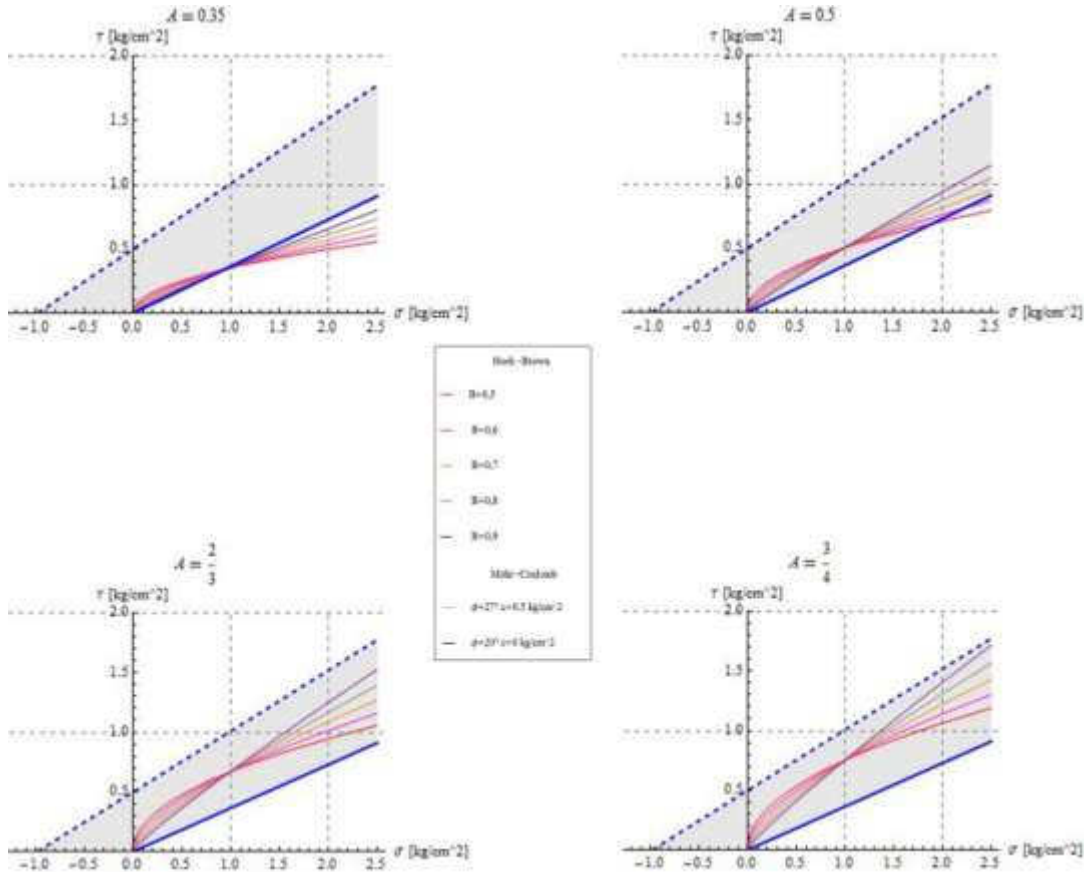


Figure 6.3
Comparison between results from Hoek–Brown and Mohr–Coulomb criteria.

Figure 6.3 shows that the Hoek-Brown curves tend to lie inside in the area of interest when the parameter A increases. $A = 0.35$ represents a limit case because the curves lie only partially in the Mohr-Coulomb area. For different values of the parameter A , instead, all the curves belong to the analyzed area.

$A = \frac{3}{4}$ is nearly equal to the limit value of the Mohr-Coulomb with a friction angle and the cohesion of 27° and 0.5 kg/cm^2 .

The relationship between the tunnel width and radius (eq.(6.6)) has been then plotted to show that the characteristic dimensions of the mole rats tunnels tend to obey to this condition.

In this case ρ is $1,6 \cdot 10^{-3} \text{ kg/cm}^3$, a typical bulk density for mole rats environment, as shown by Luna, Antinuchi e Busch, 2002. The parameters A and B

have been chosen considering the limitation imposed by Mohr-Coulomb e Hoek-Brown criteria as shown in figure 6.4.

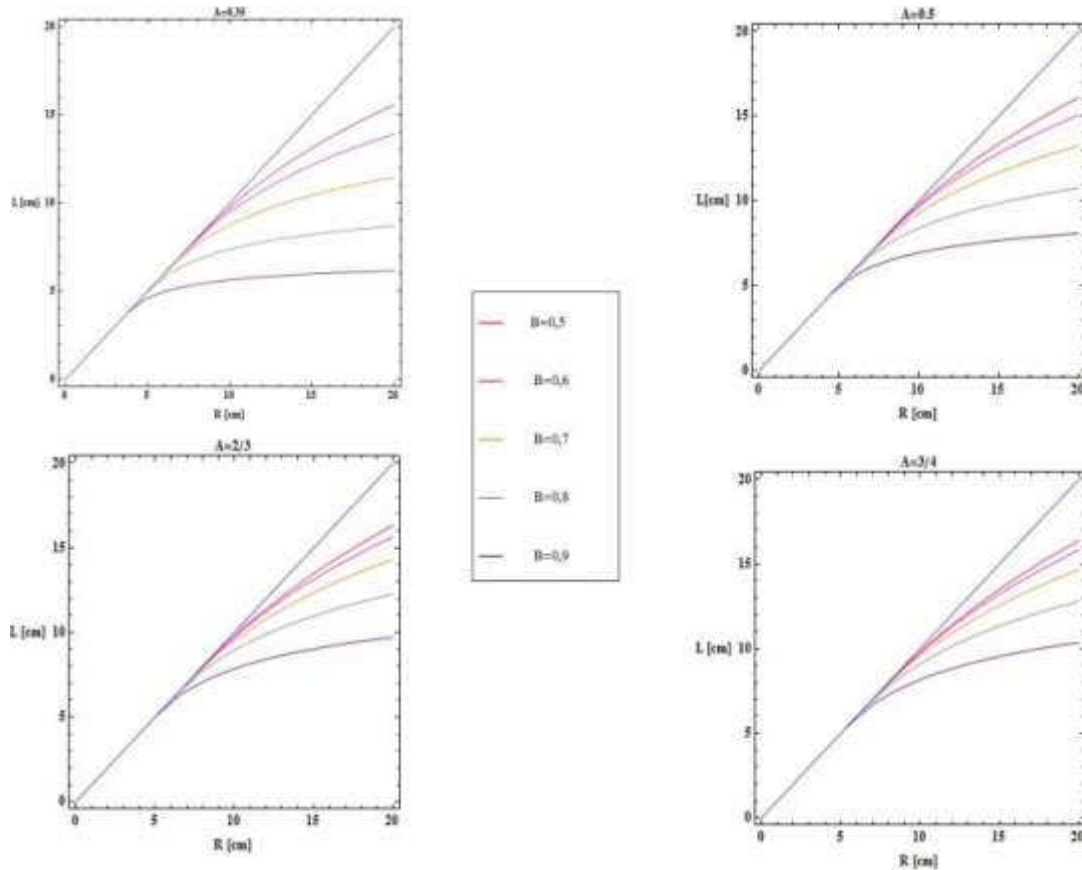


Figure 6.4
Plotting of eq (6.6)

When the parameter A increases the range of diameters which ensure the borrow stability, also increases.

For example, when the parameter A is 0.35 the borrow allowable diameters vary between 4 to 6 cm with $B=0.9$. Instead, when A is equal to $\frac{3}{4}$ the allowable range of diameters increases, varying between 6 to 8 cm.

The plots show that mole rats can build tunnels with a diameters varying between 7 and 14 cm.

In these analysis ρ is $1,6 \cdot 10^{-3} \text{ kg/cm}^3$ as reported by Luna et al. (2002).

Similar graphics can be obtained by varying A and keeping constant the parameter B or increasing the stress. In such cases it is found that mole rats can build the

tunnels a diameters varying between 16 and 30 cm. $\rho = 1.6 * 10^{-3} (\text{kg}/\text{cm}^3)$

Sumbera et al., 2004, have measured mean depth and burrow system components of silver mole rats of *Heliophobius argenteocinereus* in two mesic areas in Malawi. The study was carried out in Mulanje and Blantyre. In Mulanje, the soil, at depths where most of the burrow systems were situated, was light and soft with a bulk density that are 1.06 or 1.29 g/cm^3 instead in Blantyre the soil was hard and compact with a bulk density that are 1.5 or 1.72 g/cm^3 .

The friction angle was set at 14° and 28° , as for the sandy loam, instead the cohesion value was defined at $0 \text{ kg}/\text{cm}^2$ (lack of cohesion) and $0,5 \text{ kg}/\text{cm}^2$ (semisolid clay).

Setting $\sigma_t = 0,01 \text{ kg}/\text{cm}^2$ and $A = 0,3$: the result is shown in the fig.6.5

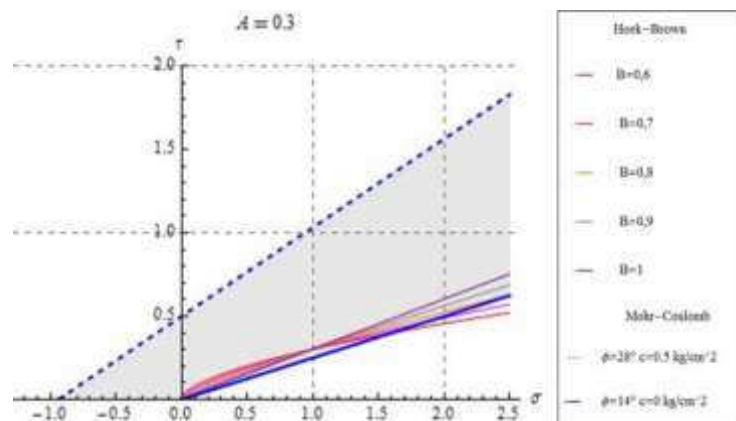


Figure 6.5:
Comparison between results from Hoek–Brown and Mohr–Coulomb criteria.

Plotting the relationship between the tunnel width and radius (eq.(6.6)) the result is:

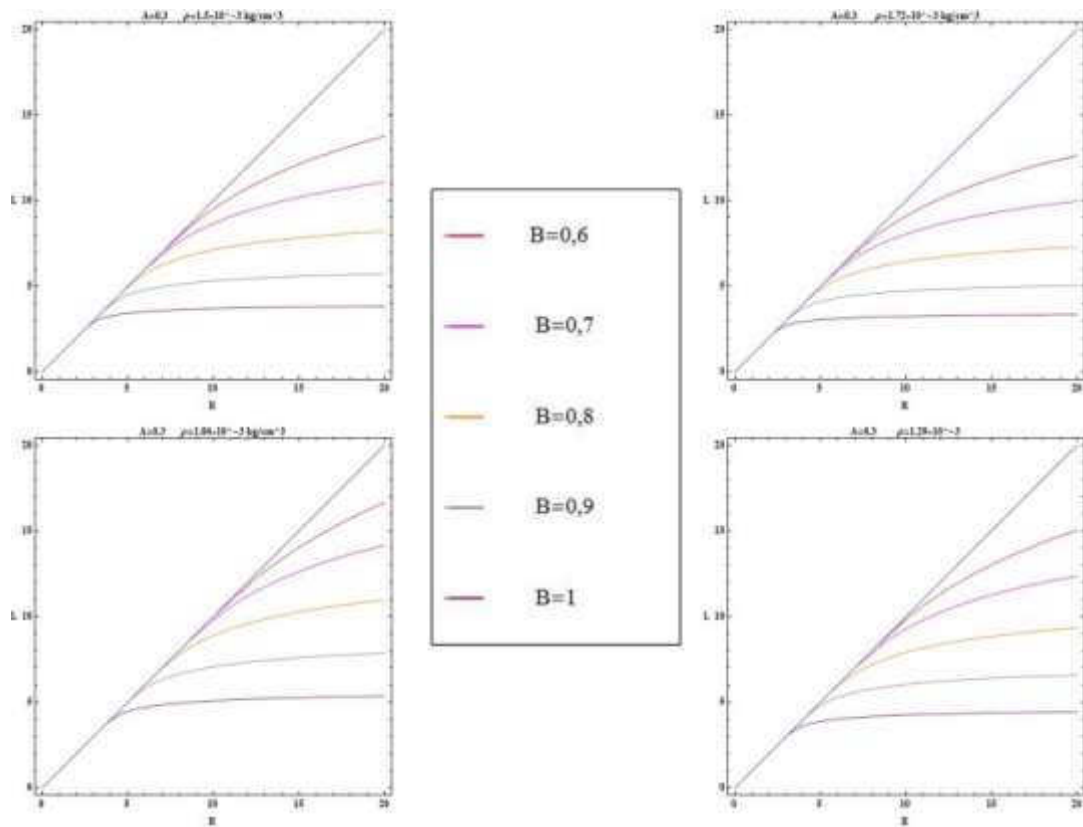


Figure 6.6
Plotting of eq (6.6)

The range of stability is 5-13 cm in the Blantyre zone and 6-14 cm in the Mulanje one.

Comparing the range of diameters considered by Sumbera et al. (5-8 cm e 6-8,5 cm in the Blantyre e Mulanje soil respectively) with our results, it can be concluded that the *Heliophobius argenteocinereus*, dig tunnels with different diameters in relation with bulk density.

In the following histogram the burrow diameters reported in articles of different authors are shown. Comparing these data with the range of diameters obtained in the present study, with the bulk density at the typical value $1,6 \cdot 10^{-3} \text{ kg/cm}^3$, the range predicted includes the actual values of burrow diameters.

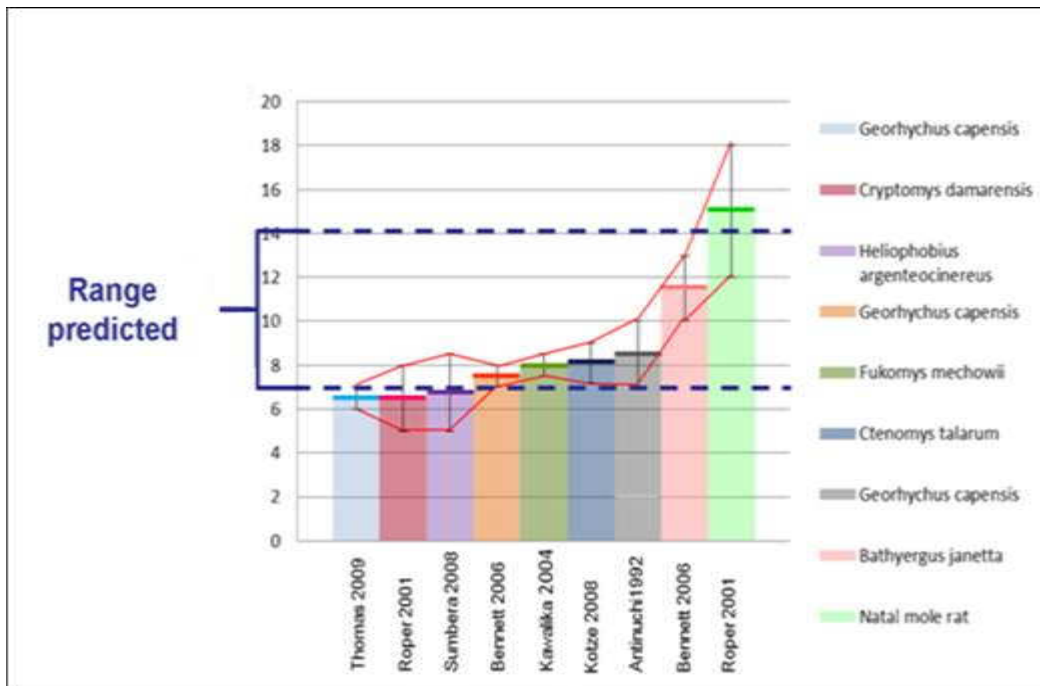


Figure 6.7

Comparison between burrows diameter found in literature and admissible diameter calculated with our model

6.5 Conclusions

Mole rats are the best excavator among subterranean rodents. Their tunnels are constructed obeying to optimal criteria and are realized with the aim of ensuring an adequate oxygen and nutrients supply as well as to avoid collapse mechanisms of the networks.

With this purpose, the objective of this work has consisted in exploring the possible mechanical relationships between the geometry of the burrows and the soil geomechanical characteristics. This approach could be utilized for investigating the possibility to formulate a new mechanical-based evolutionary hypothesis for which the overall dimensions of the mole rats also depend on the quality of soils. This would mean that the natural evolutionary process preserves and genetically select mole rat species able to reach and to excavate at depth such that the geo-mechanical quality of the resident soil increases as a result of the consolidation. This possible scenario would also allow to explain, within a mechanically perspective, the observed significant differences in size among the mole rat species. In-fact, the study

has confirmed that mole-rats dig tunnels with different diameters into the allowable range of diameters to ensure the borrow stability

2 Mechanical-based design of “fiber-reinforced” cartilage structures: “optimization over space”

Biological tissues, over millions of years of evolution, were developed into hierarchical structures with intricate architectures from nm to m that often extend into macro scale resulting in unique, species-specific overall morphology with characteristic functions that provide an advantage for the organism in its environment. As example of optimization over space we have studied fiber-reinforced cartilage structures

2.1 Cartilage

Articular cartilage is located in joints between articulating bones (fig. 6.8). It provides an almost frictionless surface for smooth joint movement, aided by the lubrication of the surrounding synovial fluid. In the knee, the meniscus lies between load bearing joint surfaces. The two menisci (fig. 6.8) absorb part of the loads that the joint experiences.

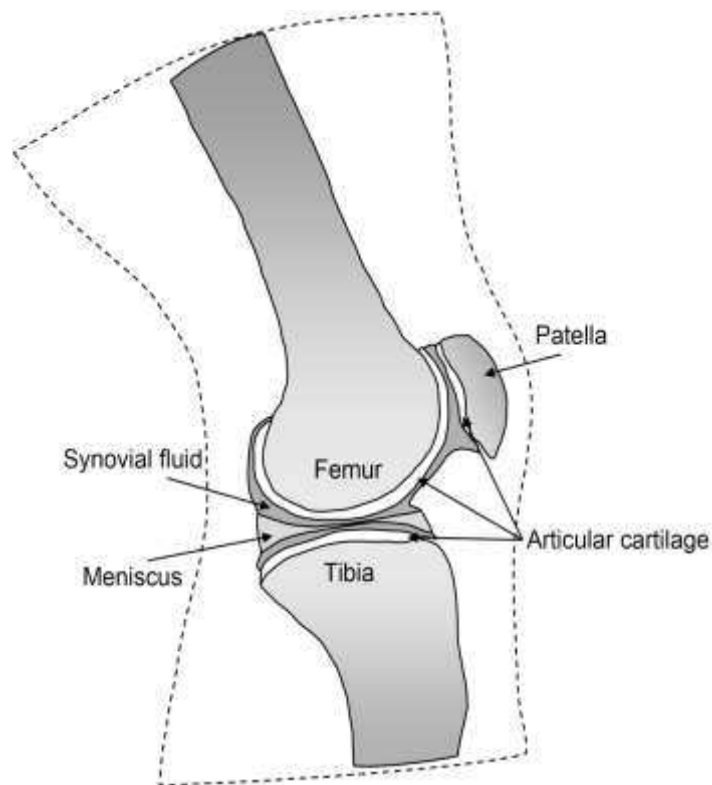


Figure 6.8

Schematic presentation of a knee joint. Frame of the knee is presented with dashed line. In this projection, only one of the two menisci is visible.

The main functions of articular cartilage are to decrease the contact stresses in the joint (Askew MJ, Mow VC, 1978) and to allow motion of the opposing surfaces with minimum friction and wear (Mow VC, Mak AF 1987). The tissue is composed of two phases, an interstitial fluid and a solid matrix. The solid matrix, accounting for 20-30% of the wet weight of the tissue, is composed of collagen fibers (65% of dry weight), proteoglycans (PGs) (25% of dry weight), chondrocytes, and other glycoproteins and lipids. The remaining 70-80% of tissue is water, most of which is freely exchangeable by diffusion, with the outside medium.

It is well known that the biochemical composition of cartilage varies significantly over the joint surface (Kiviranta I, Jurvelin J. et al., 1987) and appears to be related to joint loading (Caterson B, Lowther D.A. 1978). Many investigators have studied the effects of high and low loading on articular cartilage biochemistry.

Chondrocytes organize the collagen, proteoglycans and non-collagenous proteins into a unique and highly specialized tissue, suitable for carrying out the functions stated above.

The composition, structure and functions of chondrocytes vary depending on the depth from the surface of the cartilage. Morphologically there are four named zones, from top to bottom:

1. Superficial zone
2. Transitional zone
3. middle (radial) or deep zone and
4. calcified cartilage zone

Superficial zone

This is the thinnest of all layers (10-20% of the cartilage thickness) , composed of flattened ellipsoid cells. They lie parallel to the joint surface, and are covered by a thin film of synovial fluid, called ‘lamina splendens’ or ‘lubricin’. This protein is responsible for providing an ultimate gliding surface to the articular cartilage. Parallel arrangement of the fibrils are responsible for providing the greatest tensile and shear strength. Disruption of this zone alters the mechanical properties of the articular cartilage and thus contributes to the development of osteoarthritis. This layer also acts as a filter for the large macromolecules, thereby protecting the cartilage from synovial tissue immune system.

Transitional zone

In the middle zone, 60% of the cartilage thickness, the cell density is lower, with predominantly spheroid-shaped cells, embedded in abundant extracellular matrix. The large diameter collagen fibres are randomly arranged in this zone.

The radial zone

In the deep zone that takes up the 30% of the cartilage thickness, cells are arranged perpendicular to the surface and are spheroidal in shape. This zone contains the

largest diameter of collagen fibrils and highest concentration of proteoglycans. However, the cell density is lowest in this zone.

Calcified cartilage zone

This mineralized zone contains small volume of cells embedded in a calcified matrix and thus showing a very low metabolic activity. The chondrocytes in this zone express hypertrophic phenotype. (Abhijit M. Bhosale, James B. Richardson, 2008)

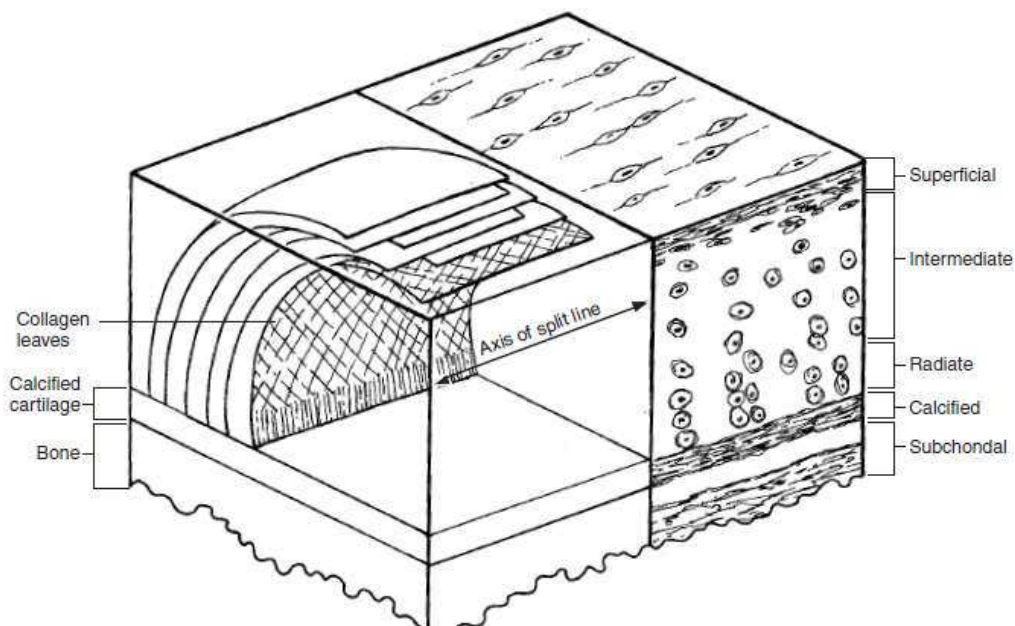


Figure 6.9

Cross sections cut through the thickness of articular cartilage on two mutually orthogonal planes. These planes are oriented parallel and perpendicular to split lines on the cartilage surface. The background shows the four zones of the cartilage: superficial, intermediate, radiate, and calcified. The foreground shows the organization of collagen fibers into “leaves” with varying structure and organization through the thickness of the cartilage. The leaves of collagen are connected by small fibers not shown in the figure.

The human knee joint is distinguished by its complex three dimensional geometry and multibody articulations that generate complex mechanical responses under physiological loads. The knee joint compliance and stability required for optimal daily function are provided by various articulations, menisci, ligaments and muscle forces.(M.Z. Bendjaballah et al. 1995)

Knee joint mechanics have consequently been the subject of a large number of studies, the majority of which are experimental and aim at the measurement of the

gross multidirectional load-displacement response of the joint under both intact and perturbed states. (Kurosawa et al. 1980).

Measurements have also been reported on the biomechanical role of the ligaments and menisci as well as the mechanism of load transfer and contact areas and pressures at the tibiofemoral and patellofemoral joints.(Maquet 1975). In spite of the continuing accumulation of experimental results, it is recognized that measurements alone are not sufficient to delineate the detailed biomechanics of the human knee joint. Various applications in orthopaedic biomechanics have long demonstrated that realistic mathematical modelling is an appropriate tool for the simulation and analysis of complex biological structures such as the human knee joint. During the last two decades, a number of analytical model studies with different degrees of sophistication and accuracy have been presented in the literature, These have mainly attempted to model the tibiofemoral joint (Rahaman 1993), while a few studies have aimed at modelling the patellofemoral joint and more recently at both the tibiofemoral and patellofemoral joints. As for finite element model investigations, no study of the entire tibiofemoral joint is yet reported in the literature. A few model studies of the menisci are found assuming simplified axisymmetric geometries for the femoral condyles, tibial plateau, and menisci with no consideration of any of the cartilage layers or of ligamentous contribution. More recently, using similar axisymmetric geometries, an analysis has been carried out considering femoral and tibial articular cartilage layers of uniform thickness .(M.Z. Bendjaballah 1995).

2.2 Mathematical model

The articular cartilage has been modeled as an orthotropy tube composed by three layers. Dmitriev et al. analyze stress distribution in a long tube with polar orthotropy. The exact elasticity solution for stress distributions in long tubes suggest that, at some combinations of elastic properties, stresses can change rapidly in radial direction or can be even of oscillatory type. They analyze the thermodynamic stability of orthotropic body and demonstrate that the oscillatory solutions can appear only in thermodynamically unstable bodies and thus, they do not have physical meaning.

In polar coordinates, the equilibrium equations in a state of plane strain in radial r , and circumferential θ directions, respectively, are

$$\frac{\partial}{\partial r}(r\sigma_r) - \sigma_\theta + \frac{\partial \tau_{r\theta}}{\partial \theta} = 0 \quad (6.7)$$

$$\frac{\partial \sigma_\theta}{\partial \theta} + \tau_{r\theta} + \frac{\partial}{\partial r}(r\tau_{r\theta}) = 0 \quad (6.8)$$

Plane strain components in terms of radial u_r , and circumferential u_θ displacements are

$$\varepsilon_r = \frac{\partial u_r}{\partial r}, \quad \varepsilon_\theta = \frac{u_r}{r} + \frac{1}{r} \frac{\partial u_\theta}{\partial \theta}, \quad \gamma_{r\theta} = \frac{\partial u_\theta}{\partial r} - \frac{u_\theta}{r} + \frac{1}{r} \frac{\partial u_r}{\partial \theta}. \quad (6.9)$$

The strain compatibility equation is given as

$$\frac{\partial^2 \varepsilon_\theta}{\partial r^2} + \frac{1}{r^2} \frac{\partial^2 \varepsilon_r}{\partial \theta^2} + \frac{2}{r} \frac{\partial \varepsilon_\theta}{\partial r} - \frac{1}{r} \frac{\partial \varepsilon_r}{\partial r} - \frac{1}{r} \frac{\partial^2 \gamma_{r\theta}}{\partial r \partial \theta} - \frac{1}{r^2} \frac{\partial \gamma_{r\theta}}{\partial \theta} = 0. \quad (6.10)$$

They consider a long tube with the axis oriented along the z -direction, subjected to axisymmetric (θ -independent) loading, and made of a material with polar orthotropy. In this case, for a cross-section situated far from the ends of the tube, one can consider only radial displacements of material points, i.e., one has $u_\theta = 0$ and all unknown stress and strain fields are the functions of radial coordinate only. Then, Eqs. (6.7)–(6.10) equation reference goes here reduce to

$$(r\sigma_r)' - \sigma_\theta = 0, \quad (6.11)$$

$$\varepsilon_r = u_r', \quad \varepsilon_\theta = \frac{u_r}{r}, \quad \gamma_{r\theta}(r) = 0, \quad (6.12)$$

$$\varepsilon_\theta'' + \frac{2}{r} \varepsilon_\theta' - \frac{1}{r} \varepsilon_r' = 0 \quad (6.13)$$

Here and in the following $()'$ denotes differentiation with respect to r .

For their purposes it is sufficient to take instead of Eq. (6.13) here the strain compatibility condition in the following form, which follows from the two first expressions of Eq. (6.12),

$$\varepsilon_r - \varepsilon_\theta = r\varepsilon'_\theta \quad (6.14)$$

Hooke's law for the orthotropic material in the polar axisymmetric case is

$$\begin{Bmatrix} \varepsilon_r \\ \varepsilon_\theta \\ \varepsilon_z \end{Bmatrix} = \begin{bmatrix} \frac{1}{E_r} & -\frac{\nu_{\theta r}}{E_\theta} & -\frac{\nu_{zr}}{E_z} \\ -\frac{\nu_{r\theta}}{E_r} & \frac{1}{E_\theta} & -\frac{\nu_{z\theta}}{E_z} \\ -\frac{\nu_{r\theta}}{E_r} & -\frac{\nu_{\theta z}}{E_\theta} & \frac{1}{E_z} \end{bmatrix} \begin{Bmatrix} \sigma_r \\ \sigma_\theta \\ \sigma_z \end{Bmatrix} \equiv \begin{bmatrix} a & d & e \\ d & b & f \\ e & f & c \end{bmatrix} \begin{Bmatrix} \sigma_r \\ \sigma_\theta \\ \sigma_z \end{Bmatrix}, \quad (6.15)$$

where has been introduced the short notations for the compliance coefficients. The compliance matrix is assumed to be symmetric with six independent elastic constants, say $E_r, E_\theta, E_z, \nu_{r\theta}, \nu_{rz}, \nu_{\theta z}$. With the help of Eq. (6.15), the Eq. (6.14) can be expressed in terms of stresses as

$$(a-d)\sigma_r + (d-b)\sigma_\theta + (e-f)\sigma_z = r(d\sigma'_r + b\sigma'_\theta + f\sigma'_z) \quad (6.16)$$

The tube can be loaded in axial direction and, for the regions remote from the tube ends, this will result in r -independent, generally speaking, nonzero axial strain $\varepsilon_z(r) = \varepsilon_z^0$, and the following relation between stress components can be deduced from Eq. (6.15):

$$e\sigma_r + f\sigma_\theta + c\sigma_z = r\varepsilon_z^0. \quad (6.17)$$

Thus, we have three equations (6.11), (6.16) and (6.17), with respect to three unknown stress components, $\sigma_r(r), \sigma_\theta(r)$ and $\sigma_z(r)$.

For the plane stress solution they have solved Eqs. (6.11), (6.16) and (6.17), in $\sigma_r(r)$ to obtain

$$r^2\sigma_r'' + 3r\sigma_r' + (1-\phi)\sigma_r + \lambda\varepsilon_z^0 = 0 \quad (6.18)$$

Where

$$\lambda = \frac{f-e}{bc-f^2}, \quad \phi = \frac{ac-e^2}{bc-f^2} \quad (6.19)$$

Note that for the isotropic material, when $a = b = c$ and $d = e = f$, we have $\phi = 1$ and $\lambda = 0$. Equation (6.18) reduces to which can be integrated to give the classical solution $\sigma_r = \frac{C_1}{r^2} + C_2$, where C_1, C_2 are the integration constants. The analyses will be carried out for the orthotropic case.

Equation (6.18) is the Euler equation which, with the help of substitution $r = e^t$, can be reduced to the equation with constant coefficients having the characteristic equation $\rho^2 + 2\rho + 1 - \phi = 0$ with the roots

$$\rho_{1,2} = -1 \pm \sqrt{\phi} \quad (6.20)$$

It will be demonstrated in the following that complex ρ_i correspond to thermodynamically unstable elastic constants and thus, they will not be considered.

For $\phi > 0$ we have two real roots, $\rho_1 \neq \rho_2$, and the solution to Eq. (6.18) is

$$\sigma_r(r) = C_1 r^{\rho_1} + C_2 r^{\rho_2} - \varepsilon_z^0 \frac{\lambda}{1 - \phi} \quad (6.21)$$

with the integration constants C_1, C_2 . Having found σ_r , be found σ_θ from Eq. (6.11) and then σ_z from Eq (6.17)

The result is

$$\sigma_\theta = (1 + \rho_1) C_1 r^{\rho_1} + (1 + \rho_2) C_2 r^{\rho_2} - \varepsilon_z^0 \frac{\lambda}{1 - \phi} \quad (6.22)$$

$$\sigma_z = -\eta_1 C_1 r^{\rho_1} - \eta_2 C_2 r^{\rho_2} + \varepsilon_z^0 \left(\frac{1}{c} + \omega \frac{\lambda}{1 - \phi} \right) \quad (6.23)$$

Where

$$\omega = \frac{e + f}{c}, \quad \eta_{1,2} = \omega + \frac{f}{c} \rho_{1,2} \quad (6.24)$$

For $\phi = 0$, there are a multiple root, $\rho_1 = \rho_2 = -1$, and the solution to Eq. (6.18) is

$$\sigma_r(r) = \left(\frac{C_1}{r} + C_2 \right) \ln r - \varepsilon_z^0 \lambda \quad (6.25)$$

As one can see from Eq. (6.19), $\phi = 0$ when $ac = e^2$ or, from Eq.(6.15), when $E_z = \nu_{zr}^2 E_r$ (Dimitriev et al 2010).

These results have been modified for studying the articular cartilage. In particular three different compliance matrixes have been considered, identifying three layers in which the cartilage is divided and which have different orientations of collagen fibers. In fact, the whole tube is made of three tube one inside the other.

In the inner layer, where the collagen fibers are oriented in the direction of the load, $E_r = E_v$, $E_\theta = E_z = E_h$, and $E_r > E_z$

where E_v and E_h are respectively the Young's modulus in vertical and horizontal direction

In the middle zone, where the collagen fibers are oriented randomly $E_r = E_\theta = E_R$, $E_z = E_h$, and $E_r = E_\theta > E_z$

where E_R is the Young's modulus of random fibres

In the upper layer, in which the collagen fibers are oriented horizontally to the load direction:

$$E_r = E_z = E_h, \quad E_\theta = E_v, \quad \text{and} \quad E_\theta > E_r = E_z$$

Since the cartilage is composed mainly of an isotropic matrix and collagen fibers, the shear lag theory can be used to study this kind of tissue as a composite material.

The elastic modulus of composite is

$$E_c = E_m (1 - \nu_f) + E_f \nu_f \eta_L \eta_0$$

The parameter η_L as shown above

$$\eta_L = 1 - \frac{2 r_f \text{Tanh} \left(l_f \sqrt{\frac{E_m}{E_f (1 + \nu_m) \log \frac{R}{r_f}}} \right)}{l_f \sqrt{\frac{E_m}{E_f (1 + \nu_m) \log \frac{R}{r_f}}}} \quad (6.26)$$

is set equal 1 because for different values of the parameters e_m, ρ, ρ_f varying between the admissible range for this model, it results ≈ 1 .

$$e_m = \frac{E_m}{E_f}, \quad e_m \in \left(\frac{1}{100}, \frac{1}{10} \right) \quad (6.27)$$

$$\rho_f = \frac{r_f}{l_f}, \quad \rho_f \in \left(\frac{1}{100}, \frac{1}{10} \right) \quad (6.28)$$

$$\rho = \frac{r_f}{R}, \quad \rho \in \left] 0, \frac{1}{2} \right[\quad (6.29)$$

Figures 6.11,6.126,7.13 provide an illustration of η_L in function of other parameters

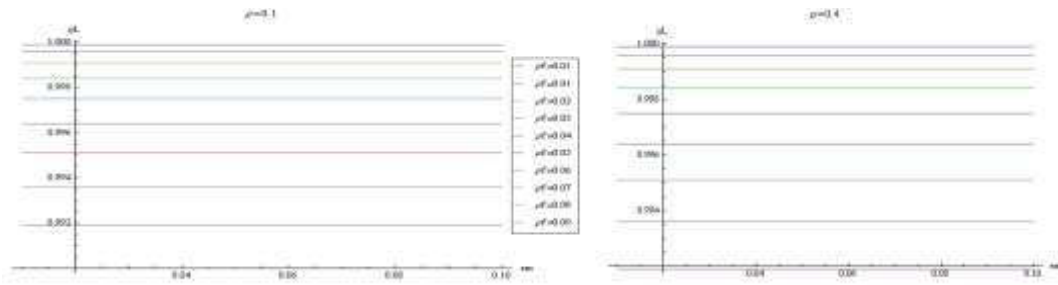


Figure 6.10

Plot of η_L varying ρ_f for two value of ρ

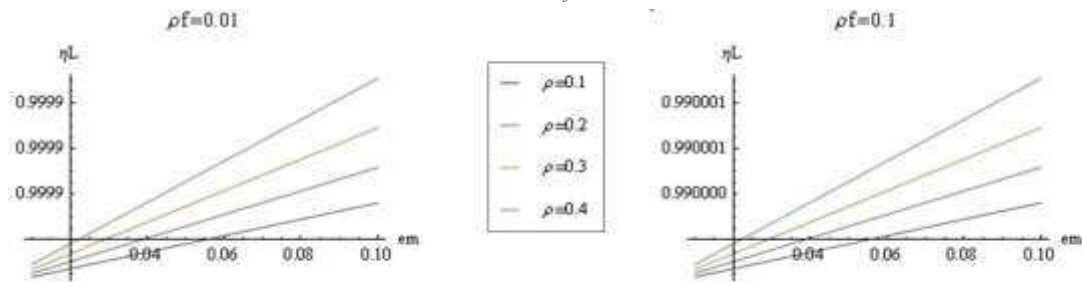


Figure 6.11

Plot of η_L varying ρ for two value of ρ_f

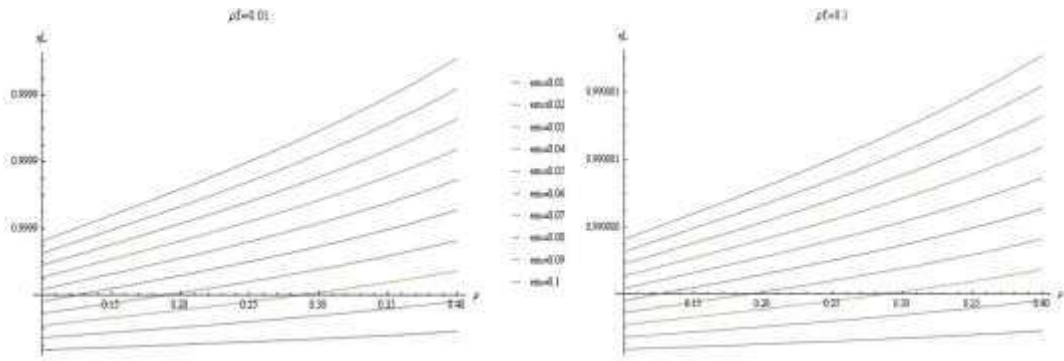


Figure 6.12

Plot of η_L varying e_m for two value of ρ_f

Referring to the Cox's model we show explicitly the elastic moduli variation E_R, E_h, E_v pointing out that collagen fibers are differently oriented in three cartilage layers

$$E_h = E_m (1 - \phi_f) \quad (6.30)$$

$$E_R = E_m (1 - \phi_f) + E_f \phi_f^2 \cos^4 \alpha \quad (6.31)$$

$$E_v = E_m (1 - \phi_f) + E_f \phi_f^2 \quad (6.32)$$

This example aims to demonstrate that collagen fibers orientation in the matrix and the thickness of different cartilage layers is the optimal one to minimize the strain energy function

We consider a tube under internal pressure p_{int} (bone-cartilage contact pressure) and external pressure p_{ext} (cartilage-cartilage contact pressure).

The solution for $\sigma_r(r), \sigma_\theta(r)$ and $\sigma_z(r)$ expressed by Eqs. (6.25)-(6.23) contains two integration constants for each tube ($C_{11}, C_{12}, C_{21}, C_{22}, C_{31}, C_{32}$) and another parameter, the axial strain ε_z^0

The other three integration constants (C_{u1}, C_{u2}, C_{u3}) derived from u_z for each layer since

$$u_z = \int \varepsilon_z dz \quad (6.33)$$

To find these constants we considered the congruence equations for each layer

$$\begin{aligned}\sigma_r^I(r_1) &= \sigma_r^{II}(r_1) \\ \sigma_r^{II}(r_2) &= \sigma_r^{III}(r_2) \\ u_r^I(r_1) &= u_r^{II}(r_1) \\ u_r^{II}(r_2) &= u_r^{III}(r_2) \\ u_z^I(r_1) &= u_z^{II}(r_1) \\ u_z^{II}(r_2) &= u_z^{III}(r_2)\end{aligned}$$

Where r_1 and r_2 are the radius of the first and second layer and I,II, III indicate the first, second and the third layer .

To find the other constants we subject the solution to the following boundary conditions:

$$\sigma_r(R_i) = -p_{int}, \quad \sigma_r(R_e) = -p_{ext}, \quad (6.34)$$

Where R_i and R_e are the inner and outer radii of the whole tube. In the case of zero axial strain, $\varepsilon_z^0 = 0$

To determine the strain energy function for the whole tube, we calculate each strain energy function for single tube representing the single layer of cartilage

$$\begin{aligned}U = U_1 + U_2 + U_3 &= \frac{1}{2} \int_0^{2\pi} \int_{r_i}^{r_1} (\sigma_r^I \varepsilon_r^I + \sigma_\theta^I \varepsilon_\theta^I) r \, dr d\theta + \\ &\frac{1}{2} \int_0^{2\pi} \int_{r_1}^{r_2} (\sigma_r^{II} \varepsilon_r^{II} + \sigma_\theta^{II} \varepsilon_\theta^{II}) r \, dr d\theta + \frac{1}{2} \int_0^{2\pi} \int_{r_2}^{r_3} (\sigma_r^{III} \varepsilon_r^{III} + \sigma_\theta^{III} \varepsilon_\theta^{III}) r \, dr d\theta\end{aligned} \quad (6.35)$$

Where U_1, U_2 and U_3 are the strain Energy function for each tube.

To complete the cartilage model we need values of the elastic moduli of matrix and collagen fibres, Poisson ration, volumetric fraction of collagen and the pressure acting on the cartilage.

In the fibers-reinforced models of cartilage, the tissue is assumed to be biphasic and the solid matrix is divided into a fibrillar and non-fibrillar part. The fibrillar part mimics collagen fibrils, while the non-fibrillar part describes mainly PGs.

The matrix of articular cartilage was assumed to be isotropic The material properties used for the cartilage are reported by Julkunen et al. 2008 and K.B. Gu, 2010..

The applied pressure are shown by Pena et al. 2005.

For different percentage of collagen volumetric fraction, varying in the usually range find in literature, the strain energy function has been calculate and the minimum has been found in function of the radius r_1 and r_2 for determinate the thickness of each cartilage layers.

As shown in the figure 6.14, 6.15 and 6.16 the thickness of the cartilage layers calculated with the mathematical model is contained in the range found in literature. In-fact the first layers in this model, varying between 10 to 20 % of the cartilage surface, the second one varying between 30-70% and the third layer varying 30%

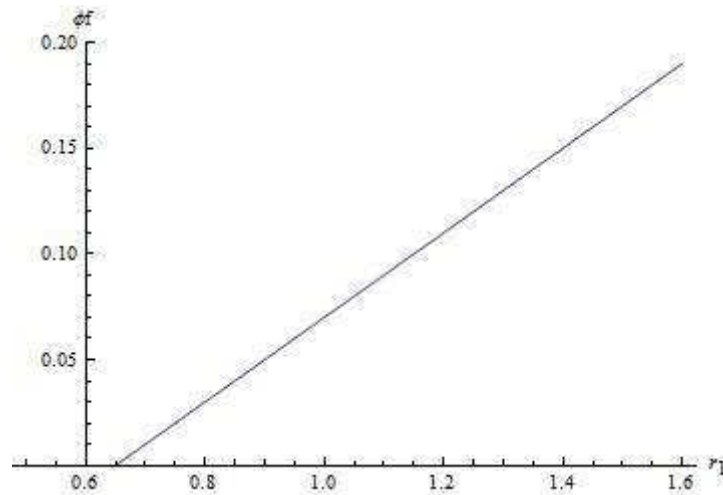


Figure 6.13

Plot of ϕ_f whit respect to r_1

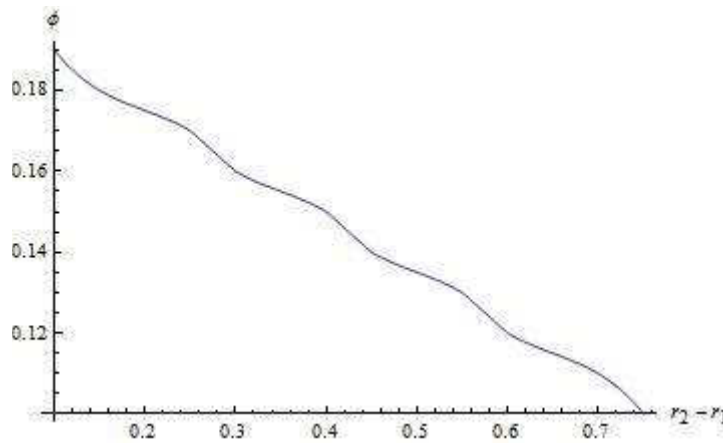


Figure 6.14

Plot of ϕ_f whit respect to central cartilage layer

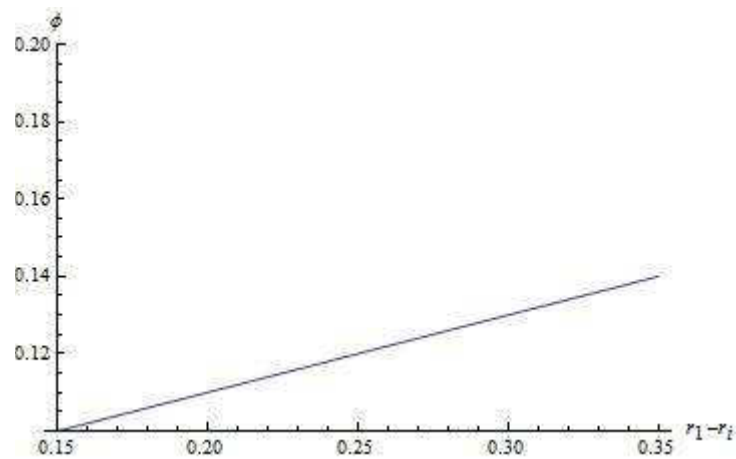


Figure 6.15

Plot of ϕ_f whit respect to inner cartilage layer

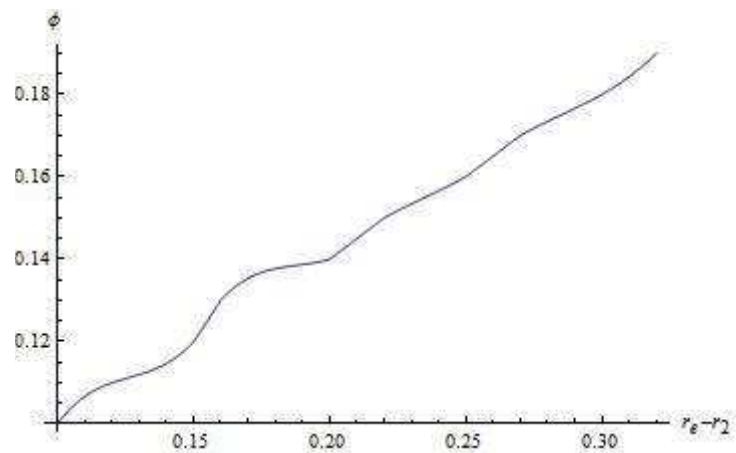


Figure 6.16

Plot of ϕ_f whit respect to superficial cartilage layer

2.3 Conclusions

Biological materials were developed into hierarchical structures with intricate architectures. This example shows how the biological tissue, in particular the articular cartilage, are made to minimized the strain energy function, in-fact the thickness of cartilage layer optimize the use of resources and by change accordingly to external stimuli.

3 Mechanical-based design of Bi-layer poroelastic plates: “optimization over space”

The poroelastic solution by Cowin (Cowin 1994) obtained for homogeneous plates was generalized to the case where the media is constituted by two components.

3.1 Introduction

The poroelasticity theory originated with the geomechanics applications to describe soils behaviour. In 1923, Terzaghi proposed a model of one dimensional consolidation to analyze the influence of pore fluid on soil deformation, but the first author who introduced a complete theory of linear poroelasticity was Biot in his papers (in 1935 and 1941). Poroelasticity has been widely used also to model biological tissues, such as bone, cartilage, arterial walls, brain and osteons, because almost all tissues have an interstitial fluid in their pores. The interstitial fluid plays the role of actor in many crucial functions, like the transport of nutrients from the vasculature to the cells in the tissue or of waste products for removal. As highlighted so far the Poroelasticity theory allows the study of the behaviour of fluid-saturated elastic porous media. A porous material is a solid containing an interconnected network of pores (voids) filled with a fluid (liquid or gas). The Biot formulation of the constitutive equations for a fluid-filled porous material started with the introduction of two new variables: the pore pressure, p , representing another stress component, and the variation in fluid content, ζ , which is a strain component. ζ represents the volume of fluid added or removed from a control volume and, so, the increment in fluid content is, essentially, the “fluid strain”. Also, by introducing of the variation of fluid content, it is necessary to introduce another constitutive equation

$$p = \frac{K_u B}{\alpha} (\zeta - \alpha e) \quad (6.36)$$

Of course, the introduction of a new constitutive equation need another equation to solve. For this purpose we use the continuity equation. The other constitutive equation of the pore theory of elasticity is the Darcy's law which links the fluid velocity to the pressure gradient. According to this law, the fluid flow is directly proportional to the permeability of the material and the pressure gradient, which drives the fluid, while it is inversely proportional to the viscosity of the fluid

$$\mathbf{q}_{fluid} = -\frac{1}{\mu_{fluid}} \mathbf{K}^p (\nabla p - \rho \mathbf{g}) \quad (6.37)$$

where μ_{fluid} is the fluid viscosity, ρ is the fluid density, \mathbf{g} is the gravity acceleration and the minus sign ensures that fluid flows from high to low pressure. The tensor \mathbf{K}_p is the anisotropic permeability tensor, because the permeability of the solid through which the fluid is flowing is not necessarily the same in all directions. In the hypothesis of permeability isotropy we obtain, $\mathbf{K}_p = \kappa \mathbf{I}$, where κ is a constant. The permeability has dimension of length squared and it is related to the pore geometry. It depends strongly on the porosity, defined as $\phi = \frac{V_{fluid}}{V_{tot}}$. The permeability is generally linked to the porosity through a power law, strictly depending on pore. Finally, the fluid velocity within the pores is related to the flux by the porosity:

$$\mathbf{v} = \frac{\mathbf{q}_{fluid}}{\phi} \quad (6.38)$$

The flux is divided by porosity to take into account that only a fraction of the total volume is available for flow. Now consider the limiting cases of this theory, the Skempton coefficient that measures how load is distributed between solid and fluid is $B=1$, if the solid is incompressible $K_u = \infty$ while if the solid matrix is incompressible, the coefficient of Biot is $\alpha = 1$. Combining these assumptions we obtain that the coefficient of Storage, which represents the ratio of the variation of

fluid content compared to pressure change under different porous conditions, is

$$\frac{1}{M} = 0 \quad \text{and the variation of fluid content is equal to the trace of strain tensor } \zeta = e$$

3.2 Formulation and solution

This theory of Biot, is used to describe the behavior of two poroelastic plates, loaded with an axial force and a bending moment, both of which are applied cyclically in time. The assumptions made to obtain a poro-elastic solution are that:

- (1) the material is isotropic;
- (2) the stress-strain relations are linear and reversible;
- (3) the strains are small;
- (4) both the liquid phase and the solid phase are compressible;
- (5) the pore fluid pressure and the pore fluid velocity are related by Darcy's law;
- (6) the deformation is quasi-static, i.e. the inertia terms are neglected;

Therefore, consider two poroelastic plates shown in (Fig.6.17), with a width w , a thickness $2d$ and a length L .

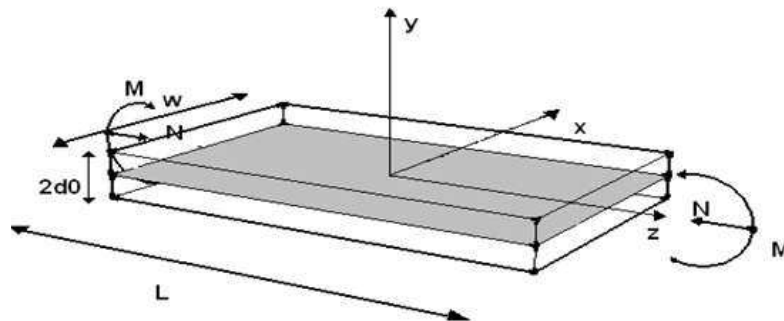


Fig. 6.17

The plates and the coordinate system employed

The boundary conditions applied at the top of the first plate and at the bottom of the second plate link the pressure gradient at the boundary to the pressure at the boundary, where η is called the leakage coefficient. This boundary condition is a combination of

$$\frac{\partial p(t, \pm d)}{\partial y} = \mp \frac{\eta}{d} \quad (6.39)$$

When $\eta = 0$ there is no leakage at the boundaries. This corresponds to the case when the surface tension at the pores on the surface of the plate is so large that no fluid communication between the plate and the environment occurs (Salzstein and Pollack, 1987). When $\eta \rightarrow \infty$ there is a free leakage at the boundaries, i.e. $p = 0$ at the boundaries. This corresponds to the case when the plate is immersed in a bath of the same fluid as that inside the plate so that a free interchange of fluid occurs between the plate and its environment. Generally η is a finite constant at each surface point. In this study, η is assumed to be a single constant (varying from 0 to ∞) on the top and bottom surfaces $y = \pm d$. On the other eight surfaces of the plate the pressure gradient is assumed to be zero in the direction normal to each of them. The following assumption, which employs the coordinate system of Fig.6.17, is made to solve the problem: all the physical quantities involved depend only on the spatial coordinate y and time t .

Because applied loadings are related to the stress components $\sigma_{xx}^{(1)}$ and $\sigma_{zz}^{(1)}$ of the stress tensor T_1 and $\sigma_{xx}^{(2)}$ and $\sigma_{zz}^{(2)}$ of the stress tensor T_2 , the loading conditions on the two plates are

$$N_x = -\left[\int_{-d}^0 \sigma_{xx}^{(2)} dy + \int_0^{d_0} \sigma_{xx}^{(1)} dy \right] = 0 \quad (6.40)$$

$$N_z = -\frac{1}{w_A} \int (\sigma_{zz}^{(1)} + \sigma_{zz}^{(2)}) dA = -\left[\int_{-d}^0 \sigma_{zz}^{(2)} dy + \int_0^{d_0} \sigma_{zz}^{(1)} dy \right] = N_0 \sin \omega t \quad (6.41)$$

$$M_x = -\left[\int_{-d}^0 y \sigma_{xx}^{(2)} dy + \int_0^{d_0} y \sigma_{xx}^{(1)} dy \right] = 0 \quad (6.42)$$

$$M_z = -\frac{1}{w_A} \int (y \sigma_{zz}^{(1)} + y \sigma_{zz}^{(2)}) dA = -\left[\int_{-d}^0 y \sigma_{zz}^{(2)} dy + \int_0^d y \sigma_{zz}^{(1)} dy \right] = M_0 \sin \omega t \quad (6.43)$$

Using the elastic plate theory we can write, for each of the four loading above, the following displacement fields :

From (6.40) we have

$$u^{(1)}_{1x} = C^{(1)}_1(t)x$$

$$u^{(1)}_{1y} = -v_1 C^{(1)}_1(t)y$$

$$u^{(1)}_{1z} = -v_1 C^{(1)}_1(t)z$$

$$u^{(2)}_{1x} = C^{(2)}_1(t)x$$

$$u^{(2)}_{1y} = -v_2 C^{(2)}_1(t)y$$

$$u^{(2)}_{1z} = -v_2 C^{(2)}_1(t)z$$

From (6.41)

$$u^{(1)}_{2x} = -v_1 C^{(1)}_2(t)x$$

$$u^{(1)}_{2y} = -v_1 C^{(1)}_2(t)y$$

$$u^{(1)}_{2z} = C^{(1)}_2(t)z$$

$$u^{(2)}_{2x} = -v_2 C^{(2)}_2(t)x$$

$$u^{(2)}_{2y} = -v_2 C^{(2)}_2(t)y$$

$$u^{(2)}_{2z} = C^{(2)}_2(t)z$$

From (6.42)

$$u^{(1)}_{3x} = -v_1 C^{(1)}_3(t)xy$$

$$u^{(1)}_{3y} = -\frac{C^{(1)}_3(t)}{2} [z^2 + v_1 (y^2 - x^2)]$$

$$u^{(1)}_{3z} = C^{(1)}_3(t)yz$$

$$u^{(2)}_{3x} = -v_2 C^{(2)}_3(t)xy$$

$$u^{(2)}_{3y} = -\frac{C^{(2)}_3(t)}{2} [z^2 + v_2 (y^2 - x^2)]$$

$$u^{(2)}_{3z} = C^{(2)}_3(t)yz$$

Form (6.43)

$$u^{(1)}_{4x} = C^{(1)}_4(t)xy$$

$$u^{(1)}_{4y} = -\frac{C^{(1)}_4(t)}{2} [x^2 + v_1 (y^2 - z^2)]$$

$$u^{(1)}_{4z} = -v_1 C^{(1)}_4(t)zy$$

$$u^{(2)}_{4x} = C^{(2)}_4(t)xy$$

$$u^{(2)}_{4y} = -\frac{C^{(2)}_4(t)}{2} [x^2 + v_2 (y^2 - z^2)]$$

$$u^{(2)}_{4z} = -v_2 C^{(2)}_4(t)zy$$

where $C_1^{(1)}(t), C_1^{(2)}(t), C_2^{(1)}(t), C_2^{(2)}(t), C_3^{(1)}(t), C_3^{(2)}(t), C_4^{(1)}(t), C_4^{(2)}(t)$, are arbitrary functions of time.

To obtain an analytical solution is considered the whole displacement field like the sum of four single components plus a further displacement field attributable to the pore fluid pressure:

$$\begin{aligned}
 \mathbf{u}_x^{(1)} &= u_{1x}^{(1)} + u_{2x}^{(1)} + u_{3x}^{(1)} + u_{4x}^{(1)} + u_x^{p_1} \\
 \mathbf{u}_y^{(1)} &= u_{1y}^{(1)} + u_{2y}^{(1)} + u_{3y}^{(1)} + u_{4y}^{(1)} + u_y^{p_1} \\
 \mathbf{u}_z^{(1)} &= u_{1z}^{(1)} + u_{2z}^{(1)} + u_{3z}^{(1)} + u_{4z}^{(1)} + u_z^{p_1} \\
 \mathbf{u}_x^{(2)} &= u_{1x}^{(2)} + u_{2x}^{(2)} + u_{3x}^{(2)} + u_{4x}^{(2)} + u_x^{p_2} \\
 \mathbf{u}_y^{(2)} &= u_{1y}^{(2)} + u_{2y}^{(2)} + u_{3y}^{(2)} + u_{4y}^{(2)} + u_y^{p_2} \\
 \mathbf{u}_z^{(2)} &= u_{1z}^{(2)} + u_{2z}^{(2)} + u_{3z}^{(2)} + u_{4z}^{(2)} + u_z^{p_2}
 \end{aligned} \tag{6.44}$$

Then we assume that the pore fluid pressure of the first plate and the pore fluid pressure of the second plate are the derivative with respect to y of an arbitrary potential function ξ_1 e ξ_2 :

$$p_1(y, t) = \frac{\partial \xi_1(y, t)}{\partial y} \quad p_2(y, t) = \frac{\partial \xi_2(y, t)}{\partial y} \tag{6.45}$$

So, the displacement fields due to the pressure are:

$$\begin{aligned}
 u_x^{p_1} &= 0 & u_x^{p_2} &= 0 \\
 u_y^{p_1} &= \frac{\Lambda_1}{4G_1} \xi_1(y, t) & u_y^{p_2} &= \frac{\Lambda_2}{4G_2} \xi_2(y, t) \\
 u_z^{p_1} &= 0 & u_z^{p_2} &= 0
 \end{aligned}$$

where Λ_1 and Λ_2 are

$$\Lambda_1 = \frac{6(v_{1u} - v_1)}{B_{01}(1 - v_1)(1 + v_{1u})} \quad \Lambda_2 = \frac{6(v_{2u} - v_2)}{B_{02}(1 - v_2)(1 + v_{2u})} \tag{6.47}$$

To solve our problem, we consider:

The conditions at the interface:

$$\begin{aligned}
 u_x^{(1)} &= u_x^{(2)} \\
 u_y^{(1)} &= u_y^{(2)} \\
 u_z^{(1)} &= u_z^{(2)} \\
 p_1 &= p_2 \\
 k_1 \nabla p_1 &= k_2 \nabla p_2
 \end{aligned} \tag{6.48}$$

showing that at the interface the three components of the displacement field, pore pressure and fluid velocity along the two plates are equal.

Recalling the fluid mass conservation equation

$$\begin{aligned}
 c_1 \nabla^2 \left(\sigma_{kk}^{(1)} + \frac{3}{B_{01}} p_1 \right) &= \frac{\partial}{\partial t} \left(\sigma_{kk}^{(1)} + \frac{3}{B_{01}} p_1 \right) \quad \text{where} \\
 c_1 &= \kappa_1 \left[\frac{2G_1(1-\nu_1)}{(1-\nu_1)} \right] \left[\frac{B_1^2(1+\nu_{1u})^2(1-2\nu_1)}{9(1-\nu_{1u})(\nu_{1u}-\nu_1)} \right]
 \end{aligned} \tag{6.49}$$

and

$$\begin{aligned}
 c_2 \nabla^2 \left(\sigma_{kk}^{(2)} + \frac{3}{B_{02}} p_2 \right) &= \frac{\partial}{\partial t} \left(\sigma_{kk}^{(2)} + \frac{3}{B_{02}} p_2 \right) \\
 \text{where } c_2 &= \kappa_2 \left[\frac{2G_2(1-\nu_2)}{(1-\nu_2)} \right] \left[\frac{B_2^2(1+\nu_{2u})^2(1-2\nu_2)}{9(1-\nu_{2u})(\nu_{2u}-\nu_2)} \right]
 \end{aligned} \tag{6.50}$$

With $\kappa_1 = k_1/\mu_1$ and $\kappa_2 = k_2/\mu_2$ are the permeability, ratio between specific permeability k_1, k_2 and viscosity μ_1, μ_2 and B_{01}, B_{02} are Skempton's coefficients.

Due to the harmonic form of the loads, we can use Euler's formula, to interpret each load and, consequently, each field displacement component, like the sum of two

exponential functions (i.e. $N_0 \sin \omega t = \frac{N_0}{2i} e^{i\omega t} - \frac{N_0}{2i} e^{-i\omega t}$).

Then, it is possible to assume that the potential functions ξ_1 and ξ_2 , introduced by (6.47), is like the product of two functions, a function of time and the another one with only space variability:

$$\xi_1(y, t) = g_1(y)q_1(t) + g_3(y)q_3(t) \qquad \xi_2(y, t) = g_1(y)q_2(t) + g_4(y)q_4(t)$$

where

$$q_1(t) = e^{i\omega t}$$

$$g_1(y) = \left(\frac{c_1}{i\omega}\right)^{\frac{3}{2}} \left(A_1 e^{\frac{\sqrt{i\omega y}}{\sqrt{c_1}}} + A_2 e^{-\frac{\sqrt{i\omega y}}{\sqrt{c_1}}} \right) + A_3 y^2 + yA_4$$

$$q_3(t) = e^{-i\omega t}$$

$$g_3(y) = \left(\frac{c_1}{-i\omega}\right)^{\frac{3}{2}} \left(B_1 e^{\frac{\sqrt{-i\omega y}}{\sqrt{c_1}}} + B_2 e^{-\frac{\sqrt{-i\omega y}}{\sqrt{c_1}}} \right) + B_3 y^2 + yB_4$$

$$q_2(t) = e^{i\omega t}$$

$$g_2(y) = \left(\frac{c_2}{i\omega}\right)^{\frac{3}{2}} \left(A_5 e^{\frac{\sqrt{i\omega y}}{\sqrt{c_1}}} + A_6 e^{-\frac{\sqrt{i\omega y}}{\sqrt{c_1}}} \right) + A_7 y^2 + yA_8$$

$$q_4(t) = e^{-i\omega t}$$

$$g_4(y) = \left(\frac{c_2}{-i\omega}\right)^{\frac{3}{2}} \left(B_5 e^{\frac{\sqrt{-i\omega y}}{\sqrt{c_2}}} + B_6 e^{-\frac{\sqrt{-i\omega y}}{\sqrt{c_2}}} \right) + B_7 y^2 + yB_8$$

Where $A_1, A_2, A_3, A_4, A_5, A_6, A_7, A_8, B_1, B_2, B_3, B_4, B_5, B_6, B_7, B_8$ are the first sixteen unknowns of our problem.

Particularly, we can write,

$$C^{(1)}_1(t) = D_1 e^{i\omega t} + D_2 e^{-i\omega t}$$

$$C^{(2)}_1(t) = D_5 e^{i\omega t} + D_6 e^{-i\omega t}$$

$$C^{(1)}_2(t) = D_3 e^{i\omega t} + D_4 e^{-i\omega t}$$

$$C^{(2)}_2(t) = D_7 e^{i\omega t} + D_8 e^{-i\omega t}$$

$$C^{(1)}_3(t) = E_1 e^{i\omega t} + E_2 e^{-i\omega t}$$

$$C^{(2)}_3(t) = E_5 e^{i\omega t} + E_6 e^{-i\omega t}$$

$$C^{(1)}_4(t) = E_3 e^{i\omega t} + E_4 e^{-i\omega t}$$

$$C^{(2)}_4(t) = E_7 e^{i\omega t} + E_8 e^{-i\omega t}$$

Where $D_1, D_2, D_3, D_4, D_5, D_6, D_7, D_8, E_1, E_2, E_3, E_4, E_5, E_6, E_7, E_8$ are further sixteen unknowns.

To calculate the values of the thirty-two unknowns we have to consider the load conditions, the two boundary conditions and conditions at the interface, putting in evidence with respect to y , $e^{i\omega t}$ and $e^{-i\omega t}$ and using polynomial identity principle we obtain thirty-two equations in thirty-two unknowns. Solving this system we have $A_1, A_2, A_3, A_4, A_5, A_6, A_7, A_8, B_1, B_2, B_3, B_4, B_5, B_6, B_7, B_8, D_1, D_2,$

$D_3, D_4, D_5, D_6, D_7, D_8, E_1, E_2, E_3, E_4, E_5, E_6, E_7, E_8$ and the analytical solution is completely determined.

For this study the software Mathematica 8 has been used, to graphically show that the profiles of the pore pressure, fluid velocity, variation of the fluid content and the stress components are the same either when we consider two coupled plates or we consider one. We use the values typical of the lacunar-canalicular level of bone as used by Cowin in his paper in the case of single poroelastic plate.

3.3 Values of the parameters

The values used are the same employed by Cowin in the case of single poroelastic plate except for the Young's moduli, which are given by two different values for both the first and second plate, chosen as the average of Young's modulus for the lacunar-canalicular level of bone (18 GPa), the Poisson's ratios, for which we have chosen three different values of the first plate, ν_1 , (0.499, 0.0 and -0.5), while for the second plate ν_2 , the value remains unchanged (0.25) and the permeability, which assume three different values, whose average is always equal to one. The bulk modulus K_f for salt water is given as 2.3 GPa. K_s , the bulk modulus of the solid phase, is estimated to be 16 GPa. The values of the drained shear moduli G_1 and G_2 are about 7.2 GPa. Λ_1 and Λ_2 are evaluated by (2.13) and they are 0.35. Permeability κ_1, κ_2 and viscosities are taken equal to 1. ρ_f and ρ_{f0} - effective and reference value of the fluid density – are respectively 0.8 and 1. The porosity for both the first plate and the second plate is chosen equal to 0.05. The thickness of the plates considered is $2d = 2$ mm. Lastly, N_0 and M_0 , amplitudes of the loading, are imposed equal to 1.

3.4 Result and qualitative remarks

In order to demonstrate the behavior of the two plates analyzed and to be able to do an efficacious comparison with the results obtained by Cowin, the pore fluid

pressure, the velocity flow profile, the variation of fluid content and the stress components σ_z and σ_x are plotted across the thickness of the plates and versus time for three different ratios of the Young's moduli (for the four values of frequency and for the four values of leakage coefficient) and – then - for four different ratios of Poisson's ratio (for the four values of frequency and for the four values of leakage coefficient). The three different values of E_1 employed are 20, 22 and 18, and consequently E_2 is equal 16, 14 and 18 respectively. The four different values of ν_1 employed are 0.499, 0.0, -0.5 and 0.25 (assuming $\nu_2=0.25$). The four frequencies are 2.693, 26.93, 269.3 and 2693, fixing the leakage coefficient $\eta = 1$. In the plot versus y , the functions are taken at the instant $t = 2\pi / 3$.

Furthermore, the average entities considered, calculated with respect to the thickness, are plotted versus time for value of loading frequency $\omega = 269.3$ fixing $\eta = 1$

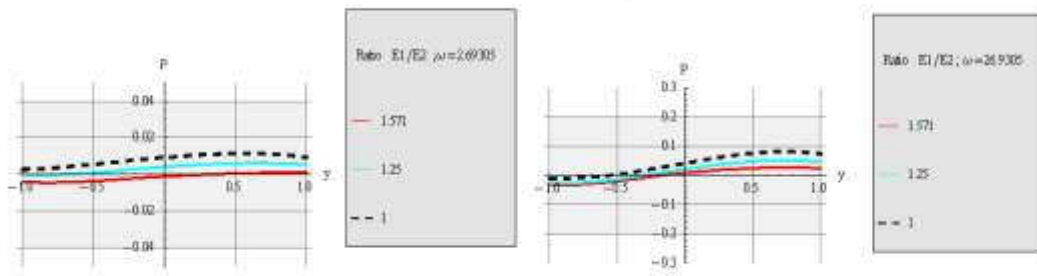


Figure. 6.18

*The pore fluid pressure distribution for $\eta = 1$ and $t = 2\pi / 3$
For different ω*

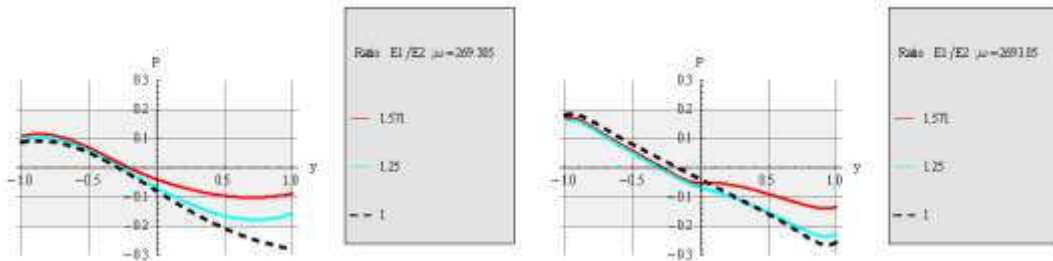


Figure. 6.19

The pore fluid pressure distribution for $\eta = 1$ and $t = 2\pi / 3$

Fig.6.18, and Fig.6.19 show the pressure profile for four different values of frequencies fixed the leakage coefficient equal 1 and for two different values of ratio of Young's moduli and considering $t = 2\pi / 3$. From the graphs we can see that the pressure profiles maintain the same trend obtained in the homogeneous case represented by a curve piecewise.

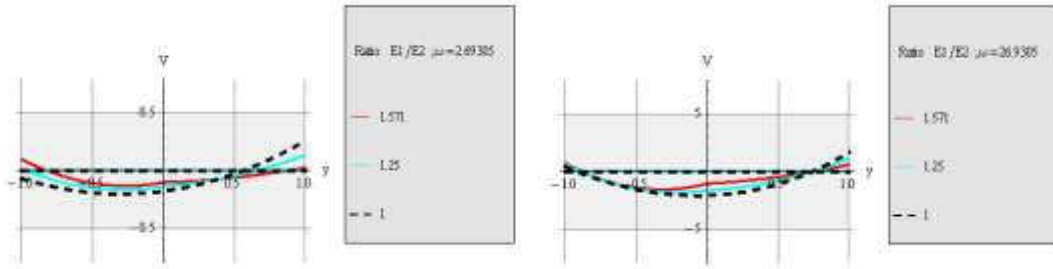


Figure 6.20

*The velocity flow profile $v(y)$ versus y for $\eta = 1$ and $t = 2\pi / 3$
For different ω*

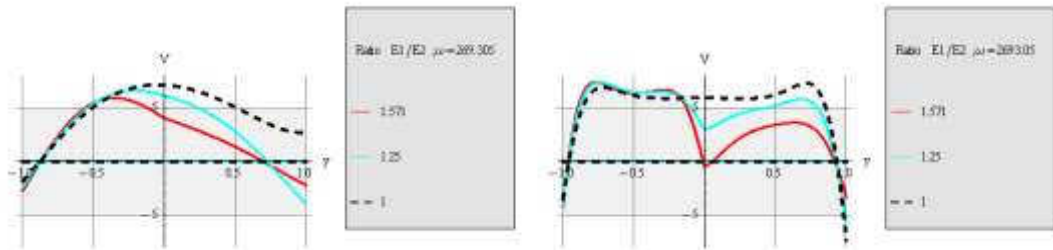


Fig. 6.21

The velocity flow profile $v(y)$ versus y for $\eta = 1$ and $t = 2\pi / 3$

Fig.6.20, and Fig 6.21 represent the behavior of velocity flow profile. Its distribution over the thickness is strongly not linear. Infact, as the ratio of Young's moduli increases the velocity decreases. A very important aspect is that for $\omega = 269.3$ we have a change of sign, which means that the fluid does not pass from low to high pressure (from medium 1 to medium 2) but it flows from low to high pressure (from medium 2 to medium 1). Also for high frequencies the fluid velocity at the interface decreases.

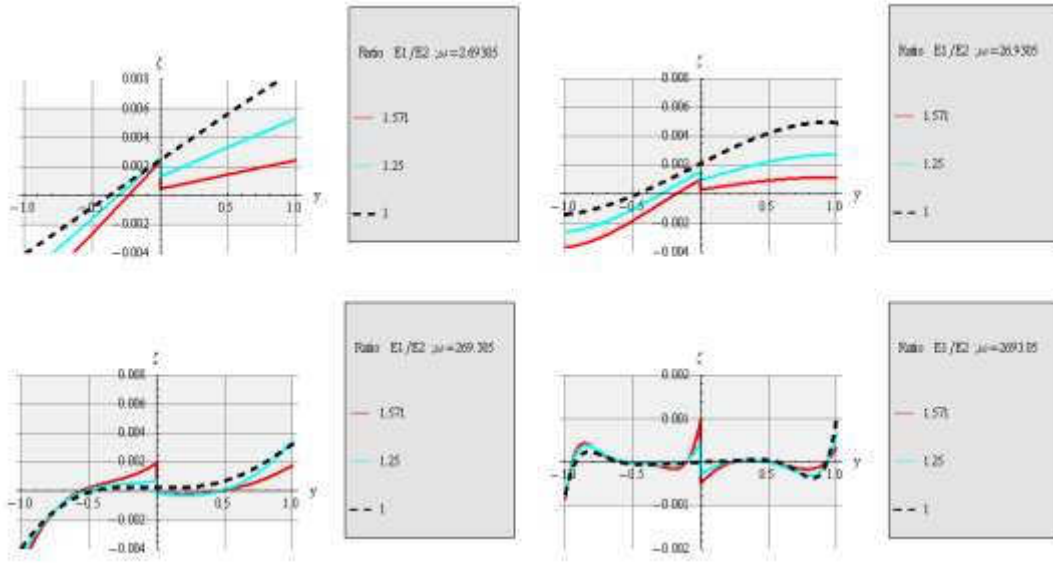


Figure 6.22

The variation of fluid content distribution for $\eta = 1$ and $t = 2\pi / 3$

The significance of these representations is related to the possibility of deducing helpful information about the distribution of the fluid, in order to predict its paths and concentrations, particularly important in many applications in poroelasticity. Graphs show a discontinuity passing from one medium to another, therefore we have the condition in which a medium is filled more than the other.

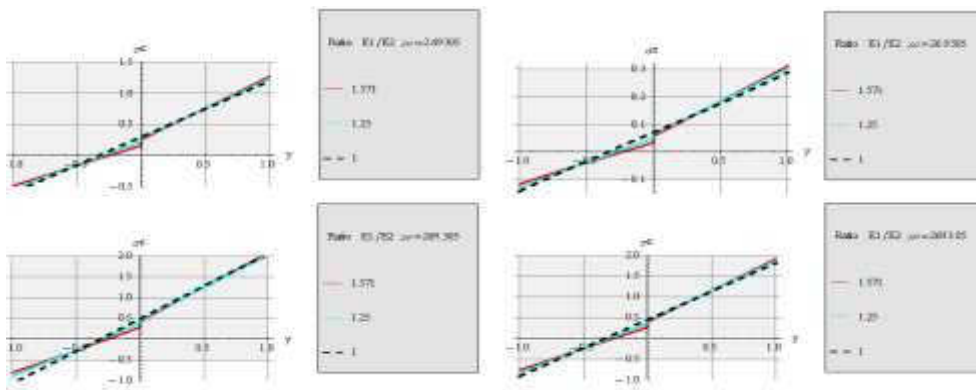


Figure 6.23

The stress σ_z distribution for $\eta = 1$ and $t = 2\pi / 3$

Fig 6.23, represent the profile of the stress tensor σ_z . The curves obtained for different Young's moduli are similar to those obtained in the homogeneous case.

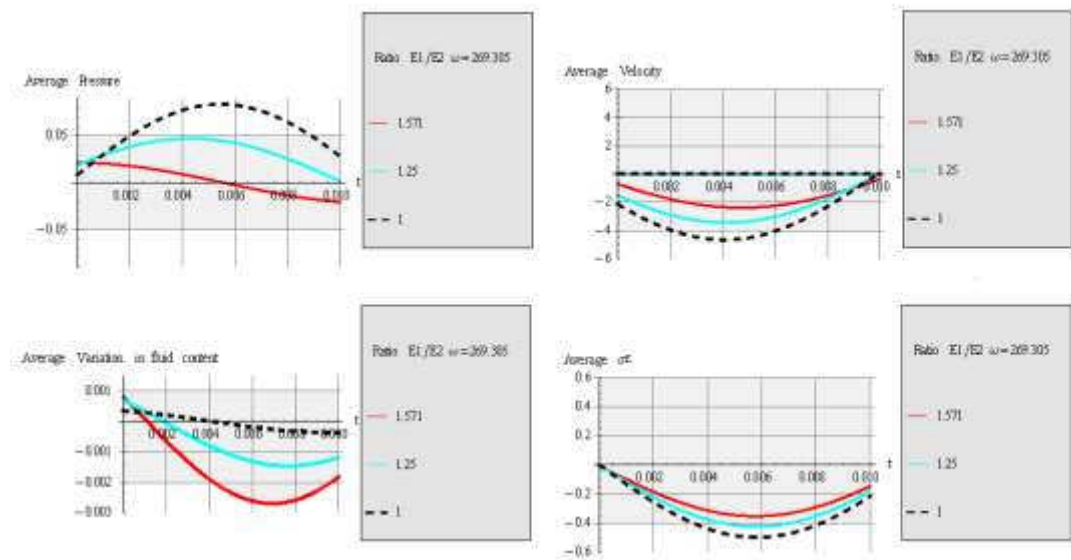


Figure 6.24

The average pressure, velocity, variation in fluid content and σ_z respect to the thickness versus t for $\eta = 1$

The plots in Fig.6.18 represent the spatially averaged entities above considered versus time for a loading frequency $\omega = 269.3$ (fixed $\eta = 1$). These profile show that the average pressure decreases with increasing the ratio of Young's moduli while the velocity of fluid increases with increasing the ratio. Now, we consider the results obtained for different values of the ratio of the Poisson's ratios.

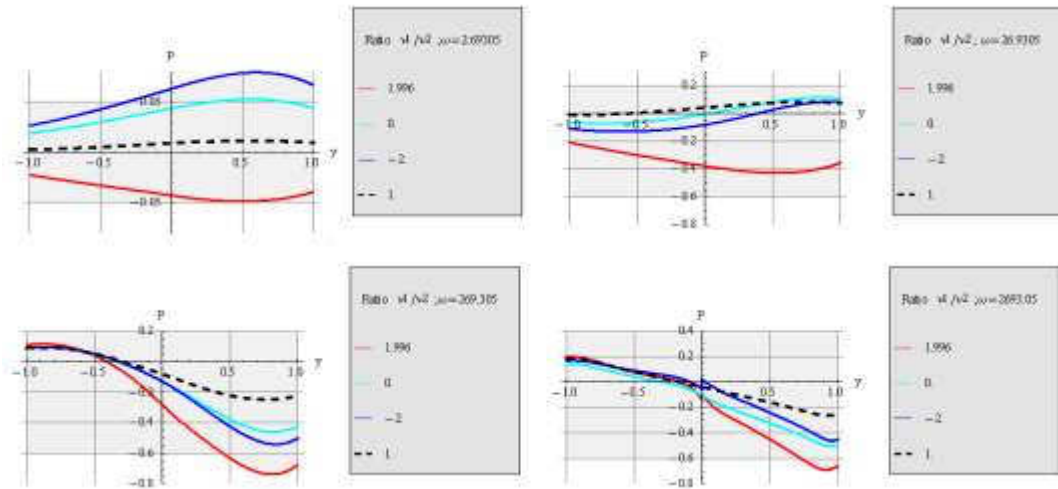


Figure 6.25

The pore fluid pressure distribution for $\eta = 1$ and $t = 2\pi / 3$

The Fig.6.25, show the variation of the pore pressure for different values of the Poisson's ratio.

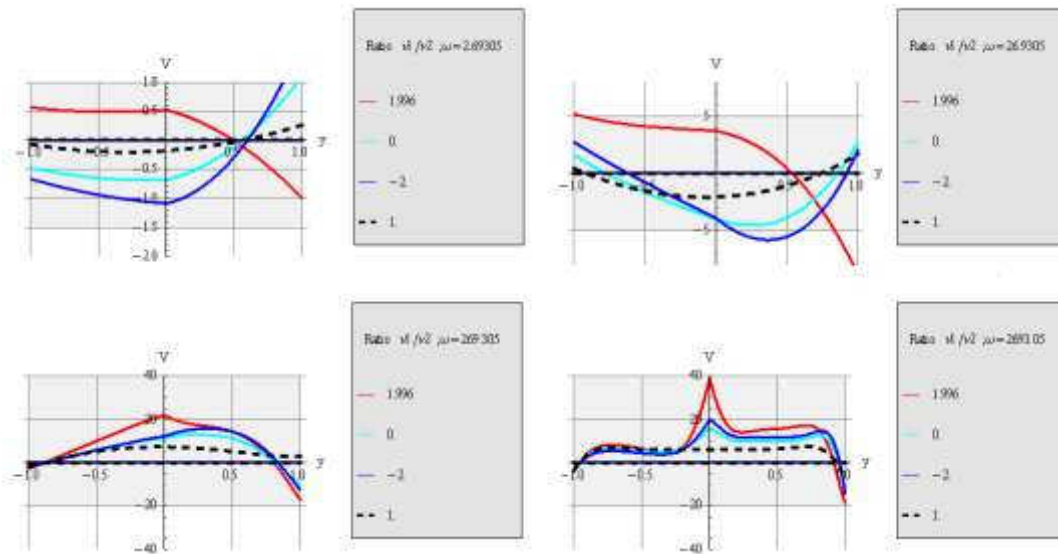


Figure 6.26

The velocity flow profile $v(y)$ versus y for $\eta = 1$ and $t = 2\pi / 3$

The Fig.6.26 represent the behavior of velocity flow profile. Its amplitude increases with increasing the frequencies. For $\omega = 269.3$ and $\omega = 2693.05$ the amplitude of velocity change of sign so the fluid flows from medium 2 to medium 1.

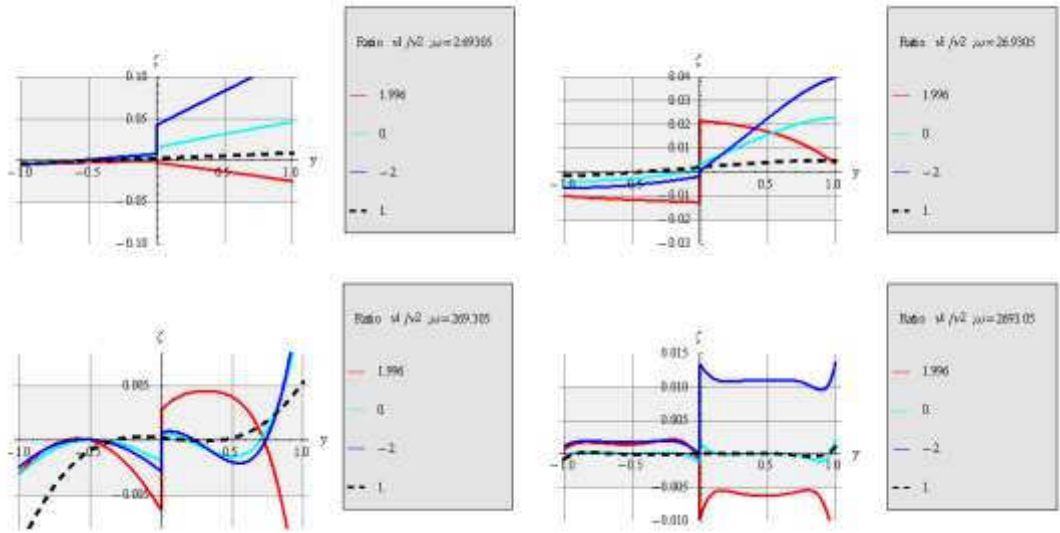


Figure 6.27

The variation of fluid content distribution for $\eta = 1$ and $t = 2\pi / 3$

The graphs represent the variation of the fluid content and the trends highlight a greater concentration of fluid in a medium than the other. In the homogeneous case we had a homogeneous distribution of the fluid.

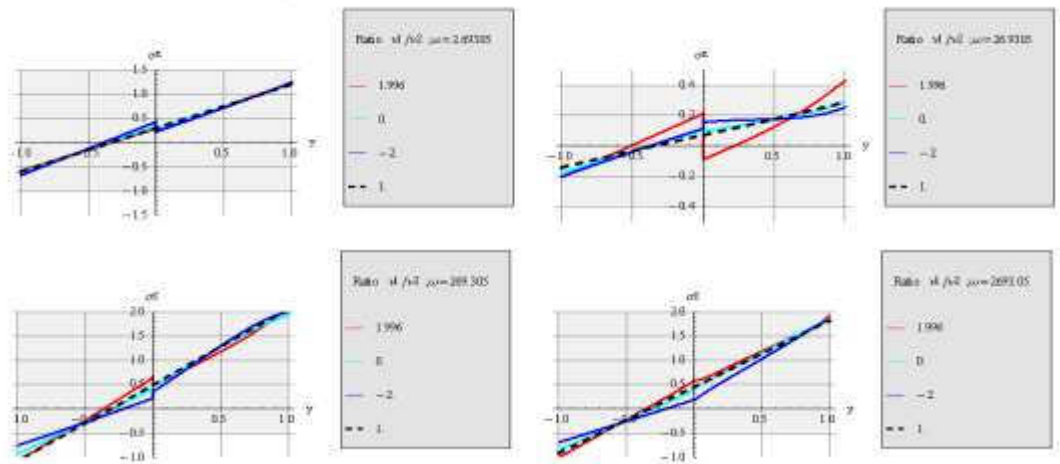


Fig. 6.28

The stress σ_z distribution for $\eta = 1$ and $t = 2\pi / 3$

The plots in Fig 6.28 demonstrate that for high frequencies the σ_z increases with increases the ratio of the Poisson's ratios.

Finally the pore fluid pressure, the velocity flow profile, the variation of fluid content and the stress components σ_z and σ_x are plotted across the thickness of the plates for four different permeability (for the three values of frequency).

The four different values of k_1 employed are 1.95, 1.9, 1.5 and 1, and consequently k_2 is equal 0.05, 0.1, 0.5 and 1 respectively. The three different values of frequencies employed are 2.693, 26.93 and 269.3 (fixing $\eta = 1$). In the plot versus y , the functions are taken at the instant $t = 2\pi / 3$.

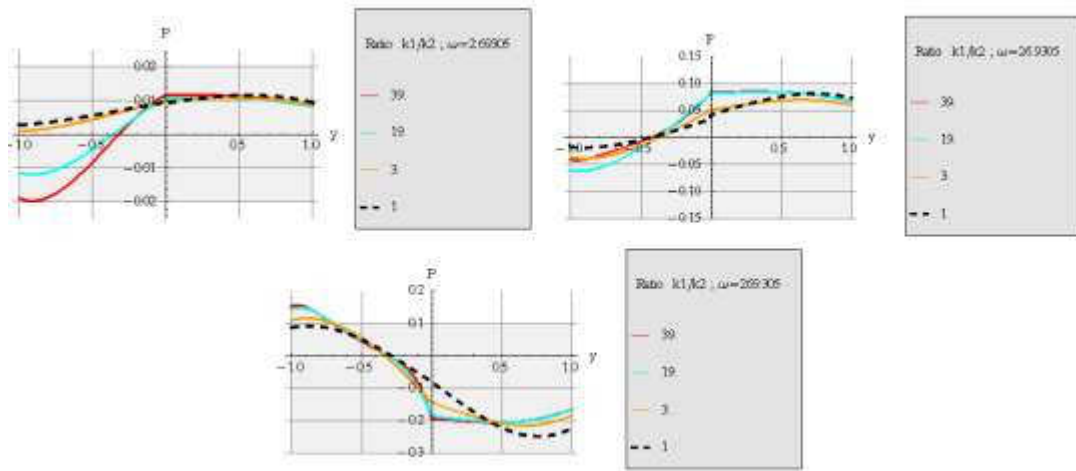


Figure. 6.29

The pore fluid pressure distribution for $\omega = 2.69305, 26.9305$ and 269.305 and $t = 2\pi / 3$

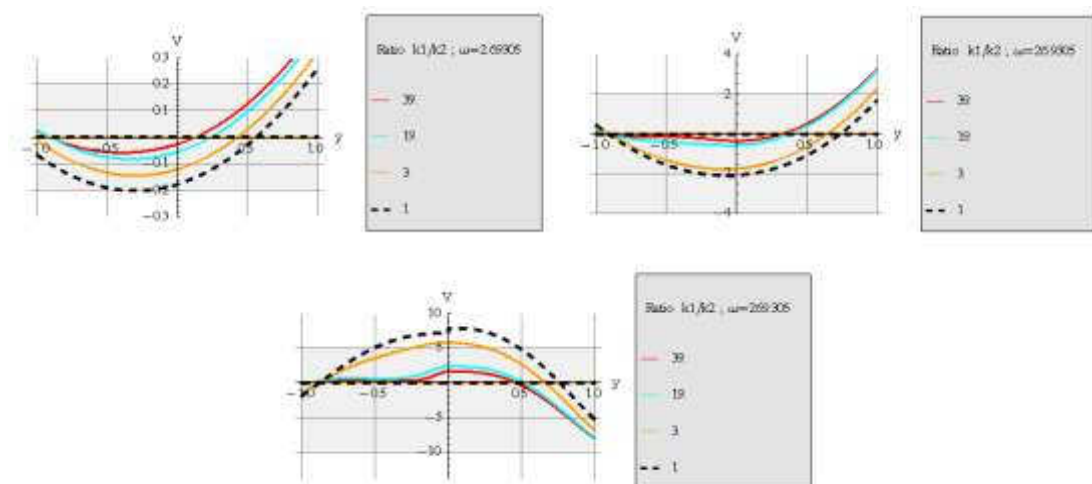


Figure. 6.30

The velocity flow profile for $\omega = 2.69305, 26.9305$ and 269.305 and $t = 2\pi / 3$

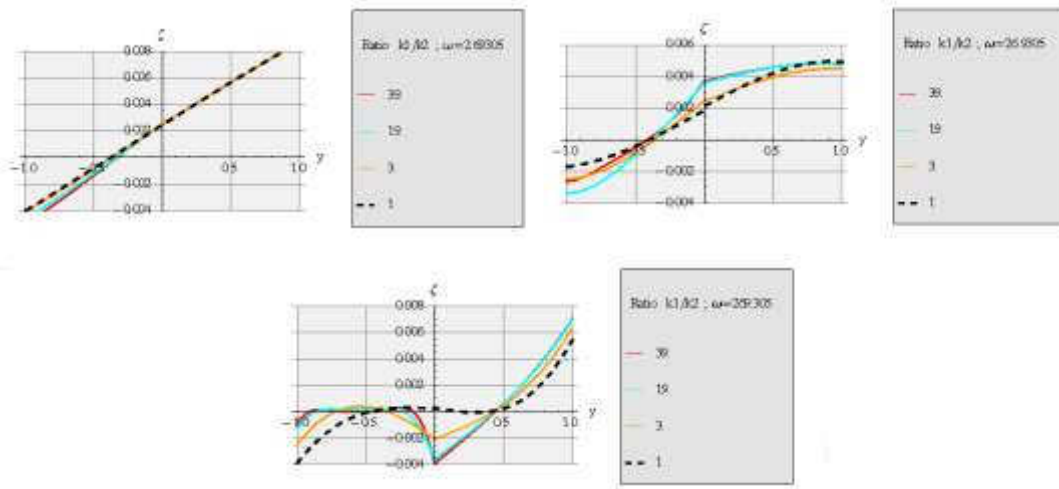


Figure 6.31

The variation of fluid content distribution for $\omega = 2.69305, 26.9305$ and 269.305 and $t = 2\pi / 3$

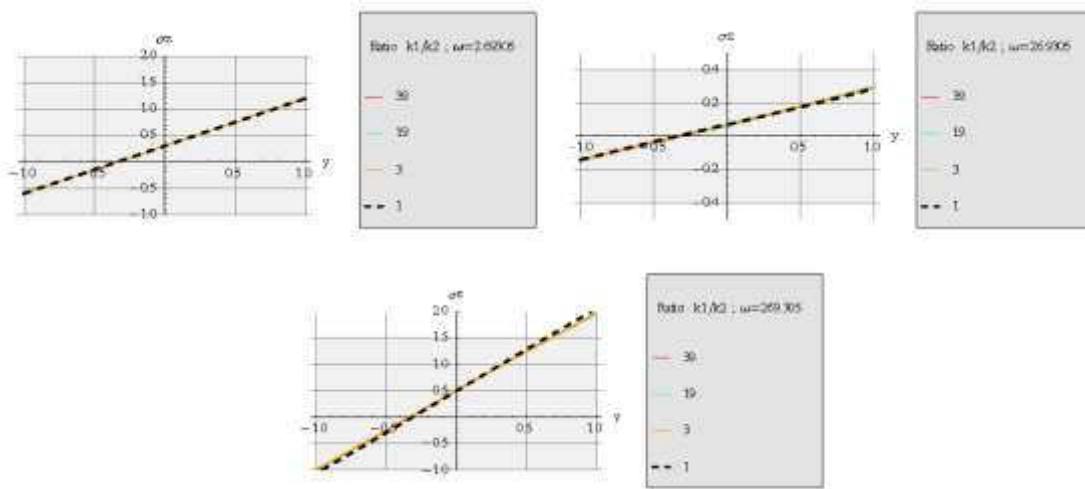


Figure 6.32

The stress σ_z distribution for $\omega = 2.69305, 26.9305$ and 269.305 and $t = 2\pi / 3$

Furthermore, the average entities considered, calculated with respect to the thickness, are plotted versus time for different values of permeability fixing $\omega = 269.3$ and $\eta = 1$

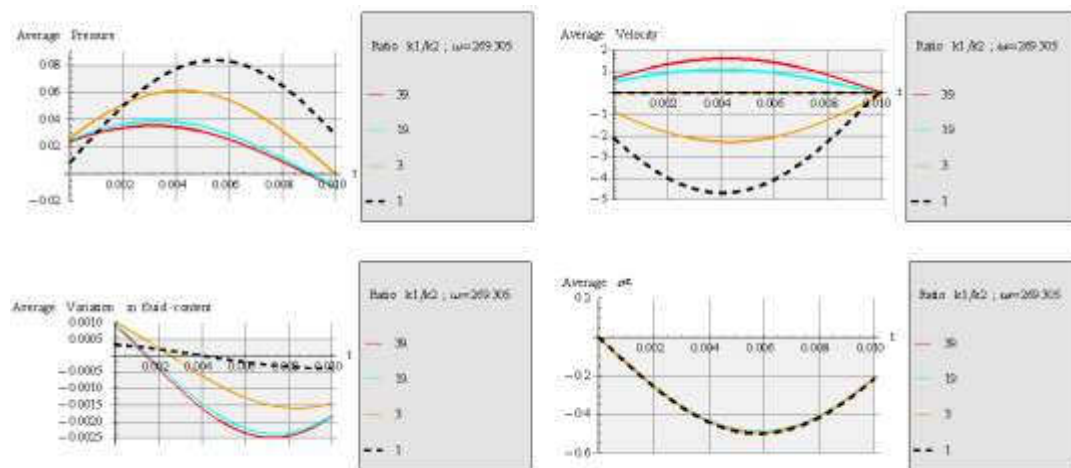


Figure 6.33

The average of pressure, fluid velocity, variation in fluid content and σ_z respect to the thickness versus t for $\eta = 1$

3.5 Conclusions

The variation of the response function, in terms of stresses, pressure and fluid content and velocity, was analyzed by using several parametric values of permeabilities values, Young's moduli and Poisson's ratios. The results allow to better interpret the adaptive processes governing many biological tissue, in which the hierarchical heterogeneous features result from optimization logics aimed to obtain best varying stiffness and permeability features.

Additionally, the analytical solution could be helpfully employed for designing controlled release systems of drugs, as those named “*mechanically activated drug delivery devices*”

CONCLUSIONS

Nature has always inspired human achievements and has led to effective materials, structures, tools, mechanisms, processes, algorithms, methods, systems, and many other benefits.

Biomimicry is a design discipline that seeks sustainable solutions by emulating nature. Through evolution, nature has ‘experimented’ with various solutions to its challenges and has improved the successful ones

Biomimetics is addressed to the design and development of new materials and structures using strategies adopted by living organisms to produce biological materials.

Specifically, Nature, or biology, experimented with the principles of physics, chemistry, mechanics, materials science, mobility, control, sensors, and many other fields that we recognize as science and engineering. The process has also involved scaling from nano and micro to macro and mega. Living systems archive the evolved and accumulated information by coding it into the species’ genes and passing the information from one generation to another through self-replication.

Nature has an enormous pool of inventions that passed the harsh test of practicality and durability in changing environment. In order to harness the most from Nature’s capabilities, it is critical to bridge between the fields of biology and engineering and to see cooperation of experts from both fields. In order to approach nature in engineering terms, it is necessary to sort biological capabilities along technological categories. Namely, one can take biologically identified characteristics and seek an analogy in terms of engineering as shown in chapter IV.

In this Phd thesis, the biological structures were classified into two main areas: experimental observation over time and experimental observation over scale.

Once the classification has been made, the biological structures were divided according to their ability to imitate Nature: they could be observed for simple imitation or for applying functioning logic. The last sub-division is related to the complexity of the problem and, therefore, the number of variables involved.

As examples of this kind of optimization, the structures of mole-rat burrows have been studied.

The Mole rats tunnels are constructed obeying to optimal criteria because they are the best excavator among subterranean rodents. The tunnels are realized with the aim of ensuring an adequate oxygen and nutrients supply as well as to avoid collapse mechanisms of the networks.

The objective of this example consists in exploring the possible mechanical-based relationship between the geometry of burrows and geo-mechanical characteristics of the soil that have evolved over time.

This approach could be utilized for investigating the possibility to formulate a new mechanical-based evolutionary hypothesis for which the overall dimensions of the mole rats also depend on the quality of soils. This would mean that the natural evolutionary process preserves and genetically select mole rat species able to reach and to excavate at depth such that the geo-mechanical quality of the resident soil increases as a result of the consolidation. This possible scenario would also allow to explain, within a mechanically perspective, the observed significant differences in size among the mole rat species. In-fact, the study has confirmed that mole-rats dig tunnels with different diameters into the allowable range of diameters to ensure the borrow stability.

Nature develops biological objects by means of growth or biologically controlled self-assembly adapting to the environmental condition and by using the most commonly found materials. As a result, biological materials and tissues are created by hierarchical structuring at all levels in order to adapt form and structure to the function, which have the capability of adaptation to changing conditions and self-healing.

As example of optimization over space, we have studied fiber-reinforced cartilage structures showing how the biological tissues are organized to minimized the strain energy function. In particular, the thickness of three layers of cartilage varying in the range of values that minimize the strain energy function.

As a final example, the poroelastic solution by Cowin (Cowin 1994) obtained for homogeneous plates was generalized to the case where the material is constituted by

two components. In order to demonstrate the behavior of the two plates analyzed and to be able to do an efficacious comparison with the results obtained by Cowin, the pore fluid pressure, the velocity flow profile, the variation of fluid content and the stress components are plotted across the thickness of the plates and versus time for different elastic moduli and Poisson's ratio

The results of this example allow to better interpret the adaptive processes governing many biological tissue, in which the hierarchical heterogeneous features result from optimization logics aimed to obtain best varying stiffness and permeability features.

The analytical solution could be used for designing controlled drug delivery system.

The core idea of this thesis, is that Nature always optimize the use of resources to reach a goal changing its shape accordingly to the functions that the structures or materials have to explicate.

In this manner it is possible design new intelligent materials and structures that mimic the rules and principles that govern Nature.

REFERENCES

- Abhijit M. Bhosale and James B. Richardson, 2008, Articular cartilage: structure, injuries and review of management, *British Medical Bulletin*; 87: 77–95
- Agarwal B. D., J. M. Lifshitz and L. J. Broutman, 1974, Elastic plastic finite element analysis of short fiber composites, *Fib. Sci. Tech.* 7, 45-62.
- Alberts, B., Johnson, A., Lewis, J., Raff, M., Roberts, K. & Walter, P. (eds) 2008 *Molecular biology of the cell*. New York, NY: Garland Science.
- Allaire, G., Kohn, R.V., 1993. Optimal design for minimum weight and compliance in plane stress using extremal microstructures. *Eur. J. Mech. A* 12: 839-878.
- Alleire, G., Bonnetier, E., Francfort, G., Jouve, F., 1997. Shape optimization by the homogenization method. *Numer. Math.* 76: 27-68.
- Alshits, V.I., Kirchner, O.K., 2001. Cylindrically anisotropic, radially inhomogeneous elastic materials. *Proc. R. Soc., A* 457, 671-693, London.
- Aksay IA, Weiner S., 1998, Biomaterials – is this really a field of research? *Curr Opin Solid State Mater Sci*;3:219–20.
- Ambrosio, L., Buttazzo, G., 1993. An optimal design problem with perimeter penalization. *Calc. Var.* 1: 55-69.
- Antinuchi.C.D., Busch C, Burrow structure in the subterranean rodent *Ctenomys talarum*, *Ctenomys talarum*. *Zeitschrift fur Saugertierkunde* 57:163-168.
- Argoubi M., Shirazi-Adl A., (1996), Poroelastic creep response analysis of a lumbar motion segment in compression, *Journal of Biomechanics*, 29, 1331-1339
- Ascenzi A., Bonucci E., (1968) The compressive properties of single osteons, *The Anatomical Record*, 161, 377-391
- Athanasiou KA., Natoli RM., (2008), *Introduction to Continuum Biomechanics*, Morgan & Claypool Publishers
- Askew MJ, Mow VC, 1978, The biomechanical function of the collagen ultrastructure of articular cartilage. *J Biomech Eng* 100:105-115.
- Banichuk, N.V., 1981. Optimization problems for elastic anisotropic bodies. *Archives of Mechanics*, 33: 347-363.
- Banichuk, N.V., 1983. *Problems and Methods in Optimal Structural Design*. Plenum Press, New York.
- Banichuk, N.V., 1996. Optimization of anisotropic properties for continuum bodies and structural elements using spectral methods of tensor analysis. *Mechanics of structure and Machines*, 24: 71-87.
- Banichuk, N.V., Kobelev, V.V., 1987. On optimal plastic anisotropy. *Prikladnaja Matematika I Mekhanika* 51: 489-495. Translated in: *Journal of Applied Mathematics and Mechanics* 51: 381-385.
- Barber, J.R., 1992. *Elasticity*. Dordrecht, Boston, London, Kluwer Academic Publishers.
- Barou O., Mekraldi S., Vico L., Boivin G., Alexandre C., Lafage-Proust MH., (2002) Relationship between Trabecular Bone Remodeling and Bone Vascularization: A Quantitative Study, *Bone*, 30(4), 604-612
- Bargel H, Koch K, Cerman Z, Neinhuis, C. 2006. Structure-function relationships of the plant cuticle and cuticular waxes – a smart material? *Functional Plant Biology*. 33(10): 893- 910.
- Bassnett, S., Missey, H., Vucemilo, I., 1999. Molecular architecture of the lens fiber cell basal membrane complex. *Journal of Cell Science* 112, 1155-2165
- Baxter L., Jain R.K., (1989), Transport of fluid and macromolecules in tumors I. Role of interstitial pressure and convection, *Microvascular Research*, 37, 77-104
- Beckers, M., 1999. Topology optimization using a dual method with discrete variables. *Struct. Optim.* 17: 14-24.

References

- Bendsøe, M.P., 1983. On obtaining a solution to optimization problems for solid elastic plates by restriction of the design space. *J. Struct. Mech.* 11: 501-521.
- Bendsøe, M.P., 1989. Optimal shape design as a material distribution problem. *Struct. Optim.* 1: 193-202.
- Bendsøe, M.P., 1995. *Optimization of Structural Topology Shape and Material*. Berlin Heidelberg: Springer Verlag.
- Bendsøe, M.P., Kikuchi, N., 1988. Generating optimal topologies in structural design using a homogenization method. *Comput. Methods. Appl. Mech. Eng.* 71, 197-224.
- Bendsøe, M.P., Guedes, J. M., Haber, R.B., Pedersen, P., Taylor, J.E., 1994. An analytical model to predict optimal material properties in the context of optimal structural design. *J. Appl. Mech.* 61: 930-937.
- Bendsøe M. P., Sigmund O., 1999 *Material interpolation schemes in topology optimization* *Archive of Applied Mechanics* 69 (1999) 635±654 Springer-Verlag 1999
- Bendjaballah M.Z., A.shirazi-Adl, Zukor D.J.,1995, *Biomechanics of the human knee joint in compression: reconstruction, mesh generation and finite element analysis*, *The knee* vol 2, pp 69-79
- Bharat Bhushan, 2009, *Biomimetics: lessons from nature – an overview*, *Philosophical . Transaction of the Royal Society A*, 367, 1445–1486
- Bhushan B, Yong C.J., Koch K. 2009. Self-Cleaning Efficiency of Artificial Superhydrophobic Surfaces. *Langmuir.* 25(5): 3240-3248.
- Biot MA., (1955), *Theory of elasticity and consolidation for a porous anisotropic solid*, *Journal of Applied Physics*, 26 (2), 182-185
- Blume, J.A., 1994. Elastic materials with coincident principal stress and strain axes. *Journal of Elasticity* 35: 275-280.
- Boehler, J.P., 1987. *Application of Tensor Functions in Solid Mechanics*. Springer, Wien.
- Bojarski, B., Iwaniec, T., 1983. Analytical foundations of the theory of quasi conformal mappings in R^n . *Annales Academiae Scientiarum, Ser. A.I. Mathematica*, 8, 257-324.
- Brody H, Ward, IM. 1971, *Modulus of short carbon and glass fibre reinforced composites*. *Poly. Eng. and Sci.* ;11(2):139.
- Budiansky, B., O'Connell, R.J., 1976. Elastic Moduli of a Cracked Solid. *Int. J. Solid Structure*, 12: 81-97.
- Bunge, G., 1970. *Texture Analysis in Material Science – Mathematical Methods*. Butterworth, London.
- Bush C., Antinuchi C.D. del Valle J.C., Kittlein MJ., Malizia AI, Vassallo AI, Zenuto RR, (2000), *Population ecology of subterranean rodents: In: Lacey EA, Patton JL, Cameron GN, Life underground*. University of Chicago Press, Chicago, 183-226
- Buttazzo, G., Dal Maso, G., 1993. An existence result for a class of shape optimization problems. *Arch. Rational Mech. Anal.* 122: 183-195.
- Capone C.C.C., (2010), *Porosity-Thermoelasticity Duality and FE-based strategies for the analysis of biological tissues*, Phd Thesis, Università di Napoli 'Federico II'
- Catterson B, Lowther DA, 1978, *Change in the metabolism of proteoglycans from sheep articular cartilage in response to mechanical stress*. *Biochim Biophys Acta* , 540:412-422
- Cauchy, A.L., 1923. *Rechercher sur l'équilibre et le mouvement intérieur des corps solides ou fluides, élastiques ou non élastique*. *Bulletin de la Société Philomatique*, 9-13 (Oeuvres (2) 2, pp. 300-304, Gauthier-Villars, Paris, 1889).
- Cauchy, A.L., 1927a. *De la pression ou tension dans un corps solide*, *Exercices de Mathématiques* 2, 42-56 (Oeuvres (2) 7, pp. 60-93, Gauthier-Villars, Paris, 1889).
- Cauchy, A.L., 1927b. *Sur les relations qui existent dans l'état d'équilibre d'un corps solide ou fluide* (Oeuvres (2) 7, pp. 141-145, Gauthier-Villars, Paris, 1889).
- Cauchy, A.L., 1928. *Sur les equations qui experiment les conditions d'équilibre ou les lois du mouvement intérieur d'un corps solide, élastique* (Oeuvres (2) 8, pp. 195-226, Gauthier-Villars, Paris, 1890).
- Cederbaum G., Li L., Schulgasser K., (2000), *Poroelastic Structures*, Elsevier
- Chadwick, P., Vianello, M., Cowin, S.C., 2001. A new proof that the number of linear elastic symmetries is eight. *Journal of the Mechanics and Physics of Solids* 49: 2471-2492.

- Chenais, D., 1975. On the existence of a solution in a domain identification problem. *J. Math. Anal. Appl.* 52: 189-289.
- Cheng Y.T., Rodak D.E., Wong C.A., Hayden C.A. 2006. Effects of micro- and nano-structures on the self-cleaning behaviour of lotus leaves. *Nanotechnology.* 17(5): 1359-1362.
- Cheng, G., Olhoff, N., 1981. An investigation concerning optimal design of solid elastic plates. *Int. J. Solids Struct.* 16: 305-323.
- Choquet-Bruhat, Y., Dewitt-Morette, C., Dillard-Bleick, M., 1977. *Analysis Manifolds and Physics.* North-Holland, Amsterdam.
- Christensen, R.M., 1979. *Mechanics of Composite Materials.* Wiley-Interscience, New York.
- Chung, M.Y, Ting, T.C.T, 1995. Line forces and dislocations in angularly inhomogeneous anisotropic piezoelectric wedges and spaces. *Philos. Mag. A* 71, 1335-1343.
- Cinquini C., Rovati M., 1995, Optimization methods in (structural) engeneering, *European Journal of Mechanics, A/Solids*, vol.14, n°3, pagg. 413-437.
- Cohen B., Lai WM., Mow VC., (1998), A Transversely Isotropic Biphasic Model for Unconfined Compression of Growth Plate and Chondroepiphysis, *Journal of Biomechanical Engineering*, 120, 491-496
- Connelly, R., Back, A., 1998. Mathematics and tensegrity. *American Scientist* 86, 142-151
- Cox H.L., 1952, The elasticity and strength of paper and other fibrous materials, *Brit. J. Appl. Phy.* 3, 72- 79
- Cowin SC., (2003), A Recasting of Anisotropic Poroelasticity in Matrices of Tensor Components, *Transport in Porous Media*, 50 (1-2), 35-56
- Cowin SC., (1989), *Bone Mechanics*, CRC Press, Boca Raton, FL.
- Cowin SC., Moss-Salentijn L., Moss ML., (1991) Candidates for the Mechanosensory System in Bone, *Journal of Biomechanical Engineering*, 113, 191-197
- Cowin SC., (2001), *Bone Mechanics Handbook*, CRC Press
- Cowin SC., (2002) Mechanosensation and fluid transport in living bone, *Journal of musculoskeletal & neuronal interactions*, 2(3), 256-260
- Cowin SC., Doty SB., (2007) *Tissue Mechanics*, Springer
- Cowin, S.C., 1985. The Relationship between the Elasticity Tensor and the Fabric Tensor, *Mechanics of Materials* 4: 137-147.
- Cowin, S.C., 1986. Wolff's law of trabecular architecture at remodelling equilibrium. *Journal of Biomechanical Engineering*, 108: 83-88.
- Cowin, S.C., 1987. Torsion of cylinders with shape intrinsic orthotropy. *J. Appl. Mech.*, 109, 778-782.
- Cowin, S.C., 1994. Optimization of the strain energy density in linear anisotropic elasticity. *Journal of Elasticity* 34: 45-68.
- Cowin, S.C., 1995. On the minimization and maximization of the strain energy density in cortical bone tissue. *Journal of Biomechanics* 28: 445-447.
- Cowin, S.C., 1997. Remarks on coaxiality of strain and stress in anisotropic elasticity. *Journal of Elasticity* 47: 83-84.
- Cowin SC., Gailani G., Benalla M., (2009) Hierarchical poroelasticity: movement of interstitial fluid between porosity levels in bones, *Philosophical Transactions of the Royal Society A*, 13, 367, 1902, 3401-3444
- Cowin SC., Mehrabadi MM., (2007), Compressible and incompressible constituents in anisotropic poroelasticity: The problem of unconfined compression of a disk, *Journal of the Mechanics and Physics of Solids*, 55, 161-193
- Cowin, S.C., Mehrabadi, M.M., 1987. On the identification of material symmetry for anisotropic elastic materials. *Quarterly Journal of Mechanics and Applied Mathematics* 40: 451-476.
- Cowin, S.C., Mehrabadi, M.M., 1992. The structure of the linear anisotropic elastic symmetries. *Journal of the Mechanics and Physics of the Solids* 40: 1459-1471.
- Cowin, S.C., Mehrabadi, M.M., 1995. Anisotropic symmetries in linear elasticity. *Applied Mechanics Review* 48: 247-285.
- Cowin, S.C., Yang, G., 2000. Material symmetry optimization by Kelvin modes. *J. Eng. Math* 37: 27-43.

References

- Cox, S., Lipton, R., 1996. Extremal eigenvalue problems for two-phase conductors. *Arch. Rational Mech. Anal.* 136: 101-118.
- Cutrera A.P., Antinuchi C.D., Mora M.S., Vassallo A.I., (2006), Home-Range and activity patterns of the south American subterranean rodent *Ctenomys Talarum*, *Journal of Mammology*, 87, 1183-1191
- Curran, D.R., Seaman, L., Shockey, D.A., 1987. Dynamic Failure of Soilds. *Physics Reports*, Nos. 5&6, 147: 253-388.
- Denton, M.J., Dearden, P.K., Sowerby, S.J., 2003. Physical law not natural selection as themajor determinant of biological complexity in the subcellular realm: new support for the pre-Darwinian conception of evolution by natural law. *Biosystems* 71, 297- 303.
- Detourney E., Cheng AHD., (1993), *Fundamentals of poroelasticity*, in: *Comprehensive Rock Engineering: Principles, Practice & Projects*, Vol. II (J. A. Hudson, ed.) Pergamon, Oxford
- Diaz, Lipton, R., 1997. Optimal material layout for 3D elastic structures. *Struct. Optim.* 13: 60-64.
- Edidin, A.A., Taylor, D.L., Bartel, D.L., 1991. Automatic assignment of bone moduli from CT data: a 3-D finite element study. *Trans. Orthop. Res. Soc.*, 16: 491.
- Eschenauer, H.A., Olhoff, N., 2001. Topology optimization of continuum structures: a review. *Applied Mechanics Review* 4: 331-390.
- Euler, L., 1757. Continuation des recherches sur la théorie du mouvement des fluids, *Hist. Acad. Berlin*, 316-361.
- Euler, L., 1771. Sectio tertia de motu fluidorum lineari potissimum aquae. *Novi Comm. Petrop.* 15: 219-360.
- Federer, H., 1969. *Geometric measure theory*, Springer- Verlag, New York.
- Fedorov, F.I., 1968. *Theory of elastic waves in crystals*. Plenum Press, New York.
- Forte, S., Vianello, M., 1996. Symmetry classes for elasticity tensor. *Journal of Elasticity* 43: 81-108.
- Fraldi, M., Cowin, S.C., 2004. Inhomogeneous elastostatic problem solutions constructed from stress-associated homogeneous solutions. *Journal of the Mechanics and Physics of Solids*, 52, 2207-2233.
- Fraldi, M., Guarracino, F., 2009. Limit analysis of collapse mechanisms in cavities and tunnels according to the Hoek–Brown failure criterion. *Int. J. Rock Mech. Min. Sci.* 46, 665–673.
- Fraldi, M., Guarracino, 2010. Analytical solutions for collapse mechanisms in tunnels with arbitrary cross sections *Int. J. Solids and Structures* 47, 216–223
- Fraldi, M., Guarracino, F., 2001. On a general property of a class of homogenized porous media. *Mech.Res.Comm.*, 28, 2, 213-221.
- Franzoso G., Zysset PK., (2009) Elastic Anisotropy of Human Cortical Bone Secondary Osteons Measured by Nanoindentation, *Journal of Biomechanical Engineering*, 131, 021001-1/11
- Fyhrie, D.P., Carter, D.R., 1986. A unifying principle relating stress to trabecular bone morphology. *Journal of Orthopaedic Research* 4: 304-317.
- Fuller, B.B., 1975. *Synergetics, Explorations in the Geometry of Thinking*. Macmillan.
- Germain, P., 1972. *Mécanique des milieux Continus*. Tome I, Masson, Paris.
- Giangreco, E., 2003. *Ingegneria delle strutture*. UTET, 2 vol.
- Gibson LJ, Ashby MF, Karam GN, Wegst U, Shercliff HR.,1995, The mechanical-properties of natural materials. 2. Microstructures for mechanical efficiency. *Proc R Soc London Ser A – Math Phys Sci*;450:141–62.
- Gonzáles, C., Segurado, J., Llorca, J., 2004. Numerical simulation of elasto-plastic deformation of composites: evolutions of the stress microfields and implications for homogenization models. *J. Mechanics and Physics of Solids* 52, 1573-1593.
- Goodman, J., Khon, R.V., Reyna, L.: Numerical study of a relaxed variational problem from optimal design. *Comput. Methods Appl. Mech. Eng.* 57:107-127.
- Gordon, J. E. 1976 *The new science of strong materials, or why you don't fall through the floor*, 2nd edn. London, UK: Pelican–Penguin
- Graham, R.L., Spencer, J.H., 1990. Ramsey theory. *Scientific American* (Jul), 80-85.
- Graham Scarr, 2009, Simple geometry in complex organisms, *Journal of Bodywork & Movement therapies* xx, 1-21

- Gu K.B., Li L.P., 2010, A human knee joint model considering fluid pressure and fiber orientation in cartilages and menisci, *medical engineering and physics*, 33, 497-503.
- Gurtin, M. E., 1972. *The Linear Theory of Elasticity*, Handbbuch der Physik, Springer, Berlin.
- Gurtin, M.E., 1981. *An introduction to continuum Mechanics*. Academic Press, New York.
- Haber, R.B., Bendsøe, M.P., Jog, C.S., 1996. A new approach to variable-topology shape design using a constraint on the perimeter. *Struct. Optim.* 11: 1-12.
- Harrigan, T.P., Mann R.W., 1984. Characterization of microstructural anisotropy in orthotropic materials using a second rank tensor. *Journal of Material Science*, 19: 761-767.
- Halpin JC, Pagano NJ. 1969,. The laminate approximation for randomly oriented fibrous composites. *J. Comp. Mater.*;3(2):720.
- Halpin JC, Tsai SW. , 1967, In Air Force Material Laboratory technical report, AFML-TR-67-423.
- Hashin, Z., Shtrikman, S., 1963. A variational approach to the theory of the elastic behaviour of multiphase materials. *J. Mech. Phys. Solids* 11: 127-140.
- He, Q.-C., Curnier, A., 1995. A more fundamental approach to damaged elastic stress-strain relations. *International J. of Solids and Structures*, 32: 1433-1457.
- Hearmon, R.F.S., 1961. *An introduction to applied anisotropic elasticity*. Oxford University Press, Oxford.
- Helnwein, P., 2001. Some remarks on the compressed matrix representation of symmetric second-order and fourth-order tensors. *Computer Methods in Applied Mechanics and Engineering* 190: 2753-2770.
- Heneghan P., Riches PE., (2008), Determination of the strain-dependent hydraulic permeability of the compressed bovine nucleus pulposus, *Journal of Biomechanics*, 41, 903-906
- Herbst M., Bennett N.C., 2006, Burrow architecture and burrowing dynamics of the endangered Namaqua dune mole rat (*Bathyergus jannetta*) (Rodentia: Batherygidae), *Journal of Zoology*, 270, 420-428.
- Hill, R., 1965a. A self-consistent mechanics of composite materials. *J. Mech. Phys. Solids*, 12, 213-22.
- Hill, R., 1967. The essential structure of constitutive laws for metal composites and polycrystals. *J. Mech. Phys. Solids*, 15, 79-95.
- Holmes MH., Mow VC., (1990), The non linear characteristics of soft gels and hydrated connective tissues in ultrafiltration, *Journal of Biomechanics*, 23, 1145-1156
- Horii, H., Nemat-Nasser, S., 1983. Overall moduli of solids with microcracks: Load-induced anisotropy. *J. Mech. Phys. Solids*, Vol. 31, 155-177.
- Huo, Y.Z., Del Piero, G., 1991. On the completeness of crystallographic symmetries in the description of symmetries of the elastic tensor. *Journal of Elasticity* 25: 203-246.
- Ilankamban, R., Krajcinovic, D., 1987. A Constitutive theory for Progressively Deteriorating Brittle Solids. *Int. J. Solids Structures*, 23, 1521-1534.
- Jackson C.R., Lubbe N.R., Robertson M.P., Setsaas T.H., J van der Waals & Bennett N.C., (2007), Soil properties and the distribution of the endangered Juliana's golden mole, *Journal of Zoology*, 274, 13-17
- Jeronimidis G. In: Elices M, editor. *Structural biological materials, design and structure–property relationships*. Amsterdam: Pergamon; 2000. p. 3–29 [chapters 1 and 2].
- Jog, C., Haber, R. B., Bendsøe, M.P., 1994. Topology design with optimized, self-adaptive materials. *Int. J. Numerical Methods Eng.* 37: 1323-1350.
- Jones, M.N., 1985. *Spherical Harmonics and Tensors for Classical Field Theory*. Wiley, New York.
- Julkunen P., Korhonen R.K., Nissi M.J. and Jurvelin J.S., 2008, Mechanical characterization of articular cartilage by combining magnetic resonance imaging and finite-element analysis—a potential functional imaging technique, *Physics in medicine and biology*, 53, 2425-2438.
- Kanatani, K., 1984. Distribution of directional data and fabric tensors. *Int. J. Engng Sci.* 22, 149-164.
- Kartvelishvili, V.M., Kobelev, V.V., 1984. Rational schemes for reinforcing laminar plates from composite materials. *Prikladnaja Matematika I Mekanika* 48: 68-80. Translated in: *Journal of Applied Mathematics and Mechanics* 48: 40-49.

References

- Keyak J.H., Meagher, J.M., Skinner, H.B., Mote, C.D., 1990. Automated three-dimensional finite element modelling of bone: a new method. *J. Biomed. Eng.*, 12: 389-397.
- Khon, R.V., Strang, G., 1986. Optimal design and relaxation of variational problems. *Commun. Pure Appl. Math.* 39: 1-25 (Part I), 139-182 (Part II), 353-377 (Part III).
- Kiviranta I, Jurvelin J, Tammi M, Saamanen AM, Helminen HJ, 1987, Weight bearing controls glycosaminoglycan concentration and articular cartilage thickness in the knee joints of young beagle dogs. *Arthritis Rheum* 30:801-809
- Kouznetsova, V., Brekelmans, W.A.M., Baaijens, F.P.T., 2001. An approach to micro-macro modeling of heterogeneous materials. *Computational Mechanics* 27, 37-48.
- Krajcinovic, D., 1996. *Damage Mechanics*. North-Holland.
- Krenchel H. *Fibre reinforcement*. Copenhagen: Akademisk Forlag, 1964.
- Kurosawa H, Fukubayashi T, Nakajima H, 1980, Load bearing mode of the knee joint physical behaviour of the knee joint with or without menisci, *Clin Orthop Rel Res*; 149: 283-90
- Lelong-Ferrand, J., 1963. *Géométrie Différentielle*. Masson, Paris.
- Lekhnitskii, S.G., 1963. *Theory of elasticity of an anisotropic elastic body*, Holden Day Inc., San Francisco.
- Lekhnitskii, S.G., 1981. *Theory of elasticity of an anisotropic elastic body*, Mir Publisher, Moscow.
- Lemaitre, J., 1986. Local Approach of Fracture, *Eng. Fracture Mech.*, 25: 523-537.
- Lemaitre, J., 1992. *A Course on Damage Mechanics*, Springer-Verlag, Berlin, Germany.
- Lemaitre, J., Chaboche, J.L., 1978. Aspect Phenomenologique de la Rupture par Endommagement, *J. Mech. Applique*, 2: 317-365.
- Lemaitre, J., Dufailly, J., 1987. Damage measurement. *Engng Fracture Mech.*, 28, 643-661.
- Lions, J.L., 1985. *Les Methodes de l'Homogenisation: Theorie et Applications en Physique*, Saint Germain Paris, Eyrolles Ed.
- Love, A.E.H., 1994. *A treatise on the mathematical theory of elasticity*, fourth ed. Dover, New York.
- Lovegrove BG ,1989, The cost of burrowing by the social mole-rats (Bathyergidae) *Cryptomys damarensis* and *Heterocephalus glaber*. The role of soil moisture. *Physiol Zool* 62, 449-469
- Lubarda, V., Krajcinovic, D., 1993. Damage Tensors and the Crack Density Distribution, *Int. J. Damage Mech.*, 48: 2859-2877.
- Luna F., Antinuchi C.D., 2006, Cost of foraging in the subterranean rodent *Ctenomys talarum*: effect of the soil hardness, *Canadian Journal of Zoology*, 84, 661-667
- Luna F, Antinuchi CD, Busch C ,2002, Digging energetics in the South American rodent, *Ctenomys talarum* (Rodentia, Ctenomyidae). *Canadian Journal of Zoology*, 80, 2144-2149
- Luna F., Antinuchi C.D., 2007, Energy and distribution in subterranean rodents: Sympatry between two species of the genus *Ctenomys*, *Comparative Biochemistry and Physiology Part A* 147, 948-954
- Luna F., Antenucci C.D., Bozinovic F., 2009, Comparative energetics of the subterranean *Ctenomys* rodents: breaking patterns, *Physiological and Biochemical Zoology*, 82(3), 226-235
- Luna F., Antinuchi C.D., 2007, Effect of tunnel inclination on digging energetics in the tuco-tuco, *Ctenomys talarum* (Rodentia: Ctenomyidae), *Naturwissenschaften*, 94, 100-106
- Luna F., Antenucci C.D., 2007, Energetics and thermoregulation during digging in the rodent tuco-tuco (*Ctenomys talarum*), *Comparative Biochemistry and Physiology Part A*, 146, 559-564
- Lurie, K.A., Cherkayev, A. V., Fedorov, A. V., 1982. Regularization of optimal design problems for bars and plates. *JOTA*, 37: 499-522 (Part I), 37: 523-543 (Part II), 42: 247-282 (Part III).
- Malliavin, P., 1972. *Géométrie Différentielle Intrinsèque*. Hermann, Paris
- Mandel, J., 1971. *Plasticité classique et viscoplasticité*. Springer-Verlag, Vienna (CISM Lecture Notes, Udine, Italy).
- Marcus, M., Mizel, V.J. 1973. Transformations by functions in Sobolev spaces and lower semicontinuity for parametric variational problems, *Bull. Amer. Math. Soc.* 79, 790-795.
- Marquet PG, Van De Berg AJ, Simonet JC, 1975, Femortibial weight-bearing areas, *J. Bone Joint Sur*; 57 A:766-71
- Mehrabadi, M.M., Cowin, S.C., 1990. Eigentensors of linear anisotropic elastic materials. *Quarterly Journal of Mechanics and Applied Mathematics* 43: 15-41.

References

- Mehrabadi MM., Cowin SC., Jaric J., (1995) Six-dimensional orthogonal tensor representation of the rotation about an axis in three dimensions, *International Journal Solids Structures*, 32, 439-44
- Marom, S.A., Linden, M., Computed aided stress analysis of long bones utilizing computer tomography. *J. Biomech.* 23:300-404.
- Marsden, J.E., Hughes, T.J.R., 1983. *Mathematical foundations of elasticity*. Prentice-Hall, Englewood Cliffs.
- Mattheck C, Kubler H., 1995, *The internal optimization of trees*. Berlin: Springer Verlag.
- Maugin, G.A., 1993. *Material inhomogeneities in elasticity*. Chapman & Hall.
- Michell A. J., 1904, The limits of economy in frame structures, *Phil. Mag. Sect. 6*, vol.8, pagg. 589-597.
- Milton, G.W., Cherkaev, A. V., 1995. Which elasticity tensor are realizable? *J. Eng. Mat. Tech.* 117: 483-493.
- Mlejnik, H.P., Schirmmacher, R., 1993. An engineering approach to optimal material distribution and shape finding. *Comput. Methods Appl. Mech. Eng.* 106: 1-26.
- Morris, M. A., Lopez-Curato, J. A., Hughes, S. P. F., An, K. N., Bassingthwaighte, J. B. and Kelly, P. J., 1982, Fluid spaces in canine bone and marrow, *Microvascular, Res.* 23, 188-200.
- Mow VC, Mak AF, 1987, Lubrication of diarthrodial joints. In: *Handbook of Bioengineering*, ed by R Skalak, S Chien, New York, McGraw-Hill, pp 5.1-5.34
- Mow VC., Kuei SC., Lai WM., Armstrong CG., 1980, Biphasic creep and stress relaxation of articular cartilage in compression: Theory and experiments, *Journal of Biomechanical Engineering*, 102, 73-84
- Nadeau, J.C., Ferrari, M., 1998. Invariant tensor-to-matrix mappings for evaluation of tensorial expressions. *Journal of Elasticity*, 52: 43-61.
- Nemat-Nasser, S., Horii, H., 1993. *Micromechanics: Overall properties of heterogeneous materials*. North-Holland.
- Netti P.A., Baxter L.T., Boucher Y., Skalak R., Jain R.K., (1995), Time-dependent behavior of interstitial fluid pressure in solid tumors: implications for drug delivery, *Cancer Research*, 55, 5451-5458
- Netti P.A., Roberge S., Boucher Y., Baxter L.T., Jain R.K., (1996), Effect of Transvascular fluid exchange on pressure-flow relationship in tumors: a proposed mechanism for tumor blood flow heterogeneity, *Microvascular Research*, 52, 27-46
- Netti P.A., Travascio F., Jain R.K., (2003), Coupled Macromolecular Transport and Gel Mechanics: Poroviscoelastic Approach, *AIChE Journal*, 49(6), 1580-1596
- Nevo E., 1999, *Mosaic evolution of subterranean mammals: regression, progression and global convergence*. Oxford university press, New York.
- Niordson, F.I.: Optimal design of plates with a constraint on the slope of the thickness function. *Int. J. Solids Struct.* 19:141-151.
- Noll, W., 1959. The foundation of classical mechanics in the light of recent advances in continuum mechanics, in *The axiomatic method, with Special Reference to Geometry and Physics*, pp. 266-281, North Holland, Amsterdam.
- Nye, J.F., 1957. *Physical properties of crystals. Their Representation by tensors and matrices*. Oxford University Press, Oxford.
- O'Donnell B. Fabrication related variations in property in injection mouldings. Ph.D. Thesis, University of Newcastle-upon-Tyne, 1990.
- Odgaard, A., Kabel, J., van Rietbergen, B., Dalstra, M., Huiskes, R., 1997. Fabric and elastic principal directions of cancellous bone are closely related. *J. Biomechanics* 30, 5: 487-495.
- Olhoff, N., Rønholt, E., Scheel, J., 1998. Topology optimization of three-dimensional structures using optimum microstructures. *Struct. Optim.* 16: 1-18.
- Onat, E.T., 1984. Effective properties of elastic materials that contain penny shaped voids. *Int. J. Engng Sci.* 22, 1013-1021.
- Onat, E.T., Leckie, F.A., 1984. Representation of mechanical behaviour in the Presence of Changing Internal Structure, *J. Appl. Mech.*, 55: 1-10.
- Pedersen, P., 1989. On optimal orientation of orthotropic materials. *Struct. Opt.* 1: 101-106.
- Pedersen, P., 1990. Bounds on elastic energy in solids of orthotropic materials. *Struct. Opt.* 2: 55-62.

- Pena E., Calvo B, Martinez M.A., Palanca D., Doblare' M., 2005, Finite element analysis of the effect of meniscal tears and meniscectomies on human knee biomechanics, *Clinical Biomechanics* 20, 498–507
- Perssinotti P., Antenucci C.D., Zenuto R., Luna F., (2009), Effect of diet quality and soil hardness on metabolic rate in the subterranean rodent *Ctenomys Talarum*, *Comparative Biochemistry and Physiology Part A*, 154, 298-307
- Petersson, J., 1998. Some convergence results in perimeter-controlled topology optimization. *Comput. Methods Appl. Mech. Eng.* 171: 123-140.
- Petersson, J., Sigmund, O., 1998. Slope constrained topology optimization. *Int. J. Numerical Methods Eng* 41:1417-1434.
- Prager, W.; Rozvany, G.I.N. 1977: Optimization of structural geometry. In: Bednarek, A.R.; Cesari, L. (eds.) *Dynamical systems*, pp. 265–293. New York: Academic Press
- Rado, T., Reichelderfer, P.V., 1955. *Continuous transformations in analysis*. Springer-Verlag, Berlin.
- Rahaman Abdel, Hafzy MS, 1994, Three-dimensional dynamic modeling of the tibio-femoral joint. In: Tarbell JM (ed) *Advances in Bioengineering ASME*
- Rho, J.Y., Hobatho, M.C., Ashman, R.B., 1995. Relation of mechanical properties to density and CT number in human bone. *Med. Eng. Phys.*, 17: 347-355.
- Riches PE., Dhillon N., Lotz J., Woods AW., McNally DS., 2002, The internal mechanics of the intervertebral disc under cyclic loading, *Journal of Biomechanics*, 35, 1263-1271
- Ringertz, U., 1993. On finding the optimal distribution of material properties. *Struct. Optim.* 5: 265-267.
- Rychlewski, J., 1984. On Hooke's law. *Prikladnaja Matematika i Mekanika* 48: 420-435; Translated in: *J. Appl. Math. Mech.* 48: 303-314.
- Romanach S., Seabloom E.W., Reichman O.J., Rogers W.E., Cameron G.N., (2005), Effect of species, sex, age, and habitat on geometry of pocket gopher foraging tunnels, *Journal of Mammalogy*, 86(4), 750-756
- Roose T., Netti PA., Munn LL., Boucher Y., Jain RK., 2003, Solid stress generated by spheroid growth estimated using a linear poroelasticity model, *Microvascular Research*, 66, 201-212
- Rossow, M. P.; Taylor, J. E.: A finite element method for the optimal design of variable thickness sheets. *AIAA J.* 11 (1973) 1566±1569
- Rovati, M., Taliercio, A., 1991. Optimal orientation of the symmetry axes of orthotropic materials. In: Eschenauer, H.A., Mattheck, C., Olhoff, N. (Eds.), *Engineering Optimization in Design Processes*. Springer-Verlag, Heidelberg, pp. 127-154.
- Rovati, M., Taliercio, A., 1993. Bounds on the elastic strain energy density in 3-D bodies with material symmetries. In: Herskowits, J. (Ed.), *Proceedings of Structural Optimization '93*, Rio de Janeiro, August 2-6, pp. 353-360.
- Rovati, M., Taliercio, A., 2003. Stationary of the strain energy density for some classes of anisotropic solids. *Int. J. of Solids and Structures.*, 40: 6043-6075.
- Rozvany, G.I.N., Zhou, M., Sigmund, O., 1994. *Topology Optimization in Structural Design*. In Adeli H (ed.): *Advances in Design Optimization*, pp. 340-399. London: Chapman and Hall.
- Rozvany, G.I.N. 2001: Aims, scope, methods, history and unified terminology of computer-aided topology optimization in structural mechanics. *Struct Multidisc Optim* 21, 90–108 Springer-Verlag 2001
- Sacchi Landriani, G., Rovati, M., 1991. Optimal 2-D structures made of composite materials. *J. Eng. Materials Technology, Transactions of the ASME* 113, 88-92.
- Salzstein, R.A., Pollack, S.R., Mak, A.F.T. and Petrov, N., (1987), Electromechanical potentials in cortical bone - A continuum approach., *J. Biomechanics*, 20, 261–270.
- Sanner, M.F., Stolz, M., Burkhard, P., Kong, X.P., Min, G., Sun, T.T., Driamov, S., Aebi, U., Stoffler, D., 2005. Visualizing nature at work from the nano to the macro scale. *NanoBiotechnology* 1, 7-21.
- Schwartz, L., 1967. *Cours d'Analyse*. Hermann, Paris.
- Sergey V. Dmitriev, Nobuhiro Yoshikawa, Sergey V. Dmitriev · Nobuhiro Yoshikawa, 2010, Rapid change of stresses in thickness direction in long orthotropic tube under internal pressure and axial load, *Acta Mech* 211, 323–33

- Seregin, G.A., Troitskii, V.A., 1981. On the best position of elastic symmetry planes in an orthotropic body. *Prikladnaja Matematika i Mekhanika* 45: 185-189; Translated in: *J. Appl. Math. Mech.* 45: 139-142.
- Sgarra, C., Vianello, M., 1997a. Directions of coaxiality between pure strain and stress in linear elasticity. *Journal of Elasticity* 46: 263-265.
- Sgarra, C., Vianello, M., 1997b. Rotations which make strain and stress coaxial. *Journal of Elasticity* 47: 217-224.
- Sichilima A.M., Bennett N.C., Faulkes C.G., Le Comber S.C., (2008), Evolution of African mole-rat sociality: burrow architecture, rainfall and foraging in colonies of the cooperatively breeding *Fukomys mechowii*, *Journal of Zoology*, 275, 276-282
- Sigmund, O., 1994. Design of Material Structures using Topology Optimization. DCAMM Special report S69, Department of Solid Mechanics, Technical University of Denmark, Lyngby.
- Sigmund, O., 1995. Tailoring materials with prescribed elastic properties. *Mech. Mat.* 20: 351-368.
- Sigmund, O.; Torquato, S., 1997, Design of materials with extreme thermal expansion using a three-phase topology optimization method. *J. Mech. Phys. Solids* 45, 1037±1067
- Sirotin, Y., Chaskolkaia, M., 1984. *Fondements de la physique des cristaux*. Éditions Mir, Moscow.
- Smith, K.T., 1983. *Primer of Modern Analysis*, Second Edition, Springer-Verlag, New York.
- Smith, G.F., Rivlin, R.S., 1958. The strain energy function for anisotropic elastic materials. *Transaction of American Mathematical Society* 88, 175-193.
- Solga A, Cerman Z, Striffler B.F., Spaeth M, Barthlott W. 2007. The dream of staying clean: Lotus and biomimetic surfaces. *Bioinspiration and Biomimetics*. 2(4): S126-S134.
- Skiliba J., Sumbera R., Chitaukali W.N., Burda H., (2009), Home-range dynamics in a solitary subterranean rodent, *Ethology*, 115, 217-226.
- Spaeth M, Solga A, Barthlott W, Cerman Z. 2006. Funktionale Bautenoberflächen: Wie testet man mikrobiellen Bewuchs? *Altbauinstandsetzung*. 11: 203–14
- Stewart, I., 1998. *Life's Other Secret: The Mathematics of the Living World*. Penguin.
- Sumbera R., Skiliba J., Elichova M., Chitaukali W.N., Burda H., (2007), Natural history and burrow system architecture of the silvery mole-rat from *Brachystegia woodland*, *Journal of Zoology*, 274, 77-84
- Sumbera R, Burda H, Chitaukali WN, Kudova J., (2003), Silvery molerats (*Heliophobius argenteocinereus*, Bathyergidae) change their burrow architecture seasonally. *Naturwissenschaften* 90:370–373
- Suquet, P., 1981a. Sur les equations de la plasticité: existence et régularité des solutions. *J. Mécanique*, 20, 3-40.
- Sutcliffe, S., 1992. Spectral decomposition of the elasticity tensor. *Journal of Applied Mechanics, Transactions of the ASME* 59: 762-773.
- Swan, C. C.; Kosaka, I., 1997, Voigt-Reuss topology optimization for structures with linear elastic material behaviours. *Int. J. Numer Methods Eng.* 40, 3033±3057
- Taya M. and R. J. Arsenault, 1989, *Metal Matrix Composites-Thermomechanical Behavior*, Pergamon Press, USA.
- Terzaghi K., (1943), *Theoretical Soil Mechanics*, Wiley, New York
- Theocaris, P.S., Sokolis, D.P., 2000a. Invariant elastic constants and eigentensors of orthorhombic, tetragonal, hexagonal and cubic crystalline media. *Acta Crystallographica Sect. A* 56: 319-331.
- Theocaris, P.S., Sokolis, D.P., 2000b. Spectral decomposition of the compliance fourth-rank tensor for orthotropic materials. *Archives of Applied Mechanics* 70: 289-306.
- Thompson AW., 1992, *On growth and form – the complete revised edition* (unaltered republication of Cambridge Univ. Press, 1942) ed.. Dover Publications.
- Ting, T.C.T., 1996. *Anisotropic elasticity- Theory and applications*. Oxford.
- Toll S., 1992, Interpolative aggregate model for short fibre composites. *J. Comp. Mater.*; 26(12):1767.
- Torquato, S., Gibiansky, L.V., Silva, M.J., Gibson, L.J., 1998. Effective mechanical and transport properties of cellular solids. *Int. J. Mech. Sci.* 40: 71-82.

References

- Torquato, S.; Gibiansky, L. V., 1998, Silva, M. J.; Gibson, L. J.: Effective mechanical and transport properties of cellular solids. *Int. J. Mech. Sci.* 40:71±82
- Tözeren, A., Skalak, R., 1989. Does fabric tensor exist for a fabric?, *Journal of Material Science*, 24, 1700-1706.
- Truesdell, C., Noll, W., 1965. The non-linear field theories of mechanics. *Handbuch der Physik*, vol. III/3, Springer, Berlin.
- Truesdell, C., Toupin, R.A., 1960. The Classical Field Theory. *Handbuch der Physik*, vol. III/1, Springer, Berlin.
- Turner, C.H., Cowin, S.C., 1987. Dependence of elastic constants of an anisotropic porous material upon porosity and fabric. *Journal of Material Science*, 22, 3178-3184.
- Urciuolo F., Imparato G., Netti PA., (2008), Effect of Dynamic Loading on Solute Transport in Soft Gels Implication for Drug Delivery, *AIChE Journal*, 54, 824-834
- Vianello, M., 1996a. Coaxiality of strain and stress in anisotropic linear elasticity. *Journal of Elasticity* 42: 283-289.
- Vianello, M., 1996b. Optimization of the stored energy and coaxiality of strain and stress in finite elasticity. *Journal of Elasticity* 44: 193-202.
- Vilenkin, N.J., 1969. *Fonctions Spéciales et Théorie de la Représentation des Groupes*. Dunod, Paris.
- Vodopyanov, S.K., Goldshtein, V.M., Reshetnyak, Yu. G., 1979. On geometric properties of function with generalized first derivatives. *Russian Math. Surveys* 34, 19-74.
- Voigt W., 1928. *Lehrbuch der Kristallphysik*. Leipzig: B.G. Teubner Verlag.
- Xie, Y. M.; Steven, G. P.: *Evolutionary Structural Optimisation*. Berlin: Springer Verlag 1997
- Wagner P, Furstner R, Barthlott W, Neinhuis C. 2003. Quantitative assessment to the structural basis of water repellency in natural and technical surfaces. *Journal of Experimental Botany*. 54(385): 1295-1303
- Wagner, L.D., Gibson, L.J., 2000. The mechanical behaviour of interpenetrating phase composites - I: modelling. *International Journal of Mechanical Science* 42, 925-942.
- Walpole, L.J., 1984. Fourth-rank tensors of the thirty-two crystal classes: multiplication tables. *Proceedings of the Royal Society of London A* 391: 149-179.
- Wong, T.-f., 1985. Geometric Probability Approach to the Characterization and Analysis of Microcracking in Rocks, *Mech. of Materials*, 4: 261-276.
- Zhang D., Cowin SC., (1994) Oscillatory bending of a poroelastic beam, *J. Mech. Phys. Solids*, Vol. 42, No. 10, 1575-1599
- Zhou, M., Rozvany, G.I.N., 1991. The COC Algorithm, Part II: Topological geometrical and generalized shape optimization. *Comput. Methods Appl. Mech. Eng.* 89: 309-336.
- Zysset, P.K., Curnier, A., 1995. An alternative model for anisotropic elasticity based on fabric tensors, *Mech. of Materials*, 21: 243-250.